

# Longitudinal Target-Spin Azimuthal Asymmetry in Deeply-Virtual Compton Scattering

## DISSERTATION

zur Erlangung des akademischen Grades  
doctor rerum naturalium  
(Dr. rer. nat.)  
im Fach Physik

eingereicht an der  
Mathematisch-Naturwissenschaftlichen Fakultät I  
Humboldt-Universität zu Berlin

von  
Herrn Magister Mikhail Kopytin  
geboren am 21.09.1977 in St. Petersburg, Russland

Präsident der Humboldt-Universität zu Berlin:  
Prof. Dr. Christoph Marksches

Dekan der Mathematisch-Naturwissenschaftlichen Fakultät I:  
Prof. Thomas Buckhout, PhD

Gutachter:

1. Prof. Dr. Michael Düren
2. Prof. Dr. Hermann Kolanoski
3. Prof. Dr. Thomas Lohse

eingereicht am:	17 Mai 2006
Tag der mündlichen Prüfung:	22 August 2006



## Abstract

As a generalization of the usual Parton Distribution Functions (PDFs) Generalized Parton Distributions (GPDs), introduced a decade ago, contain additional information about quark and gluon distributions in the plane transverse to the direction of motion of the nucleon. Strong interest in GPDs was triggered by the work of X. Ji who demonstrated that in the forward limit GPDs can give information about the total angular momentum carried by quarks (gluons) in the nucleon. The hard exclusive electroproduction of a real photon, called Deeply Virtual Compton Scattering (DVCS), appears to be the theoretically cleanest way to access GPDs experimentally. This process has a final state identical to that of the Bethe-Heitler (BH) process where the photon is radiated from either incoming or outgoing lepton. Both processes are experimentally indistinguishable as their amplitudes interfere. The interference term involves linearly the amplitudes of the DVCS process giving access to GPDs.

In this thesis results from HERMES are reported on an azimuthal asymmetry with respect to the spin of the proton target, which is attributed to the interference between the Bethe-Heitler process and the DVCS process. The asymmetry, also referred to as the longitudinal target-spin asymmetry (LTSA), gives access mainly to the polarized GPD  $\tilde{H}$ . The kinematic dependences of the LTSA on  $t$ ,  $x_B$  and  $Q^2$  are measured and compared with the corresponding measurements on the deuteron. The results are compared with theoretical calculations and with the recent CLAS measurements.

The data, used for analysis in this thesis, have been accumulated by the HERMES experiment at DESY scattering the HERA 27.6 GeV positron beam off hydrogen and deuterium gas targets.

Additionally, production tests of the HELIX128 3.0 chip are discussed. The chip is the frontend readout chip of the silicon recoil detector. The latter is a part of the HERMES recoil detector, which is built around the target area in order to detect the recoiling products of exclusive processes. The primary goal of this detector is to facilitate a more complete study of DVCS by registering also the recoiling protons.

## Keywords:

DVCS, LTSA, azimuthal, HELIX

## Zusammenfassung

Als eine Verallgemeinerung der gewöhnlichen Partonverteilungsfunktionen (PDF) enthalten die vor etwa zehn Jahren eingeführten verallgemeinerten Partonverteilungen (GPD) zusätzliche Informationen über die Quark- und Gluonverteilungen in der zur Bewegungsrichtung des Nukleons senkrechten Ebene. Starkes Interesse an den GPD wurde durch die Arbeit von X. Ji hervorgerufen, der demonstrierte, dass die GPD im Vorwärtslimit Informationen über den Gesamtdrehimpuls liefern, der von den Quarks (Gluonen) im Nukleon getragen wird. Die harte exklusive Elektroerzeugung eines reellen Photons, genannt ‘Tiefvirtuelle Compton Streuung’ (DVCS) ist der theoretisch klarste praktisch gangbare Weg, experimentellen Zugang zu den GPD zu ermöglichen. Dieser Prozess hat einen Endzustand, der identisch zu dem des Bethe-Heitler (BH) Prozesses ist, bei welchem das Photon entweder vom ein- oder auslaufenden Lepton emittiert wird. Beide Prozesse sind experimentell ununterscheidbar, daher interferieren ihre Amplituden. Der Interferenzterm enthält linear die Amplituden des DVCS Prozesses, was den direkten Zugang zu den GPD erlaubt.

In der vorliegenden Arbeit werden Ergebnisse vom Experiment HERMES präsentiert, welche eine azimutale Asymmetrie bezüglich des Spins des Protontargets zeigen, die von der Interferenz zwischen dem Bethe-Heitler- und dem DVCS-Prozess herrührt. Diese Asymmetrie, auch als longitudinale Target-Spin Asymmetrie (LTSA) bezeichnet, erlaubt hauptsächlich den Zugang zur polarisierten GPD  $\tilde{H}$ . Die kinematische Abhängigkeit der LTSA von  $t$ ,  $x_B$  und  $Q^2$  wurde gemessen und mit vorhandenen Messungen am Deuteron verglichen. Die Ergebnisse wurden mit theoretischen Berechnungen und mit aktuellen Messungen des CLAS-Experiments verglichen.

Die Daten, die zur Analyse in der vorliegenden Arbeit verwendet werden, wurden am HERMES Experiment bei DESY genommen, wobei im HERA-Speicherring Positronenstrahlen der Energie 27.5 GeV an Wasserstoff- und Deuterium-Gas-Targets gestreut wurden.

Darüber hinaus werden Produktionstests des HELIX-128 3.0 chips diskutiert. Der Chip ist ein Frontend-Auslesechip beim Silizium-Rückstossdetektor. Letzterer ist Teil des HERMES-Rückstossdetektors, welcher den Target-Bereich umschliesst, um die Rückstossprodukte der exklusiven Prozesse zu detektieren. Das primäre Ziel dieses Detektors ist es, eine vollständigere Untersuchung von DVCS durch zusätzliche Registrierung der Rückstossprotonen zu ermöglichen.

### **Schlagwörter:**

DVCS, LTSA, azimutal, HELIX

# Contents

<b>1</b>	<b>Introduction</b>	<b>1</b>
<b>2</b>	<b>Generalized Parton Distributions</b>	<b>5</b>
2.1	General Formalism in Deep Inelastic Scattering . . . . .	5
2.2	Formalism of Generalized Parton Distributions . . . . .	7
2.2.1	Definition of Generalized Parton Distributions . . . . .	8
2.2.2	Twist-three Generalized Parton Distributions . . . . .	9
2.3	Basic properties of Generalized Parton Distributions . . . . .	10
2.3.1	Ji's Relation . . . . .	11
2.4	Models of Generalized Parton Distributions . . . . .	12
2.4.1	Parameterization of the Generalized Parton Distribu- tions H and E . . . . .	12
2.4.2	Parameterization of the Generalized Parton Distribu- tion H-tilde . . . . .	15
2.4.3	Parameterization of the Generalized Parton Distribu- tion E-tilde . . . . .	15
<b>3</b>	<b>Deeply Virtual Compton Scattering</b>	<b>17</b>
3.1	Deeply Virtual Compton Scattering in Terms of Generalized Parton Distributions . . . . .	17
3.2	Interference with the Bethe-Heitler Process . . . . .	20
3.3	Angular Dependence of the Photoproduction Cross Section . .	23
3.4	Longitudinal Target-Spin Asymmetry . . . . .	23
3.5	Beam-Spin and Beam-Charge Asymmetries . . . . .	25
3.6	Transverse Target-Spin Asymmetry . . . . .	27
<b>4</b>	<b>The HERMES Experiment</b>	<b>29</b>
4.1	The HERA Beam . . . . .	30
4.1.1	Beam Polarization Measurement . . . . .	31
4.1.2	Luminosity Monitor . . . . .	33
4.2	HERMES Internal Gas Target . . . . .	34

4.2.1	The Longitudinally Polarized Gas Target . . . . .	34
4.3	Tracking System . . . . .	37
4.4	Particle Identification . . . . .	38
4.4.1	Transition Radiation Detector . . . . .	39
4.4.2	Preshower and Electromagnetic Calorimeter . . . . .	39
4.5	HERMES Trigger . . . . .	41
4.6	Recoil Detector . . . . .	42
<b>5</b>	<b>Data Selection</b>	<b>45</b>
5.1	Data Processing . . . . .	45
5.2	Data Quality . . . . .	46
5.3	Event Selection . . . . .	46
5.3.1	Selection of DIS Events . . . . .	47
5.3.2	Selection of Exclusive Events . . . . .	49
5.4	Beam Polarization Balancing . . . . .	54
5.5	Data Normalization . . . . .	55
<b>6</b>	<b>Monte Carlo Studies</b>	<b>59</b>
6.1	Event Simulation . . . . .	59
6.2	Data-to-Monte Carlo Comparison . . . . .	61
6.3	Background Contributions . . . . .	64
6.4	Resolution Studies . . . . .	66
<b>7</b>	<b>Extraction of the Longitudinal Target-Spin Asymmetry</b>	<b>73</b>
7.1	Measurement of the Longitudinal Target-Spin Asymmetry . .	73
7.2	Fit Method . . . . .	74
7.3	Results and Cross Check . . . . .	76
7.4	Systematic Studies . . . . .	78
7.4.1	Geometric Stability of the Measured Asymmetry . . . .	78
7.4.2	Stability of the Result over the Data Taking Period . .	80
7.4.3	Fit Stability . . . . .	81
7.4.4	Study of H0 Hodoscope Efficiency . . . . .	83
7.4.5	Contribution from pi0-background . . . . .	84
7.4.6	Calorimeter Miscalibration and Misalignment . . . . .	88
7.4.7	Contribution from the Transverse TSA to the Longi- tudinal TSA . . . . .	91
7.4.8	Smearing Effects . . . . .	92
7.4.9	Number of Bins in phi . . . . .	95
7.5	Systematic Uncertainties . . . . .	96

<b>8</b>	<b>Results and Discussion</b>	<b>99</b>
8.1	Comparison with Theoretical Calculations. . . . .	103
8.2	Comparison with the CLAS Measurements . . . . .	109
<b>9</b>	<b>Conclusions and Outlook</b>	<b>115</b>
<b>A</b>	<b>HELIX128 3.0 Production Tests</b>	<b>129</b>
A.1	Layout of the Silicon Module Control . . . . .	131
A.2	HELIX128 3.0 . . . . .	132
A.3	Test Method . . . . .	135
A.3.1	Programming of the Chip's Registers . . . . .	136
A.3.2	Running Modes and Control Tokens . . . . .	139
A.3.3	Reset . . . . .	142
A.3.4	Synchronicity Monitor . . . . .	142
A.3.5	Addressing . . . . .	142
A.4	Production Test Stand . . . . .	143
A.4.1	Hardware Components . . . . .	146
A.4.2	Test Stand Timing . . . . .	147
A.4.3	Labeling of Chips . . . . .	151
A.4.4	Test Sequence . . . . .	152
A.5	Analysis of the Memory Cell Properties . . . . .	154
A.5.1	Representation of the Chip's Output Signal . . . . .	155
A.5.2	Chip Selection . . . . .	157
A.6	Chip Sorting . . . . .	162
A.6.1	Sorting Procedure . . . . .	162
A.6.2	Results . . . . .	163
A.7	Conclusion . . . . .	166





# List of Figures

2.1	Diagram of the inclusive DIS process in lowest order QED. Here $k$ ( $k'$ ) is the 4-momentum of the incoming (scattered) electron $e$ ( $e'$ ), $q^*$ and $p$ are the 4-momenta of the virtual photon $\gamma^*$ and the nucleon $N$ , respectively. . . . .	5
2.2	Left: Diagram of forward Compton scattering ( $\gamma^*p \rightarrow \gamma^*p$ ). Right: Diagram of deeply virtual Compton scattering ( $\gamma^*p \rightarrow \gamma p$ ). In the diagrams $p$ ( $q$ ) and $p'$ ( $q'$ ) are the 4-momenta of the proton (photon) in the initial and final states, respectively. The diagrams are taken from [Die03]. . . . .	7
2.3	Dependence of the partonic interpretation of GPDs on the relation between $x$ and $\xi$ . The diagram is taken from [Die03]. . . . .	8
3.1	The $\gamma^*p \rightarrow \gamma p$ cross section as a function of $Q^2$ at fixed $W = 82$ GeV (left) and as a function of $W$ at fixed $Q^2 = 8 \text{ GeV}^2$ (right), $ t  < 1 \text{ GeV}^2$ . The inner error bars represent the statistical and the full error bars the combined statistical and systematic uncertainty. The figures are from Ref. [A <sup>+</sup> 05b]. . . . .	19
3.2	Diagrams of the DVCS process (a) and of initial and final state radiation of the scattering lepton (BH process) (b). . . . .	20
3.3	Kinematics of the DVCS process. The momenta of the incoming and scattered positrons ( $k$ and $k'$ ) define the scattering plane. The momenta of the virtual and real photons ( $q^*$ and $q$ ) define the production plane. The azimuthal angle $\phi$ is the angle between the scattering and the production plane. . . . .	21

3.4	The dependence of the cross sections of the DVCS and BH processes and their interference term on the angle between the virtual and real photons $\theta_{\gamma^*\gamma}$ in the HERMES acceptance. The panels a), b), c) correspond to numerical model calculations A), B), D) in Ref. [KN02], respectively. The dotted line corresponds to the BH process, the dashed one to the DVCS process, the dash-dotted one to the interference term and the solid one to the total cross section. The figures are taken from Ref. [Kor05]. . . . .	22
3.5	Beam spin asymmetry $A_{LU}$ (left) and beam charge asymmetry $A_C$ (right) for hard exclusive electroproduction of photons off the proton as function of the azimuthal angle $\phi$ . The solid curves show the results of the indicated fits with the values given in the plots. . . . .	26
3.6	Kinematics of the DVCS process for transverse target polarization. The angle $\phi_S$ denotes the azimuthal angle of the polarization vector of the transversely polarized target $\vec{S}_\perp$ with respect to the scattering plane, measured about the direction of the virtual photon. . . . .	27
4.1	Schematic diagram of the HERMES experiment. . . . .	29
4.2	Schematic diagram of the HERA accelerator layout until 2000. . . . .	31
4.3	Schematic view of the HERMES longitudinally polarized target. From left to right: Atomic Beam Source (ABS), target chamber with cell and magnet, and diagnostic system composed by Target Gas Analyzer (TGA) and Breit-Rabi Polarimeter (BRP). The locations of the radio-frequency transition (RFT) units are indicated. . . . .	35
4.4	Hyperfine energy levels of hydrogen atoms as a function of the magnetic holding field (Breit-Rabi diagram) and corresponding labeling. The field values are scaled with the corresponding critical field $B_C = 11.7$ mT and energy values with the corresponding hyperfine energy. . . . .	36
4.5	Schematic diagram of the HERMES preshower and calorimeter. . . . .	40
4.6	Schematic diagram of the HERMES recoil detector. . . . .	42

5.1	Distribution of DIS events in the kinematic $\nu$ - $Q^2$ plane. Dashed and dash-dotted lines indicate requirements on $\theta$ and $W^2$ applied to the data, respectively. Dotted lines indicate requirements on $\nu$ and $Q^2$ . Solid lines demonstrate the dependences of $Q^2$ on $\nu$ for certain $x_B$ values (shown in the figure). Note that the cuts on $x_B$ and the upper cut on $Q^2$ are not applied here. . . . .	49
5.2	Distributions of the variable $t$ calculated according to Eqs. 5.2 and 5.3 (dashed and solid lines) for the exclusive BH/DVCS process with either a proton (left) or nucleon resonance (right) in the final state. The distributions are compared with the generated value of $t$ (dotted line). The distributions are based on Monte Carlo studies (see chapter 6). . . . .	51
5.3	Missing-mass spectrum of one-photon events for the combined sample of 96d0 and 97d1 productions. The vertical lines correspond to the requirement on the exclusive sample. . . . .	52
5.4	Distributions of kinematic variables for the exclusive samples selected from the data accumulated in 1996 (open points) and 1997 (closed points). The data is normalized to the number of DIS events accumulated in each year. . . . .	53
5.5	Spectrum of beam polarization for 96d0 (dashed line) and 97d1 (solid line) productions. The vertical solid line corresponds to the lower cut on the beam polarization. The vertical dotted line separates samples with positive and negative beam polarization. . . . .	54
6.1	Missing-mass squared distributions for data and MC (upper panels) and MC-to-data ratios (lower panels). The full missing mass range and the exclusive region only are shown in the left and right panels, respectively. The vertical line corresponds to the requirement on the exclusive sample. . . . .	62
6.2	Missing-mass squared distributions for data (right) and MC (left) fitted with a Gaussian. . . . .	62
6.3	Distributions of kinematic variables of the selected exclusive sample for data (closed points) and MC (open points) . . . . .	63
6.4	$M_x^2$ -dependence of the normalized yields of the simulated processes (upper panel) and their fractional contributions (lower panel). The vertical line corresponds to the cut to define the exclusive sample. . . . .	64

6.5	Dependences of the fractional process contributions on $t$ , $\theta_{\gamma^*\gamma}$ , $Q^2$ and $x_B$ , for the selected exclusive sample. Note that the dash-dotted line represents the sum of all background contributions. . . . .	65
6.6	The momentum (top) and angular (bottom) resolution of the HERMES spectrometer for scattered positrons from the elastic BH/DVCS process (1997 geometry; “ <i>force bridge</i> ”, <i>NOVC</i> , <i>NODVC</i> reconstruction method, see Ref. [Wan97]). The momentum resolution in every bin is obtained from Gaussian fits in order to exclude long tails of the distributions caused by Bremsstrahlung in the detector (see figure 6.7). . . . .	67
6.7	Distributions of the difference between the reconstructed and generated momenta of positrons. . . . .	67
6.8	Distributions of the longitudinal ( $vert_z$ ) and transverse ( $vert_t$ ) vertices (left panels) and the dependences of the corresponding resolutions on the positron momentum (right panels). The resolutions are normalized to the corresponding dimensions of the target cell. . . . .	68
6.9	A 2-dimensional ( $Q^2, x_B$ ) distribution (top left) and dependence of $\langle Q^2 \rangle$ on positron momentum (top right) for exclusive BH/DVCS events. Resolutions in $Q^2$ and $x_B$ as functions of the corresponding variables (bottom left and right panels). The resolutions are obtained from Gaussian fits. . . . .	69
6.10	Dependence of the resolution in the azimuthal angle $\phi$ on the angle between the virtual and real photons $\theta_{\gamma^*\gamma}$ (top left) and the corresponding resolution of $\theta_{\gamma^*\gamma}$ (top right) for exclusive BH/DVCS events. A 2-dimensional distribution of events vs. $\theta_{\gamma^*\gamma}$ and $t$ (bottom left). Dependence of the $t$ -resolution on $t$ (bottom right). . . . .	70
7.1	Dependence of the LTSA on the azimuthal angle. The result of this analysis (closed points) was cross checked by Z.Ye [Ye05] (open points). . . . .	76
7.2	Dependences of LTSA amplitudes $A_{UL}^{\sin \phi}$ (left) and $A_{UL}^{\sin 2\phi}$ (right) on $M_x$ , $t$ , $Q^2$ and $x_B$ . The result of this analysis (closed points) was cross checked by Z.Ye [Ye05] (open points). . . . .	77

7.3	Left: Schematics of the detector sections used for the study of the geometrical stability. The typical geometry of a DVCS event at HERMES is shown: the photon hits the quadrant opposite with respect to the one hit by the positron. Right: Dependence of the beam polarization on the run number (time). Four time periods (two for each year) are chosen in order to study the stability of the measurements over the data taking time. . . . .	79
7.4	$t$ -dependence of the amplitudes extracted with 3, 4 and 5-parameter functions defined in Eqs. 7.9, 7.10 and 7.11. . . . .	81
7.5	$x_B$ -dependence of the amplitudes extracted with 3, 4 and 5-parameter functions defined in Eqs. 7.9, 7.10 and 7.11. . . . .	82
7.6	$Q^2$ -dependence of the amplitudes extracted with 3, 4 and 5-parameter functions defined in Eqs. 7.9, 7.10 and 7.11. . . . .	82
7.7	Dependence of $A_{UL}^{\sin\phi}$ and $A_{UL}^{\sin 2\phi}$ on $-t$ with (open circles) and without (closed circles) correction for H0 inefficiency. . . . .	83
7.8	Dependence on $z$ of the analyzing power $A_{UL}^{\sin\phi}(z)$ for $\pi^+$ , $\pi^0$ , and $\pi^-$ production on the deuteron (upper panel) and on the proton (lower panel). The figure is taken from Ref.[A <sup>+</sup> 03]. . . .	84
7.9	Distribution of $z_{\pi^0}$ (top left) and dependence of $\langle z_{\pi^0} \rangle$ on $t$ (top right), $Q^2$ (bottom left) and $x_B$ (bottom right). Based on a MC study for semi-inclusive $\pi^0$ s contaminating the exclusive sample. The error bars correspond to the RMS of the $z_{\pi^0}$ distribution in every bin. . . . .	85
7.10	From left to right: Distribution of invariant mass for two detected photons, used for event separation in a two-photon analysis; dependence of $A_{UL}^{\sin\phi}$ and $A_{UL}^{\sin 2\phi}$ on missing mass (amplitudes have inverted sign here), calculated for the most energetic photon out of the two detected ones (error bars represent the statistical error); dependence of $\langle z_{\pi^0} \rangle$ on missing mass based on the MC study for semi-inclusive $\pi^0$ contaminating the exclusive sample (error bars correspond to the RMS of the $z_{\pi^0}$ distribution in every bin). . . . .	86
7.11	Distributions of $E/P$ ratios of detected exclusive positrons (no missing-mass requirements) for 96d0 (left) and 97d1 (right) data productions. The fit is done with a sum of Gaussian and polynomial. The parameter $P2$ of the fit represents the mean value of the Gaussian. . . . .	89

7.12	Kinematics of the DVCS process for a longitudinally polarized target. The angle $\theta_{\gamma^*}$ denotes the angle between the virtual photon and the polarization vector of the longitudinally polarized target $\vec{S}$ , aligned along the direction of the incoming positron. . . . .	91
7.13	Dependence of the reconstructed LTSA amplitudes $A_{UL}^{\sin\phi}$ and $A_{UL}^{\sin 2\phi}$ on $\theta_{\gamma^*\gamma}$ (left) and $-t$ (right). The input asymmetry is a $\sin 2\phi$ harmonic with the amplitude $A = -0.5$ (indicated with dash-dotted lines). . . . .	94
7.14	Dependence of the measured amplitudes $A_{UL}^{\sin\phi}$ and $A_{UL}^{\sin 2\phi}$ extracted with the <i>fit method</i> , on the number of $\phi$ -bins. . . . .	96
8.1	The longitudinal target spin asymmetry $A_{UL}$ for hard electro-production of photons on proton (left) and deuteron (right), as a function of the azimuthal angle $\phi$ for the exclusive sample. The solid curves represent the results of the indicated fits, numerical values are given in the figure as well. The shown central values and statistical errors are exactly the same as HERMES preliminary results released in May 2005 [KY <sup>+</sup> 05, Kop05].	100
8.2	The longitudinal target spin asymmetry $A_{UL}^{\sin\phi}$ (left) and $A_{UL}^{\sin 2\phi}$ (right) <i>vs</i> $-t$ , $Q^2$ and $x_B$ as measured on proton and on deuteron. The error bars (bands) represent the statistical (systematic) uncertainty. The shown central values and statistical errors are exactly the same as HERMES preliminary results released in May 2005 [KY <sup>+</sup> 05, Kop05], while systematic errors are updated. . . . .	101
8.3	The $\sin\phi$ (top) and $\sin 2\phi$ (bottom) amplitudes of the longitudinal target-spin asymmetry on the proton (left) and the deuteron (right) as a function of $-t$ . The inner error bars represent the statistical uncertainty and the full error bars the quadratic superposition of statistical and systematic uncertainties. The measurement is compared with theoretical calculations [GPV01]. For details on the model parameters see text. . . . .	104
8.4	The $\sin\phi$ (top) and $\sin 2\phi$ (bottom) amplitudes of the longitudinal target-spin asymmetry on the proton (left) and the deuteron (right) as a function of $Q^2$ . Notations are the same as in figure 8.3. . . . .	105

8.5	The $\sin \phi$ (top) and $\sin 2\phi$ (bottom) amplitudes of the longitudinal target-spin asymmetry on the proton (left) and the deuteron (right) as a function of $x_B$ . Notations are the same as in figure 8.3. . . . .	106
8.6	The $\sin \phi$ (left) and $\sin 2\phi$ (right) amplitudes of the longitudinal target-spin asymmetry on the proton as a function of $-t$ . The inner error bars represent the statistical uncertainty and the full error bars the statistical and systematic uncertainties added in quadrature. The measurement is compared with theoretical calculations [BMK02, Mül04]. . . . .	107
8.7	The $\sin \phi$ (left) and $\sin 2\phi$ (right) amplitudes of the longitudinal target-spin asymmetry on the proton as a function of $x_B$ (top) and $Q^2$ (bottom). Notations are the same as in figure 8.6.	108
8.8	The $\sin \phi$ amplitudes of the longitudinal target-spin asymmetry as functions of $-t$ (left) and $\xi$ measured at HERMES and CLAS. The measurements are compared with theoretical calculations [VGG01] using the $\xi$ -dependent GPD parameterization ( $b_{val} = b_{sea} = 1$ ). The dash-dotted (dashed) lines correspond to the calculations at the HERMES (CLAS) kinematics. The CLAS measurements and the corresponding model calculations are reproduced from Ref. [CABE06]. . . . .	110
A.1	HERMES Silicon Recoil Detector . . . . .	129
A.2	Schematic diagram of the silicon module control sequence. The module contains 8 chips for readout, 4 chips per side. . .	131
A.3	Schematic diagram of the HELIX128 chip . . . . .	132
A.4	Schematics of the HELIX serial readout. . . . .	133
A.5	Schematics of the HELIX daisy chain tokens and fail safe tokens. For the broken chip, fail safe tokens of the next and the previous chips are used. In this case the broken chip is excluded from the readout in order to keep the chain running.	134
A.6	Oscilloscope picture of the chip's test pulse output for two TP signal cycles. The output signal has a stair case shape that correspond to the shape of the injected charge. For every next TP cycle the chip's response swaps the charge. . . . .	135
A.7	Dependence of the chip's current consumption vs. the register setting. The other registers are set to their default values. The current consumption for the default register settings $309 \pm 56$ mA is subtracted. The measurements are done for the power line +2 V. . . . .	138
A.8	Production test stand . . . . .	143

A.9	<i>Driver card</i> with the <i>driver chip</i> mounted on top of it and the <i>probe card</i> . The insert shows a magnification of the chip under test. . . . .	144
A.10	Probe Card Map. The dark pads are probed by the card. . . .	145
A.11	Schematics of the production test stand. . . . .	146
A.12	Schematics of the programmable delay. The delay is based on the programmable prescaler, therefore the step of the delay is defined by the clock frequency (for 10.4 MHz the delay step is 96 ns). Delay limitations: The maximum delay length is defined by the width of the signal after the <i>dual timer</i> module. The trigger period should be at least twice as shorter as the signal width after the <i>dual timer</i> module. . . . .	147
A.13	HELIX timing . . . . .	147
A.14	Oscilloscope plots for the control signals of the chip under test. The uppermost curve stands for the <i>Data Valid</i> signal, generated by the <i>test board</i> . The middle curve for the output signals of the <i>driver chip</i> and CHuT. The lowest curve for the measured signal. . . . .	149
A.15	Oscilloscope plots for the control signals of the chip under test. Notations are the same as in figure A.14 . . . . .	150
A.16	Schematics of the chip's labeling. The wafer's labels are located on its bottom side. . . . .	152
A.17	The pedestal levels of the HELIX memory cells. The left side plot is for a good chip. The right one shows the case of a single broken memory cell. Its pedestal level is far above the level of the other cells. . . . .	157
A.18	Normalized distributions of the pedestal related parameters for all chips that passed the selection. Panel a: pedestal levels of the channels of all such chips. Panel b: noise of all the memory cells. Panel c: spread of the pedestal levels of the memory cells within one channel. Panel d: the same as panel c, but the spread is measured after the CMN correction, as defined in Eq. A.5 (HADC method). . . . .	159
A.19	Normalized distributions of the memory cell spread in test pulse amplification within one channel for all channels of all chips that passed the selection. . . . .	159
A.20	Difference between the pedestal levels of the memory cells and the corresponding pedestal levels of the channels. . . . .	161



A.21	Left: distribution of the chip's parameters used for the sorting procedure. Right: dependence of the chip parameter on the chip's score. The numbers correspond to the groups (explained in the text). . . . .	164
A.22	Distributions of the chip's parameters for the chips selected for the silicon detector project. Left panels are for the chips of the <i>group 1</i> (high gain chips). Right panels are for the chips of the <i>group 2</i> (low gain chips). The open histogram shows the distributions for all the chips that passed the production test. . . . .	165



# List of Tables

5.1	List of data quality parameters controlled by <i>bad bits</i> that are required to be zero in the analysis of data with the longitudinally polarized target. . . . .	47
5.2	Average beam polarization $\langle P_B \rangle$ , the number of DIS events $N_{DIS}$ and the number of exclusive events $N_{excl}$ for data sets of every beam helicity and every target spin state. The ratio $L/C$ is the integrated luminosity $L$ normalized by the luminosity constant $C$ (see Eq. 5.7). The symbol $\rightarrow$ ( $\leftarrow$ ) denotes positive (negative) beam polarization, and $\Leftarrow$ ( $\Rightarrow$ ) denotes target spin antiparallel (parallel) to the beam direction. . . . .	55
6.1	Fractions of the main processes in the selected exclusive sample.	65
7.1	The numbers of DIS and exclusive events for the two analyses.	78
7.2	Amplitudes $A_{UL}^{\sin \phi}$ and $A_{UL}^{\sin 2\phi}$ measured with the requirement on the hit position of the detected positron to be in one of four calorimeter quadrants (as defined in figure 7.3). . . . .	79
7.3	Amplitudes $A_{UL}^{\sin \phi}$ and $A_{UL}^{\sin 2\phi}$ measured over various periods of data taking (see figure 7.3, right). Parentheses indicate the periods of the same year of data taking. . . . .	80
7.4	The fractions of the elastic ( $\eta_{el.}$ ), associated ( $\eta_{ass.}$ ), exclusive and semi-inclusive $\pi^0$ processes ( $\eta_{\pi^0}$ ) and the number of events ( $N_{excl.}$ ) in the exclusive sample (not corr.) and the corresponding deviations for the samples with the the photon energy $E_\gamma$ corrected by factors 1.014 and 1/1.014. . . . .	90
7.5	Amplitudes $A_{UL}^{\sin \phi}$ and $A_{UL}^{\sin 2\phi}$ and the number of exclusive events for corrected and not corrected measured photon hit position $y_\gamma^{(>0)}$ . The last line of the table shows the deviation of the asymmetry caused by the correction. . . . .	91
7.6	Fractions of reconstructed amplitudes to the input amplitude $A = -0.5$ generated with either $\sin \phi$ or $\sin 2\phi$ input harmonic.	93

7.7	Relative difference between the reconstructed amplitude $A_{UL}^{\sin 2\phi}$ and the initial amplitude $A = -0.5$ , depending on the number of $\phi$ -bins. The smearing effect is excluded. . . . .	95
7.8	Contributions of various systematic uncertainties to the total systematic uncertainty for the $\sin \phi$ and $\sin 2\phi$ amplitudes of the LTSA measured on the proton from 1996-97 data. Here the sources of the uncertainties are: 1. - target polarization measurement, 2. - calorimeter miscalibration, 3. - calorimeter misalignment, 4. - smearing and binning effects, 5. - background asymmetry. . . . .	98
8.1	The range of kinematic variables and their mean values for the exclusive sample. . . . .	99
8.2	The amplitudes $A_{UL}^{\sin \phi}$ and $A_{UL}^{\sin 2\phi}$ of the $\sin \phi$ and $\sin 2\phi$ harmonics of the longitudinal target-spin asymmetry on the proton and the deuteron [Ye05] for the average kinematics of the exclusive sample, as given in table 8.1. . . . .	100
8.3	The amplitude $A_{UL}^{\sin \phi}$ of the $\sin \phi$ harmonic of the longitudinal target-spin asymmetry on the proton per kinematic bin in $-t$ , $Q^2$ and $x_B$ at the respective average kinematics. . . . .	112
8.4	The amplitude $A_{UL}^{\sin 2\phi}$ of the $\sin 2\phi$ harmonic of the longitudinal target-spin asymmetry on the proton per kinematic bin in $-t$ , $Q^2$ and $x_B$ at the respective average kinematics. . . . .	113
8.5	The amplitude $A_{UL}^{\sin 3\phi}$ of the $\sin 3\phi$ harmonic of the longitudinal target-spin asymmetry on the proton per kinematic bin in $-t$ , $Q^2$ and $x_B$ at the respective average kinematics. The amplitude is extracted with the fit function defined in Eq. 7.10.	114
A.1	Register settings for the maximum and minimum chip's power consumption for the power line +2 V. The last column shows the default settings of the chip registers. . . . .	137

A.2	The settings of the <i>driver chip</i> and the <i>chip under test</i> (ChUT). The ChUT was programmed as the first (1st) or/and last (last) one in the daisy chain; into fail safe modes for the left and right sides fail safe tokens ( $FS_L$ and $FS_R$ , respectively). Values 1 (0) denote that the corresponding mode of the chip is acti- vated (not activated). The position of the <i>jumper</i> (Jumper) between <i>HTO</i> and <i>RTI</i> tokens of the ChUT is shown (opened or closed). Running condition of the daisy chain of the two chips (either running (Y) or not (N)) is a criterion of the fail- ure of the tokens. Short explanation is given in a Comment column.	140
-----	---	-----



# Chapter 1

## Introduction

The spin of the electron was introduced in 1924 by Wolfgang Pauli as "two-valued quantum degree of freedom". It was needed for postulating the exclusion principle in order to describe the structure of atoms. In early 1925 Ralph Kronig suggested that spin is the intrinsic angular momentum of the electron. This allowed to explain the fine structure of the atomic energy levels as the result of the interaction of the dipole moment of an electron with the electric field of a nucleus. Later, spin was also assigned to nuclei explaining the hyperfine structure of the atomic spectrum caused by dipole-dipole interactions between electron and nucleus.

At higher energies, which became available several decades later with the development of accelerators, it became possible to access the constituents of the nucleon, called partons (quarks, antiquarks and gluons), and to study their properties. The study of inclusive and semi-inclusive Deep Inelastic Scattering (DIS) reveals information about longitudinal momentum and polarization carried by partons within nucleons and nuclei. This information is encoded in spin-averaged (unpolarized) and spin-dependent (polarized) Parton Distribution Functions (PDFs).

The interest in physics of the nucleon spin increased strongly due to the so-called spin crisis. As it was reported by the EMC collaboration in 1987 [A<sup>+</sup>88], only a fraction of the nucleon spin can be attributed to the quark spins. In general, the spin of the nucleon receives contributions from valence quarks  $\Delta u_v$  and  $\Delta d_v$ , sea quarks  $\Delta q_s$ , orbital angular momentum of quarks  $L^Q$ , and from total angular momentum of gluons  $J^G$ :

$$\frac{1}{2} = \frac{1}{2} \underbrace{\overbrace{\{\Delta u_v + \Delta d_v + \Delta q_s\}}^{\Delta\Sigma}}_{J^Q} + L^Q + J^G. \quad (1.1)$$

The results of SMC [A<sup>+</sup>98b], and later more precise measurements of HER-

MES [A<sup>+</sup>99], demonstrated that the contribution of quark spins  $\Delta\Sigma$  to the spin of the proton is about 30%. Accessing the other components of the proton spin is a non-trivial experimental task. Today, the only method known is the one to extract the orbital angular momentum of quarks  $L^Q$ . It is based on the measurement of the total angular momentum of quarks  $J^Q$  using the so-called Generalized Parton Distributions (GPDs).

GPDs were introduced a decade ago as a unified description of hard exclusive processes in the Bjorken regime [M<sup>+</sup>94, Rad96]. As a generalization of the usual PDFs they contain additional information about quark and gluon distributions in the plane transverse to the direction of motion of the nucleon. This is a consequence of the off-forward nature of GPDs that unifies properties of both PDFs and nucleon form factors. Strong interest in GPDs was triggered by the work of X. Ji [Ji97b, Ji97a] who demonstrated that in the forward limit GPDs can give information about the total angular momentum  $J^Q$  ( $J^G$ ) carried by quarks (gluons) in the nucleon. With the knowledge of  $\Delta\Sigma$  available from experiments it can allow to access the orbital angular momentum of quarks  $L^Q$  for the first time.

The presently cleanest way to access GPDs is to study Deeply Virtual Compton Scattering (DVCS), the hard exclusive electroproduction of a real photon. This process has a final state identical to that of the Bethe-Heitler (BH) process where the photon is radiated from either the incoming or the outgoing lepton. Both processes are experimentally indistinguishable as their amplitudes interfere. The interference term involves linearly the amplitudes of the DVCS process. It can be measured through certain cross section asymmetries that allow to access the real and the imaginary part of DVCS amplitudes. Since the BH process is exactly calculable in terms of QED, the measurement of the interference term is very informative because it is sensitive to both magnitudes and phases of the DVCS amplitudes.

In this work the analysis of the single-spin asymmetry in the DVCS cross section with respect to the polarization of a *longitudinally* polarized proton target is discussed. The asymmetry is also referred to as Longitudinal Target Spin Asymmetry (LTSA). Interest in the LTSA comes from its sensitivity to the polarized GPDs. These GPDs are not involved in the determination of the total angular momentum of quarks in the nucleon, but they appear in the description of the other processes, as e.g. meson production. The measurements are based on data taken by the HERMES experiment in the years 1996 and 1997.

The HERMES experiment located in the HERA storage ring was originally designed to study the spin structure of proton and neutron using deep inelastic electron-nucleon scattering. It is a fixed-target experiment that uses the longitudinally polarized electron or positron beam of HERA at an energy



---

of 27.5 GeV. The main advantage of the HERMES experiment with respect to most other spin experiments is its polarized gas target. Its low density allows to reduce bremsstrahlung and secondary interactions providing clean experimental conditions to study final state particles.

A new *recoil detector* (RD) [HER02] is presently being commissioned at HERMES to allow for more detailed studies of hard exclusive processes. Located around the target, it is designed to detect the recoiling reaction products and to suppress background. The main objective of the RD is to detect the recoiling proton from the BH/DVCS process. The recoil detector consists of three main components: a silicon detector, located in the vacuum of the HERA beam, a scintillating fibre tracker and a photon detector. In order to discriminate protons from pions, the silicon detector is used not only for tracking but also for the measurement of the energy deposited by the traversing particles. This brings strict requirements to the readout electronics. As a significant part of the work on this thesis the production tests of the readout chip HELIX128 3.0 of the silicon detector were performed. A special selection procedure was developed in order to select chips that fit the project requirements.

The structure of this thesis is as follows. The formalism of GPDs and their theoretical models are introduced in chapter 2. DVCS and its azimuthal asymmetries that allow access to GPDs are discussed in chapter 3. The HERMES detector is described in chapter 4. Criteria used in this analysis for data selection are discussed in chapter 5. The Monte Carlo simulation of the processes contributing to the selected sample is described in chapter 6. The method used for asymmetry extraction, systematic studies and systematic uncertainties are given in chapter 7. The final result on the measured LTSA, its comparison with the deuteron data and theoretical calculations are discussed in chapter 8. Conclusions and outlook follow in chapter 9. In addition, the production tests of the HELIX chip are discussed in appendix A.



## Chapter 2

# Generalized Parton Distributions

### 2.1 General Formalism in Deep Inelastic Scattering

One of the cleanest ways to study the nucleon structure is to use a virtual photon produced in Deep Inelastic Scattering (DIS). In lowest order QED this process can be described by one-photon exchange as shown in figure 2.1. The virtual photon  $\gamma^*$ , produced by the incoming electron  $e$ , interacts with

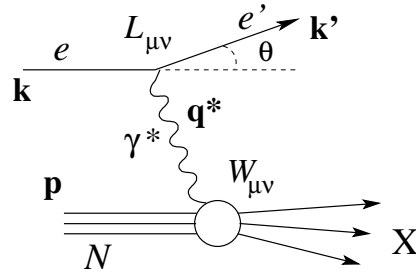


Figure 2.1: Diagram of the inclusive DIS process in lowest order QED. Here  $k$  ( $k'$ ) is the 4-momentum of the incoming (scattered) electron  $e$  ( $e'$ ),  $q^*$  and  $p$  are the 4-momenta of the virtual photon  $\gamma^*$  and the nucleon  $N$ , respectively.

the nucleon's constituents. In case of inclusive DIS only the scattered electron  $e'$  is analyzed and the other products of the reaction are ignored. The kinematics of the reaction is defined by the 4-momenta  $k$ ,  $k'$ ,  $q^*$  and  $p$  of the incoming and scattered electrons, the virtual photon and the nucleon, respectively. In case of a fixed-target experiment Lorentz invariant variables

needed for the process description can be written as:

$$\begin{aligned}
s &\equiv (k + p)^2, \\
Q^2 &\equiv -q^{*2} \equiv -(k - k')^2 = 4EE' \sin^2 \frac{\theta}{2}, \\
\nu &\equiv \frac{p q^*}{M} = E - E', \\
W^2 &\equiv (p + q^*)^2 = M^2 + 2M\nu - Q^2,
\end{aligned} \tag{2.1}$$

where  $E$  and  $E'$  are the energies of the incoming and scattered electrons,  $M$  is the nucleon mass,  $\theta$  is the scattering angle as shown in figure 2.1,  $s$  is the center-of-mass energy squared of the lepton-nucleon system,  $Q^2$  denotes the virtuality of the produced photon,  $W^2$  is the square of the invariant mass of the virtual photon-proton system and  $\nu$  is the energy loss of the scattered electron in the laboratory system. Two additional dimensionless variables are defined:

$$\begin{aligned}
x_B &= \frac{Q^2}{2p q^*} = \frac{Q^2}{2M\nu} \quad \text{and} \\
y &= \frac{p q^*}{p k} = \frac{\nu}{E}.
\end{aligned} \tag{2.2}$$

Here  $x_B$  denotes the fraction of the 4-momentum of the nucleon carried by the struck quark. In the laboratory system the variable  $y$  has a meaning of the relative energy loss of the scattered electron. Both variables are allowed within the range  $0 < x_B, y \leq 1$ .

The DIS cross section can be written in the form [AEL95]:

$$\frac{d^2\sigma}{d\Omega dE'} = \frac{\alpha^2}{2MQ^2} \frac{E'}{E} L^{\mu\nu} W_{\mu\nu}, \tag{2.3}$$

where  $L^{\mu\nu}$  is the leptonic tensor, which is calculable in QED, and  $W_{\mu\nu}$  is the hadronic tensor that contains information about the nucleon structure. At present there is no way to calculate the hadronic tensor from first principles. In order to describe the interaction of the virtual photon with the nucleon the optical theorem is used. It relates the cross section of the virtual photon absorption ( $\gamma^* p \rightarrow X$ ) and the imaginary part of the forward Compton scattering amplitude,  $A_{fC}(\gamma^* p \rightarrow \gamma^* p)$ , (figure 2.2, left) as:

$$\sigma_{\gamma^* p \rightarrow X} \sim \text{Im} [A_{fC}(\gamma^* p \rightarrow \gamma^* p)]. \tag{2.4}$$

The factorization of the amplitude  $A_{fC}$  allows the separation of the process of hard virtual-photon scattering, calculable in perturbation theory; the remaining part is the phenomenological Parton Distribution Function (PDF)

$q(x_B)$ :

$$A_{fC} = \sum_q C_q(x_B, x) \otimes q(x), \quad (2.5)$$

where  $C_q(x_B, x)$  is a hard scattering coefficient for scattering off a parton of type  $q$  and  $x$  is the momentum fraction of the parton. The symbol  $\otimes$  denotes convolution. In case of forward Compton scattering the final and initial states of the process are identical, hence there is no momentum transfer (Mandelstam  $t = 0$ ) and the PDF  $q(x_B)$  represents the probability density for finding a parton of the flavor  $q$  with a specific momentum fraction  $x_B$  in the nucleon.

## 2.2 Formalism of Generalized Parton Distributions

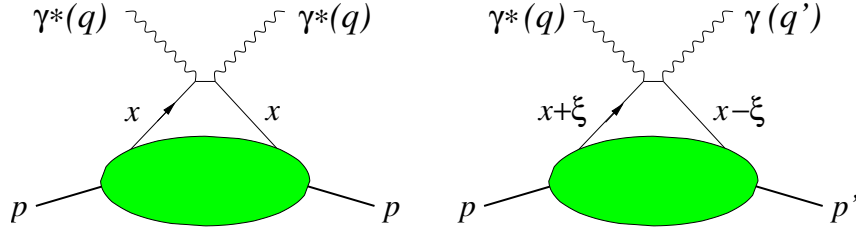


Figure 2.2: Left: Diagram of forward Compton scattering ( $\gamma^* p \rightarrow \gamma^* p$ ). Right: Diagram of deeply virtual Compton scattering ( $\gamma^* p \rightarrow \gamma p$ ). In the diagrams  $p$  ( $q$ ) and  $p'$  ( $q'$ ) are the 4-momenta of the proton (photon) in the initial and final states, respectively. The diagrams are taken from [Die03].

Generalized Parton Distributions (GPDs) can be defined based on the factorization of the amplitude of the Deeply Virtual Compton Scattering (DVCS) process ( $\gamma^* p \rightarrow \gamma p$ ) (figure 2.2, right). The factorization theorem proven in Ref. [CF99] for the Bjorken limit ( $Q^2, s \gg M^2$ , with  $x_B$  fixed) allows to represent the amplitude in analogy to the case of inclusive DIS (see Eq. 2.5) with GPD functions  $F^q(x, \xi, t)$  instead of PDFs

$$A_{DVCS} = \sum_q C_q(\xi, x) \otimes F^q(x, \xi, t), \quad (2.6)$$

where  $C_q(\xi, x)$  is a hard scattering coefficient as in Eq. 2.5,  $t$  is the momentum transfer (Mandelstam  $t$ ) between the initial and final photons and  $x$  is an unobservable internal variable that together with  $\xi$  defines the longitudinal

momentum fractions of the partons in the process ( $x \pm \xi$ , as it is shown in figure 2.2, right). The variable  $\xi$  is a fraction of the longitudinal momentum transfer between both partons, known also as the skewness parameter, which in the Bjorken limit is given by:

$$\xi = x_B \frac{1 + \frac{t}{2Q^2}}{2 - x_B + x_B \frac{t}{Q^2}} \simeq \frac{x_B}{2 - x_B}. \quad (2.7)$$

GPDs contain more information than PDFs, because DVCS is not a symmetric process, as compared to forward Compton scattering (see figure 2.2). This allows a small but finite momentum transfer between initial and final states ( $t \neq 0$ ) making GPDs sensitive to additional partonic degrees of freedom. Being defined in such a way GPDs can not be interpreted as probability functions anymore, but rather as two-parton correlation functions in the nucleon that have various partonic interpretations depending on the relation between  $x$  and  $\xi$  (see figure 2.3):

- $\xi < x$  GPDs describe emission and reabsorption of partons with the longitudinal momentum fraction  $x \pm \xi$ ,
- $-\xi \leq x \leq \xi$  GPDs are sensitive to parton-antiparton correlations in the nucleon,
- $x < -\xi$  GPDs describe emission and reabsorption of antipartons.

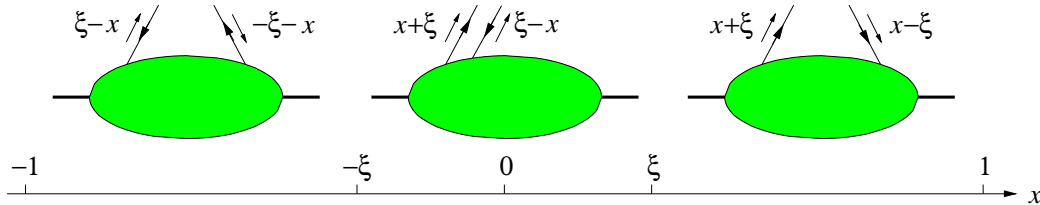


Figure 2.3: Dependence of the partonic interpretation of GPDs on the relation between  $x$  and  $\xi$ . The diagram is taken from [Die03].

### 2.2.1 Definition of Generalized Parton Distributions

GPDs parameterize matrix elements of quark (and gluon) bilocal operators between nucleon states with non-equal momenta [Ji98]:

$$\int \frac{dz^-}{2\pi} e^{ixP^+z^-} \langle p' | \bar{q}(-\frac{1}{2}z) \gamma^+ q(\frac{1}{2}z) | p \rangle \Big|_{z^+=0, \mathbf{z}=0}$$

$$\begin{aligned}
&= \frac{1}{P^+} \left[ H^q(x, \xi, t) \bar{u}(p') \gamma^+ u(p) + E^q(x, \xi, t) \bar{u}(p') \frac{i\sigma^{+\alpha} \Delta_\alpha}{2m} u(p) \right], \\
&\int \frac{dz^-}{2\pi} e^{ixP^+z^-} \langle p' | \bar{q} \left( -\frac{1}{2}z \right) \gamma^+ \gamma_5 q \left( \frac{1}{2}z \right) | p \rangle \Big|_{z^+=0, \mathbf{z}=0} \\
&= \frac{1}{P^+} \left[ \widetilde{H}^q(x, \xi, t) \bar{u}(p') \gamma^+ \gamma_5 u(p) + \widetilde{E}^q(x, \xi, t) \bar{u}(p') \frac{\gamma_5 \Delta^+}{2m} u(p) \right], \quad (2.8)
\end{aligned}$$

where  $q(\frac{1}{2}z)$  is the quark field operator and  $H(x, \xi, t)$ ,  $E(x, \xi, t)$  and  $\widetilde{H}(x, \xi, t)$ ,  $\widetilde{E}(x, \xi, t)$  are the twist-2 GPDs. Here  $\bar{u}(p')$  and  $u(p)$  are the Dirac spinors corresponding to the final and initial nucleons and  $p$  and  $p'$  are the momenta of the nucleon in the initial and final states (see figure 2.2). The superscripts  $+$  and  $-$  denote the positive and negative light-cone coordinates,  $P = (p + p')/2$  is the average nucleon momentum and  $z$  is the light cone coordinate.

The pairs of GPDs  $H(x, \xi, t)$ ,  $E(x, \xi, t)$  and  $\widetilde{H}(x, \xi, t)$ ,  $\widetilde{E}(x, \xi, t)$  introduced in (2.8) are related to the off-forward matrix elements of the vector and axial-vector quark operators, respectively. Hence the former pair of functions  $(H, E)$  conserves the target helicity and the latter  $(\widetilde{H}, \widetilde{E})$  does not.

These new distributions are more general than ordinary parton distributions, because they combine the concepts of both PDFs, defined also through the bilocal operators for processes with no momentum transfer between the initial and final states, and elastic form factors, defined only in case of finite momentum transfer. The latter give the dependence of GPDs on the four-momentum transfer  $t$ .

Gluon GPDs can be introduced in analogy to quark GPDs. Since gluon GPDs are beyond the scope of this work, all further considerations of GPDs concern only quark GPDs. More details about gluon GPDs can be found in e.g. [Ji98].

### 2.2.2 Twist-three Generalized Parton Distributions

The definition of twist-two GPDs in Eq. 2.8 is done in LO of perturbative QCD. When power corrections are taken into account at leading order  $\alpha_s$ , for every twist-two function  $F = \{H, E, \widetilde{H}, \widetilde{E}\}$  a pair of twist-three GPDs  $F_\pm^3 = \{H_\pm^3, E_\pm^3, \widetilde{H}_\pm^3, \widetilde{E}_\pm^3\}$  is defined for the generalized current operators. The subscript  $\pm$  denotes the even ( $-$ ) and odd ( $+$ ) parity functions.

Operators defining twist-three functions can be decomposed in a gauge invariant way into two parts [BM00], one of them is solely expressed in twist-two GPDs, and the other, the “genuine twist-3” part, is related to quark-gluon correlations in the nucleon. Hence every twist-three GPD can be decomposed into two parts, as well

$$F_\pm^3 = F_\pm^{WW} + F_\pm^{qGq}, \quad (2.9)$$

where  $F_{\pm}^{WW}$  is the so-called Wandzura-Wilczek (WW) term expressed in twist-two GPDs and  $F_{\pm}^{qGq}$  is the twist-three part carrying new information about dynamic processes in the nucleon.

## 2.3 Basic properties of Generalized Parton Distributions

PDFs are limiting cases of GPDs, because PDFs and GPDs are defined as diagonal and non-diagonal matrix elements of the same light-cone bilocal operators (see Eq. 2.8). In the forward limit ( $t \rightarrow 0$ ,  $\xi \rightarrow 0$ ) twist-two GPDs are reduced to the regular unpolarized ( $q(x)$ ) and polarized ( $\Delta q(x)$ ) PDFs:

$$\begin{aligned} H^q(x, 0, 0) &= q(x), & \widetilde{H}^q(x, 0, 0) &= \Delta q(x) \quad \text{for } x > 0, \\ H^q(x, 0, 0) &= -\bar{q}(-x), & \widetilde{H}^q(x, 0, 0) &= \Delta \bar{q}(-x) \quad \text{for } x < 0. \end{aligned} \quad (2.10)$$

From the definition of the matrix elements of the bilocal operators it follows that its integration over the momentum fraction  $x$  gives matrix elements of local quark operators. Hence  $x$ -moments of GPDs are related to the corresponding form factors as:

$$\begin{aligned} \int_{-1}^1 dx H^q(x, \xi, t) &= F_1^q(t), & \int_{-1}^1 dx E^q(x, \xi, t) &= F_2^q(t), \\ \int_{-1}^1 dx \widetilde{H}^q(x, \xi, t) &= g_A^q(t), & \int_{-1}^1 dx \widetilde{E}^q(x, \xi, t) &= g_P^q(t), \end{aligned} \quad (2.11)$$

where  $F_1^q(t)$  and  $F_2^q(t)$  are the Dirac and Pauli form factors and  $g_A^q(t)$  and  $g_P^q(t)$  are the axial and pseudoscalar ones, respectively.

A non-trivial and important property of GPDs used in their factorization is the polynomiality of their Mellin moments [Ji97b, Ji97a]. Due to Lorentz invariance the Mellin moments of the GPDs  $H$  and  $E$  are polynomials in  $\xi$  of the order of  $n + 1$  [Die03]:

$$\begin{aligned} \int_{-1}^1 dx x^n H^q(x, \xi, t) &= \sum_{\text{even } i=0}^n (2\xi)^i A_{n+1,i}^q(t) + \text{mod}(2, n)(2\xi)^{n+1} C_{n+1}^q(t), \\ \int_{-1}^1 dx x^n E^q(x, \xi, t) &= \sum_{\text{even } i=0}^n (2\xi)^i B_{n+1,i}^q(t) - \text{mod}(2, n)(2\xi)^{n+1} C_{n+1}^q(t). \end{aligned} \quad (2.12)$$

Here the terms with the highest  $\xi^{n+1}$  for odd  $n$  are equal and opposite for moments of  $H^q$  and  $E^q$ . This property leads to introduction of the so-called D-term in GPDs discussed in section 2.4.



For spin-dependent GPDs the sum rules are similar to those in Eq. 2.12:

$$\begin{aligned}\int_{-1}^1 dx x^n \widetilde{H}^q(x, \xi, t) &= \sum_{\text{even } i=0}^n (2\xi)^i \widetilde{A}_{n+1,i}^q(t), \\ \int_{-1}^1 dx x^n \widetilde{E}^q(x, \xi, t) &= \sum_{\text{even } i=0}^n (2\xi)^i \widetilde{B}_{n+1,i}^q(t),\end{aligned}\quad (2.13)$$

where the highest power of  $\xi$  is  $n$  instead of  $n+1$  making the D-term contribution absent in the GPDs  $\widetilde{H}^q$  and  $\widetilde{E}^q$ .

### 2.3.1 Ji's Relation

Strong interest in GPDs was triggered by the work of X. Ji [Ji97b, Ji97a], where he demonstrated that in the forward limit GPDs give information about the total angular momentum  $J^Q$  ( $J^G$ ) of quarks (gluons) in the nucleon. According to Ji's relation the total angular momentum carried by every quark species is related to the second moment of the sum of the corresponding unpolarized GPDs as:

$$J^q = \frac{1}{2} \lim_{t \rightarrow 0} \int_{-1}^1 dx x \left[ H^q(x, \xi, t) + E^q(x, \xi, t) \right]. \quad (2.14)$$

The contributions to the spin  $\frac{1}{2}$  of the nucleon can be written in gauge invariant form as:

$$\frac{1}{2} = \frac{1}{2} \underbrace{\Delta\Sigma + L^Q}_{J^Q} + J^G, \quad (2.15)$$

where  $\Delta\Sigma$  is the contribution of quark spins,  $L^Q$  is the orbital angular momentum of all quarks and  $J^G$  is the total angular momentum of gluons in the nucleon. Using Ji's relation for  $J^q$  (see Eq. 2.14) and information about  $\Delta\Sigma$ , known from inclusive and semi-inclusive polarized DIS measurements (e.g. Refs. [A<sup>+</sup>98b, A<sup>+</sup>99]),  $L^Q$  can be obtained based on the knowledge of the total angular momentum of quarks:

$$J^Q = \sum_q J^q = \frac{1}{2} \Delta\Sigma + L^Q. \quad (2.16)$$

Hence Ji's relation opens access to the orbital momentum of quarks for the first time. As it follows from Eq. 2.15, the knowledge of  $J^Q$  reveals, in principle, the total angular momentum  $J^G$  of gluons as well.

## 2.4 Models of Generalized Parton Distributions

The first model calculations of GPDs were performed in the MIT bag model [JM97]. This approach does not take into account the chiral symmetry, also its non-field-theoretical nature leads to negative antiquark distributions [GPV01]. The quark-soliton model [Dia98] used already for the calculation of PDFs and form factors treats these problems correctly, opening the way for the calculation of GPDs [P<sup>+</sup>98, PPG00]. Although model calculations are very important for understanding the non-perturbative mechanisms accessible through GPDs, presently it is more common to use phenomenological parameterizations of GPDs in order to estimate the expected observables.

In this work the phenomenological approach developed in [GPV01] is used. Based on the known basic GPD properties and on the available models it can be used for the parameterization of the twist-2 GPDs  $H^q$ ,  $E^q$ ,  $\widetilde{H}^q$  and  $\widetilde{E}^q$  for each quark flavor  $q$  ( $u, d, s$ ) in the region of relatively small values of  $-t$  ( $< 1 \text{ GeV}^2$ ). Twist-3 GPDs are partially taken into account by the Wandzura-Wilczek (WW) term  $F_{\pm}^{WW}$ . The correlation term  $F^{qGq}$  is not included, since no reliable theoretical approach exists yet to model it.

### 2.4.1 Parameterization of the Generalized Parton Distributions $H$ and $E$

Due to their polynomiality property GPDs can be represented in terms of so-called double distributions (DDs) [GPV01]:

$$F(x, \xi, t) = \int_{-1}^1 d\beta \int_{-1+|\beta|}^{1-|\beta|} d\alpha \delta(\beta + \alpha\xi - x) f(\beta, \alpha, t), \quad (2.17)$$

where  $f(y, z, t)$  is the DD of the corresponding GPD  $F(x, \xi, t)$ . The advantage of this new function  $f(y, z, t)$  is that its dependence on  $x$  ( $s$ -channel) and  $\xi$  ( $t$ -channel) can be separated making the modeling more straightforward. In such approach the highest power of  $\xi^{n+1}$  of the GPDs  $H$  and  $E$  in the sum of Eq. 2.12 is zero, making the parameterization incomplete. Adding the so-called D-term completes the representation of these GPDs in terms of DDs [GPV01]:

$$\begin{aligned} H^q(x, \xi, t) = & \int_{-1}^1 d\beta \int_{-1+|\beta|}^{1-|\beta|} d\alpha \delta(\beta + \alpha\xi - x) F^q(\beta, \alpha, t) + \\ & + \theta\left[1 - \frac{x^2}{\xi^2}\right] D^q\left(\frac{x}{\xi}, t\right), \end{aligned}$$

$$E^q(x, \xi, t) = \int_{-1}^1 d\beta \int_{-1+|\beta|}^{1-|\beta|} d\alpha \delta(\beta + \alpha\xi - x) K^q(\beta, \alpha, t) - \theta\left[1 - \frac{x^2}{\xi^2}\right] D^q\left(\frac{x}{\xi}, t\right). \quad (2.18)$$

As it follows from the polynomiality [GPV01], the D-term contributes to both GPDs  $H^q$  and  $E^q$  with opposite sign and its relation to the highest power of  $\xi$  is defined through the Mellin moments:

$$C_{n+1}^q(t) = \int_{-1}^1 d\frac{x}{\xi} \left(\frac{x}{\xi}\right)^n D^q\left(\frac{x}{\xi}, t\right).$$

The D-term being defined only in the region  $|x/\xi| \leq 1$  appears from the contribution of isolated mesonic states to the GPDs [BMK02].

The  $t$  independent part of the GPD,  $F^q(x, \xi) \equiv F^q(x, \xi, t=0)$ , is modeled using the factorization of the DD as

$$F^q(\beta, \alpha) = h(\beta, \alpha) q(\beta), \quad (2.19)$$

where  $q(\beta)$  is the regular parton density function and  $h(\beta, \alpha)$  is a profile function parameterized through a one-parameter ansatz [Rad01]:

$$h(\beta, \alpha) = \frac{\Gamma(2b+2)}{2^{2b+1}\Gamma^2(b+1)} \frac{[(1-|\beta|)^2 - \alpha^2]^b}{(1-|\beta|)^{2b+1}}. \quad (2.20)$$

In the forward limit ( $\alpha = 0$ )  $h(\beta, \alpha)$  mimics a mesonic-like two-parton state with a longitudinal momentum  $\beta$ . The parameter  $b$  in Eq. 2.20 defines the “skewness” of the GPD, namely its sensitivity to the dependence on  $\xi$ . In the limiting case  $b \rightarrow \infty$  the GPD becomes independent of  $\xi$  and is reduced to the forward distribution, e.g.  $H^q(x, \xi) = q(x)$ . In the model  $b$  is a free parameter for the valence quark contribution ( $b_{val}$ ) or the sea/antiquark contribution ( $b_{sea}$ ) that can in principle be extracted from observables of hard electroproduction processes, but is still unknown at present.

The main constraint on the  $t$ -dependence of GPDs is given by the sum rule of Eq. 2.11. Elastic form factors for the quark flavor  $q = u, d$  in the proton are related to the proton and neutron form factors, using  $SU(2)$  isospin symmetry. The relations between Dirac form factors and the corresponding single quark contributions to the proton form factors are defined as:

$$\begin{aligned} F_1^u &= 2F_1^p + F_1^n + F_1^s, \\ F_1^d &= 2F_1^n + F_1^p + F_1^s, \end{aligned} \quad (2.21)$$

where  $F_1^p$  and  $F_1^n$  are the proton and neutron Dirac form factors, respectively. The strangeness form factor of the nucleon  $F_1^s$  is expected to be small and set to zero. A similar relation holds for the Pauli form factors  $F_2$ .

For the axial vector form factors the isospin decomposition gives

$$g_A^u = \frac{1}{2}g_A + \frac{1}{2}g_A^0, \quad g_A^d = -\frac{1}{2}g_A + \frac{1}{2}g_A^0, \quad (2.22)$$

where  $g_A$  ( $g_A^0$ ) are the isovector (isoscalar) axial form factors of the nucleon. A similar relation exists for the pseudoscalar form factor  $g_P^q$ .

The  $t$ -dependence of the DD part of the GPD  $H$  can be modeled in two ways. The simplest parameterization valid in the small  $-t$  region is the *factorized* ansatz:

$$\begin{aligned} H^u(x, \xi, t) &= H^u(x, \xi) F_1^u(t)/2, \\ H^d(x, \xi, t) &= H^d(x, \xi) F_1^d(t), \\ H^s(x, \xi, t) &= 0, \end{aligned} \quad (2.23)$$

where  $F_1^u(t)$  and  $F_1^d(t)$  are the elastic form factors for the quark flavors  $u$  and  $d$  in the proton, respectively. The factorized ansatz satisfies both the sum rule constraints (see Eq. 2.11) and the forward limits of the distributions (see Eq. 2.10).

Another approach in modeling the  $t$ -dependence of GPDs is the so-called *Regge ansatz*. In the small  $-t$  region the  $t$ -dependence can be described by a simple Regge-theory motivated ansatz. In this approach the DD defined in Eq. 2.18 is modeled as:

$$F^q(\beta, \alpha, t) = h(\beta, \alpha) q(\beta) \frac{1}{|\beta|^{\alpha' t}}, \quad (2.24)$$

where  $h(\beta, \alpha)$  is the same profile function as in Eq. 2.20 and  $\alpha'$  is the slope of the Regge ansatz, which can be extracted from the cross section measurements of hadron-hadron reactions [Col77].

The odd nature of the D-term allows to expand its  $t$  independent part  $D(x/\xi)$  in odd Gegenbauer polynomials. Its parameterization includes odd terms of the expansion up to the fifth power in  $x/\xi$ , estimated using the calculation of GPDs in the quark soliton model. The  $t$  dependence of the D-term is assumed to be the same as that of the DD part of the GPD  $H$ .

The parameterization of the GPD  $E^q$  is similar to that of  $H^q$  apart from the fact that there is no analogy to the function  $E^q$  in the forward limit. It can only be constrained by the sum rules defined in Eqs. 2.11 and 2.14. The DD  $K^q(\beta, \alpha)$  (see Eq. 2.18) of the function  $E^q$  can be written in analogy with Eq. 2.19 as:

$$K^q(\beta, \alpha) = h(\beta, \alpha) e^q(\beta), \quad (2.25)$$

where the profile function  $h(\beta, \alpha)$  was defined in Eq. 2.20 and the forward distribution  $e^q(\beta)$  is a function based on the forward quark distribution

$q(\beta)$  [GPV01]. Ji's relation (see Eq. 2.14) can be used to constrain the GPD  $E^q$  resulting in a dependence of the constructed function  $e^q(\beta)$  on the total angular momentum  $J^q$  of quark flavor  $q$ . Hence  $J^q$  enters the parameterization of the GPD  $E^q$  as a free parameter that can be extracted from experimental observables [ENVY05].

The  $t$ -dependence of the GPD  $E^q$  is modeled in analogy with that of  $H^q$ , namely with either factorized or Regge-inspired ansätze.

### 2.4.2 Parameterization of the Generalized Parton Distribution $\tilde{H}$

As it was discussed in section 2.3, the D-term does not contribute to the spin dependent GPDs  $\tilde{H}$  and  $\tilde{E}$ . Hence the GPD  $\tilde{H}$  can be expressed in terms of double distributions (see Eq. 2.17) as:

$$\tilde{H}^q(x, \xi) = \int_{-1}^1 d\beta \int_{-1+|\beta|}^{1-|\beta|} d\alpha \delta(\beta + \alpha\xi - x) \tilde{F}^q(\beta, \alpha), \quad (2.26)$$

where  $\tilde{F}^q(\beta, \alpha)$  is the corresponding DD that is parameterized in analogy to Eq. 2.19 with the forward polarized parton distribution  $\Delta q(\beta)$ . With the factorized  $t$ -dependence in the small  $-t$  region the corresponding DDs are

$$\begin{aligned} \tilde{F}^u(\beta, \alpha, t) &= h(\beta, \alpha) \Delta u_V(\beta) g_A^u(t)/g_A^u(0), \\ \tilde{F}^d(\beta, \alpha, t) &= h(\beta, \alpha) \Delta d_V(\beta) g_A^d(t)/g_A^d(0), \end{aligned} \quad (2.27)$$

where  $h(\beta, \alpha)$  is the profile function defined in Eq. 2.20 and  $g_A^q(t)$  is the axial quark form factor related to the nucleon ones as given in Eq. 2.22. The antiquark contribution to  $\tilde{H}^q$  is not taken into account in this model.

### 2.4.3 Parameterization of the Generalized Parton Distribution $\tilde{E}$

The GPD  $\tilde{E}^q$  is constrained only through the sum rule of Eq. 2.11 by the pseudoscalar form factor  $g_P^q(t)$ . Due to the spontaneously broken chiral symmetry, in the region of small  $t$  this form factor is dominated by the contribution of the pion pole. In chiral quark-soliton model calculations the pion pole part of  $\tilde{E}^q$  dominates over a wide range of  $t$  and  $\xi$  values, and in the limit of  $t \rightarrow m_\pi^2$  it exactly reduces to the pion pole contribution.

Based on these findings, the GPD  $\tilde{E}^q$  is assumed to be governed by the pion pole:

$$\tilde{E}^u = -\tilde{E}^d = \frac{1}{2} \tilde{E}_{\pi\text{-pole}}. \quad (2.28)$$

The  $t$ -dependence of  $\tilde{E}_{\pi\text{-pole}}$  is defined by the sum rule of Eq. 2.11 in terms of  $g_P^q(t)$ . According to the partonic interpretation of GPDs discussed in section 2.2, quarks and antiquarks couple to the pion field of the nucleon in the region  $-\xi \leq x \leq \xi$ . Hence  $\tilde{E}_{\pi\text{-pole}}$  is modeled as:

$$\tilde{E}_{\pi\text{-pole}} = \theta(-\xi \leq x \leq \xi) g_P^q(t) \frac{1}{2} \Phi_{as} \left( \frac{x}{\xi} \right), \quad (2.29)$$

where  $\Phi_{as} \left( \frac{x}{\xi} \right)$  is the asymptotic representation of the pion distribution amplitude as introduced in Ref. [GPV01].

# Chapter 3

## Deeply Virtual Compton Scattering

### 3.1 Deeply Virtual Compton Scattering in Terms of Generalized Parton Distributions

Deeply Virtual Compton Scattering is the process of hard electroproduction of a real photon (see figure 2.2):

$$\gamma^*(q) + N(p) \rightarrow \gamma(q') + N(p'),$$

where  $p$  ( $q$ ) and  $p'$  ( $q'$ ) are the 4-momenta of the proton (photon) in the initial and final state, respectively. In the general case of Compton scattering with a *virtual* photon in the final state ( $\gamma^*p \rightarrow \gamma^*p$ ) the helicity amplitudes of the process are given by [Die03]:

$$M_{\lambda'\mu',\lambda\mu} = \epsilon_\alpha T^{\alpha\beta} \epsilon_\beta'^*, \quad (3.1)$$

where  $\epsilon$  ( $\epsilon'$ ) and  $\mu$  ( $\mu'$ ) denote the polarization vector and helicity state of the initial (final) photon, respectively, and  $\lambda$  ( $\lambda'$ ) is the helicity of the initial (final) proton. The hadronic tensor  $T^{\alpha\beta}$  is given by the time-ordered product of the electromagnetic currents of quarks  $J_{em}$ , sandwiched between hadronic states with different momenta:

$$T^{\alpha\beta} = i \int d^4x e^{i(q+q')x/2} \langle p' | T J_{em}^\alpha(-\frac{1}{2}x) J_{em}^\beta(\frac{1}{2}x) | p \rangle. \quad (3.2)$$

Note that in Eq. 3.1 the polarization vectors  $\epsilon$  and  $\epsilon'$  and the hadronic tensor  $T^{\alpha\beta}$  define the helicity states of the photons ( $\mu$ ,  $\mu'$ ) and the protons ( $\lambda$ ,  $\lambda'$ ) in the initial and final states.

In leading order of perturbation theory the amplitudes are represented as:

$$\begin{aligned}
M_{++,++} &= \sqrt{1-\xi^2} \left( \mathcal{H} + \widetilde{\mathcal{H}} - \frac{\xi^2}{1-\xi^2} (\mathcal{E} + \widetilde{\mathcal{E}}) \right), \\
M_{-+,-+} &= \sqrt{1-\xi^2} \left( \mathcal{H} - \widetilde{\mathcal{H}} - \frac{\xi^2}{1-\xi^2} (\mathcal{E} - \widetilde{\mathcal{E}}) \right), \\
M_{++, -+} &= \frac{\sqrt{t_0 - t}}{2m} (\mathcal{E} - \xi \widetilde{\mathcal{E}}), \\
M_{-+, ++} &= -\frac{\sqrt{t_0 - t}}{2m} (\mathcal{E} + \xi \widetilde{\mathcal{E}}),
\end{aligned} \tag{3.3}$$

where  $t_0$  is the minimum possible value of  $-t$  at given  $\xi$ , and  $m$  is the mass of the nucleon. The functions  $\mathcal{H}$ ,  $\mathcal{E}$ ,  $\widetilde{\mathcal{H}}$  and  $\widetilde{\mathcal{E}}$  introduced in Eq. 3.3 are Compton Form Factors (CFFs), which are flavor sums of convolutions of the corresponding leading-twist GPDs  $H$ ,  $E$ ,  $\widetilde{H}$  and  $\widetilde{E}$  with hard scattering amplitudes (known up to NLO in pQCD). For the case of the production of a *real* photon the twist-two CFFs read as:

$$\begin{aligned}
\{\mathcal{H}, \mathcal{E}\}(\xi, t) &= \\
&\sum_q e_q^2 \int_{-1}^1 dx \{H^q, E^q\}(x, \xi, t) \left( \frac{1}{\xi - x - i0} - \frac{1}{\xi + x - i0} \right) + \mathcal{O}(\alpha_s), \\
\{\widetilde{\mathcal{H}}, \widetilde{\mathcal{E}}\}(\xi, t) &= \\
&\sum_q e_q^2 \int_{-1}^1 dx \{\widetilde{H}^q, \widetilde{E}^q\}(x, \xi, t) \left( \frac{1}{\xi - x - i0} + \frac{1}{\xi + x - i0} \right) + \mathcal{O}(\alpha_s),
\end{aligned} \tag{3.4}$$

where the curly brackets indicate that the equation is valid for one of the elements enclosed.

The *unpolarized* cross section of the DVCS process depends on CFFs as:

$$\begin{aligned}
\frac{1}{2} \sum_{\lambda' \lambda} |M_{\lambda' +, \lambda +}|^2 &= (1 - \xi^2) (|\mathcal{H}|^2 + |\widetilde{\mathcal{H}}|^2) - \left( \xi^2 + \frac{t}{4m^2} \right) |\mathcal{E}|^2 - \\
&\quad - \xi^2 \frac{t}{4m^2} |\widetilde{\mathcal{E}}|^2 - 2\xi^2 \text{Re}(\mathcal{H}^* \mathcal{E} + \widetilde{\mathcal{H}}^* \widetilde{\mathcal{E}}),
\end{aligned} \tag{3.5}$$

the corresponding *polarized* combinations for it read:

$$\begin{aligned}
\frac{1}{2} \sum_{\lambda'} \left( |M_{\lambda' +, ++}|^2 - |M_{\lambda' +, -+}|^2 \right) &= \\
&= 2\text{Re} \left[ (1 - \xi^2) \mathcal{H}^* \widetilde{\mathcal{H}} - \left( \frac{\xi^2}{1+\xi} + \frac{t}{4m^2} \right) \xi \mathcal{E}^* \widetilde{\mathcal{H}} - \xi^2 (\mathcal{H}^* \mathcal{E} + \widetilde{\mathcal{H}}^* \widetilde{\mathcal{E}}) \right].
\end{aligned} \tag{3.6}$$

The CFFs  $\mathcal{F} = \{\mathcal{H}, \widetilde{\mathcal{H}}, \mathcal{E}, \widetilde{\mathcal{E}}\}$  have different relations of their real and imaginary parts to the corresponding GPDs  $F = \{H, \widetilde{H}, E, \widetilde{E}\}$ . In leading



order of perturbation theory the imaginary part follows from the definition of CFFs (see Eq. 3.4) [BMK02]:

$$\text{Im}\mathcal{F} = \pi \sum_q e_q^2 \left( F^q(\xi, \xi, t) \mp F^q(-\xi, \xi, t) \right), \quad (3.7)$$

i.e. it is sensitive to the respective GPDs along the line  $x = \pm\xi$ . The real part of CFFs can be written as:

$$\text{Re}\mathcal{F} = - \sum_q e_q^2 \left[ P \int_{-1}^1 dx F^q(x, \xi, t) \left( \frac{1}{x - \xi} \pm \frac{1}{x + \xi} \right) \right], \quad (3.8)$$

where  $P$  denotes Cauchy's principal value. The integrand in Eq. 3.8 contributes mainly in the region close to the line  $x = \pm\xi$ , being enhanced there

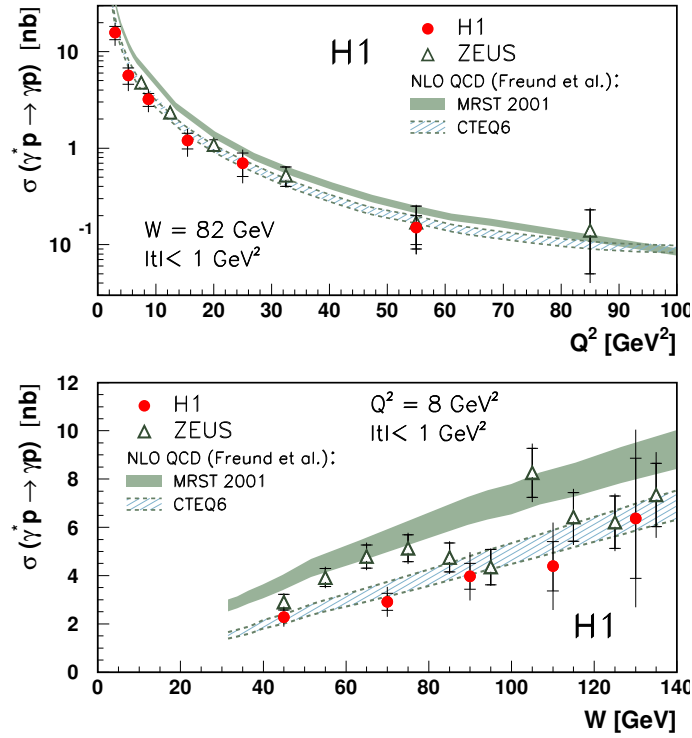


Figure 3.1: The  $\gamma^*p \rightarrow \gamma p$  cross section as a function of  $Q^2$  at fixed  $W = 82$  GeV (left) and as a function of  $W$  at fixed  $Q^2 = 8$  GeV<sup>2</sup> (right),  $|t| < 1$  GeV<sup>2</sup>. The inner error bars represent the statistical and the full error bars the combined statistical and systematic uncertainty. The figures are from Ref. [A<sup>+</sup>05b].

by the propagators  $1/(x \mp \xi)$ . Hence the DVCS process being described in terms of CFFs is sensitive to GPDs mainly in the region of  $x = \pm \xi$ .

First measurements of the DVCS cross section were performed by the HERA experiments H1 [A<sup>+</sup>05b] and Zeus [C<sup>+</sup>03]. In figure 3.1 the obtained dependences of the DVCS cross section on  $Q^2$  and  $W$  are shown. The results are compared with the theoretical predictions made by Freund et al. [FMS03] at NLO QCD for two different sets of PDFs (MRST 2001 and CTEQ6) used for modeling GPDs.

### 3.2 Interference with the Bethe-Heitler Process

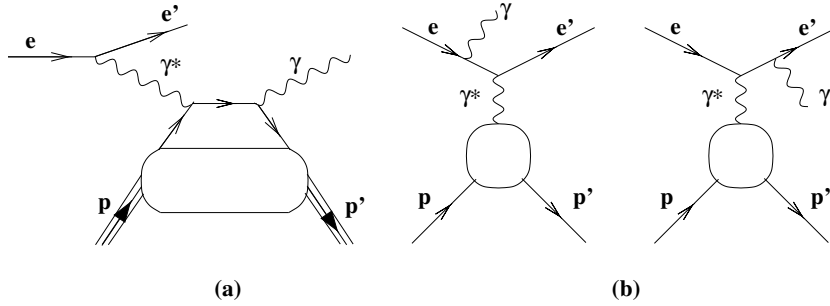


Figure 3.2: Diagrams of the DVCS process (a) and of initial and final state radiation of the scattering lepton (BH process) (b).

The DVCS process has an identical final state with the Bethe-Heitler (BH) process where the photon is radiated from incoming or outgoing lepton (see figure 3.2). This makes them experimentally indistinguishable and leads to the interference between their amplitudes. This yields the following cross section for real photon production:

$$\frac{d\sigma}{dx_B dQ^2 dt |d\phi} = \frac{\alpha_{em}^3 x_B y^2}{8\pi Q^4} \frac{1}{\sqrt{1 + 4x_B^2 m^2/Q^2}} \frac{1}{e^6} [|\tau_{BH}|^2 + |\tau_{DVCS}|^2 + I], \quad (3.9)$$

where  $\phi$  is the azimuthal angle defined by the lepton scattering plane and the photon production plane (see figure 3.3). The amplitude of the BH process  $\tau_{BH}$  is exactly calculable in Quantum Electrodynamics with the knowledge of the Dirac and Pauli form factors [MT69, E<sup>+</sup>01].

The interference term

$$I = \tau_{DVCS} \tau_{BH}^* + \tau_{DVCS}^* \tau_{BH}$$

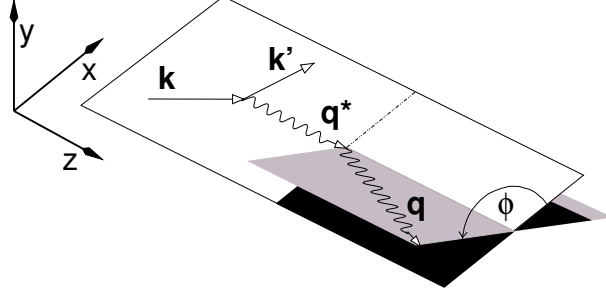


Figure 3.3: Kinematics of the DVCS process. The momenta of the incoming and scattered positrons ( $k$  and  $k'$ ) define the scattering plane. The momenta of the virtual and real photons ( $q^*$  and  $q$ ) define the production plane. The azimuthal angle  $\phi$  is the angle between the scattering and the production plane.

can be written at leading twist accuracy as:

$$I \propto \frac{\pm 1}{P(\cos \phi)} \left( \cos \phi \operatorname{Re} \widehat{M}_{++} - P_l \sqrt{1 - \epsilon^2} \sin \phi \operatorname{Im} \widehat{M}_{++} - \right. \\ \left. - S_L [\sin \phi \operatorname{Im} \widehat{M}_{++}^L - P_l \sqrt{1 - \epsilon^2} \cos \phi \operatorname{Re} \widehat{M}_{++}^L] \right), \quad (3.10)$$

where the sign  $\pm$  is the charge of the lepton beam with polarization  $P_l$ , scattered on a target with longitudinal polarization  $S_L$ . Here  $\epsilon$  is the ratio of fluxes of longitudinal to transverse initial virtual photons in the DVCS process and the factor  $P(\cos \phi)$  coming from the lepton propagators in the Bethe-Heitler process gives an additional  $\phi$  dependence as [Die03]:

$$P(\cos \phi) = 1 - 2 \cos \phi \sqrt{\frac{2(1 + \epsilon)}{\epsilon} \frac{1 - \xi}{1 + \xi} \frac{t_0 - t}{Q^2}} + \mathcal{O}\left(\frac{1}{Q^2}\right). \quad (3.11)$$

In case of an *unpolarized* target ( $S_L = 0$ ) the amplitude  $\widehat{M}_{++}$  is a linear combination of the CFFs  $\mathcal{H}$ ,  $\widetilde{\mathcal{H}}$  and  $\mathcal{E}$ :

$$\widehat{M}_{++} = \sqrt{1 - \xi^2} \frac{\sqrt{t_0 - t}}{2m} \left[ F_1 \mathcal{H} + \xi (F_1 + F_2) \widetilde{\mathcal{H}} - \frac{t}{4m^2} F_2 \mathcal{E} \right], \quad (3.12)$$

where  $F_1$  and  $F_2$  are the Dirac and Pauli form factors, respectively.

In case of a *polarized* target ( $S_L \neq 0$ ) the amplitude  $\widehat{M}_{++}^L$  is defined by another linear combination of CFFs  $\mathcal{H}$ ,  $\widetilde{\mathcal{H}}$ ,  $\mathcal{E}$  and  $\widetilde{\mathcal{E}}$ :

$$\widehat{M}_{++}^L = \sqrt{1 - \xi^2} \frac{\sqrt{t_0 - t}}{2m} \left[ F_1 \widetilde{\mathcal{H}} + \xi (F_1 + F_2) \left( \mathcal{H} + \frac{\xi}{1 + \xi} \mathcal{E} \right) - \right. \\ \left. - \left( \frac{\xi}{1 + \xi} F_1 + \frac{t}{4m^2} F_2 \right) \xi \widetilde{\mathcal{E}} \right]. \quad (3.13)$$

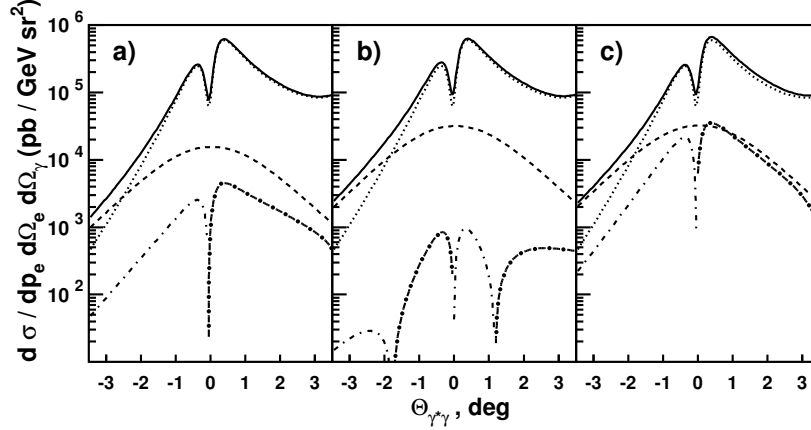


Figure 3.4: The dependence of the cross sections of the DVCS and BH processes and their interference term on the angle between the virtual and real photons  $\theta_{\gamma^*\gamma}$  in the HERMES acceptance. The panels a), b), c) correspond to numerical model calculations A), B), D) in Ref. [KN02], respectively. The dotted line corresponds to the BH process, the dashed one to the DVCS process, the dash-dotted one to the interference term and the solid one to the total cross section. The figures are taken from Ref. [Kor05].

Note that the subscripts ++ in Eqs. 3.12 and 3.13 denote positive helicity of both initial (virtual) and final (real) photons.

Numerical calculations in Ref. [KN02] show the relation between the BH and DVCS cross sections and the interference term for the average kinematics in the HERMES acceptance. The results for an unpolarized proton target and an unpolarized positron beam, shown in figure 3.4, demonstrate the dominance of the BH process in most of the HERMES kinematic region. This implies that direct measurements of the DVCS cross section at HERMES would lead to big systematic uncertainties due to the subtraction of the BH process. At HERMES, the CFFs can be accessed best through the interference term  $I$  in asymmetry measurements. Since CFFs contribute to the interference term linearly such approach gives an additional advantage over cross section measurements because it provides information about both magnitude and phase of CFFs.

### 3.3 Angular Dependence of the Photoproduction Cross Section

The squared amplitudes  $|\tau_{BH}|^2$  and  $|\tau_{DVCS}|^2$  and the interference term  $I$  introduced in Eq. 3.9 can be represented at next-to-leading order accuracy as sum of the sine and cosine harmonics in the azimuthal angle  $\phi$  as [BMK02]:

$$|\tau_{BH}|^2 = \frac{e^6}{x_B^2 y^2 (1 + \epsilon^2)^2 t P(\phi)} \times \left\{ c_0^{BH} + \sum_{n=1}^2 c_n^{BH} \cos(n\phi) + s_1^{BH} \sin(\phi) \right\}, \quad (3.14)$$

$$|\tau_{DVCS}|^2 = \frac{e^6}{y^2 Q^2} \left\{ c_0^{DVCS} + \sum_{n=1}^2 [c_n^{DVCS} \cos(n\phi) + s_n^{DVCS} \sin(n\phi)] \right\}, \quad (3.15)$$

$$I = \frac{\pm e^6}{x_B y^3 P(\phi) t} \left\{ c_0^I + \sum_{n=1}^3 [c_n^I \cos(n\phi) + s_n^I \sin(n\phi)] \right\}, \quad (3.16)$$

where the  $+$  ( $-$ ) sign in the interference term stands for a negatively (positively) charged lepton beam and the factor  $P(\phi)$  is defined in Eq. 3.11.

The Fourier coefficients  $c_0^{DVCS}$ ,  $c_0^I$ ,  $c_1^I$  and  $s_1^I$  contribute to the amplitudes at twist-two and  $c_1^{DVCS}$ ,  $s_1^{DVCS}$ ,  $c_2^I$  and  $s_2^I$  at twist-three level. The coefficients  $c_3^I$  and  $s_3^I$  and  $c_2^{DVCS}$ ,  $s_2^{DVCS}$  get contributions from twist-two double helicity-flip *gluon* GPDs discussed in detail in Ref. [BMK02].

The coefficients of higher harmonics of the DVCS amplitude and of the interference term are kinematically suppressed with respect to the lower ones with the factor  $K_{sup.}$  defined as:

$$K_{sup.} \simeq \sqrt{-\frac{t}{Q^2} (1 - x_B)(1 - y)}. \quad (3.17)$$

The factor enters the coefficients  $(c, s)_{n=1,2,3}$  as  $(K_{sup.})^n$ .

A detailed discussion on the contributions of CFFs to all Fourier coefficients at NLO accuracy can be found in Ref. [BMK02].

### 3.4 Longitudinal Target-Spin Asymmetry

The Longitudinal Target Spin Asymmetry (LTSA)  $A_{UL}$  is calculated for an unpolarized beam  $B^U$  as difference of cross sections for target helicity states antiparallel ( $T^+$ ) and parallel ( $T^-$ ) to the beam direction

$$A_{UL} = \frac{\sigma^{B^U T^+} - \sigma^{B^U T^-}}{\sigma^{B^U T^+} + \sigma^{B^U T^-}}, \quad (3.18)$$

where  $\sigma$  is the photoproduction cross section introduced in Eq. 3.9. The  $\phi$  dependence of the asymmetry with respect to the target spin can be expanded in Fourier series, as shown in Eqs. 3.14, 3.15, 3.16, giving the main contributions of the harmonics to the asymmetry as [BMK02]:

$$A_{UL}(\phi) \simeq \frac{\frac{K_I}{P(\phi)}(\sum_{n=1}^3 s_{L,n}^I \sin n\phi) - K_{DVCS}(\sum_{n=1}^2 s_{L,n}^{DVCS} \sin n\phi)}{\frac{K_{BH}}{P(\phi)}(c_{unp,0}^{BH} + c_{unp,1}^{BH} \cos \phi + \dots) + \dots}, \quad (3.19)$$

where  $K_I$ ,  $K_{DVCS}$  and  $K_{BH}$  are kinematic coefficients with no dependence on azimuthal angle and  $P(\phi)$  as defined in Eq. 3.11 gives an additional  $\phi$  dependence due to BH propagators.

To the extent that the leading BH-term  $c_0^{BH}$  dominates the denominator of Eq. 3.19 the azimuthal dependence of the asymmetry can be rewritten as the sum of  $\sin \phi$  and  $\sin 2\phi$  harmonics that contribute to the asymmetry with amplitudes  $A_{UL}^{\sin \phi}$  and  $A_{UL}^{\sin 2\phi}$  as:

$$A_{UL}(\phi) \simeq A_{UL}^{\sin \phi} \sin \phi + A_{UL}^{\sin 2\phi} \sin 2\phi. \quad (3.20)$$

Assuming the dominance of the interference term over the DVCS cross section for the longitudinally polarized proton target, the amplitudes of the  $\sin \phi$  and  $\sin 2\phi$  harmonics read:

$$\begin{aligned} A_{UL}^{\sin \phi} &\propto \frac{1}{c_{unp,0}^{BH}} s_{L,1}^I, \\ A_{UL}^{\sin 2\phi} &\propto \frac{1}{c_{unp,0}^{BH}} s_{L,2}^I, \end{aligned} \quad (3.21)$$

where the Fourier coefficient  $s_{L,1}^I$  is proportional to the imaginary part of the polarized amplitude  $\widehat{M}_{++}^L$  introduced in Eq. 3.13. In terms of CFFs it reads:

$$\begin{aligned} s_{L,1}^I &\propto \text{Im} \left[ \sqrt{1 - \xi^2} \frac{\sqrt{t_0 - t}}{2m} \left[ F_1 \widetilde{\mathcal{H}} + \xi(F_1 + F_2)(\mathcal{H} + \frac{\xi}{1 + \xi} \mathcal{E}) - \right. \right. \\ &\quad \left. \left. - (\frac{\xi}{1 + \xi} F_1 + \frac{t}{4m^2} F_2) \xi \widetilde{\mathcal{E}} \right] \right]. \end{aligned} \quad (3.22)$$

The kinematically suppressed coefficient  $s_{L,2}^I$  gets contributions of GPDs at twist-three level. It has the same dependence on the CFFs as the coefficient  $s_{L,1}^I$  in Eq. 3.22, but with the twist-two CFFs  $\mathcal{F} = \{\mathcal{H}, \widetilde{\mathcal{H}}, \mathcal{E}, \widetilde{\mathcal{E}}\}$  replaced by the effective functions  $\mathcal{F}^{eff} = \{\mathcal{H}^{eff}, \widetilde{\mathcal{H}}^{eff}, \mathcal{E}^{eff}, \widetilde{\mathcal{E}}^{eff}\}$  which are combinations of twist-two and twist-three functions [BMK02] and can be represented as:

$$\mathcal{F}^{eff} \equiv -2\xi \left( \frac{1}{1 + \xi} \mathcal{F} + \mathcal{F}_+^3 - \mathcal{F}_-^3 \right), \quad (3.23)$$

where  $\mathcal{F}_\pm^3$  are twist-tree CFFs that are defined in analogy with twist-two CFFs (cf. Eq. 3.4). Note that the subscripts  $-$  and  $+$  denote the even and odd parts of twist-three GPDs, respectively.

Due to the fact that the values of  $\xi$  accessible experimentally in a fixed-target experiment are small,  $\mathcal{O}(0.1)$ , in measurements of the LTSA the main contribution to the amplitude  $\widehat{M}_{++}^L$  arises from the CFF  $\widetilde{\mathcal{H}}$ . Hence the amplitudes  $A_{UL}^{\sin\phi}$  and  $A_{UL}^{\sin 2\phi}$  of the  $\sin\phi$  and  $\sin 2\phi$  harmonics of the asymmetry are sensitive to the CFF  $\widetilde{\mathcal{H}}$  at twist-two and twist-three level, respectively, i.e.:

$$\begin{aligned} A_{UL}^{\sin\phi} &\sim \text{Im}\widetilde{\mathcal{H}}, \\ A_{UL}^{\sin 2\phi} &\sim \text{Im}\widetilde{\mathcal{H}}^{eff}. \end{aligned} \quad (3.24)$$

According to the relation between the imaginary part of CFFs and the corresponding GPDs described in Eq. (3.7) measurements of the LTSA provide experimental access to the polarized GPD  $\widetilde{H}$  in the region  $x \approx \xi$ .

As it follows from Eq. 3.19, a  $\sin 3\phi$  harmonic contributes to the interference term of the DVCS and BH cross sections. The corresponding amplitude  $A_{UL}^{\sin 3\phi}$  is sensitive to the double helicity-flip *gluon* GPDs. These GPDs are defined in term of the gluon bilocal current operator in analogy with quark GPDs introduced in section 2.2.1. Since the amplitude  $A_{UL}^{\sin 3\phi}$  is kinematically suppressed by a factor of  $\frac{Q^2 K_{sup}^2}{M(2-x_B)^2}$  with respect to the leading amplitude  $A_{UL}^{\sin\phi}$ , the contribution of the  $\sin 3\phi$  harmonic to the interference term is expected to be negligible at HERMES kinematics. Hence the consideration of these double helicity-flip gluon GPDs are beyond the scope of this work. More details can be found in e.g. Ref. [BMK02].

The detailed discussion of the analysis of the LTSA obtained from HERMES data, as performed in the context of this thesis, will be presented in the following chapters.

### 3.5 Beam-Spin and Beam-Charge Asymmetries

In case of an unpolarized target the  $\phi$ -dependence of the cross section asymmetry with respect to the charge (spin) of the lepton beam gives access to the real (imaginary) part of the unpolarized amplitude  $\widehat{M}_{++}$  introduced in Eq. 3.12.

For an unpolarized beam of charge  $C$  the Beam-Charge Asymmetry

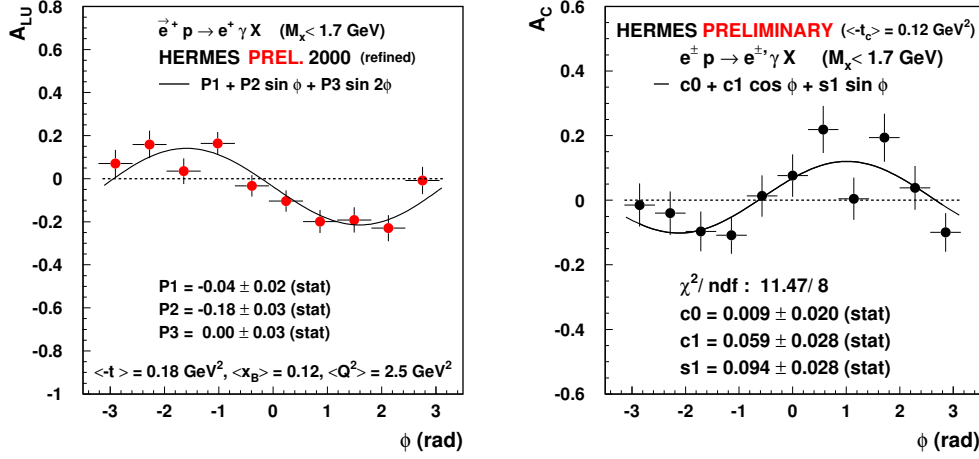


Figure 3.5: Beam spin asymmetry  $A_{LU}$  (left) and beam charge asymmetry  $A_C$  (right) for hard exclusive electroproduction of photons off the proton as function of the azimuthal angle  $\phi$ . The solid curves show the results of the indicated fits with the values given in the plots.

(BCA) is defined as:

$$A_C(\phi) = \frac{d\sigma^+(\phi) - d\sigma^-(\phi)}{d\sigma^+(\phi) + d\sigma^-(\phi)}, \quad (3.25)$$

where the superscript  $+$  and  $-$  denote the lepton beam charge. For a longitudinally ( $L$ ) polarized beam the Beam-Spin Asymmetry is defined as:

$$A_{LU}(\phi) = \frac{d\sigma^{\rightarrow}(\phi) - d\sigma^{\leftarrow}(\phi)}{d\sigma^{\rightarrow}(\phi) + d\sigma^{\leftarrow}(\phi)}, \quad (3.26)$$

where  $\rightarrow$  and  $\leftarrow$  denote the beam spin parallel and antiparallel to the beam direction, respectively.

With the same assumption about the denominators of Eqs. 3.25 and 3.26 as for the LTSA in section 3.4, at leading twist accuracy the azimuthal dependence of BCA and BSA is reduced to  $\sin \phi$  and  $\cos \phi$  as

$$\begin{aligned} A_C &\propto \frac{1}{c_{0,U}^{BH}} c_{1,U}^I \cos \phi \propto \text{Re} \widehat{M}_{++} \cos \phi, \\ A_{LU} &\propto \frac{1}{c_{0,U}^{BH}} c_{1,U}^I \sin \phi \propto \text{Im} \widehat{M}_{++} \sin \phi. \end{aligned} \quad (3.27)$$



Note that in case of the BSA the exact expression of the denominator of Eq. 3.26 has the same contributions of the Fourier coefficients and of the corresponding harmonics as those of the LTSA in the denominator of Eq. 3.18.

In the experimentally accessible region of  $\xi$  the main contribution to the amplitude  $\widehat{M}_{++}$  arises from the GPD  $H$ . Hence measurements of BSA and BCA give access to the imaginary and real part of the CFF  $\mathcal{H}$ , respectively.

The BSA and BCA on an unpolarized proton target were measured at HERMES [A<sup>+</sup>01a, Ell04, Now05]. Their azimuthal dependences shown in figure 3.5 demonstrate the expected  $\sin\phi$  and  $\cos\phi$  behavior. Note that the sizable  $\sin\phi$  contribution to the BCA arises from the unbalanced beam polarization ( $\langle P_l \rangle \neq 0$ ).

### 3.6 Transverse Target-Spin Asymmetry

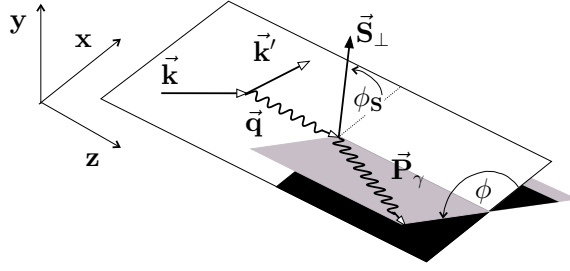


Figure 3.6: Kinematics of the DVCS process for transverse target polarization. The angle  $\phi_S$  denotes the azimuthal angle of the polarization vector of the transversely polarized target  $\vec{S}_\perp$  with respect to the scattering plane, measured about the direction of the virtual photon.

In case of *transverse* target polarization the azimuthal dependence of the interference term  $I_{TP}$  of the BH/DVCS cross section becomes sensitive to the amplitudes  $\widehat{M}_N$  and  $\widehat{M}_S$  (defined below):

$$I_{TP} \propto \frac{\pm e^6}{x_B y^3 P(\phi)} \left[ \text{Im} \widehat{M}_N \sin(\phi - \phi_S) \cos \phi + \text{Im} \widehat{M}_S \cos(\phi - \phi_S) \sin \phi \right]. \quad (3.28)$$

Here  $\phi_S$  is the azimuthal angle of the vector of transverse target polarization  $\vec{S}_\perp$  with respect to the lepton production plane (see figure 3.6) and the other notations are the same as in Eq. 3.10. The amplitudes are sensitive to the following CFFs as:

$$\widehat{M}_N \sim -\frac{t}{4M^2} [F_2 \mathcal{H} - F_1 \mathcal{E}],$$

$$\widehat{M}_S \sim -\frac{t}{4M^2} [F_2 \widetilde{\mathcal{H}} - F_1 \xi \widetilde{\mathcal{E}}], \quad (3.29)$$

where  $F_1$  and  $F_2$  are Dirac and Pauli form factors, respectively.

The Transverse Target-Spin Asymmetry (TTSA) is defined as:

$$A_{UT}(\phi, \phi_S) = \frac{1}{\langle |\vec{S}_\perp| \rangle} \frac{d\sigma(\phi, \phi_S) - d\sigma(\phi, \phi_S + \pi)}{d\sigma(\phi, \phi_S) + d\sigma(\phi, \phi_S + \pi)}. \quad (3.30)$$

Two leading amplitudes  $A_{UT}^{\sin(\phi-\phi_S)\cos\phi}$  and  $A_{UT}^{\cos(\phi-\phi_S)\sin\phi}$  of the TTSA are related to the amplitudes defined in Eq. 3.29 as:

$$\begin{aligned} A_{UT}^{\sin(\phi-\phi_S)\cos\phi} &\propto \text{Im}\widehat{M}_N, \\ A_{UT}^{\cos(\phi-\phi_S)\sin\phi} &\propto \text{Im}\widehat{M}_S. \end{aligned} \quad (3.31)$$

Hence the amplitude  $A_{UT}^{\sin(\phi-\phi_S)\cos\phi}$  of the TTSA is sensitive to the GPD  $E$  that contributes to Ji's relation (see section 2.3.1) and thus a measurement of the TTSA together with the BSA and BCA can give an access to the total angular momentum of quarks in the nucleon [ENVY05].

## Chapter 4

# The HERMES Experiment

HERMES (*HERA MEasurement of Spin*) is a fixed-target experiment, one of the four experiments using the HERA (*Hadron Electron Ring Anlage*) storage ring at DESY in Hamburg. The HERMES experiment was originally designed to study the spin structure of proton and neutron, using deep inelastic electron nucleon scattering. It employs the polarized electron or positron beam of 27.57 GeV energy of HERA. The schematic diagram of the HERMES spectrometer is shown in figure 4.1. The main advantage of the HERMES experiment with respect to most other spin experiments is its polarized internal gas target. Located in the vacuum of the HERA beam the target gas has very high purity. The low density of the target allows to reduce bremsstrahlung and secondary interactions, providing clean experimental conditions to study

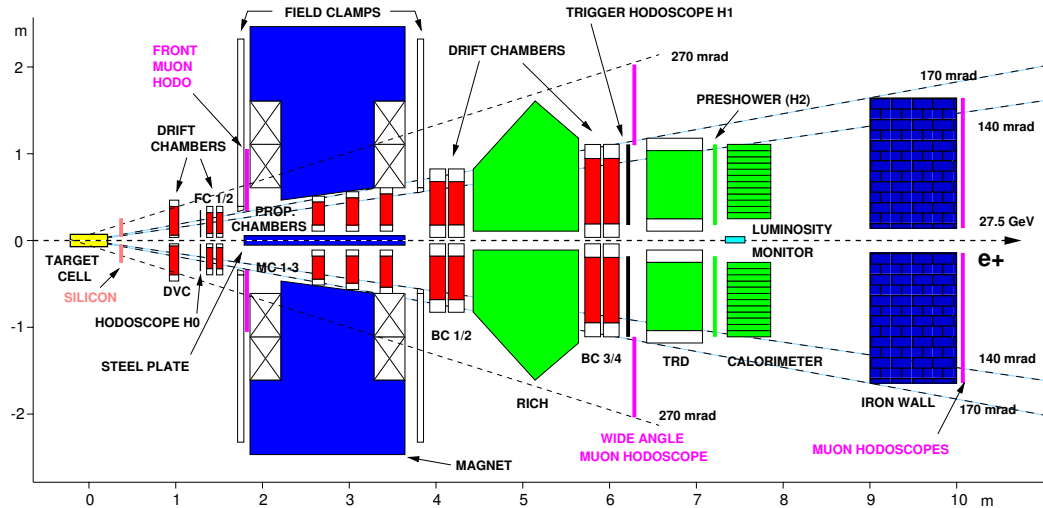


Figure 4.1: Schematic diagram of the HERMES experiment.

final state particles. Particles produced in the interaction of the beam with the target are tracked by the drift chambers located before and after the dipole magnet. The gap of the magnet defines the acceptance of the detector of  $40 \text{ mrad} < |\theta_y| < 140 \text{ mrad}$  and  $|\theta_x| < 170 \text{ mrad}$  in vertical and horizontal directions, respectively. In order to comply with the particle deflection in the magnet, the horizontal acceptance is increased to  $|\theta_x| < 270 \text{ mrad}$  behind the magnet. The field of the magnet is mapped and together with the tracking system the magnet is used for momentum measurements of charged particles. The momentum resolution is about  $\delta P/P \sim 1\%$ . A lead-glass calorimeter together with scintillator hodoscopes is used for event triggering. The calorimeter is also used for detection of photons, providing an energy resolution of about 5%. Particle identification is based on the responses of the Transition Radiation Detector (TRD), the preshower hodoscope and the calorimeter. The efficiency of positron identification is about 98% with a hadron contamination estimated to be less than 0.5%. The Ring Imaging Čerenkov Detector (RICH) allows identification of hadrons, namely pions, protons and kaons. Note that a threshold Čerenkov detector was used until the RICH was installed in 1998. The luminosity is measured by a small electromagnetic calorimeter (luminosity monitor) located around the positron beam pipe. A detailed description of the HERMES detector can be found in Ref. [A<sup>+</sup>98a]. In this chapter the detector components used for this analysis will be discussed.

## 4.1 The HERA Beam

HERA is a 6.3 km circumference storage ring located at DESY in Hamburg. It provides a positron or electron beam with a momentum of 27.57 GeV/c and a proton beam with a momentum of 920 GeV/c (see figure 4.2). HERMES makes use of the polarized electron/positron beam only. The polarization of electrons/positrons at HERA is built up due to self-polarization of the beam in bremsstrahlung: the so-called Sokolov-Ternov effect [ST64]. The effect is based on a small asymmetry in the spin-flip probability with respect to the spin direction of the particle, due to synchrotron radiation in the magnetic field. The probability for the particle spin to flip into a state with the spin parallel to the magnetic field is higher than to flip into an antiparallel state. Hence with time the beam becomes self-polarized in the direction of the magnetic field of the bending magnets of the storage ring. The beam polarization increases with time as:

$$P_B = P_{max}(1 - e^{-t/\tau}), \quad (4.1)$$

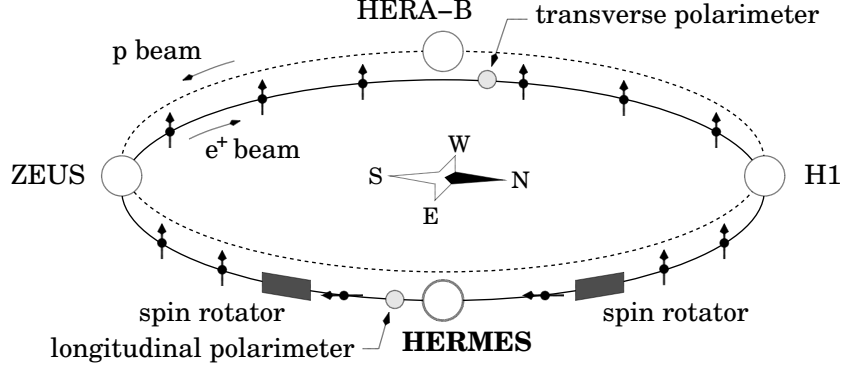


Figure 4.2: Schematic diagram of the HERA accelerator layout until 2000.

where  $P_{max}$  is the maximum polarization that can be reached due to this effect and  $\tau$  is a time constant. The theoretical value of  $P_{max}$  does not depend on the characteristics of the machine and is equal to about 92%. The time constant depends on the bending radius in the magnetic field  $\rho$  and on the Lorentz factor of the particle  $\gamma = E/m_e$  as:

$$\tau = P_{max} \frac{m_e}{\hbar c^2 r_e} \frac{\rho^3}{\gamma^5}, \quad (4.2)$$

where  $r_e$  is the classical electron radius. In case of HERA the average bending radius is about  $\rho = 707$  m and for the beam energy  $E = 27.5$  GeV the factor  $\gamma = 53800$  [Dür95]. The corresponding time constant is about 37 min. Various depolarization effects influence the beam in a real machine. Due to imperfections of the magnetic field and the alignment of the magnets, beam-beam interaction between the electron/positron and proton beams, the maximum polarization is reduced to about 60% with the rise time being about 25 min.

Transverse polarization of the beam is rotated to longitudinal one and then back by spin rotators [BS86] located before and after the HERMES experiment area (see figure 4.2). The relativistic motion of the spin vector is described by the Thomas-Bargmann-Michel-Telegdi (T-BMT) equation [BMT59]. Since the spin vector precesses about the direction of the magnetic field, the spin direction is rotated by  $90^\circ$  by a set of horizontal and vertical bending magnets (see Ref. [BS86] for detail), called spin rotator.

#### 4.1.1 Beam Polarization Measurement

The beam polarization is monitored by two polarimeters. The Transverse POLarimeter (TPOL) [B<sup>+</sup>93, B<sup>+</sup>94] is located in the region of HERA-West

(see figure 4.2) and measures the transverse polarization of the beam. The Longitudinal POLarimeter (LPOL) [B<sup>+</sup>02], located in the HERMES area in between the two spin rotators, measures the longitudinal beam polarization. Both polarimeters employ polarized Compton scattering for their measurements.

In case of transverse ( $P_y$ ) and longitudinal ( $P_z$ ) polarization of the positron beam, the differential cross section for Compton scattering of polarized photons off positrons can be written as:

$$\frac{d\sigma_C}{d\Omega} = \frac{1}{2}r_e^2 \left(\frac{k_f}{k_i}\right)^2 \left[\Sigma_0 + S_1\Sigma_1 + S_3(P_y\Sigma_{2,y} + P_z\Sigma_{2,z})\right], \quad (4.3)$$

where  $k_i$  and  $k_f$  are the initial and final photon momenta in the positron rest frame and  $S_1$  and  $S_3$  are the linear and circular components of the polarization of the initial photon, respectively. Unpolarized and polarized terms of the Compton cross section are denoted with  $\Sigma_0$  and  $\Sigma_{1,2}$ , respectively. Spin dependent terms of the cross section are essential for the beam polarization measurements.

Both the TPOL and the LPOL make use of a circularly polarized photon beam. In case of the TPOL a 10 W argon-ion laser is used to provide photons with an energy of 2.41 eV. The linearly polarized continuous photon beam is converted by a Pockels cell to circularly polarized light. The beam helicity is switched between left and right with a frequency of about 90 Hz. For the LPOL a Nd:YAG pulse laser is used with a photon energy of 2.33 eV. The linearly polarized photon beam is converted to a circularly polarized one with a Pockels cell, alternating helicity at each pulse. The transport of the photon beams to their interaction area (with the positron beam) is accomplished by remotely controlled sets of mirrors.

The energy of the positron beam is very high with respect to the energy of the photons produced by the lasers, hence in the laboratory system the photons are backscattered in a narrow cone. In case of the TPOL a tungsten scintillator sandwich calorimeter is used for the detection of the photons. The calorimeter is separated into two halves above and below the beam pipe allowing to measure the energy and vertical hit position of the photons. In case of the LPOL, the photons are detected by a calorimeter consisting of four Čerenkov NaBi(WO<sub>4</sub>)<sub>2</sub> crystals arranged in a  $2 \times 2$  matrix.

In the measurement of the transverse beam polarization the TPOL employs the fact that the  $\Sigma_{2,y}$  term of the Compton cross section has an azimuthal dependence [Bec00]. The vertical spatial asymmetry measured by the TPOL calorimeter is related to the beam polarization as:

$$\Delta y(E_\gamma) = \frac{\langle y(E_\gamma) \rangle^- - \langle y(E_\gamma) \rangle^+}{2} = \Delta S_3 \cdot P_y \cdot \Pi_y(E_\gamma), \quad (4.4)$$

where  $\langle y(E_\gamma) \rangle^\pm$  is the mean vertical position of the distributions of the Compton photons in the respective helicity state and  $\Delta S_3 = (S_3^+ - S_3^-)/2$  is the mean magnitude of the circular light polarization. The analyzing power  $\Pi_y(E_\gamma)$  is derived from the knowledge of the cross section of the Compton scattering.

In case of the longitudinally polarized beam the Compton cross section has almost no azimuthal dependence. Since the energy spectrum of the backscattered Compton photons depends on their helicity states, the beam polarization is extracted through a measurement of the asymmetry of the energy deposited by the photons in the calorimeter of the LPOL. The asymmetry is related to the positron beam polarization as:

$$A(\Delta S_3, P_z) = \Delta S_3 \cdot P_z \cdot \Pi, \quad (4.5)$$

with the same notations as in Eq. 4.4.

The accuracy of the beam polarization measurement is dominated by the systematic error, both for TPOL and LPOL. The fractional systematic error of the measured polarization is about 3.4% in 1996/1997 for the TPOL and about 4.0% in 1997 for the LPOL [Bec00].

### 4.1.2 Luminosity Monitor

The LUMInosity monitor (LUMI) [B<sup>+</sup>01a] is a pair of calorimeters mounted close to the beam pipe 7.2 m downstream of the HERMES target (see figure 4.1). The calorimeters are Čerenkov NaBi(WO<sub>4</sub>)<sub>2</sub> crystals arranged in a  $3 \times 4$  matrix and coupled to individual photo-multipliers. Each calorimeter is  $66 \times 88 \text{ mm}^2$  at its front side.

The luminosity of the positron beam is obtained from the measurement of the coincidence rate of the processes with well known cross sections. The measured processes are elastic scattering of beam electrons off the atomic target electrons  $e^+ + e^- \rightarrow e^+ + e^-$  (Bhabha scattering) and their annihilation  $e^+ + e^- \rightarrow 2\gamma$ . The cross sections of both processes can be calculated up to third order accuracy in QED. The luminosity is extracted as the ratio of the integrated coincidence rate measured by the LUMI to the sum of the cross sections (for details see section 5.5).

The systematic uncertainty for the absolute luminosity measurements is 6.3 – 6.4% and that for the relative luminosity measurements 0.9 – 1.5% [B<sup>+</sup>01a].

## 4.2 HERMES Internal Gas Target

The HERMES experiment employs an internal polarized gas target [A<sup>+</sup>05a] located inside the HERA vacuum. The main advantage of such a target with respect to an external gaseous, liquid or solid target is the purity of the target material. The lay-out of the target as an open-ended storage cell allows to avoid beam depolarization caused by traversing additional material. An additional advantage of the HERMES target is its ability to flip the target polarization within milliseconds. The storage cell can also be fed with unpolarized gases. Unpolarized data with gaseous targets  $^1\text{H}_2$ ,  $^2\text{H}_2$ ,  $^3\text{He}$ ,  $^{14}\text{N}$ ,  $^{20}\text{Ne}$  and  $^{84}\text{Kr}$  were taken. Until 2000 the experiment was operated with the longitudinally polarized  $^3\text{He}$ ,  $^1\text{H}_2$  and  $^2\text{H}_2$  targets. Over the HERA long shutdown the target was modified and from 2002-2005 transverse target polarization was used. In this analysis the data taken with the longitudinally polarized proton target in 1996 and 1997 is used.

### 4.2.1 The Longitudinally Polarized Gas Target

The main disadvantage of a polarized gas target is its low density. When the density of the gas in the target increases, the depolarization processes increase as well. A special construction of the target cell is needed to keep both the target thickness and the target polarization reasonably high. The HERMES storage cell is a 40 cm long, open-ended aluminum tube with an elliptical cross section of  $30 \times 10 \text{ mm}^2$ . The wall thickness of the cell is made less than  $100 \text{ }\mu\text{m}$  in order to reduce multiple scattering of the particles produced in interactions between beam and target gas. A schematic view of the longitudinally polarized target is shown in figure 4.3. The polarized gas from the Atomic Beam Source (ABS) is injected into the storage cell at its center and pumped out by a differential pumping system at its both ends. The diffusion of the gas through the storage cell increases the way of the beam through the target gas. The polarization of the gas in the storage cell is kept by a magnetic field of high uniformity of 335 mT (for the proton), aligned antiparallel to the positron beam. The main source of depolarization of the gas in the storage cell are collisions of the atoms with the walls of the cell. Since the probability of such collisions decreases with lower gas temperatures, the storage cell is cooled cryogenically to 100 K, allowing to increase the gas density. In case of the proton the typical polarized gas thickness is about  $10^{14} \text{ atoms/cm}^2$ .

The longitudinally polarized proton target was employed at HERMES in 1996 and 1997. The polarized atomic gas was produced by the ABS from hydrogen gas over several steps. Hydrogen atomized from the molecular gas



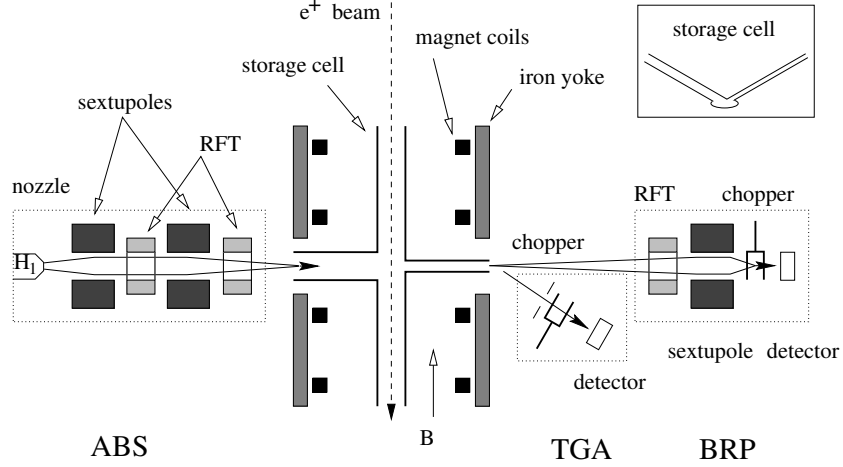


Figure 4.3: Schematic view of the HERMES longitudinally polarized target. From left to right: Atomic Beam Source (ABS), target chamber with cell and magnet, and diagnostic system composed by Target Gas Analyzer (TGA) and Breit-Rabi Polarimeter (BRP). The locations of the radio-frequency transition (RFT) units are indicated.

by a radio frequency discharge is injected into the ABS (from left to right in figure 4.3). Sextupole magnets separate the atoms with two hyperfine states  $|m_s, m_I\rangle$  (see figure 4.4) with electron spin polarization  $m_s = +\frac{1}{2}$  with respect to the beam direction, namely  $|1\rangle = |+\frac{1}{2}, +\frac{1}{2}\rangle$  and  $|2\rangle = |+\frac{1}{2}, -\frac{1}{2}\rangle$ . The other two states  $|3\rangle = |-\frac{1}{2}, -\frac{1}{2}\rangle$  and  $|4\rangle = |-\frac{1}{2}, +\frac{1}{2}\rangle$  are rejected and pumped away. Two Radio Frequency Transitions (RFT) are used for selection of either positive or negative nuclear spin polarization  $m_I$ . Weak field transition and strong field transition (the first and second RFTs in figure 4.3) allow hyperfine transitions of the states  $|1\rangle \leftrightarrow |3\rangle$  and  $|2\rangle \leftrightarrow |4\rangle$ , respectively. Hence by activating one of these RFTs, the nuclear polarization with respect to the target holding field can be flipped quickly. In order to keep the systematic errors caused by the target in asymmetry measurements low, the nuclear polarization of the target is reversed about every 60 seconds at HERMES.

The target polarization is monitored by the Target Gas Analyzer (TGA) and by the Breit Rabi Polarimeter (BRP). A small fraction of the target gas is transported through the sampling tube to the TGA and BRP (see figure 4.3). The TGA allows to measure the fraction of the atoms recombined to molecules. The measurements are carried out by the Quadrupole Mass Spectrometer (QMS). The BRP measures the relative population of the

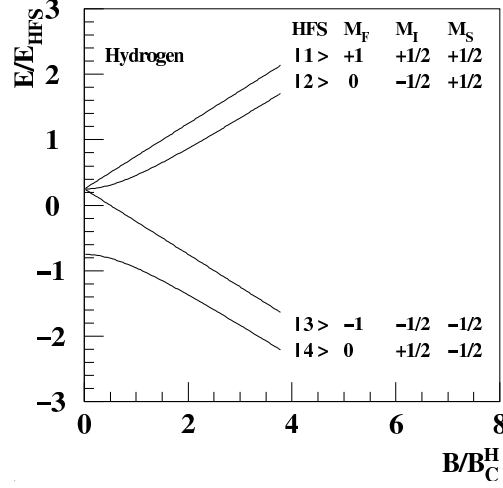


Figure 4.4: Hyperfine energy levels of hydrogen atoms as a function of the magnetic holding field (Breit-Rabi diagram) and corresponding labeling. The field values are scaled with the corresponding critical field  $B_C = 11.7$  mT and energy values with the corresponding hyperfine energy.

hyperfine states of atomic hydrogen. The construction of the BRP is similar to that of the ABS which allows to separate the atomic hyperfine states and then to analyze them with the QMS. Based on these measurements, the polarization of the target gas can be calculated as:

$$P_T = \alpha_0 \cdot P_{BRP} \cdot [\alpha_R + (1 - \alpha_R) \cdot \beta], \quad (4.6)$$

where  $\alpha_0$  is the fraction of atoms injected by the ABS to the target cell, and  $(1 - \alpha_R)$  is the fraction of atoms in the target cell recombined to molecules, as measured by the TGA. The polarization of the atoms  $P_{BRP}$  is measured by the BRP and  $\beta$  denotes the fraction of the polarization carried by the recombined molecules. For the longitudinally polarized proton target in 1997 the measured values from Eq. 4.6 are as follows:  $\alpha_0 = 0.960 \pm 0.010$ ,  $\alpha_R = 0.945 \pm 0.035$  and  $\langle |P_{BRP}| \rangle = 0.908 \pm 0.016$  for both spin states. The value of  $\beta$  is not accessible in a direct measurement at HERMES. Its upper limit is estimated from inclusive asymmetry measurements as  $\beta = 0.68 \pm 0.09$  (stat.)  $\pm 0.06$  (syst.) [A<sup>+</sup>05a].

In 1997 the resulting polarization of the target is  $\langle |P_T| \rangle = 0.850 \pm 0.032$  for both spin states corresponding to a relative measurement uncertainty of about  $\delta \langle |P_T| \rangle / \langle |P_T| \rangle = 3.8\%$  [Bec03]. Since in 1996 the operation of the target was not optimal due to the limited performance of the monitoring system, the target polarization is calculated as polarization measured in 1997

scaled by the ratio of the inclusive asymmetries measured in 1997 and 1996. As result for 1996 the relative error of the target polarization measurement is increased to about 5.5% and the target polarization is  $\langle |P_T| \rangle = 0.759 \pm 0.042$  for both spin states. The average target polarization for the 1996 and 1997 data taking periods is calculated as averaged polarizations of each year weighted by the corresponding integrated luminosities. It results in  $\langle |P_T| \rangle = 0.824 \pm 0.035$  ( $\delta \langle |P_T| \rangle / \langle |P_T| \rangle = 4.2\%$ ) for both spin states [Bec03].

### 4.3 Tracking System

Charged particles produced in interactions of the beam with the target are detected in the upper and lower halves of the HERMES spectrometer by the *tracking system* that consists of two sets of drift chambers located before and after the dipole magnet (see figure 4.1). The horizontally deflecting magnet operated with an integrated field strength of 1.3 Tm separates the detector into the front and back parts. Together with the tracking system the magnet is used for the momentum measurements of the particles.

In the front part of the detector the chambers FC 1/2 [B<sup>+</sup>01b] are employed for the reconstruction of vertices and scattering angles of the produced particles. In the back part the chambers BC 1/2 and BC 3/4 [B<sup>+</sup>98] are used for the reconstruction of particle tracks after their deflection by the magnet. The information about the particle track is used for the calculation of the momentum of the particle and for its identification. Each BC or FC detector has two times three planes, namely one plane with vertical wires (X plane) for the measurement of the horizontal coordinate  $x$  and two planes with wires tilted by  $+30^\circ$  and  $-30^\circ$  (U and V planes) with respect to the vertical wires. The size of the drift cells is 7 mm and 15 mm for FCs and BCs, respectively. The chambers use a gas mixture of 5% CO<sub>2</sub>, 5% CF<sub>4</sub> and 90% Ar at a pressure slightly above the atmospheric one. The spatial resolution per plane is about 225  $\mu\text{m}$  for the FCs and 275 (300)  $\mu\text{m}$  for the BCs 1/2 (3/4).

In 1997 the Drift Vertex Chambers (DVCs) [A<sup>+</sup>98a] were installed in addition in the front region of the detector. Since the resolution of the tracking turned out to improve only slightly, the DVCs are not used in this analysis due to compatibility reasons. The chambers MC 1-3 [A<sup>+</sup>01b] are located in the gap of the magnet. Since the chambers are operated in a strong magnetic field, they are built as Multi-Wire Proportional Chambers (MWPC). Originally the MCs were designed to match between the front and back tracks. Due to the improved track reconstruction procedure (so called “force bridge” method) [Wan97], now they are mainly used for tracking of the low energy particles ( $P < 2$  GeV) that are deflected in the magnet away

of the acceptance of the back part of the detector. The MCs are not used in this analysis.

A momentum resolution  $\delta P/P < 2.2\%$  and an angular resolution  $\delta\theta < 1.4$  mrad was achieved for the HERMES configuration with the Čerenkov detector installed until 1998. With the RICH detector installed the resolution became  $\delta P/P < 2.6\%$  and  $\delta\theta < 1.8$  mrad.

## 4.4 Particle Identification

Four detectors are employed for the particle identification at HERMES, namely the RICH (Čerenkov before 1998) detector, the Transition Radiation Detector (TRD), the preshower detector (H2) and the calorimeter (see figure 4.1). In order to discriminate an electron/positron (further referred to as a lepton) from a hadron, for the response of each PID detector to every reconstructed track a conditional probability  $\mathcal{L}_d^{e(h)}$  is calculated that the signal measured by the detector is caused by a lepton (hadron). The magnitude  $\mathcal{L}_d^{e(h)}$  calculated with the maximum likelihood method [Wen03] is related to the probability  $\mathcal{P}_d^{e(h)}$  of the detected particle to be a lepton (hadron) by Bayes' theorem:

$$\mathcal{P}_d^{e(h)} = \frac{\phi^{e(h)} \mathcal{L}_d^{e(h)}}{\phi^h \mathcal{L}_d^h + \phi^e \mathcal{L}_d^e}, \quad (4.7)$$

where  $\phi^{e(h)}$  is the lepton (hadron) flux. For each detector a PID parameter can be defined as the ratio of the lepton and hadron conditional probabilities, related to the ratio of the corresponding probabilities as [Kai97, Wen03]:

$$PID_d = \log_{10} \left( \frac{\mathcal{L}_d^e}{\mathcal{L}_d^h} \right) = \log_{10} \left( \frac{\mathcal{P}_d^e}{\mathcal{P}_d^h} \right) + \log_{10} \Phi, \quad (4.8)$$

where  $\Phi = \phi^h/\phi^e$  is the flux ratio that has only a small influence in Eq. 4.8 in case of HERMES kinematics. A positive  $PID_d$  value indicates that the track of a detected particle originates more probably from a lepton rather than to a hadron. A negative value has the opposite interpretation. The PID parameters can be combined for several detectors in order to increase the efficiency of the particle identification. In this analysis a combined response of the preshower and calorimeter,  $PID_2$ , together with a response of the six TRD modules,  $PID_5$ , is used, where

$$PID_2 = \log_{10} \left( \frac{\mathcal{L}_{pre.}^e \mathcal{L}_{calo.}^e}{\mathcal{L}_{pre.}^h \mathcal{L}_{calo.}^h} \right) \quad \text{and} \quad PID_5 = \log_{10} \left( \frac{\prod_{i=1}^6 \mathcal{L}_{TRDi}^e}{\prod_{i=1}^6 \mathcal{L}_{TRDi}^h} \right).$$

A cut on the total PID parameter  $PID = PID_2 + PID_5 > 2$  allows to identify a scattered positron with very high efficiency ( $> 98\%$ ) with very low hadron contamination ( $\sim 1\%$ ).

The RICH detector [A<sup>+</sup>02] is used mainly for hadron identification. Since it does not influence the PID efficiency of leptons at DVCS kinematics, its response was not used for PID in previous DVCS analyses [Ell04, Kra05]. In this analysis the Čerenkov detector is not used for compatibility reasons.

#### 4.4.1 Transition Radiation Detector

In order to discriminate leptons from hadrons the TRD [A<sup>+</sup>98a] employs Transition Radiation (TR) that is emitted by highly relativistic particles when traversing the border of two media with different dielectric constants. This effect is caused by a difference of the Coulomb field induced by a particle in each medium. In order to keep continuity of the field at the border TR is emitted. The total energy of TR emitted in the cone with an opening angle  $\theta \simeq 1/\gamma$  is

$$E = \frac{2}{3} \alpha \omega_p \gamma, \quad (4.9)$$

where  $\alpha$  is the fine structure constant,  $\omega_p$  is the plasma frequency of the medium, and  $\gamma$  is the Lorentz factor. At HERMES energies only leptons emit a significant amount of TR. Hence the lepton/hadron discrimination is based on the energy deposited by a particle in the TRD.

The intensity of the TR emitted at one boundary is small. In order to increase the number of boundaries traversed by a particle the HERMES TRD material is made as an irregular mesh of thin polyethylene/polypropylene fibers arranged in the 6.35 cm thick modules. The energy deposited in the module is detected by a multi-wire proportional chamber that uses 90% Xenon and 10% CH<sub>4</sub> gas. Xenon is used due to its short absorption length for soft X-ray mostly emitted as TR at high energies. Each HERMES TRD half (the upper and lower one) is built from six consecutive modules of such design.

#### 4.4.2 Preshower and Electromagnetic Calorimeter

Both halves of the preshower hodoscope (H2) installed in front of the calorimeter (see figure 4.5) consists of 42 vertical 1 cm thick and 9.3 cm wide plastic scintillator paddles that overlap each other by 2-3 cm for better efficiency. Each paddle is read out by a photo-multiplier at the outer end. The paddles are located behind a lead sheet of 1.1 cm thickness (two radiation length) that initiates electro-magnetic showers from traversing leptons. Hence the

energy deposited in the preshower by leptons is higher than that deposited by hadrons, which are minimum ionizing particles, allowing their discrimination.

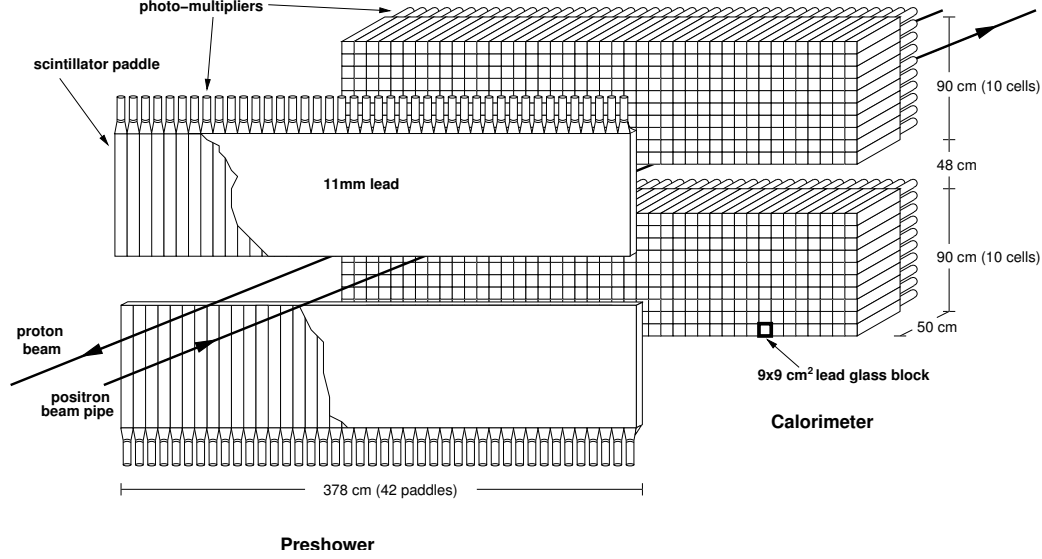


Figure 4.5: Schematic diagram of the HERMES preshower and calorimeter.

The electromagnetic calorimeter [A<sup>+</sup>98c] is used for several purposes. Originally designed as a part of the PID and (lepton) trigger systems, it is also used for photon detection (hit position and energy measurement). The calorimeter consists of 50 cm long blocks of  $9 \times 9 \text{ cm}^2$  cross section made of radiation-resistant F101 lead-glass and arranged in a  $40 \times 10$  array. The two halves of the calorimeter are located above and below the beam pipe. Due to the block thickness (about 18 radiation length), the energy of the leptons converted into electromagnetic showers in the lead glass material is almost fully deposited in the calorimeter. In contrast to leptons, hadrons deposit only a small fraction of their energy due to ionization losses and nuclear interactions. Hence the measurement of the ratio  $E/p$  of the particle's energy deposited in the calorimeter to its momentum measured by the tracking system, can be used as a good criterion for lepton identification.

From test beam measurements of a smaller prototype of the calorimeter the energy resolution was determined as  $\sigma(E)/E [\%] = 5.1/\sqrt{E [\text{GeV}]} + 1.5$  with a linearity within 1% for electrons in the energy range from 1 GeV to 30 GeV [A<sup>+</sup>98c]. The resolution of the HERMES calorimeter turned out to be slightly worse due to the influence of the preshower detector and imperfections in the calorimeter blocks. The coordinate of the hit position of a lepton or photon can be measured by the calorimeter based on the measure-

ments of the energy deposited by the particle in a  $3 \times 3$  array of blocks. It is calculated as average coordinate of the array with the coordinate of each block weighted by the logarithm of the energy deposited in the block. The resolution of the measured hit position is about 0.7 cm [Kra05].

## 4.5 HERMES Trigger

The trigger system selects events related to the physics of interests and it suppresses background. At HERMES, a variety of first-level triggers [A<sup>+</sup>98a] is used for the discrimination of various physics processes and for the monitoring of the detector. In this analysis *trigger 21* is employed for event selection and *trigger 18* is used for systematic studies of possible trigger inefficiencies (see section 7.4.4). *Trigger 21* is the main physics trigger at HERMES. It selects DIS events requiring a positron with energy above a certain threshold to not having been bent out of the spectrometer before having traversed one full detector half. The triggered event is required to have coincident signals from the hodoscopes H0, H1, H2 (preshower) and the calorimeter (see figure 4.1). Their responses are required to be synchronized with the HERA beam. *Trigger 18* has the same requirements as *trigger 21* except for the response from H0. The calorimeter and preshower (H2) were discussed in section 4.4.2. The hodoscope H1 has the same construction as the preshower detector but without the lead sheet in front of it. Located in the forward region of the spectrometer, each half of the hodoscope H0 consists of one plastic scintillator paddle of 3.2 mm thickness. Each half is read out by two photo-multipliers in order to secure stability in the high-rate environment.

The signal from H0 ensures that the positron traversed the forward part of the spectrometer before it initiated showers in the preshower and calorimeter. This requirement allows to suppress background from the proton beam, which traverses the HERMES experiment at the same height as the lepton beam, with an offset of 72 cm. The signal from the hodoscope H1 prevents the shower initiated by the photon in the preshower and calorimeter to be associated with the positron. The signal from the preshower is required to be above the minimum-ionizing signal, ensuring electromagnetic shower development. The response of the calorimeter is required to be above a threshold of 1.4 GeV for polarized, and above 3.5 GeV for unpolarized data taking. The higher threshold in the latter case is required due to the higher density of the unpolarized target with respect to that of the polarized one, which increases the background. The cut on the calorimeter response affects the energy range of the detected DIS positrons: the thresholds 1.4 GeV and 3.5 GeV correspond to cuts  $y < 0.95$  and  $y < 0.87$ , respectively. Note that

in 1996 the calorimeter threshold was still set to 3.5 GeV also for polarized data taking. For compatability between the years of data taking this cut is used for the data analyzed in this thesis.

The time for the trigger decision at HERMES is about 400 ns. After a trigger has been generated all the relevant data is read out from the HERMES subdetectors within about 10 ms. Triggers generated over the readout time are rejected. The dead time of the spectrometer is calculated as a ratio of the number of rejected triggers to the total number of accepted ones. Typical values for the dead time at HERMES are well below 10%.

## 4.6 Recoil Detector

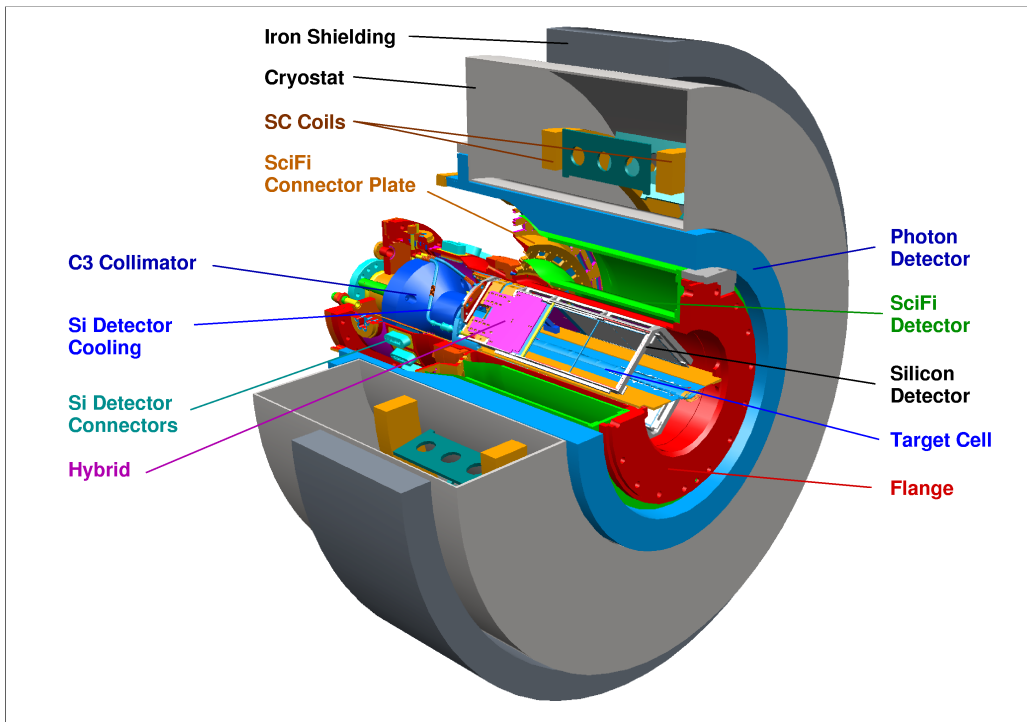


Figure 4.6: Schematic diagram of the HERMES recoil detector.

A new Recoil Detector (RD) [HER02] is presently being commissioned at HERMES for the study of hard exclusive processes. Located around the target it is designed to detect the recoiling products of reactions of interest and to suppress background. The main objective of the RD is to detect the



recoiling proton from the DVCS process. The RD consists of three main components (see figure 4.6): a silicon strip detector surrounding the target cell inside the beam vacuum, a scintillating fibre tracker and a photon detector consisting of three layers of tungsten radiator and scintillator. The detectors are placed inside of the superconducting magnet that generates a longitudinal magnetic field of about 1 Tesla. The silicon detector and the fiber detector cover a momentum range of the recoiling protons from 0.1 GeV/c to 1.5 GeV/c. The PID of the RD, based on the energy deposition in the silicon and in the scintillating fibers, allows to discriminate protons from pions for proton momenta up to 650 MeV/c [Kra05]. In case of the DVCS process the RD is expected to improve the  $t$ -resolution and to suppress the background by about a factor of 10.

The silicon detector contains four twin modules positioned in a diamond shape inside the HERA beam vacuum. Every module contains two silicon sensors of the TIGRE design produced by MICRON Semiconductors Ltd. The sensors are 300  $\mu\text{m}$  thick,  $99 \times 99 \text{ mm}^2$  double-sided silicon strip detectors with a readout pitch of 758  $\mu\text{m}$  and 128 readout channels per side. The silicon sensors are read out by a HELIX128 3.0 chip [FB<sup>+</sup>97]. The silicon detector measures the momentum of the recoil protons within the momentum range from 100 MeV/c to 400 MeV/c. For higher proton momenta it is used as a tracker. Calibration measurements of the detector demonstrated an energy resolution of about 2% for protons with kinetic energy between 4.9 MeV and 9 MeV [Pic05] and about 3% for MIPs with a detection efficiency close to 99% [HMG<sup>+</sup>05].

Proton momenta above 250 MeV/c are measured by the Scintillating Fibre Tracker (SFT), which consists of two barrels of 1 mm Kuraray SCFS-78 fibres. Each barrel has 2 parallel and 2 stereo ( $10^\circ$ ) layers. The barrels are constructed as a self-supporting structure in order to minimize the material traversing by the particles. The detector is used for particle momentum measurements and also for proton discrimination.

The photon detector is a three-layer calorimeter made of plastic scintillator modules of 28 cm length and of  $2 \times 1 \text{ cm}^2$  cross section with a tungsten converter of 2 cm placed before it as inner layer. The innermost layer of the scintillators is oriented parallel to the beam axis and the two outermost layers have stereo angles of  $\pm 45^\circ$ . The detector is used for the detection of photons, especially those originating from  $\Delta^+$  resonances.

A significant part of the work on this thesis was dedicated to the production tests of the HELIX128 3.0 chip [KGL<sup>+</sup>05], which is the frontend readout chip for the silicon detector in the RD project. First, the production tests are necessary to spot possible production defects of the chips. About 50% of the tested chips were found to have various defects. Second, the unique de-

sign of the HERMES silicon recoil detector brings additional requirements to the performance of the readout chip. Measurements of the deposited energy require high uniformity of the chip response. The large size of the readout pitch of the silicon sensor requires full functionality of every channel of the chip. Hence the production tests were also used for the selection of those chips that suit best to the project requirements.

The work made in this thesis in the framework of the HELIX production tests includes development of the procedure of the production tests, design and construction of the semi-automatic test stand, analysis of the results of the chip tests, development of the chip selection criteria and selection of the chips for the readout of the silicon recoil detector. Details of this work are discussed in Appendix A.

# Chapter 5

## Data Selection

### 5.1 Data Processing

For each triggered event the digital responses of all HERMES detector components are stored into a file in Experimental Physics Input Output (EPIO) format at local discs and at the DESY computer center tape robot. The data is processed by a series of programs in order to reconstruct every event and gather all the information necessary for analysis into so called micro-Data Summary Tape ( $\mu$ DST) file.

Firstly, with the knowledge of the structure of the response of each detector, the raw data stored as EPIO file is decoded by the Hermes De-Coder (HDC) program. The output of HDC is converted into the database format Aleph Data Model (ADAMO) and sent to the Hermes Reconstruction Code (HRC). The HRC performs track reconstruction based on a fast tree search of the hits in the tracking chambers [Wan97]. With input information about detector alignment and calibration and the field map of the spectrometer magnet it calculates vertices and momenta of reconstructed tracks. The output of the program is merged together with the slow control information and stored as  $\mu$ DST files.

One  $\mu$ DST file corresponds to one run that is defined by the size of about 500 MB of the data stored in EPIO format. Every run is subdivided into so called bursts. Every burst corresponds to about 10 seconds of data taking being the typical time of slow control readout. Slow control information about beam and detector performance normally changes much slower than the event rate (at HERMES the average trigger rate is about 300 Hz). Hence for the optimization of the stored information a separation of slow control and data streams is done.

## 5.2 Data Quality

Data from a longitudinally polarized proton target were accumulated in the years 1996 and 1997 of HERMES running. The corresponding data productions 96d0 and 97d1 produced by the data quality group based on the best knowledge of the detector are used in this analysis.

In order to select data of sufficient quality so called *bad bits* are used. *Bad bits* are defined for every burst for the most commonly used slow control parameters. If a parameter or a combination of parameters related to the performance of corresponding detector components (e.g. functionality of the target ABS) are within acceptable ranges, the corresponding bit of *bad bits* is set to zero, otherwise to one. A list of *bad bits* for every burst is provided by the HERMES data quality group and available as text file.

*Bad bits* required to be zero in this analysis are shown in table 5.1. Bursts that passed requirements of *bad bits* are accepted and several additional cuts are applied to the detector parameters not encoded in *bad bits*. All quality cuts applied to the data can be written as:

- $\text{badbits} \& (0x5DBF97FD) \equiv 0$ : cut on *bad bits*.
- $\text{g1Quality.iTrdDQ} \equiv 3$ : TRD is correctly checked.
- $|\text{g1Beam.rPolFit}| < 80\%$ : beam polarization has a reasonable value.
- $0.8 < \text{g1DAQ.rDeadCorr21} \leq 1$ : cut on the value of the dead time correction (dead time of the detector is required to be small).
- $5 < \text{g1Beam.rLumiRate} < 3000$ : reasonable value of LUMI-rate.
- $0.5 < |\text{g1Target.rPol}| \leq 1.5$ : data with small or illegal values of the target polarization is rejected.

## 5.3 Event Selection

The selection of BH/DVCS event candidates among those that passed the requirements of the data quality cuts is done in several steps. Firstly, events with exactly one positron that fulfills all the DIS requirements are selected. These events are referred to as *DIS events*. Secondly, from the *DIS events* those with exactly one photon are selected. Additional cuts are applied in order to suppress background processes with respect to the BH/DVCS process. Events passed through these cuts are referred to as *one-photon events*. Finally, events originating from the BH/DVCS processes are selected using the missing mass technique. They are referred to as *exclusive events*.

bit number	Details
0	select longitudinally polarized target
2	select reasonable dead time of the detector
3	burst length $L_{burst}$ is within 0 sec. $< L_{burst} \leq 11$ sec.
4	beam current $I_{beam}$ is within 5 mA $\leq I_{beam} \leq 50$ mA
5	select reasonable luminosity
6	not first burst in a run
7	good $\mu$ DST records
8	PID information is available
9	data is analyzable
10	polarized data
12	logbook data quality information is available
15	polarized target
16	target is functional
17	no dead blocks is calorimeter
18	no dead blocks is H2 or LUMI
19	TRD is functional
20	no high voltage trips
21	set for consistency with other productions
23	$\alpha_0$ value is reasonable
24	$\alpha_R$ value is reasonable
26	set for consistency with other productions
27	set for consistency with other productions
28	valid beam polarization measurements
30	select reasonable dead time

Table 5.1: List of data quality parameters controlled by *bad bits* that are required to be zero in the analysis of data with the longitudinally polarized target.

The cuts used for the selection of every mentioned type of events were mainly developed in Ref. [Ell04] for the period of HERMES running after 1998, when the RICH detector was installed instead of the threshold Čerenkov detector. In this analysis the cuts are confirmed for 1996 and 1997 data taking by Monte Carlo studies that will be discussed in chapter 6.

### 5.3.1 Selection of DIS Events

Events triggered by *trigger 21* (see section 4.5) are required to have exactly one positively charged track. Its response in the PID detectors should satisfy

the requirement  $PID_2 + PID_5 > 2$  (see details in section 4.4) ensuring the track being  $10^2$  times more likely a positron than a hadron. Since the value  $PID_2$  depends on the response of the calorimeter, in order to avoid inefficiencies that appear at areas close to the calorimeter's edges, fiducial requirements are applied. The hit position of the positron in the calorimeter reconstructed by the tracking system must satisfy the constraints  $|x_{calo}| < 175$  cm and  $30$  cm  $< |y_{calo}| < 108$  cm. In order to ensure correct tracking and vertex reconstruction by HRC and to reduce external background, the vertex of the scattered positron is required to be within the dimensions of the gas target, i.e.  $|z_{vertex}| < 18$  cm and  $t_{vertex} < 0.75$  for longitudinal and transverse vertex components, respectively.

In order to ensure the hard electroproduction regime of the BH/DVCS process, the relation  $Q^2 \gg M_p$  must be kept, where  $M_p$  is the proton mass. As a compromise with the limited statistics a cut  $Q^2 > 1$  GeV<sup>2</sup> is applied. Although the cut  $W^2 > 8$  GeV<sup>2</sup> does not affect the exclusive sample, it is introduced in order to reject events from the resonance region that are not described by the fragmentation model used in the Monte Carlo code of this analysis. For compatibility between the years of data taking with various calorimeter threshold used, a cut  $\nu < 22$  GeV is applied. An upper cut on  $Q^2$  and cuts on the  $x_B$ -range are used in order to fix the range of the variables. These cuts do not affect the exclusive sample.

The distribution of the selected DIS events in the kinematic  $\nu$ - $Q^2$  plane is shown in figure 5.1 (without cuts on  $x_B$  and the upper cut on  $Q^2$ ). All cuts applied for the selection of *DIS events* are

- *trigger 21* has fired,
- one positively charged track with  $PID_2 + PID_5 > 2$ ,
- fiducial constraints  $|x_{calo}| < 175$  cm and  $30$  cm  $< |y_{calo}| < 108$  cm,
- reconstructed vertex  $|z_{vertex}| < 18$  cm and  $t_{vertex} < 0.75$  cm,
- $1$  GeV<sup>2</sup>  $< Q^2 < 10$  GeV<sup>2</sup>,
- $W^2 > 8$  GeV<sup>2</sup>,
- $\nu < 22$  GeV,
- $0.05 < x_B < 0.35$ .

For positrons the longitudinal position of the calorimeter, with respect to the target center, is taken at 738 cm, as provided by the HERMES calorimeter group.

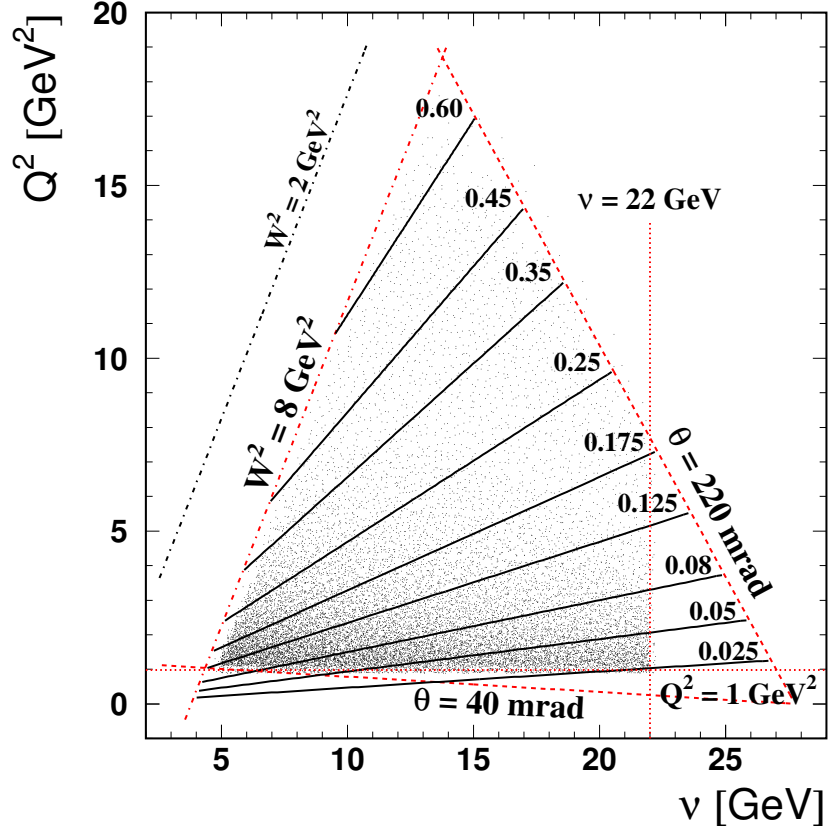


Figure 5.1: Distribution of DIS events in the kinematic  $\nu$ - $Q^2$  plane. Dashed and dash-dotted lines indicate requirements on  $\theta$  and  $W^2$  applied to the data, respectively. Dotted lines indicate requirements on  $\nu$  and  $Q^2$ . Solid lines demonstrate the dependences of  $Q^2$  on  $\nu$  for certain  $x_B$  values (shown in the figure). Note that the cuts on  $x_B$  and the upper cut on  $Q^2$  are not applied here.

### 5.3.2 Selection of Exclusive Events

A photon from the BH/DVCS process can be detected only by the calorimeter at HERMES, while the tracking system is sensitive only to charged particles. Hence selected DIS events are required to have exactly one trackless cluster in the calorimeter meaning that no track of a charged particle is associated to the cluster by the HRC program. A cut on the corresponding preshower response  $E_{pre} > 1$  MeV is applied to account for the fact that the HERMES

calorimeter was only calibrated for measurements of energy deposited by electrons or positrons, not by photons. As it is demonstrated in Ref. [Ell04], such a cut improves the energy resolution of the detected photon requiring it to start electro magnetic shower development already in the preshower and not only in the calorimeter. Also, this cut rejects clusters produced by background protons originating from the proton beam and by neutrons from DIS reactions. In order to improve agreement between data and Monte Carlo in the semi-inclusive region, a cut on the energy of the cluster  $E_\gamma > 5$  GeV is applied. Note that this cut does not affect the exclusive sample. Fiducial restrictions  $|x_{calo}| < 125$  cm and  $33$  cm  $< |y_{calo}| < 105$  cm are applied requiring the photon to hit the effective calorimeter area. Since the kinematics of the photon is defined by the calorimeter measurements, the boundaries on  $y_{calo}$  for photons are set more restrictive than those for positrons. A smaller range of  $x_{calo}$  for photons is chosen due to a difference in acceptance between photons and positrons. Since trajectories of positrons are bent by the magnet they can hit a wider range in the calorimeter plane than photons.

As it was demonstrated in Ref. [Ell04] and as it will be discussed in chapter 6 of this work, according to Monte Carlo studies an effective way for background suppression is to set the upper cut on the angle between the real and the virtual photons as  $\theta_{\gamma^*\gamma} < 45$  mrad. This angle is defined as:

$$\theta_{\gamma^*\gamma} = \arccos \left( \frac{\vec{q}^* \vec{q}}{|\vec{q}^*| |\vec{q}|} \right), \quad (5.1)$$

where the vectors  $\vec{q}^*$  and  $\vec{q}$  were defined in section 3.2. Also, a lower cut on  $\theta_{\gamma^*\gamma}$  must be chosen due to the finite resolution. In the region of  $\theta_{\gamma^*\gamma}$  values close to zero the azimuthal angle  $\phi$  is not defined anymore and therefore this region should be excluded from the analysis. This is done in Ref. [Ell04] requiring  $\theta_{\gamma^*\gamma}$  to be above its resolution of 2 mrad (see section 6.4). Studies in Ref. [Kra05] and in section 7.4.8 of this work demonstrate that due to strong smearing in the region of small  $\theta_{\gamma^*\gamma}$ , the lower cut on  $\theta_{\gamma^*\gamma}$  must be increased up to 5 mrad. Hence the angle is required to be within the range  $5 \text{ mrad} < \theta_{\gamma^*\gamma} < 45 \text{ mrad}$ .

It will be demonstrated in section 6.3 that the background contribution to the exclusive sample grows with higher values of transferred momentum  $-t$ . On the other hand, the cut on  $\theta_{\gamma^*\gamma}$  rejects most background events in the exclusive sample reducing statistics at high  $-t$  values. Hence the upper cut on  $-t$  is applied mainly in order to limit the  $t$ -range.

The resolution in  $t$  can be strongly improved if it is calculated under the assumption of exclusivity of the process [Ell04]. According to its usual



definition:

$$t = (q^* - q)^2 = -Q^2 - 2E_\gamma(\nu - \sqrt{\nu^2 + Q^2} \cos \theta_{\gamma^* \gamma}), \quad (5.2)$$

where the 4-vectors  $q^*$  and  $q$  are defined as in figure 3.3. As it follows from Eq. 5.2, the resolution in reconstructed  $t$  depends strongly on the measurement accuracy of the photon energy  $E_\gamma$ . In order to exclude this dependence,  $t$  can be calculated in three-particle kinematics as:

$$t = \frac{-Q^2 - 2\nu(\nu - \sqrt{\nu^2 + Q^2} \cos \theta_{\gamma^* \gamma})}{1 + \frac{1}{M_x}(\nu - \sqrt{\nu^2 + Q^2} \cos \theta_{\gamma^* \gamma})}, \quad (5.3)$$

where for the exclusive process the missing mass  $M_x$  is set to the mass of the proton  $M_p$ . Such a definition improves the  $t$  resolution for the BH/DVCS process while it is meaningless for the background. Distributions of the variable  $t$  calculated according to Eqs. 5.2 and 5.3 for the exclusive BH/DVCS process with either a proton or excited resonances in the final state are shown in figure 5.2. The distributions are compared with the generated value of  $t$  in each case. Having a proton in the final state of the BH/DVCS process, the distribution of  $t$  calculated in exclusive kinematics (Eq. 5.3) is similar to that calculated for real  $t$ . In this analysis  $t$  is calculated as in Eq. 5.3. The range of  $-t$  is limited by  $-t < 7 \text{ GeV}^2$ . Events that conform with the cuts discussed above are referred to as *one-photon events*.

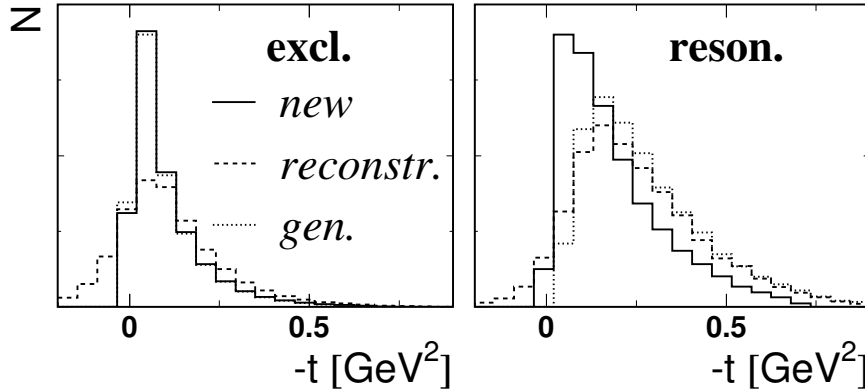


Figure 5.2: Distributions of the variable  $t$  calculated according to Eqs. 5.2 and 5.3 (dashed and solid lines) for the exclusive BH/DVCS process with either a proton (left) or nucleon resonance (right) in the final state. The distributions are compared with the generated value of  $t$  (dotted line). The distributions are based on Monte Carlo studies (see chapter 6).

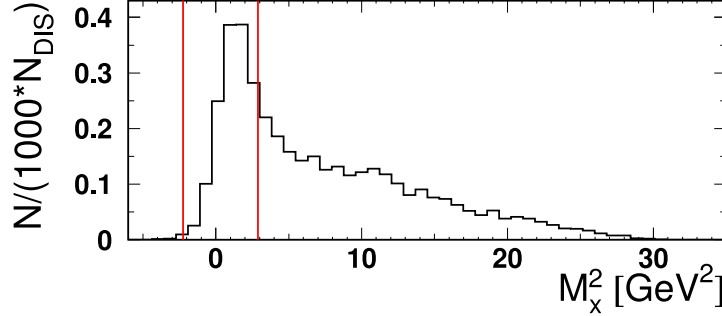


Figure 5.3: Missing-mass spectrum of one-photon events for the combined sample of 96d0 and 97d1 productions. The vertical lines correspond to the requirement on the exclusive sample.

For the years of data taking used in this analyses the recoiling proton from BH/DVCS reaction was not detected. For the identification of the exclusive process the missing mass of the reaction is calculated as:

$$M_x^2 = (k + P - k' - q)^2, \quad (5.4)$$

where the 4-vectors  $k$ ,  $P$ ,  $k'$  and  $q$  are defined as in figure 3.3. The distribution of missing mass for *one-photon events* shown in figure 5.3 demonstrates that an additional cut on missing mass is needed for the selection of the exclusive sample. Boundaries on the missing mass  $M_x$  of the BH/DVCS process are set around the proton mass as a compromise between the selected statistics and the background contribution to the exclusive sample. According to Ref. [Ell04] and supported by studies that will be explained in section 6.3, the exclusive sample in this analysis corresponds to the missing mass range  $-1.5 \text{ GeV} < M_x < 1.7 \text{ GeV}$ .

A comparison of the distributions of the above discussed variables for the exclusive samples of 1996 and 1997 is shown in figure 5.4. Normalized to the numbers of DIS events accumulated in each year, the distributions demonstrate consistency between the two years within statistical errors.

Summarizing the above discussion, the cuts used in this analyses for selection of *one-photon events* are

- requirement on a *DIS event* (see section 5.3.1),
- one trackless cluster in the calorimeter,
- preshower response  $E_{pre} > 1 \text{ MeV}$ ,
- photon energy  $E_\gamma > 5 \text{ GeV}$ ,

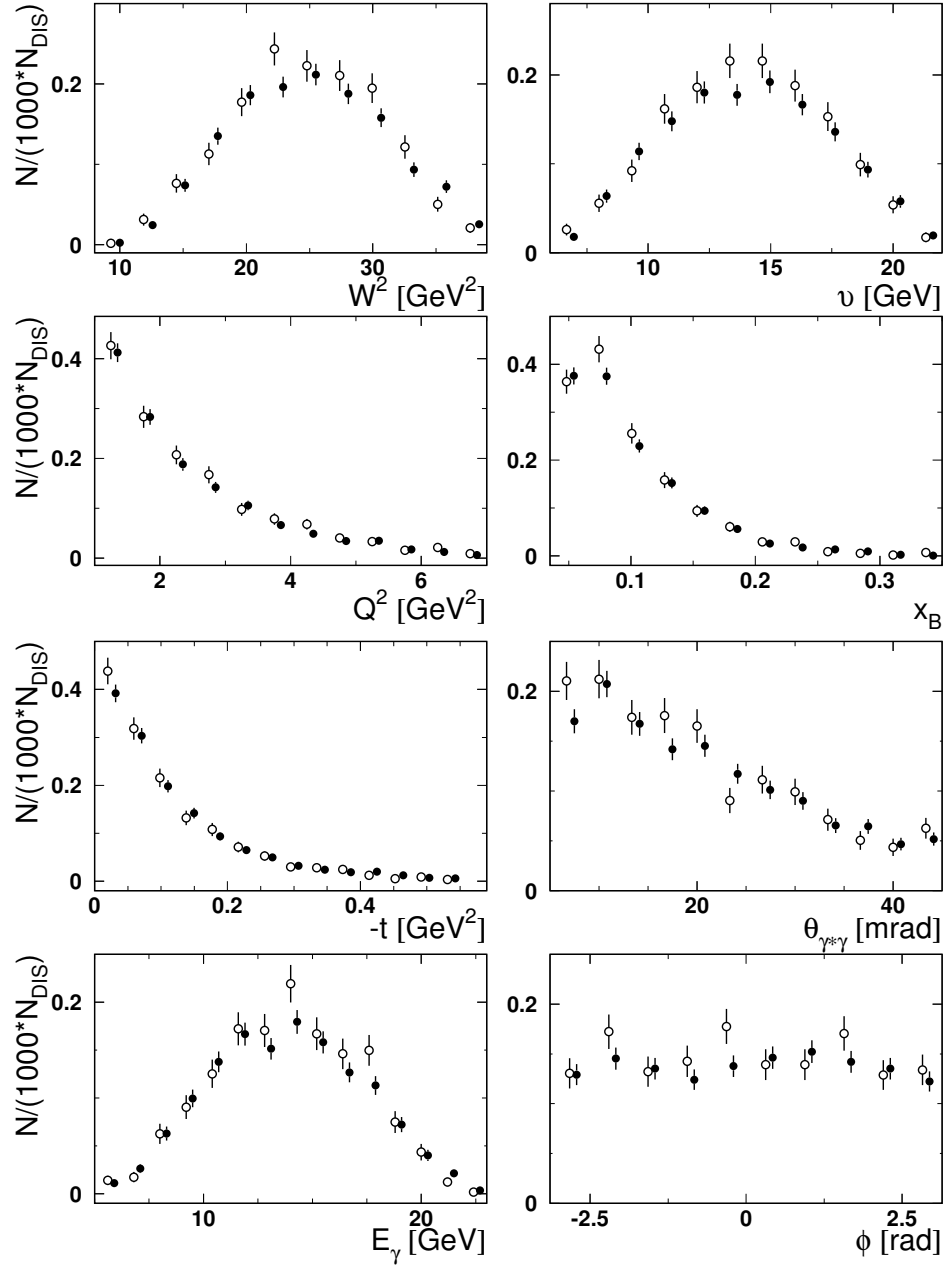


Figure 5.4: Distributions of kinematic variables for the exclusive samples selected from the data accumulated in 1996 (open points) and 1997 (closed points). The data is normalized to the number of DIS events accumulated in each year.

- fiducial restrictions  $|x_{calo}| < 125$  cm and  $33$  cm  $< |y_{calo}| < 105$  cm,
- $5$  mrad  $< \theta_{\gamma^*\gamma} < 45$  mrad,
- $-t < 7$  GeV<sup>2</sup>.

Note that in contrast to Refs. [Ell04, Kra05] in this work no correction is applied to the photon energy  $E_\gamma$  nor to the photon's hit position  $y_{calo}$ , due to reasons that will be discussed in section 7.4.6. Nevertheless, due to the difference in the development of electro-magnetic showers in the calorimeter for photons and positrons, their average centers are different. According to the results of a detailed study in Ref. [Kra05] for photons, the calorimeter position with respect to the target center is taken at 732 cm.

*Exclusive events* are selected with the cut on missing mass  $-1.5$  GeV  $< M_x < 1.7$  GeV [Ely02].

## 5.4 Beam Polarization Balancing

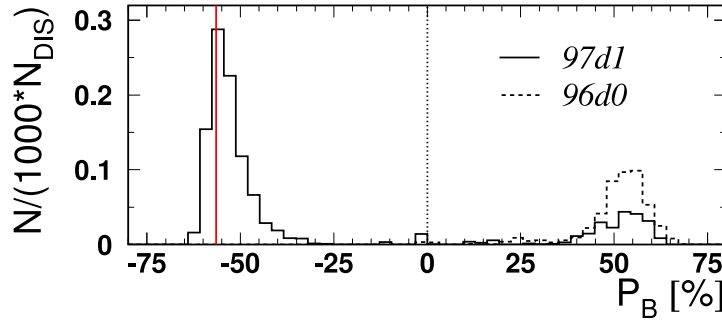


Figure 5.5: Spectrum of beam polarization for 96d0 (dashed line) and 97d1 (solid line) productions. The vertical solid line corresponds to the lower cut on the beam polarization. The vertical dotted line separates samples with positive and negative beam polarization.

As it will be discussed in section 7.1, the method used in this analyses for LTSA measurements requires the average beam polarization to be balanced according to Eq. 7.2. In order to fulfill the requirement of Eq. 7.2, a lower cut on the beam polarization  $P_B > -56.5\%$  is applied (see figure 5.5) for the combined data sample of both years. By convention the sample has positive beam polarization for  $P_B \geq 0$  and negative one for  $P_B < 0$ . As a result for every target-spin state two samples with positive and negative beam

polarization are selected with the absolute values of the beam polarization being the same within the error of the beam polarization measurement. The average beam polarization  $\langle P_B \rangle$ , the number of DIS events  $N_{DIS}$  and the number of exclusive events  $N_{excl.}$ , selected for every beam helicity and every target spin state, are shown in table 5.2.

	$\rightarrow\leftarrow$	$\leftarrow\leftarrow$	$\rightarrow\Rightarrow$	$\leftarrow\Rightarrow$	total
$\langle P_B \rangle, \%$	50.3	-50.2	50.5	-50.1	-
$N_{DIS}$					
96d0	275971	1708	295325	1813	574817
97d1	147898	451748	158624	418356	1176626
<b>total</b>	<b>423869</b>	<b>453456</b>	<b>453949</b>	<b>420169</b>	<b>1751443</b>
$N_{excl.}$					
96d0	404	3	433	3	843
97d1	174	661	216	560	1611
<b>total</b>	<b>578</b>	<b>664</b>	<b>649</b>	<b>563</b>	<b>2454</b>
$L/C \cdot 10^{-7}$					
96d0	1.6381	0.0098	1.6533	0.0108	3.3119
97d1	0.9257	2.6334	0.9357	2.5969	7.0917
<b>total</b>	<b>2.5638</b>	<b>2.6432</b>	<b>2.589</b>	<b>2.6077</b>	<b>10.0404</b>

Table 5.2: Average beam polarization  $\langle P_B \rangle$ , the number of DIS events  $N_{DIS}$  and the number of exclusive events  $N_{excl}$  for data sets of every beam helicity and every target spin state. The ratio  $L/C$  is the integrated luminosity  $L$  normalized by the luminosity constant  $C$  (see Eq. 5.7). The symbol  $\rightarrow$  ( $\leftarrow$ ) denotes positive (negative) beam polarization, and  $\leftarrow$  ( $\Rightarrow$ ) denotes target spin antiparallel (parallel) to the beam direction.

## 5.5 Data Normalization

In this work the integrated luminosity  $L$  for every beam helicity and every target spin state is used as normalization for the extraction of the asymmetry (see Eq. 7.4). It is related to the luminosity  $\mathcal{L}$  by integration over the data taking period,  $L = \int dt \mathcal{L}$ . For the case of a fixed-target experiment the luminosity is defined as:

$$\mathcal{L} = \frac{I\rho}{e}, \quad (5.5)$$

where  $I$  denotes the current of the beam,  $\rho$  denotes the target density and  $e$  is the elementary charge. The observed event rate  $R$  of a given process is related to the luminosity as:

$$R = \sigma \mathcal{L}, \quad (5.6)$$

where  $\sigma$  is the cross section of the process. As it was discussed in section 4.1.2, the measurement of the luminosity at HERMES is based on the knowledge of the cross sections of Bhabha and Møller scattering. The coincidence rate  $R_{LUMI}$  of such events, measured by the luminosity monitor, gives the relation to the integrated luminosity of every burst with a certain beam helicity and a given target spin state as:

$$L = \mathcal{E} \mathcal{C} \frac{A}{Z} \int dt R_{LUMI}, \quad (5.7)$$

where  $A$  ( $Z$ ) denotes the number of nucleons (protons) per nucleus,  $\mathcal{E}$  is the overall efficiency of the HERMES detector, which will be discussed below, and  $\mathcal{C}$  is a luminosity constant that contains cross sections of the Bhabha and Møller processes. In case of a polarized target the knowledge of the target polarization is needed for the calculation of  $\mathcal{C}$ , thereby increasing the systematic error of the measured luminosity.

For the HERMES polarized gas target, which has very stable running conditions over long time periods, it is possible to use an improved method that does not require target polarization measurements. For every burst the ratio of the coincidence rate  $R_{LUMI}$  to the beam current  $I$  is calculated, so that together with Eqs. 5.5 and 5.6 it can be written as:

$$\frac{R_{LUMI}}{I} = \sigma \frac{\rho}{e}. \quad (5.8)$$

The density of the target  $\rho$  can be assumed to be constant over a long time period, hence the ratio in Eq. 5.8 depends only on the cross section  $\sigma$  and hence depends on the target spin state. In order to exclude the dependence on the target spin state, the ratio is averaged over target spin states by fitting the ratio  $\frac{R_{LUMI}}{I}$  vs. time. The result of this fit, multiplied by beam current, gives the so-called fitted coincidence rate  $R_{LUMI}^{fitted}$  that depends only on the unpolarized part of the cross section. In this case the same constant  $\mathcal{C}$  as for an unpolarized target can be used for the calculation of the integrated luminosity of data taken with a polarized target.

The efficiency  $\mathcal{E}$  in Eq. 5.7 is mainly defined by the dead time of the HERMES detector. It is continuously monitored by the DAQ system. The trigger efficiency to be discussed in section 7.4.4 will be demonstrated to be very high. Possible sources of inefficiency originating from particle detection

and track finding are well under control and known to be small. Since for an asymmetry measurement absolute normalization is not a necessary ingredient it is more important that the two corresponding efficiencies stay constant over a long time scale and therefore their contribution to  $\mathcal{E}$  can be neglected.

As a result the integrated luminosity used for asymmetry normalization in this analysis can be written for the proton target case as:

$$L = \mathcal{C} \mathcal{E}_{trig21} t_{burst} R_{LUMI}^{fitted}, \quad (5.9)$$

where  $\mathcal{E}_{trig21}$  is the detector efficiency due to the dead time measured for *trigger 21* and  $t_{burst}$  is the length of the burst. Note that for asymmetry normalization the knowledge of the constant  $\mathcal{C}$  is not necessary.

In general, every process with a known cross section can be used for luminosity calculation. It is convenient to use the DIS process for normalization with events selected as described in section 5.3.1. As it follows from Eq. 5.6, the integrated luminosity  $L$  is proportional to the yield of DIS events  $N_{DIS}$ . For asymmetry measurements and the relative comparison of various data samples absolute normalization is not necessary and  $N_{DIS}$  can be used for such normalizations, as long as the DIS cross section is the same for the selected samples.

Since in general the DIS cross section contains also the “polarized” components, DIS yields can not be used for the normalization of data samples taken with a polarized target. In this case the relation between  $N_{DIS}$  and  $L$  is not constant anymore and it depends on the target spin state. Nevertheless in this work DIS yields are used for data-to-Monte Carlo comparisons, on the one hand. This becomes possible due to the relatively fast flipping of target-spin states at HERMES that makes the resulting sample unpolarized. On the other hand, for LTSA measurements, where data samples with different target spin states are separated, only the integrated luminosity is used for normalization.





# Chapter 6

## Monte Carlo Studies

Since the recoiling nucleon in the DVCS process was not detected at HERMES for data taking until 2005, the exclusive sample is reconstructed using the missing mass method, as it was discussed in section 5.3.2. In this case the selected sample receives contributions not only from the processes of interest, but also from background processes that can influence the measured asymmetries. Additional uncertainties in the measurements can originate from acceptance effects and smearing due to the finite resolution of the spectrometer. In order to study possible influences of these uncertainties onto the measured asymmetry a Monte Carlo simulation has been used.

### 6.1 Event Simulation

As processes of different nature contribute to the exclusive sample, several generators were used, namely:

- **DIS\_NG** for the simulation of the semi-inclusive background.
- **gmc\_dvcs** for the simulation of exclusive DVCS and BH events without and with excitation of resonances in the final state.
- **excl\_pion** for the simulation of “exclusive  $\pi^0$ ” background.

Diffractive meson production contributes to the selected exclusive sample also through decays of e.g. the  $\omega$ -meson. This process can be simulated with the PYTHIA [Sjö94] generator. Since its fractional contribution to the background is expected to be small [Kra05] it is not taken into account in this analysis.

The program **DIS\_NG** is based on the generator PEPSI [MSV92], a Monte Carlo program for polarized deep-inelastic leptonproduction that is

based on the LEPTO [IER97] code used for the simulation of unpolarized deep-inelastic scattering. The process of hard scattering of a virtual gamma on a parton is generated according to the polarization-dependent QCD cross-section in first order of the strong coupling constant  $\alpha_s$ . The hadronization of the partons produced in the interaction and any further decay of unstable particles is done by the JETSET code [Sjö94], using the LUND string-fragmentation model [AGIS83]. Radiative processes for polarized and unpolarized DIS were taken into account in the lowest order of QED by the RADGEN [ABR99] code.

The program **gmc\_dvcs** [Kra05] is used for the simulation of the DVCS and BH processes at HERMES energies. The BH process is simulated both for the elastic case and with excitation of resonances from a nucleon in the final state. The processes are simulated using the knowledge on their cross sections. In the case of DVCS the model used in the program is based on a phenomenological approach similar to the one discussed in section 2.4. For the simulation of the BH process an analytical approach developed by Mo and Tsai [MT69, E<sup>+</sup>01] is used. The simulation of the excitation of the resonances in the BH process is based on the Brasse parameterization [B<sup>+</sup>78] of the  $W$ -dependence of the corresponding cross section measured at SLAC [S<sup>+</sup>75].

The program **excl\_pion** [Had04] is based on **gmc\_dvcs** with the same models for GPDs but modified for exclusive  $\pi^0$  production. This code together with the program **DIS\_NG** is used for the simulation of the exclusive and semi-inclusive  $\pi^0$  productions that are the main background processes contributing the exclusive sample.

The products of the reactions simulated by the above mentioned programs are tracked through the detector by the HMC program that is based on the GEANT code [CER93]. In this analysis the geometry of the simulated detector is used according to 1997 settings that corresponds to the HERMES configuration for the years of running with a longitudinally polarized proton target.

After simulation of the detector responses, MC events are treated in the same way as real data, i.e. reconstructed by the HRC program and stored as ADAMOs tables by the  $\mu$ DST writing program, as it was discussed in section 5. Additional MC-related tables are stored in order to keep the information about the type of the event and the history of its development, giving relations between the particles reconstructed in the detector and the original ones generated by MC programs.

Due to a known problem in the HMC simulation of the particle energy deposited in the calorimeter [Ell04, Kra05], instead of using the energy provided by HMC the knowledge of the real energy of the hit particle is used in this analysis. The real energy  $E$  of the particle known from the MC table

g1Mtrack was smeared with the documented calorimeter resolution [A<sup>+</sup>98c]:

$$\frac{\sigma(E)}{E}[\%] = \frac{5.1 \pm 1.1}{\sqrt{E(\text{GeV})}} + (2.0 \pm 0.5) + \frac{10.0 \pm 2.0}{E(\text{GeV})}, \quad (6.1)$$

and used for missing mass reconstruction and event selection. For better agreement with the data the parameters of Eq. 6.1 were increased by 10%, keeping their values within the declared errors.

## 6.2 Data-to-Monte Carlo Comparison

The real data is compared with the generated MC data sample. The event selection for the MC is the same as for the real data as discussed in section 5, but without data quality cuts. Since the efficiency of particle identification is very high at HERMES, for MC it was assumed to be 100%. Both MC and data were normalized to DIS events (for details see section 5.5).

As it was discussed in a previous analysis [Ell04], the fragmentation model of JETSET fails in the region  $W < 2$  GeV, which in the case of a DIS event at HERMES energies corresponds to the region of the energy of the detected photon  $E_\gamma < 3$  GeV. Later studies demonstrated that this energy limit can be increased up to 5 GeV without influence on the exclusive sample but with a much better description of the semi-inclusive region by the fragmentation model. In this analysis the cut  $E_\gamma < 5$  GeV is used.

An absolute comparison of the missing mass squared distributions of data and of MC yields, each normalized to the yields of inclusive DIS events, is shown in figure 6.1. The MC yield is about 20% higher than that of data in the exclusive region (note that no additional reweighting is applied to the MC). The kinematic distributions of the normalized yields for the exclusive sample, shown in figure 6.3, demonstrate a good agreement in shape between data and MC except for the azimuthal angle  $\phi$ , where the shape of the distribution depends on the calorimeter calibration. As demonstrated in Ref. [Kra05], a recalibration of the calorimeter for a different position of the center of the electro-magnetic shower development can slightly improve the agreement between data and MC in the case of  $\phi$ .

Note that due to the fact that at HERMES kinematics the DVCS process is suppressed with respect to the BH process by at least one order of magnitude, the contribution of the DVCS process was omitted in this analysis for background and resolution studies, using only the BH process. Depending on the GPD model, used in simulation, DVCS can give an additional contribution to the MC yields of up to 10%.

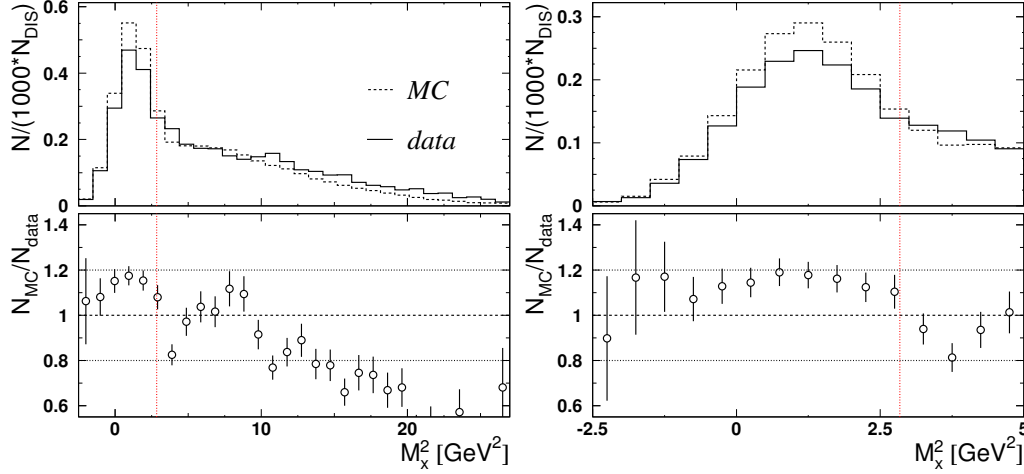


Figure 6.1: Missing-mass squared distributions for data and MC (upper panels) and MC-to-data ratios (lower panels). The full missing mass range and the exclusive region only are shown in the left and right panels, respectively. The vertical line corresponds to the requirement on the exclusive sample.

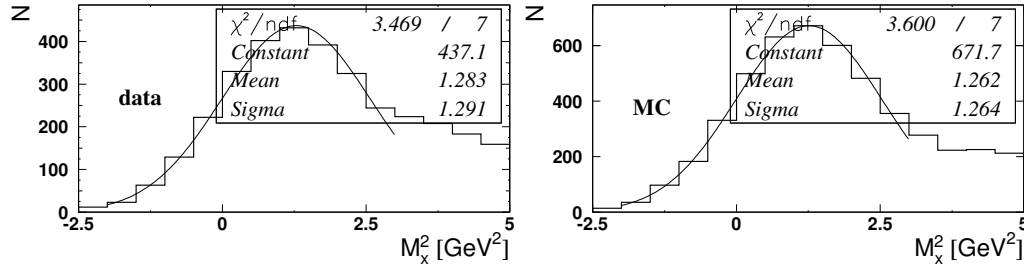


Figure 6.2: Missing-mass squared distributions for data (right) and MC (left) fitted with a Gaussian.

The reconstructed missing-mass squared depends on the energy of the detected photon (see Eq. 5.4). In case of MC the resolution of the photon energy is defined by Eq. 6.1. The missing mass distributions fitted with a Gaussian in the exclusive region are shown in figure 6.2 for data and MC. Similar peak position and width of the  $M_x^2$  distribution for data and for MC indicate a proper simulation of the energy of the detected photon.

The above demonstrated agreement between real data and MC indicates that all important processes contributing to the selected exclusive sample are taken into account. As it will be discussed in section 7.5, the second order ra-

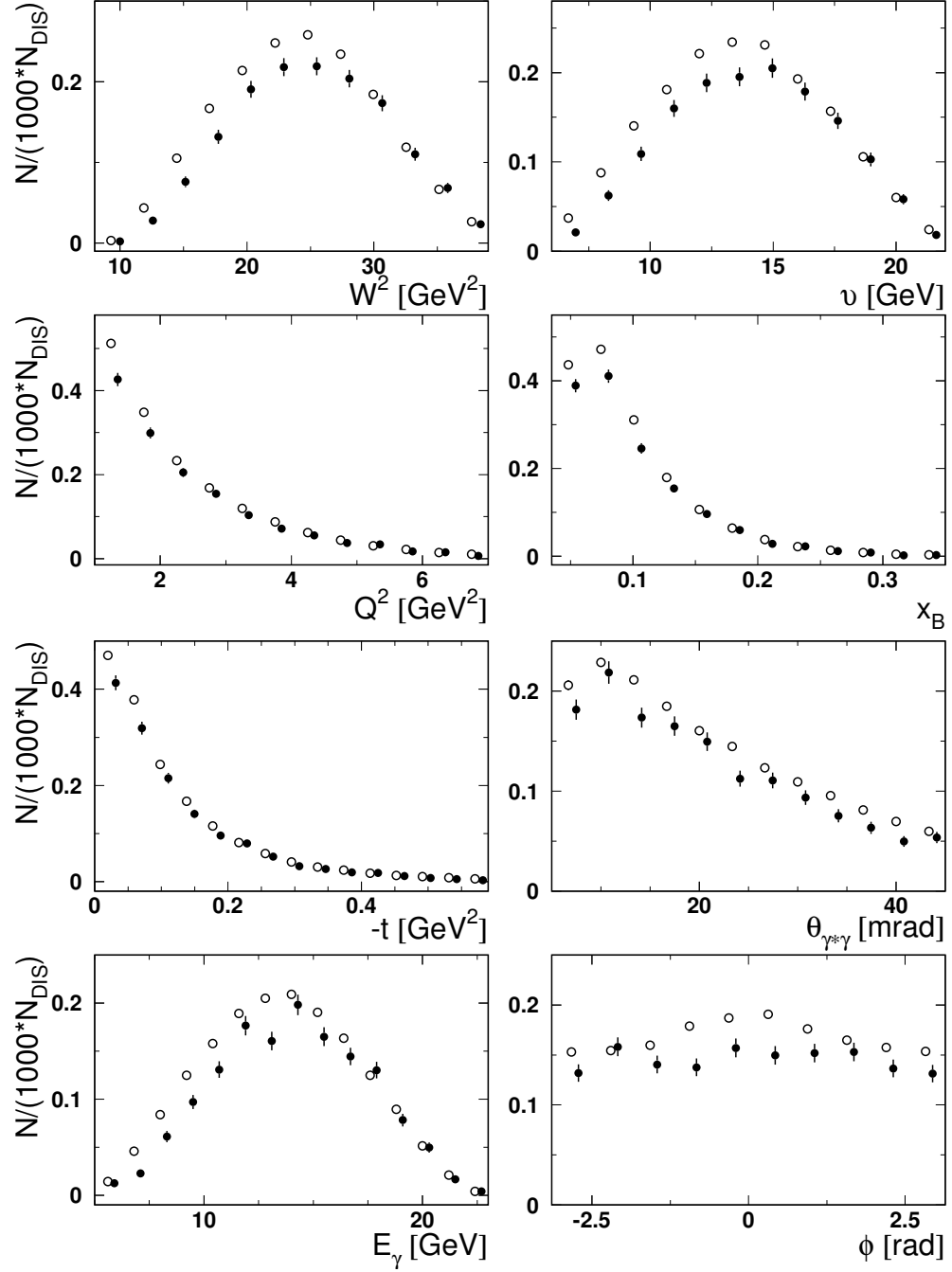


Figure 6.3: Distributions of kinematic variables of the selected exclusive sample for data (closed points) and MC (open points)

diative corrections can reduce the cross section of the BH/DVCS process by about 20% [V<sup>+</sup>00]. The MC used in this analysis includes radiative processes at leading order (LO) QED. Hence in future analyses the MC with radiative corrections implemented at next-to-leading order may improve the data description in the exclusive region. Nevertheless, the agreement demonstrated in this section is good enough for the systematic studies.

### 6.3 Background Contributions

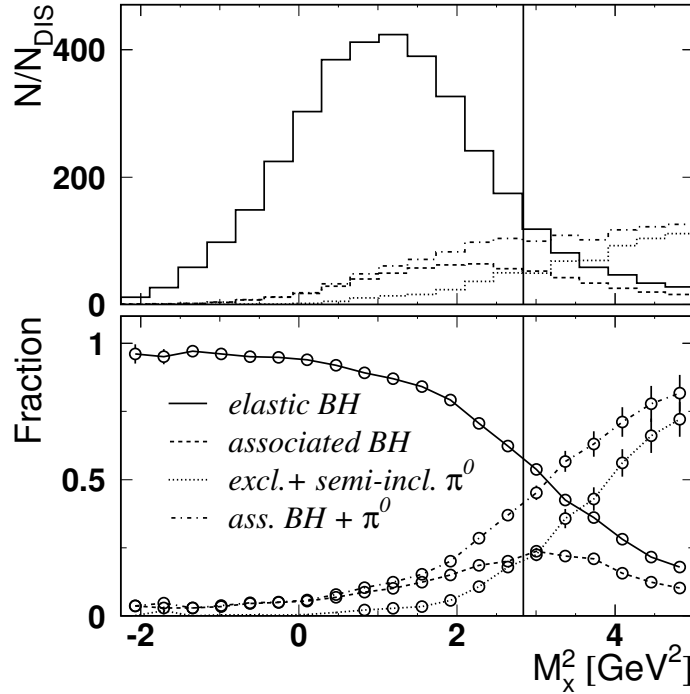


Figure 6.4:  $M_x^2$ -dependence of the normalized yields of the simulated processes (upper panel) and their fractional contributions (lower panel). The vertical line corresponds to the cut to define the exclusive sample.

In order to study the influence of the background processes on the measured asymmetry their fractional contributions to the selected sample were studied. The dependences of the normalized yields of the processes and of their relative fractional contributions, on the missing mass  $M_x^2$  are shown in figure 6.4. The BH process with the proton staying intact in the final state is called *elastic BH*, the BH process with resonance excitation is called *associated BH*. Exclusive and semi-inclusive  $\pi^0$  contributions are shown together

due to the small fraction of the exclusive  $\pi^0$  process in the selected sample. Also in systematic studies (see next chapter) the influence of  $\pi^0$  production on the measured LTSA is based on the combined semi-inclusive and exclusive  $\pi^0$  measurement. The cut on the missing mass  $M_x^2 < 2.89 \text{ GeV}^2$ , defined in Ref. [Ely02], selects the region with dominance of the process of interest. The contributions of the processes to the selected missing mass region are shown in table 6.1.

	elastic BH	associated BH	semi-inclusive $\pi^0$	exclusive $\pi^0$
fraction	85%	10%	4%	1%

Table 6.1: Fractions of the main processes in the selected exclusive sample.

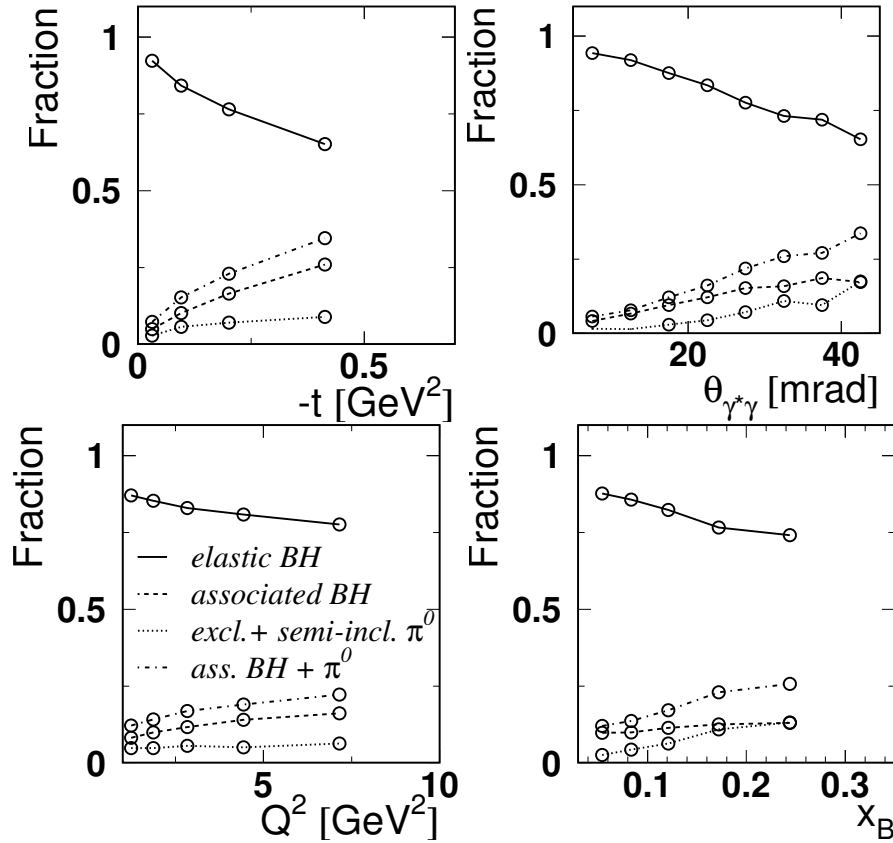


Figure 6.5: Dependences of the fractional process contributions on  $t$ ,  $\theta_{\gamma^*\gamma}$ ,  $Q^2$  and  $x_B$ , for the selected exclusive sample. Note that the dash-dotted line represents the sum of all background contributions.

For the selected exclusive sample the dependences of the process fractional contributions vs.  $\theta_{\gamma^*\gamma}$ ,  $t$ ,  $Q^2$  and  $x_B$  are shown in figure 6.5. The background behavior obtained with the 1997 settings of the detector geometry used in the MC simulation of this analysis is compatible with the results of earlier studies [Ell04, Kra05] performed for the detector geometry with 1999 settings. Hence all the main cuts used in this analysis for the exclusive event selection can be considered consistent with those used in Refs. [Ell04, Kra05].

In figure 6.5, a strong dependence of the fractional contribution of the background processes on  $t$  and  $\theta_{\gamma^*\gamma}$  can be seen. Note that the similar behavior of these two variables is due to their strong correlation at HERMES kinematics (see figure 6.10). The contribution of the *associate BH* process increases for the higher bins, and for the last  $t$ -bin it is about 25%.

Although quantitative predictions for Associated DVCS (ADVCS) production are available [FPS98, GMV03] these results can not be applied at HERMES kinematics [Kra05]. Hence the measured asymmetry can not be corrected for the effect of associated production, and the asymmetry generated by the associated production is included into the final result for the LTSA (see following sections). The same approach is used in earlier works for BSA and BCA in Refs. [Ell04, Kra05].

A separation of elastic DVCS and BH production from the associated one will be possible at HERMES after installation of the recoil detector [HER02] that will be able to detect the decay products of the produced resonances and so help excluding them from the exclusive sample (cf. section 4.6).

## 6.4 Resolution Studies

The resolution of the DIS-related kinematic variables depends on the accuracy of the measurement of the momentum vector of the scattered positron. The dependence of the resolution in positron momentum and scattering angle on positron momentum for the elastic BH/DVCS process for 1997 HERMES geometry is shown in figure 6.6. The better momentum resolution of slower positrons is due to their bigger deflection by the spectrometer magnet. In case of the angle resolution the behavior is opposite. As it was mentioned in section 4.3, the so-called “force bridge” method [Wan97] is used for the front track reconstruction. This method linearly extrapolates the front and back tracks of the particle towards the magnet center and matches them there with a certain accuracy, yielding additional points for the reconstruction of the front track. Since the slower positrons are stronger deflected by the magnet, they traverse a longer distance in the magnetic field of the magnet. Due to the non-uniformity of the magnetic field, the linear extrapolation of their



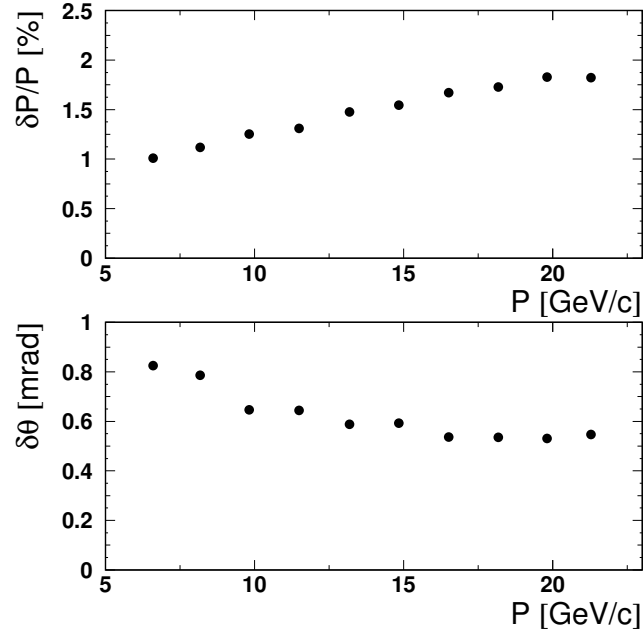


Figure 6.6: The momentum (top) and angular (bottom) resolution of the HERMES spectrometer for scattered positrons from the elastic BH/DVCS process (1997 geometry; “*force bridge*”, *NOVC*, *NODVC* reconstruction method, see Ref. [Wan97]). The momentum resolution in every bin is obtained from Gaussian fits in order to exclude long tails of the distributions caused by Bremsstrahlung in the detector (see figure 6.7).

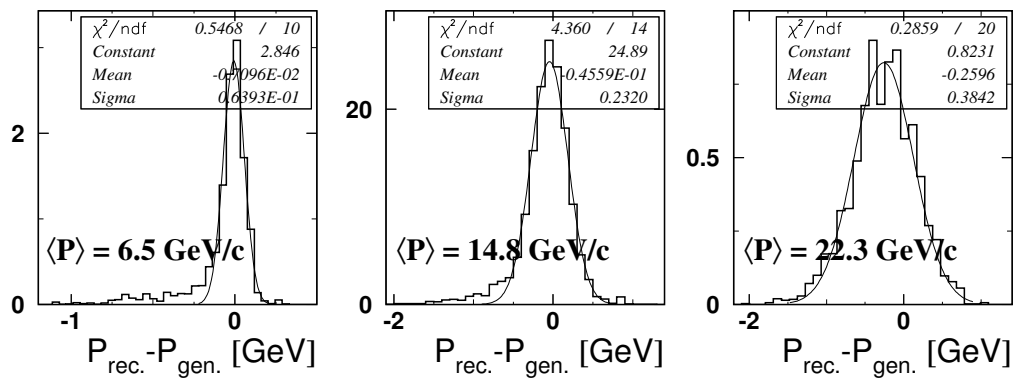


Figure 6.7: Distributions of the difference between the reconstructed and generated momenta of positrons.

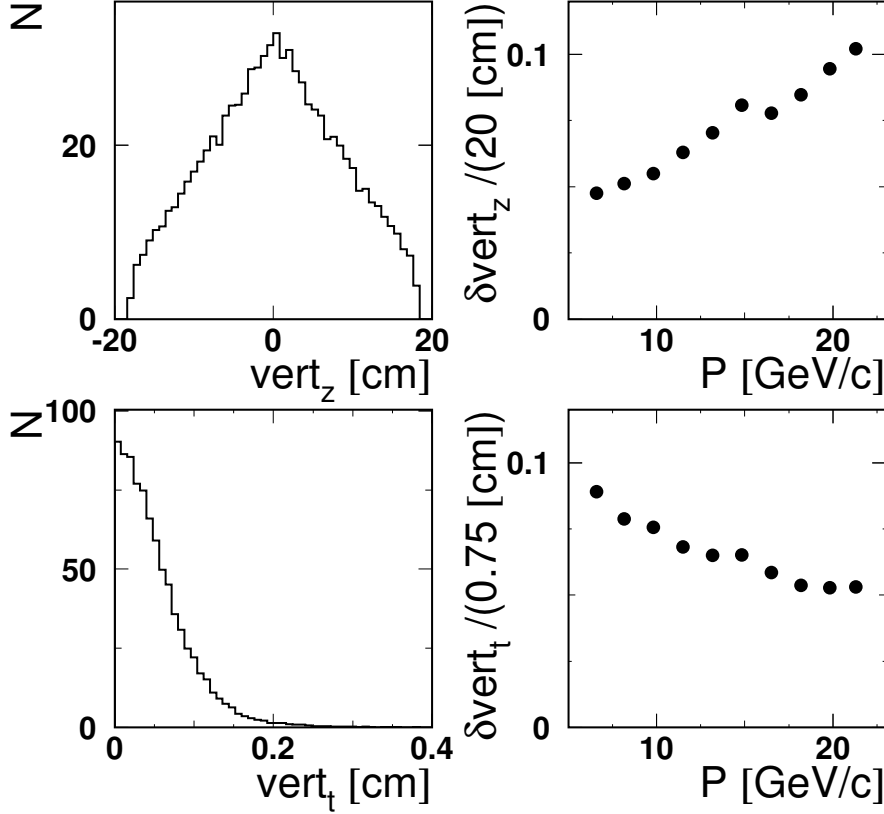


Figure 6.8: Distributions of the longitudinal ( $vert_z$ ) and transverse ( $vert_t$ ) vertices (left panels) and the dependences of the corresponding resolutions on the positron momentum (right panels). The resolutions are normalized to the corresponding dimensions of the target cell.

front and back tracks is less accurate than that for faster positrons. Hence the angular resolution is better for faster positrons. Note that for the 1997 geometry of the detector the resolutions in momentum and scattering angle are better than those for the 2000 geometry (see e.g. Ref. [Kra05]) due to installation of the RICH detector in 1998, which introduced additional material for traversing particles.

Distributions of the longitudinal and transverse vertices and the dependence of their resolutions on the positron momentum are shown in figure 6.8. Note that the vertex in this context is the interaction point of the beam with the target. Since the projection of the positron momentum on the transverse

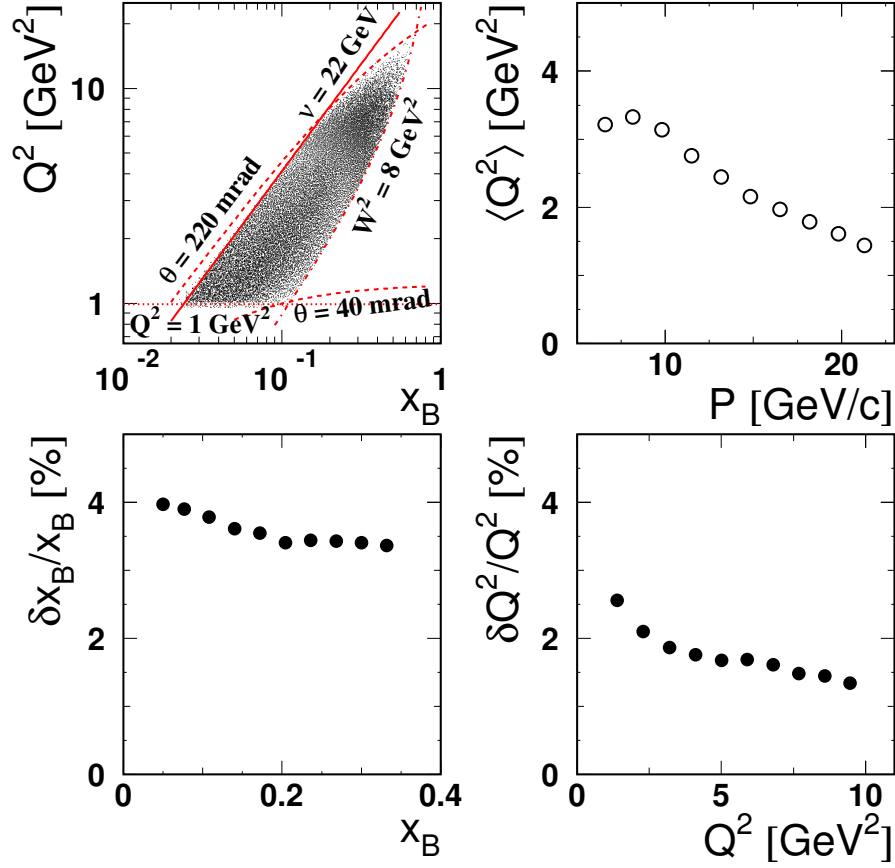


Figure 6.9: A 2-dimensional  $(Q^2, x_B)$  distribution (top left) and dependence of  $\langle Q^2 \rangle$  on positron momentum (top right) for exclusive BH/DVCS events. Resolutions in  $Q^2$  and  $x_B$  as functions of the corresponding variables (bottom left and right panels). The resolutions are obtained from Gaussian fits.

(longitudinal) axis is smaller (larger) for faster positrons, the absolute resolution of the transverse (longitudinal) vertex is better (worse). Note that the triangular shape of the longitudinal vertex distribution reflects the density distribution of the target gas in the storage cell.

The fixed-target kinematics defines the relation between  $Q^2$  and  $x_B$ . In case of the HERMES experiment,  $x_B$  is correlated with  $Q^2$  as it is shown in figure 6.9. The resolution in  $x_B$  and  $Q^2$  depends on the momentum resolution of the positron and on the positron scattering angle (see Eqs. 2.1, 2.2). The mean value of  $Q^2$  is inversely related to the value of the momentum of the scattered positron. The resolution in the variables  $Q^2$  and  $x_B$  and their

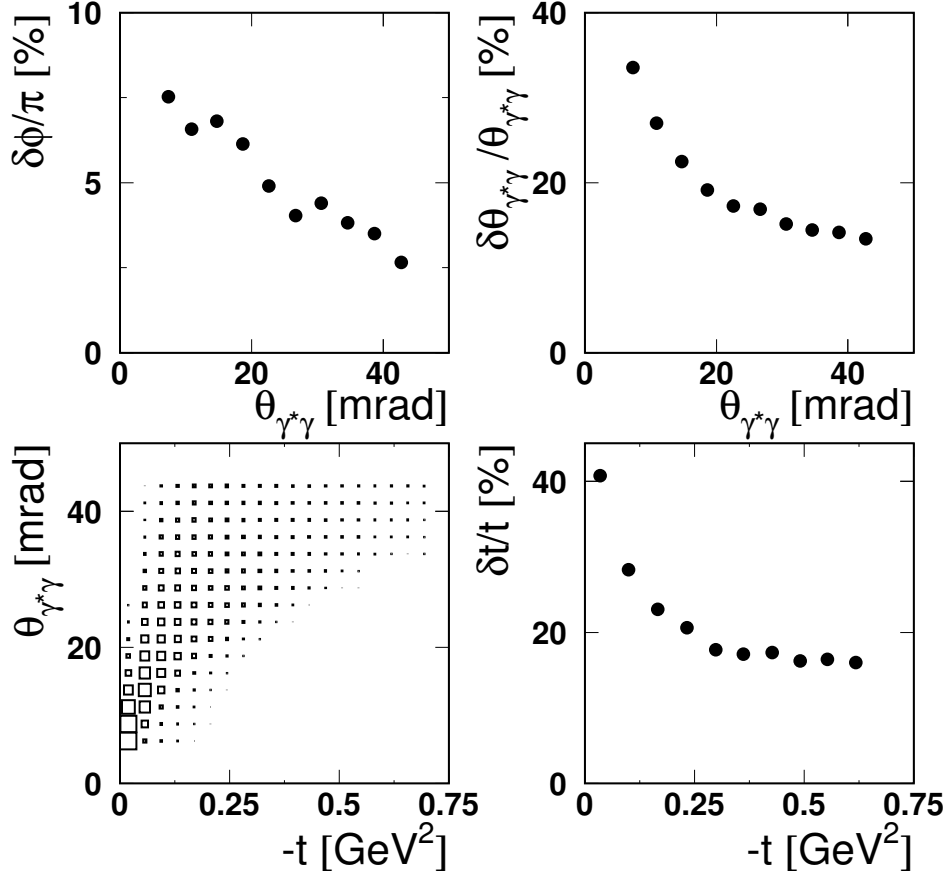


Figure 6.10: Dependence of the resolution in the azimuthal angle  $\phi$  on the angle between the virtual and real photons  $\theta_{\gamma^*\gamma}$  (top left) and the corresponding resolution of  $\theta_{\gamma^*\gamma}$  (top right) for exclusive BH/DVCS events. A 2-dimensional distribution of events vs.  $\theta_{\gamma^*\gamma}$  and  $t$  (bottom left). Dependence of the  $t$ -resolution on  $t$  (bottom right).

dependence on the positron momentum is shown in figure 6.9. The contribution of the resolution in the scattering angle dominates and defines the behavior of the  $Q^2$ - and  $x_B$ -resolutions.

The resolution in the azimuthal angle  $\phi$  depends on the reconstruction accuracy of the production and scattering planes (see figure 3.3). The scattering plane is defined by the momentum vectors  $\vec{k}$  and  $\vec{k}'$  of the initial and scattered positrons. The production plane is defined by the momentum vectors  $\vec{q}^*$  and  $\vec{q}$  of the virtual and real photons, respectively. In case of the virtual photon the accuracy of  $\vec{q}^*$  reconstruction is driven by the measure-

ment of the vector  $\vec{k}'$ . The direction of the momentum vector of the real photon  $\vec{q}$  is defined by the vertex position of the scattered positron and by the hit position of the photon in the calorimeter. Note that the energy of the photon measured in the calorimeter is used only for the selection of the exclusive events. The vertex resolution was discussed above (see figure 6.8). The resolution of the hit position by the calorimeter is discussed in detail in Ref. [Kra05]. With the logarithmic weighting technique of the hit coordinate reconstruction [Ell04] the resolution of the photon hit position in the calorimeter is about 0.76 cm [Kra05].

The accuracy of the scattering plane definition depends on how well the vectors  $\vec{q}^*$  and  $\vec{q}$  are separated. The closer the vectors are to each other, the bigger is the ambiguity in the plane definition. Therefore the resolution in the azimuthal angle  $\phi$  depends on the angle between virtual and real photons,  $\theta_{\gamma^*\gamma}$ . As shown in figure 6.10, the  $\phi$ -resolution is better for the region of larger values of  $\theta_{\gamma^*\gamma}$  where the resolution of  $\theta_{\gamma^*\gamma}$  improves with respect to that in the region of small values of  $\theta_{\gamma^*\gamma}$ .

The accuracy of the  $t$ -measurement also depends on the resolution of the vectors  $\vec{q}^*$  and  $\vec{q}$ . For the calculation of  $t$  the exclusivity of the process is assumed (see Eq. 5.3) and the resolution in  $t$  is mostly driven by the resolution in  $\theta_{\gamma^*\gamma}$ . Since the variable  $t$  is correlated with the angle  $\theta_{\gamma^*\gamma}$ , the dependence of the resolution in  $t$  is similar to that in  $\theta_{\gamma^*\gamma}$  (see figure 6.10). The large uncertainty of the angle measurement at small  $\theta_{\gamma^*\gamma}$  values brings in a large uncertainty in the measurements of  $\phi$  and  $t$  in the region of small  $\theta_{\gamma^*\gamma}$  and  $-t$ .

The resolution in the azimuthal angle explains the large smearing in the measured azimuthal asymmetry that will be discussed in section 7.4.8. Smearing effects are especially large in the first  $t$ -bin where, as discussed above, the uncertainty in the definition of the scattering plane is largest.



# Chapter 7

## Extraction of the Longitudinal Target-Spin Asymmetry

### 7.1 Measurement of the Longitudinal Target-Spin Asymmetry

As discussed in section 3.4, the Longitudinal Target Spin Asymmetry (LTSA) must be calculated according to Eq. 3.18 for the case of an unpolarized beam. Since the positron beam at HERA is polarized additional requirements to the data must be applied in order to avoid a contribution of the double-spin asymmetry to the resulting LTSA. Two approaches are possible in this case. The most straightforward one is to combine data samples with positive and negative beam polarizations in such a way that the resulting sample has zero average polarization. The second approach is based on the knowledge (see detailed expressions for the Fourier coefficients of Eqs. 3.14, 3.15, 3.16 in Ref. [BMK02]) that for a given target polarization state  $T$  the cross section of unpolarized photoproduction  $\sigma^{B^U T}$  can be rewritten as:

$$\sigma^{B^U T} = \frac{\sigma^{B^+ T} + \sigma^{B^- T}}{2}. \quad (7.1)$$

The cross sections  $\sigma^{B^+ T}$  and  $\sigma^{B^- T}$  for data taken with positively and negatively polarized beam, respectively, must be taken with the same absolute values of their average beam polarizations:

$$|\langle P_{beam}^{B^+ T} \rangle| = |\langle P_{beam}^{B^- T} \rangle|. \quad (7.2)$$

Since at HERMES the target polarization flipped between the two states much faster than the beam polarization, the requirement of Eq. 7.2, once

fulfilled for one target spin state, is valid for the other state as well. Also the average beam polarization for every target spin state becomes zero, as it is required in the first method. In this analysis the second approach is used as it is more general.

Using the definition of the LTSA for an unpolarized beam in Eq. 3.18 together with Eq. 7.1, with the requirement on the beam-polarization balancing of Eq. 7.2, the definition of the LTSA can be rewritten for the case of the polarized beam as:

$$A_{UL} = \frac{(\sigma^{\rightarrow\leftarrow} + \sigma^{\leftarrow\leftarrow}) - (\sigma^{\rightarrow\Rightarrow} + \sigma^{\leftarrow\Rightarrow})}{(\sigma^{\rightarrow\leftarrow} + \sigma^{\leftarrow\leftarrow}) + (\sigma^{\rightarrow\Rightarrow} + \sigma^{\leftarrow\Rightarrow})}. \quad (7.3)$$

Here  $\rightarrow$  ( $\leftarrow$ ) and  $\leftarrow$  ( $\Rightarrow$ ) denote positive (negative) beam polarization and target spin, respectively. Note that positive (negative) target spin is antiparallel (parallel) to the beam direction. Since the asymmetry depends linearly on the average target polarization  $\langle|P_T|\rangle$ , Eq. 7.3 is normalized by it and can be rewritten according to Eq. 5.6 as:

$$A_{UL}(\phi) = \frac{1}{\langle|P_T|\rangle} \frac{\left(\frac{N^{\rightarrow\leftarrow}(\phi)}{L^{\rightarrow\leftarrow}} + \frac{N^{\leftarrow\leftarrow}(\phi)}{L^{\leftarrow\leftarrow}}\right) - \left(\frac{N^{\rightarrow\Rightarrow}(\phi)}{L^{\rightarrow\Rightarrow}} + \frac{N^{\leftarrow\Rightarrow}(\phi)}{L^{\leftarrow\Rightarrow}}\right)}{\left(\frac{N^{\rightarrow\leftarrow}(\phi)}{L^{\rightarrow\leftarrow}} + \frac{N^{\leftarrow\leftarrow}(\phi)}{L^{\leftarrow\leftarrow}}\right) + \left(\frac{N^{\rightarrow\Rightarrow}(\phi)}{L^{\rightarrow\Rightarrow}} + \frac{N^{\leftarrow\Rightarrow}(\phi)}{L^{\leftarrow\Rightarrow}}\right)}, \quad (7.4)$$

where  $N^{BT}$  and  $L^{BT}$  are photon yield and integrated luminosity of the data set of every beam polarization and target spin state, respectively. The integrated luminosity is calculated as in Eq. 5.9 (for details see section 5.5).

The statistical error of the asymmetry defined in Eq. 7.4 is calculated assuming Poisson distributions of the input yields  $N^{BT}$  and can be written as:

$$\delta A_{UL}(\phi) = \frac{2}{\langle|P_T|\rangle} \sqrt{\left(\frac{k^{\leftarrow}}{(k^{\leftarrow} + k^{\Rightarrow})^2}\right)^2 (\delta k^{\Rightarrow})^2 + \left(\frac{k^{\Rightarrow}}{(k^{\leftarrow} + k^{\Rightarrow})^2}\right)^2 (\delta k^{\leftarrow})^2}, \quad (7.5)$$

where  $k^{\leftarrow(\Rightarrow)} = \frac{N^{\rightarrow\leftarrow(\Rightarrow)}(\phi)}{L^{\rightarrow\leftarrow(\Rightarrow)}} + \frac{N^{\leftarrow\leftarrow(\Rightarrow)}(\phi)}{L^{\leftarrow\leftarrow(\Rightarrow)}}$  and its corresponding error is

$$\delta k^{\leftarrow(\Rightarrow)} = \sqrt{\frac{N^{\rightarrow\leftarrow(\Rightarrow)}}{(L^{\rightarrow\leftarrow(\Rightarrow)})^2} + \frac{N^{\leftarrow\leftarrow(\Rightarrow)}}{(L^{\leftarrow\leftarrow(\Rightarrow)})^2}}. \quad (7.6)$$

Note that the error of measurement of the integrated luminosity is assumed to be very small, therefore it is not included in the error of the asymmetry.

## 7.2 Fit Method

As it was discussed in section 3.4, the azimuthal dependence of the LTSA allows to access the GPD  $\widetilde{H}$ . The amplitudes of the  $\sin \phi$  and  $\sin 2\phi$  harmon-



ics are sensitive to the corresponding CFF  $\widetilde{\mathcal{H}}$  at twist-two and twist-three levels, respectively (see Eq. 3.24). In order to extract these amplitudes the so called *fit method* is used in this analysis.

The amplitudes of the asymmetry, calculated for every  $\phi$ -bin as in Eq. 7.4, are extracted by a fit to the function:

$$A_{UL}(\phi) = s_0 + A_{UL}^{\sin\phi} \sin\phi + A_{UL}^{\sin 2\phi} \sin 2\phi, \quad (7.7)$$

for a certain number of  $\phi$ -bins. The amplitudes  $A_{UL}^{\sin\phi}$  and  $A_{UL}^{\sin 2\phi}$  of the LTSA are discussed in detail in section 3.4. Although the constant term  $s_0$  has no physical interpretation, its consistency with zero demonstrates a consistent normalization of the data samples with opposite target polarizations. The  $\sin 3\phi$  harmonic is not included in the fit function since its amplitude is consistent with zero and it has, as also *cosine* terms, no influence on the  $A_{UL}^{\sin\phi}$  and  $A_{UL}^{\sin 2\phi}$  amplitudes (see section 7.4.3).

Fitting the asymmetry with the function defined in Eq. 7.7 and calculating the statistical error of the fit parameters is accomplished by the MINUIT program [CER94] that performs minimization of the corresponding  $\chi^2$  as a function of the fit parameters.

Such extraction method has two natural limitations. Firstly, it depends on the number of  $\phi$ -bins. A study of the dependence of the stability of the fit result on the number of bins in section 7.4.9 demonstrates that the bigger the number of  $\phi$ -bins is, the closer the result of the fit is to the real amplitudes. On the other hand, for a correct calculation of the errors of the fit parameters every  $\phi$ -bin should contain a minimum of 5 events. Since the method works reliably for ten and more  $\phi$ -bins and because of limited data statistics, the number of  $\phi$ -bins used for extraction of the amplitudes is set to 10 in this analysis.

For the *fit method* the result for, e.g., the  $A_{UL}^{\sin\phi}$  coefficient of Eq. 7.7 can be written in the analytical limit as [Kra05]:

$$A_{UL}^{\sin\phi} = \frac{1}{\pi} \int_{-\pi}^{\pi} \frac{\frac{d\sigma^{\leftarrow}}{d\phi} - \frac{d\sigma^{\rightarrow}}{d\phi}}{\frac{d\sigma^{\leftarrow}}{d\phi} + \frac{d\sigma^{\rightarrow}}{d\phi}} \sin\phi d\phi, \quad (7.8)$$

where  $\sigma^{\leftarrow}$  ( $\sigma^{\rightarrow}$ ) is the photoproduction cross section for unpolarized beam and positive (negative) target spin orientation. Due to the orthogonality of *sine* and *cosine* functions the *fit method* allows to extract the amplitudes of the harmonics of interest without interference effects.

The representation of the *fit method* in Eq. 7.8 demonstrates its advantage compared to the *moment method* used in earlier DVCS analyses in e.g. Ref. [Ell04]. In case of the *fit method* numerator and denominator of

Eq. 7.8 are integrated thereby canceling the contribution of the BH propagators  $P(\cos \phi)$  to the cross sections (see Eqs. 3.14, 3.16). In case of the *moment method* numerator and denominator are integrated separately, adding an additional  $\phi$ -dependence from  $P(\cos \phi)$  (see Eq. 3.11) to the measured asymmetry moments.

A detailed MC study comparing the *fit method* and the *moment method* for the extraction of amplitudes of asymmetries was performed in Ref. [Kra05]. Although the *fit method* was demonstrated to be clearly superior in the amplitude reconstructions, it still has inefficiencies due to acceptance, smearing and binning effects. The influence of these effects on the measured LTSA will be discussed in section 7.4.

### 7.3 Results and Cross Check

For the exclusive events selected as described in chapter 5, the longitudinal target-spin asymmetry is calculated as defined in Eq. 7.4 for the average target polarization  $\langle |P_t| \rangle = 0.824 \pm 0.035$  (for details see section 4.2.1). The amplitudes  $A_{UL}^{\sin \phi}$  and  $A_{UL}^{\sin 2\phi}$  of the corresponding harmonics of the azimuthal dependence of the asymmetry are extracted with the *fit method* as discussed in section 7.2. The analysis procedure was repeated in an independent analysis by Z. Ye [Ye05] in order to check its consistency. Hence the results of

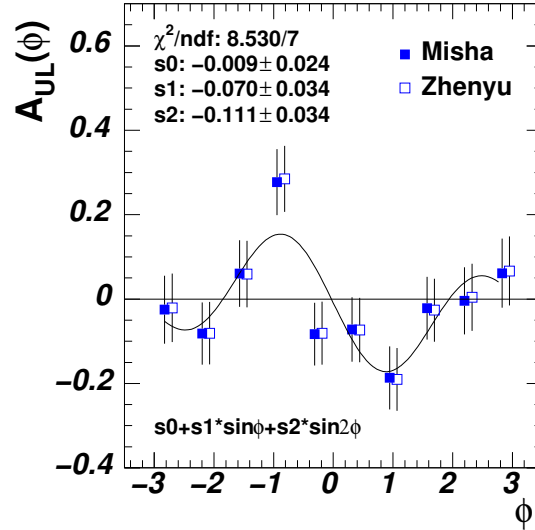


Figure 7.1: Dependence of the LTSA on the azimuthal angle. The result of this analysis (closed points) was cross checked by Z.Ye [Ye05] (open points).

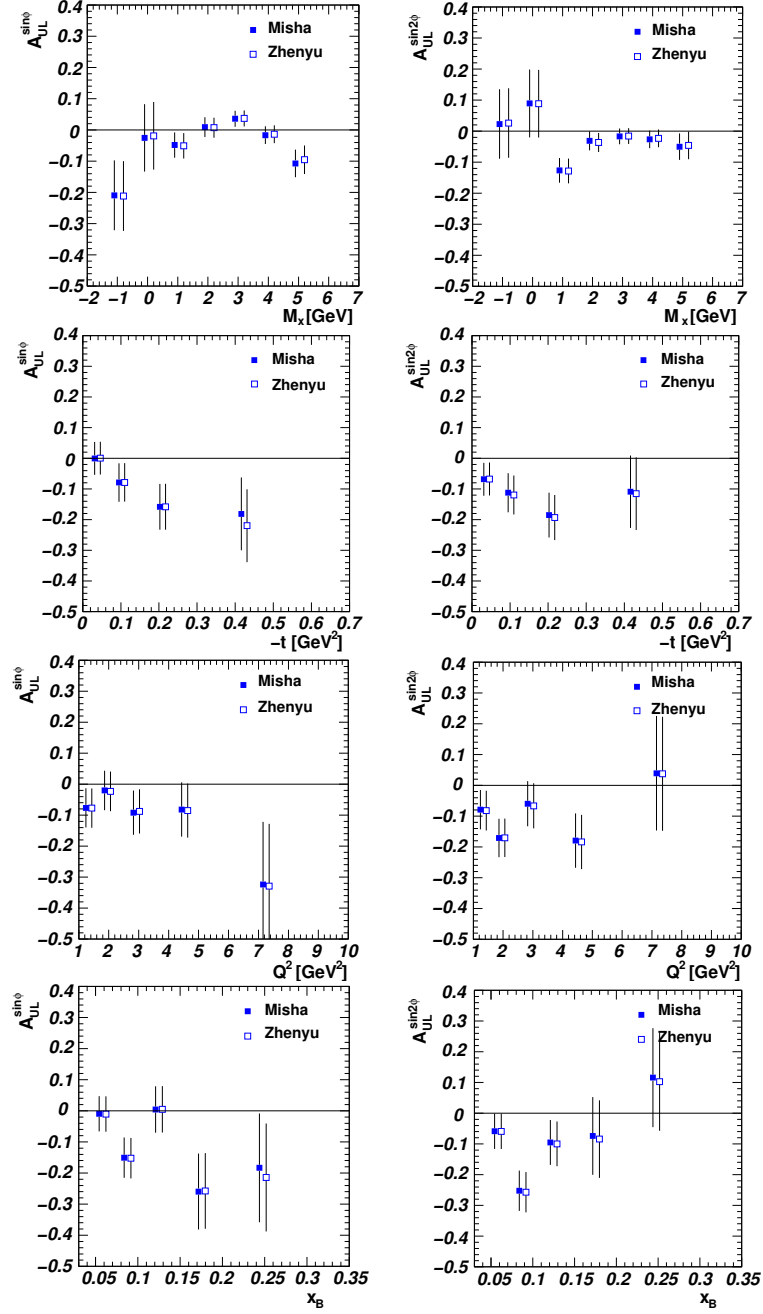


Figure 7.2: Dependences of LTSA amplitudes  $A_{UL}^{\sin \phi}$  (left) and  $A_{UL}^{\sin 2 \phi}$  (right) on  $M_x$ ,  $t$ ,  $Q^2$  and  $x_B$ . The result of this analysis (closed points) was cross checked by Z.Ye [Ye05] (open points).

	Number of DIS / Exclusive Events			
	$B^+T^+$	$B^-T^+$	$B^+T^-$	$B^-T^-$
This work	423869 / 578	453456 / 649	453949 / 664	420169 / 563
Z.Ye	423905 / 573	453468 / 647	453989 / 663	420205 / 561

Table 7.1: The numbers of DIS and exclusive events for the two analyses.

the asymmetry measurement discussed in this section are shown together with the results of the cross check. The numbers of selected *DIS events* (see section 5.3.1) as well as *exclusive events* (see section 5.3.2) for every beam polarization ( $B$ ) and target spin state ( $T$ ) are shown in table 7.1. The discrepancy between the two analyses is demonstrated to be less than 1%.

The dependence of the LTSA on the azimuthal angle and the corresponding amplitudes of the  $\sin\phi$  and  $\sin 2\phi$  harmonics are shown in figure 7.1. As it will be discussed in detail in chapter 8, for the average kinematics  $\langle Q^2 \rangle = 2.5 \text{ GeV}^2$ ,  $\langle x_B \rangle = 0.10$  and  $\langle -t \rangle = 0.12 \text{ GeV}^2$  the fit of the asymmetry with the function defined in Eq. 7.7 results in the amplitudes  $A_{UL}^{\sin\phi} = -0.071 \pm 0.034(stat.)$  and  $A_{UL}^{\sin 2\phi} = -0.113 \pm 0.034(stat.)$  (see table 8.2). These amplitudes are consistent with the fit result of the cross check analysis shown in figure 7.1. Note that the constant term of the fit function  $s_0$  is consistent with zero. The dependences of  $A_{UL}^{\sin\phi}$  and  $A_{UL}^{\sin 2\phi}$  on  $M_x$ ,  $t$ ,  $Q^2$  and  $x_B$ , extracted with the *fit method* for every kinematic bin, are shown in figure 7.2.

## 7.4 Systematic Studies

### 7.4.1 Geometric Stability of the Measured Asymmetry

The dependence of the LTSA on the position of the positron hit in the calorimeter is studied in order to locate possible geometrical detector inefficiencies. Since the available statistics is rather limited, only four calorimeter sections (see figure 7.3, left) are studied. The kinematics of DVCS events at HERMES sets the relation for the hit position between positron and corresponding photon. The latter hits the opposite quadrant with respect to the one hit by the positron. Hence the studied detector sectors give information about possible inefficiencies not only for the tracking system that carries the positron but also about the calorimeter that is used for the photon detection.

The amplitudes of the measured asymmetry for every detector quadrant are shown in table 7.2. Due to the deflection by the spectrometer magnet

positrons are bent towards the left side of the detector. Hence more statistics are accumulated for the detector quadrants 2 and 3. The amplitude values measured in every detector section are in agreement within one standard deviation of the statistical error.

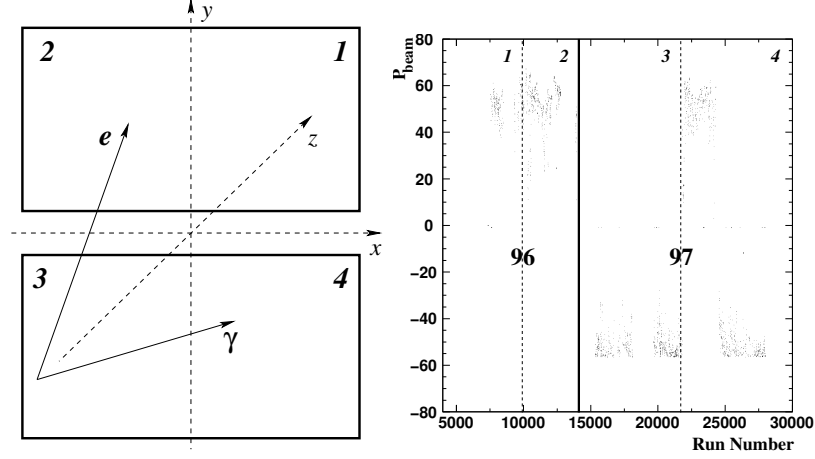


Figure 7.3: Left: Schematics of the detector sections used for the study of the geometrical stability. The typical geometry of a DVCS event at HERMES is shown: the photon hits the quadrant opposite with respect to the one hit by the positron. Right: Dependence of the beam polarization on the run number (time). Four time periods (two for each year) are chosen in order to study the stability of the measurements over the data taking time.

Quadrant Number	$A_{UL}^{\sin \phi}$	$A_{UL}^{\sin 2\phi}$
1	$-0.066 \pm 0.082$	$-0.057 \pm 0.082$
2	$-0.054 \pm 0.060$	$-0.094 \pm 0.059$
3	$-0.100 \pm 0.059$	$-0.149 \pm 0.059$
4	$-0.011 \pm 0.086$	$-0.137 \pm 0.085$
all	$-0.070 \pm 0.034$	$-0.111 \pm 0.034$

Table 7.2: Amplitudes  $A_{UL}^{\sin \phi}$  and  $A_{UL}^{\sin 2\phi}$  measured with the requirement on the hit position of the detected positron to be in one of four calorimeter quadrants (as defined in figure 7.3).

### 7.4.2 Stability of the Result over the Data Taking Period

The data used in this analysis was collected over two years of running. In order to find possible detector inefficiencies that vary over this data taking period, two periods with a similar amount of collected data are selected for every year. The limits of the selected periods in run numbers are defined as (see figure 7.3, right):

- 1996 (96d0):
  - range 1:** from 5000 to 10000
  - range 2:** from 10000 to 14000
- 1997 (97d1):
  - range 3:** from 14000 to 22000
  - range 4:** from 22000 to 30000

The measured amplitudes of the asymmetry for various combinations of the selected period are shown in table 7.3. Note that, since the *sine* amplitudes are not affected by the double spin asymmetry (as can be seen e.g. from Eqs. 58, 59, 60 of Ref. [BMK02]), no beam balancing is done for the demonstrated results. The results are consistent over the periods within one standard deviation of the statistical error.

Time Periods	$A_{UL}^{\sin \phi}$	$A_{UL}^{\sin 2\phi}$
3,4	$-0.125 \pm 0.048$	$-0.093 \pm 0.048$
4	$-0.113 \pm 0.060$	$-0.073 \pm 0.059$
1,(3,4)	$-0.079 \pm 0.040$	$-0.074 \pm 0.041$
2,(3,4)	$-0.089 \pm 0.037$	$-0.129 \pm 0.037$
(1,2),4	$-0.062 \pm 0.046$	$-0.106 \pm 0.046$
(1,2),3	$-0.050 \pm 0.042$	$-0.132 \pm 0.042$
all	$-0.070 \pm 0.034$	$-0.111 \pm 0.034$

Table 7.3: Amplitudes  $A_{UL}^{\sin \phi}$  and  $A_{UL}^{\sin 2\phi}$  measured over various periods of data taking (see figure 7.3, right). Parentheses indicate the periods of the same year of data taking.

### 7.4.3 Fit Stability

As discussed in section 7.2, the amplitudes extracted with the *fit method* are expected to be insensitive to other harmonics that can contribute to the asymmetry. In order to study the stability of the fit and the possible influence of other harmonics on the *sine* amplitudes, the LTSA was fitted with the following 3, 4 and 5-parameter fit functions:

$$f_3(\phi) = s_0 + s_1 \sin \phi + s_2 \sin 2\phi, \quad (7.9)$$

$$f_4(\phi) = s_0 + s_1 \sin \phi + s_2 \sin 2\phi + s_3 \sin 3\phi, \quad (7.10)$$

$$f_5(\phi) = s_0 + s_1 \sin \phi + s_2 \sin 2\phi + s_3 \sin 3\phi + c_2 \cos 2\phi. \quad (7.11)$$

The 3-parameter fit function (Eq. 7.9) is the same as the function used in this analysis for the extraction of the amplitudes  $A_{UL}^{\sin \phi}$  and  $A_{UL}^{\sin 2\phi}$  (see Eq. 7.7). The 4-parameter fit function (Eq. 7.10) includes additionally the amplitude  $A_{UL}^{\sin 3\phi}$  ( $s_3$ ) of the  $\sin 3\phi$  harmonic that is sensitive to DVCS amplitudes involving the double helicity-flip *gluon* GPDs. Note that the amplitude  $A_{UL}^{\sin 3\phi}$  is expected to be kinematically suppressed with respect to the amplitudes  $A_{UL}^{\sin \phi}$  and  $A_{UL}^{\sin 2\phi}$  (for details see section 3.4). The 5-parameter fit function

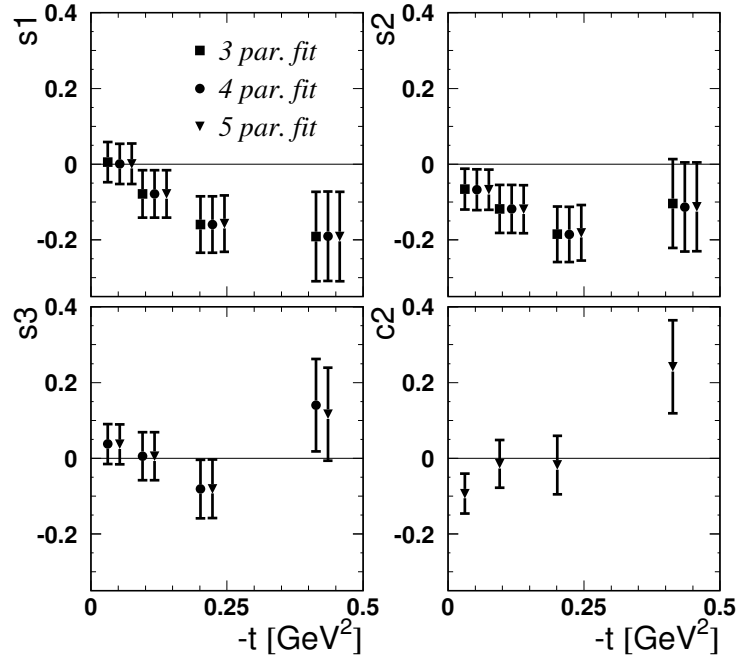


Figure 7.4:  $t$ -dependence of the amplitudes extracted with 3, 4 and 5-parameter functions defined in Eqs. 7.9, 7.10 and 7.11.

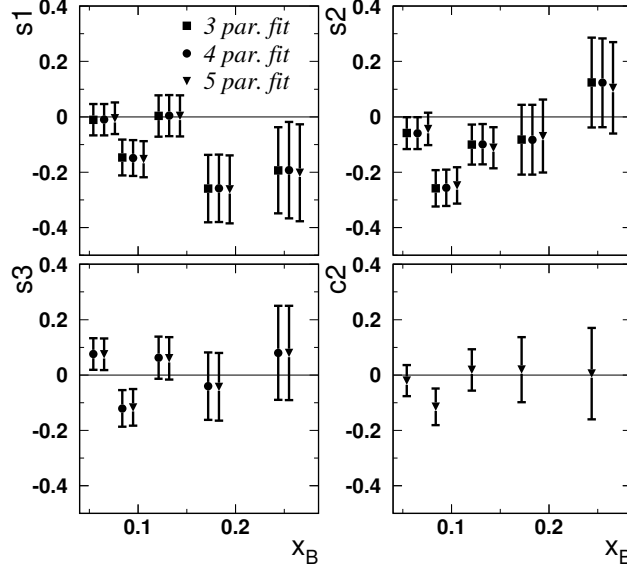


Figure 7.5:  $x_B$ -dependence of the amplitudes extracted with 3, 4 and 5-parameter functions defined in Eqs. 7.9, 7.10 and 7.11.

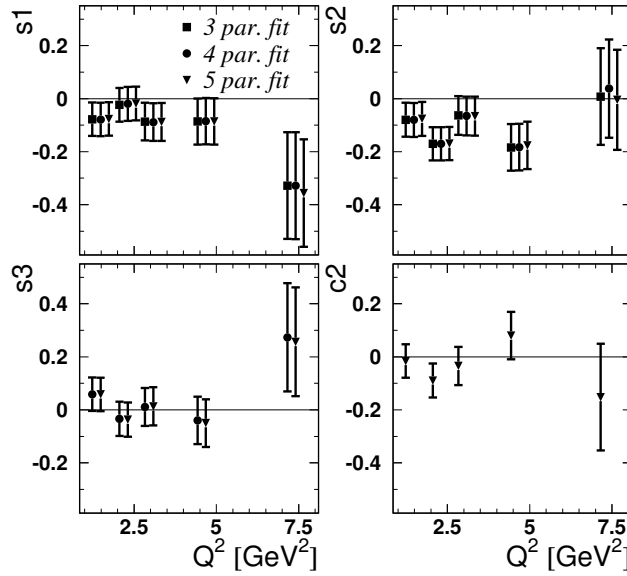


Figure 7.6:  $Q^2$ -dependence of the amplitudes extracted with 3, 4 and 5-parameter functions defined in Eqs. 7.9, 7.10 and 7.11.



(Eq. 7.11) includes the  $\cos 2\phi$  harmonic. Although this harmonic does not have a physical interpretation in case of the LTSA, it is taken into account in this systematic study, as it has the biggest amplitude among all *cosine* harmonics.

The kinematic dependences of the amplitudes extracted with the 3, 4 and 5-parameter fit functions are shown in figures 7.4, 7.5 and 7.6. As it was expected, the additional harmonics have a weak influence on the amplitudes  $A_{UL}^{\sin\phi}$  and  $A_{UL}^{\sin 2\phi}$ . The amplitude  $A_{UL}^{\sin 3\phi}$  is consistent with zero, as also the amplitude  $c_2$ . Hence the 3-parameter fit function is finally used in this analysis.

#### 7.4.4 Study of H0 Hodoscope Efficiency

Local radiation damage of the H0 hodoscope can cause an inefficiency of *trigger 21* (for details see section 4.5), so that the main trigger for the exclusive event selection may depend on the performance of the hodoscope. A spatial dependence of such an inefficiency can generate a false asymmetry.

The influence of the H0 inefficiency on the trigger has been studied with the method proposed in Ref. [Nar02] and was already used in earlier DVCS analyses [Ell04, Kra05]. It is based on *trigger 18* that is the same as *trigger 21* but does not require the response of the H0 hodoscope. Hence the efficiency of the H0 hodoscope can be measured as:

$$\varepsilon_{H0} = N_{tr21}/N_{tr18},$$

where  $N_{tr21}$  and  $N_{tr18}$  are the yields of the DIS events from *trigger 21* and

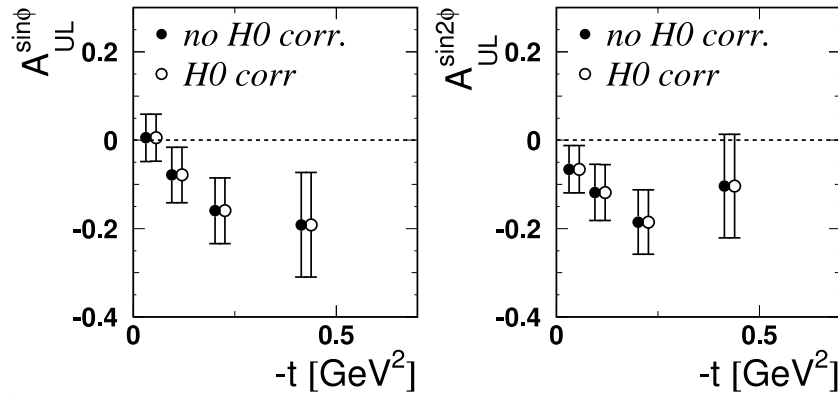


Figure 7.7: Dependence of  $A_{UL}^{\sin\phi}$  and  $A_{UL}^{\sin 2\phi}$  on  $-t$  with (open circles) and without (closed circles) correction for H0 inefficiency.

*trigger 18*, respectively. The hodoscope efficiency  $\varepsilon_{H0}$  measured with a step of 2 cm over the hodoscope's area is found to be more than 99% for both 96d0 and 97d1 productions everywhere. Such a high efficiency demonstrates low radiation damage of the hodoscope in the first years of HERMES data taking. For such a good efficiency the measured asymmetry amplitudes are affected by less than 0.1%, (see figure 7.7) making the influence of this effect negligible. Hence no correction for an H0 hodoscope inefficiency is applied in this analysis.

#### 7.4.5 Contribution from $\pi^0$ -background

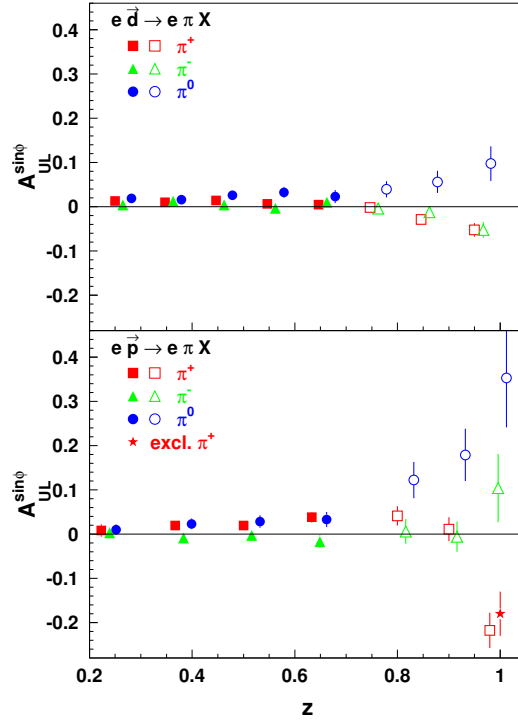


Figure 7.8: Dependence on  $z$  of the analyzing power  $A_{UL}^{\sin\phi}(z)$  for  $\pi^+$ ,  $\pi^0$ , and  $\pi^-$  production on the deuteron (upper panel) and on the proton (lower panel). The figure is taken from Ref.[A<sup>+</sup>03].

As it was discussed in section 6.3, exclusive and semi-inclusive  $\pi^0$  productions together contribute to the selected exclusive sample as background by about of 5% of events. The measurement of single-spin azimuthal asymmetries in semi-inclusive electroproduction of  $\pi^0$  on a longitudinally polarized hydrogen and deuterium targets at HERMES [A<sup>+</sup>03, Sch02] demonstrates a

sizable amplitude of the  $\sin \phi$  harmonic of the asymmetry (see figure 7.8). It can contribute to the measured LTSA through one of the photons produced in the decay of  $\pi^0$  which is misidentified as the photon from the DVCS process, because the second one remained undetected, as it left the acceptance.

The measured amplitude has a strong dependence on the fractional energy of the produced pion  $z_{\pi^0}$ , defined as:

$$z_{\pi^0} = E_{\pi^0}/\nu, \quad (7.12)$$

where  $E_{\pi^0}$  is energy of the pion. In order to estimate the value of  $z_{\pi^0}$  of background  $\pi^0$  particles a MC study was done for the semi-inclusive  $\pi^0$  sample that gives the main contribution of produced  $\pi^0$ s to the selected data sample. The study shows that the average  $z_{\pi^0}$  of the background  $\pi^0$ s is approximately

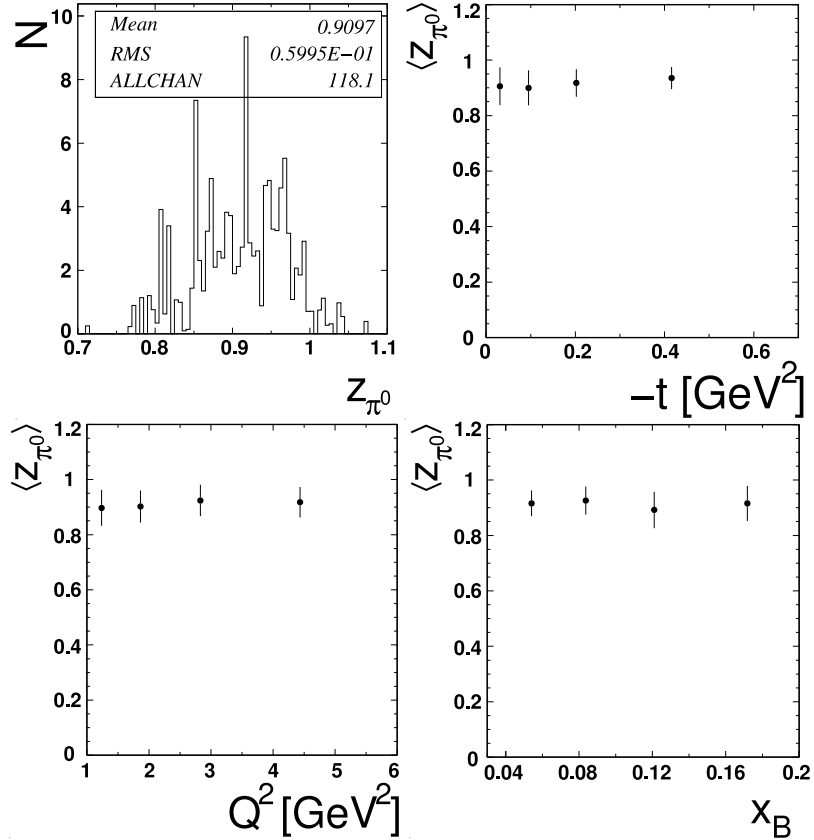


Figure 7.9: Distribution of  $z_{\pi^0}$  (top left) and dependence of  $\langle z_{\pi^0} \rangle$  on  $t$  (top right),  $Q^2$  (bottom left) and  $x_B$  (bottom right). Based on a MC study for semi-inclusive  $\pi^0$ s contaminating the exclusive sample. The error bars correspond to the RMS of the  $z_{\pi^0}$  distribution in every bin.

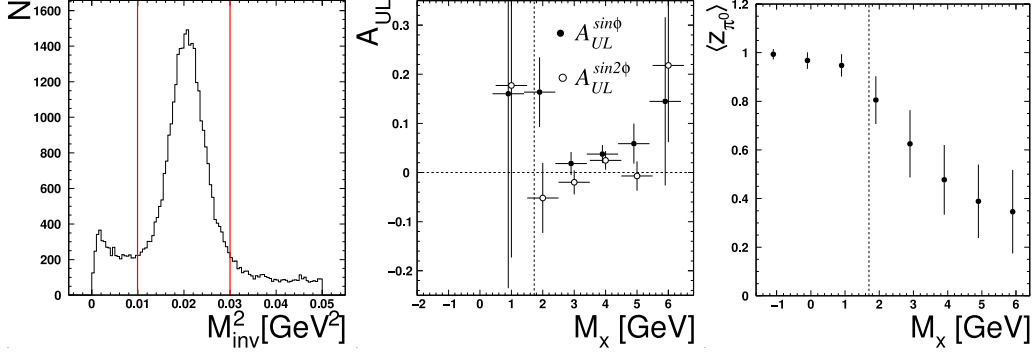


Figure 7.10: From left to right: Distribution of invariant mass for two detected photons, used for event separation in a two-photon analysis; dependence of  $A_{UL}^{\sin\phi}$  and  $A_{UL}^{\sin 2\phi}$  on missing mass (amplitudes have inverted sign here), calculated for the most energetic photon out of the two detected ones (error bars represent the statistical error); dependence of  $\langle z_{\pi^0} \rangle$  on missing mass based on the MC study for semi-inclusive  $\pi^0$  contaminating the exclusive sample (error bars correspond to the RMS of the  $z_{\pi^0}$  distribution in every bin).

$\langle z_{\pi^0} \rangle = 0.9$  (at  $\langle x_B \rangle = 0.13$ ) and it has a weak dependence on the variables  $t$ ,  $Q^2$  and  $x_B$  (see figure 7.9). The amplitudes measured at HERMES which correspond to this fractional energy of  $\pi^0$ s are  $A_{UL}^{\sin\phi} = 0.18 \pm 0.06(stat.)$  and  $A_{UL}^{\sin 2\phi} = 0 \pm 0.06(stat.)$  (for the amplitude  $A_{UL}^{\sin 2\phi}$  only the  $x_B$ -dependence is published, which is consistent with zero at  $x_B = 0.13$ ).

These results are in good agreement with the so-called two-photon analysis. With the hypothesis that the original  $\pi^0$  asymmetry is carried by the leading (the fastest) photon of the two produced in the decay of the  $\pi^0$ , the analyses repeats the procedure of asymmetry extraction as for the BH/DVCS process, but for the leading photons of the detected  $\pi^0$ s. Events selected for a two-photon analysis pass the same cuts as for the BH/DVCS case, but two trackless clusters corresponding to two photons are required to be detected by the calorimeter instead of one. The invariant mass of two detected photons is required to correspond to the range  $0.01 < M_{inv}^2 < 0.029$  providing clean  $\pi^0$  separation (see figure 7.10, left panel). About 75% of the semi-inclusive background events from  $\pi^0$  decay in the BH/DVCS exclusive sample are single photon hits in the calorimeter [Kra05]. Hence the LTSA was calculated for the most energetic photon out of the two detected ones, assuming that it carries most of the asymmetry of the parent  $\pi^0$ . The dependence of the amplitudes  $A_{UL}^{\sin\phi}$  and  $A_{UL}^{\sin 2\phi}$  on the missing mass calculated for the leading

photon as if it originated from the BH/DVCS process, is shown in figure 7.10, central panel.

The measured behavior of  $A_{UL}^{\sin\phi}$  is explained well by the missing-mass dependence of the relative energy  $z_{\pi^0}$  of the  $\pi^0$  from which the detected photon originated, as extracted from the MC study (see figure 7.10, right panel). In the missing-mass region corresponding to the selected exclusive sample of the BH/DVCS process,  $z_{\pi^0}$  is close to unity, which corresponds to the quite sizable  $\sin\phi$  amplitude measured for semi-inclusive  $\pi^0$  production (see figure 7.8). In the semi-inclusive region of missing mass,  $z_{\pi^0}$  drops to much smaller values that is compatible with the slightly positive amplitude  $A_{UL}^{\sin\phi}$  of the asymmetry of the one-photon sample in the non-exclusive region (figure 7.2 top left panel). The observed  $A_{UL}^{\sin 2\phi}$  is consistent with zero over the full range of missing mass.

Although the two-photon analysis demonstrates good agreement with the results measured in semi-inclusive pion production, the kinematics of the photons used for asymmetry measurements of  $\pi^0$ s differs from the kinematics of those constituting the background to the BH/DVCS process in the selected exclusive sample. Hence the measurements mentioned above (figure 7.8) can not be used for a correction of the asymmetry measurement of the BH/DVCS process and a possible contribution of background  $\pi^0$  production to the measured asymmetry is taken into account as a systematic uncertainty. The impact of the asymmetry  $A_{UL}^{\pi^0}$  generated by the background  $\pi^0$ s, on the measured asymmetry  $A_{UL}$  can be estimated as asymmetry corrected for the  $\pi^0$  contribution as:

$$A_{UL}^{corr.} = \frac{1}{1 - \eta_{\pi^0}} A_{UL} - \frac{\eta_{\pi^0}}{1 - \eta_{\pi^0}} A_{UL}^{\pi^0}, \quad (7.13)$$

where  $\eta_{\pi^0} = N_{\pi^0}/N_{tot}$  is the fraction of  $\pi^0$  production in the exclusive sample. The value  $\eta_{\pi^0}$  is taken from the MC study (e.g.  $\eta_{\pi^0} = 0.05$  for the combined sample, see table 6.1). The systematic uncertainty for every amplitude is calculated as maximum deviation between the corresponding amplitudes of the measured and corrected asymmetries  $A_{UL}$  and  $A_{UL}^{corr.}$ , respectively. The latter is calculated for the limiting cases of the asymmetry  $A_{UL}^{\pi^0}$  of the background  $\pi^0$ s as it was done in Eq. 7.13. The limiting cases of  $A_{UL}^{\pi^0}$  are based on the results from Ref. [A<sup>+</sup>03] (figure 7.8) and taken as mean value of the amplitude plus and minus three standard deviations (e.g.  $A_{UL}^{\pi^0 \sin\phi} \pm 3 \cdot \delta A_{UL}^{\pi^0 \sin\phi}$ ) measured at  $z_{\pi^0} = 0.9$ , resulting in  $0.18 \pm 3 \cdot 0.06$  and  $0 \pm 3 \cdot 0.06$  for the amplitudes  $A_{UL}^{\pi^0 \sin\phi}$  and  $A_{UL}^{\pi^0 \sin 2\phi}$ , respectively.

In order to study the influence of the  $\pi^0$  background on the measured LTSA, the upper cut on the missing-mass, used for the exclusive sample selection, was reduced from  $M_x < 1.7$  GeV to  $M_x < 1.4$  GeV. In this

case the fraction of  $\pi^0$ s contributing the selected sample reduces from 5% to about 2%. The azimuthal dependence was measured and the *sine* amplitudes were extracted for this reduced sample. The resulting amplitudes  $A_{UL}^{\sin\phi} = -0.078 \pm 0.039(\text{stat.})$  and  $A_{UL}^{\sin 2\phi} = -0.116 \pm 0.040(\text{stat.})$  are consistent with the amplitudes measured in the original missing-mass range. Hence the contribution of  $\pi^0$ s to the exclusive sample does not have a strong influence to the measured LTSA.

#### 7.4.6 Calorimeter Miscalibration and Misalignment

Intense studies of the calorimeter performance carried out in Refs. [Ell04, Kra05] demonstrate the following problems for scattered positrons at the kinematics of the DVCS process at HERMES:

- the energy of the positron measured in the calorimeter differs from the energy provided by the tracking system.
- the hit position of the positron reconstructed by the upper half of the calorimeter differs from the hit position provided by the tracking system.

In this analysis the photon is required to be converted into an electro magnetic shower already in the preshower detector (see section 5.3.2) in order to improve the resolution in the photon energy. Nevertheless the response of the calorimeter to the positron differs from its response to the electro magnetic shower caused by the photon in the preshower detector. Hence results of the analysis on the difference between the tracking system and the calorimeter derived for the positron case can not be applied to the photon case for a correction of the above mentioned problems. Still, this information can be used in order to estimate corresponding systematic errors.

#### Reconstruction of the Photon Energy

In order to estimate the miscalibration of the energy measurement in the calorimeter with respect to the one from the tracking system, the ratio of the positron energy measured by the calorimeter to the positron momentum measured by the tracking system is formed for positrons that passed all exclusive cuts. Due to the lack of statistics the missing-mass cut is not applied, nevertheless the energy range of the selected positrons is similar to the energy range of the photons in the exclusive sample.

In order to measure the average miscalibration factor the distribution of the corresponding ratio (see figure 7.11) is fitted with a convolution of

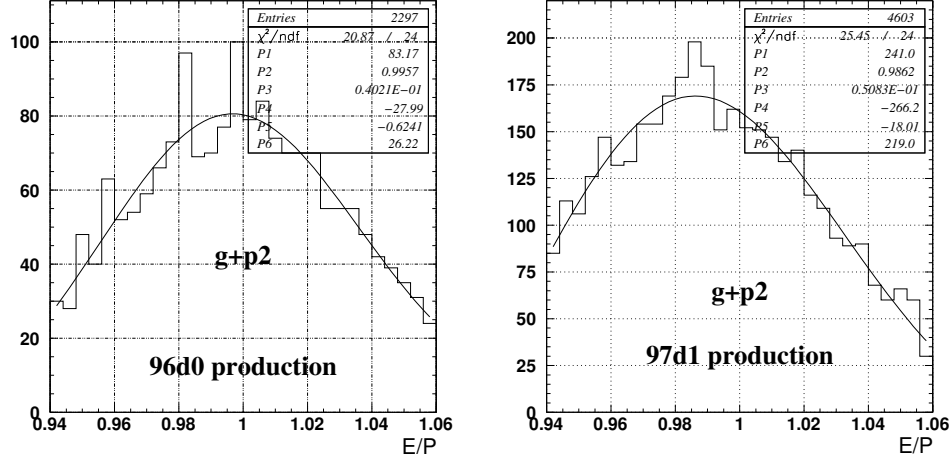


Figure 7.11: Distributions of  $E/P$  ratios of detected exclusive positrons (no missing-mass requirements) for 96d0 (left) and 97d1 (right) data productions. The fit is done with a sum of Gaussian and polynomial. The parameter  $P2$  of the fit represents the mean value of the Gaussian.

Gaussian and polynomial. The biggest miscalibration of the calorimeter with respect to the tracking system is measured for the 97d1 production. The calorimeter underestimates the energy of the detected positron by a factor 1.014. Due to the above mentioned reasons the results shown in figure 7.11 can not be applied directly for the correction of the photon energy. The number 1.014 is taken as a typical scale of the miscalibration in the studied data sample and used for the calculation of the corresponding systematic error.

In this analysis the photon energy  $E_\gamma$  is used only for missing-mass calculations and its scaling affects only the number of events in the exclusive data sample and the fractions of the contributing processes. The systematic error is estimated as maximum possible deviation of the asymmetry caused by the deviation of the fractional contributions of the processes to the exclusive sample. Using MC studies the fractions of the processes were calculated for the data samples with the photon energy corrected by factors 1.014 and  $1/1.014$ . The corresponding deviations of the process fractions are shown in table 7.4. Note that the shift of the peak position of the missing-mass distribution caused by the correction of the photon energy is about 150 MeV down (up) for the scaling factor 1.014 ( $1/1.014$ ). The deviation of the asymmetry of every process ( $pr.$ ) is calculated by scaling the maximum possible asymmetry  $A_{pr.}^{max}$  contributed by the process to the selected sample with the

	$\eta_{el.}, \%$	$\eta_{ass.}, \%$	$\eta_{\pi^0}, \%$	$N_{excl.}$
not corr.	84.5	10.4	5.0	2454
$\Delta(E_\gamma \cdot 1.014)$	-0.7	-0.1	0.8	134
$\Delta(E_\gamma/1.014)$	0.8	0.1	-0.9	-166

Table 7.4: The fractions of the elastic ( $\eta_{el.}$ ), associated ( $\eta_{ass.}$ ), exclusive and semi-inclusive  $\pi^0$  processes ( $\eta_{\pi^0}$ ) and the number of events ( $N_{excl.}$ ) in the exclusive sample (not corr.) and the corresponding deviations for the samples with the the photon energy  $E_\gamma$  corrected by factors 1.014 and 1/1.014.

corresponding deviation of its fraction  $\Delta\eta_{pr.}$  as:

$$\delta A_{pr.}^{calo} = \Delta\eta_{pr.} A_{pr.}^{max}. \quad (7.14)$$

For the exclusive and semi-inclusive  $\pi^0$ s the maximum possible asymmetry is estimated as contribution of  $\pi^0$ s to the systematic error of the measured LTSA, which was calculated in section 7.4.5. In case of elastic BH/DVCS production the result of the measurement is used. Setting the asymmetry of the associated BH/DVCS to its extreme cases  $A_{ass.}^{max} = \pm 1$ , the maximum possible asymmetry of the elastic production  $A_{el.}^{max}$  is extracted from the relation:

$$A_{el.}^{max} \eta_{el.} + A_{ass.}^{max} \eta_{ass.} = A_{UL} \pm 3 \cdot \delta A_{UL}, \quad (7.15)$$

where  $A_{UL}$  and  $\delta A_{UL}$  are the measured LTSA and the corresponding statistical error and  $\eta_{el.}$  ( $\eta_{ass.}$ ) is the fraction of the elastic (associated) BH/DVCS production in the selected sample. The signs  $\pm$  in Eq. 7.15 are set to plus or minus so that the absolute value of  $A_{el.}^{max}$  gets its maximum.

The contributions of all the processes to the total systematic error caused by the photon energy measurement in the calorimeter are calculated for every kinematic bin and added quadratically.

## Reconstruction of the Photon Hit Position

In Ref. [Kra05] it was demonstrated that for scattered positrons the hit position in the calorimeter reconstructed by the upper half of the calorimeter  $y_{calo.}^{(>0)}$  is related to that given by the tracking system  $y_{track.}$  by  $y_{track.} = y_{calo.}^{(>0)} - 0.5$  cm. As it was discussed above, this result can not be applied for a correction of the photon hit position. Hence this knowledge is used for the calculation of a systematic uncertainty. The deviation between the asymmetries measured with and without correction (see table 7.5) is assigned as the systematic error caused by the misalignment of the calorimeter. Note that



	$A_{UL}^{\sin\phi}$	$A_{UL}^{\sin 2\phi}$	# of excl. events
no correction	$-0.071 \pm 0.034$	$-0.113 \pm 0.034$	2454
$y_{\gamma}^{(>0)} - 0.5cm$	$-0.069 \pm 0.034$	$-0.114 \pm 0.034$	2422
deviation	0.002	0.001	

Table 7.5: Amplitudes  $A_{UL}^{\sin\phi}$  and  $A_{UL}^{\sin 2\phi}$  and the number of exclusive events for corrected and not corrected measured photon hit position  $y_{\gamma}^{(>0)}$ . The last line of the table shows the deviation of the asymmetry caused by the correction.

this correction affects not only the number of events in the exclusive sample, but also the measurement of the azimuthal angle. Hence in order to estimate with MC studies its impact on the measured LTSA, addition model assumptions are required on the azimuthal dependence of the measured asymmetry. Hence this uncertainty is estimated from data as described above.

#### 7.4.7 Contribution from the Transverse TSA to the Longitudinal TSA

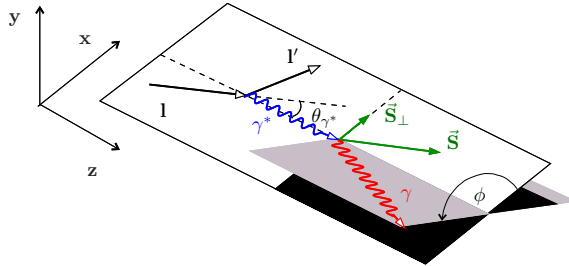


Figure 7.12: Kinematics of the DVCS process for a longitudinally polarized target. The angle  $\theta_{\gamma^*}$  denotes the angle between the virtual photon and the polarization vector of the longitudinally polarized target  $\vec{S}$ , aligned along the direction of the incoming positron.

The polarization vector of the longitudinally polarized target is aligned either parallel or antiparallel to the beam direction at HERMES. Due to the kinematics of the reaction (figure 7.12) there is a small, but finite angle  $\theta_{\gamma^*}$  between the beam and the virtual photon directions, which projects the longitudinal polarization of the target into a certain transverse one with respect to the virtual photon. Therefore, the generated TTSA  $A_{UT}$  (for details see section 3.6) can contribute to the measured LTSA  $A_{UL}$ .

This effect was analytically studied in Ref. [DS05] with the result that the measured asymmetry  $A_{UL}$  gets a contribution from the “genuine” LTSA  $A_{UL}^*$  and the “genuine” TTSA  $A_{UT}^*$  as:

$$A_{UL} = \cos \theta_{\gamma^*} A_{UL}^* - \sin \theta_{\gamma^*} A_{UT}^* (\phi_S = 0), \quad (7.16)$$

where  $\phi_S$  is the azimuthal angle of the vector of transverse target polarization with respect to the lepton production plane (see figure 3.6). Note that  $\phi_S = 0$  for the kinematics shown in figure 7.12. At the average kinematics of this analysis the angle  $\theta_{\gamma^*}$  is measured as  $\langle \sin \theta_{\gamma^*} \rangle = 0.08$ , that makes the LTSA sensitive to a contribution of the generated TTSA, but a possible dilution of the real  $A_{UL}^*$  in Eq. 7.16 is negligible as the value of  $\langle \cos \theta_{\gamma^*} \rangle$  is close to unity.

The azimuthal dependence of the TTSA (see Ref. [DS05]) makes the amplitude  $A_{UL}^{\sin \phi}$  not sensitive to the generated TTSA, and the amplitude  $A_{UL}^{\sin 2\phi}$  gets contributions from the two leading azimuthal amplitudes  $A_{UT}^{\sin(\phi-\phi_S) \cos \phi}$  and  $A_{UT}^{\cos(\phi-\phi_S) \sin \phi}$  as:

$$A_{UL}^{\sin 2\phi} = \cos \theta_{\gamma^*} A_{UL}^{\sin 2\phi} - \sin \theta_{\gamma^*} \left( A_{UT}^{\sin(\phi-\phi_S) \cos \phi} + A_{UT}^{\cos(\phi-\phi_S) \sin \phi} \right) \Big|_{\phi_S=0}. \quad (7.17)$$

Preliminary measurements of the TTSA at HERMES yield the amplitudes [Y<sup>+</sup>05]:

$$\begin{aligned} A_{UT}^{\sin(\phi-\phi_S) \cos \phi} &= -0.133 \pm 0.054(\text{stat.}) \pm 0.038(\text{syst.}), \\ A_{UT}^{\cos(\phi-\phi_S) \sin \phi} &= 0.038 \pm 0.051(\text{stat.}) \pm 0.015(\text{syst.}), \end{aligned}$$

which according to Eq. 7.17 indicates only a small contribution of the generated TTSA to the measured LTSA. Note that this contribution tends to decrease the absolute value of  $A_{UL}^{\sin 2\phi}$  due to the negative value of the amplitude  $A_{UT}^{\sin(\phi-\phi_S) \cos \phi}$  that enters Eq. 7.17 with a negative sign.

Since the measurements of the TTSA amplitudes are still preliminary and the effect of a contribution of the TTSA to the LTSA is seen to be small, the final LTSA is not corrected for this effect, which the small generated TTSA contribution has to the amplitude  $A_{UL}^{\sin 2\phi}$ .

### 7.4.8 Smearing Effects

The influence of smearing effects on the measured asymmetry is studied with MC generators that allow to compare the asymmetry of the data set before and after tracking and reconstruction. There are two possible ways to generate the asymmetry of the BH/DVCS process in MC.

The method used in Ref. [Kra05] is based on model predictions for these GPDs which contribute to the asymmetry. This method has the advantage that it takes into account the kinematic dependence of the asymmetry and reproduces the experimental conditions, although this information is model dependent.

The other method is based on generating an artificial asymmetry of the BH process that has no LTSA. Since the experimental results demonstrate sizable contributions only from  $\sin \phi$  and  $\sin 2\phi$  harmonics to the LTSA, the cross section of the BH process  $\sigma_{BH}$  is to be weighted with

$$1 \pm A \sin(N\phi), \quad (7.18)$$

in order to generate the asymmetry in MC data. This is applied to data with positive and negative target polarization, respectively, where  $N = 1, 2$  selects the *sine* harmonic of interest,  $A$  is the amplitude of the selected harmonic and  $\phi$  is the non-smeared azimuthal angle. Within such an approach the introduced asymmetry has no kinematic dependence, nevertheless it can be used as a good estimate of the expected smearing effects. The results are found to be compatible with those of the first method.

Although the first approach is more preferable and can be implemented using the generator **gmc\_dvcs** (see section 6.1), at the time of making this analysis, the CFF  $\mathcal{H}$  necessary for the simulation of the LTSA was not modeled in the generator. Hence the second approach is used for the MC studies with the input amplitude value  $A = -0.5$ .

In order to study the smearing of the amplitude of a certain harmonic and its cross talk to the other harmonic, two MC samples with only the elastic BH process are produced with an asymmetry generated separately for the  $\sin \phi$  and  $\sin 2\phi$  harmonics. The results are shown in table 7.6 as fractions of the reconstructed amplitudes with respect to the input amplitude  $A = -0.5$  generated with either  $\sin \phi$  or  $\sin 2\phi$  input harmonic of the LTSA, at average kinematics. The measured smearing reduces the absolute values of the amplitudes both for the  $\sin \phi$  and  $\sin 2\phi$  harmonics, but gives them

reconstructed	input harmonic	
	$\sin \phi$	$\sin 2\phi$
$A_{UL}^{\sin \phi}/A$	-2%	17%
$A_{UL}^{\sin 2\phi}/A$	2%	-15%

Table 7.6: Fractions of reconstructed amplitudes to the input amplitude  $A = -0.5$  generated with either  $\sin \phi$  or  $\sin 2\phi$  input harmonic.

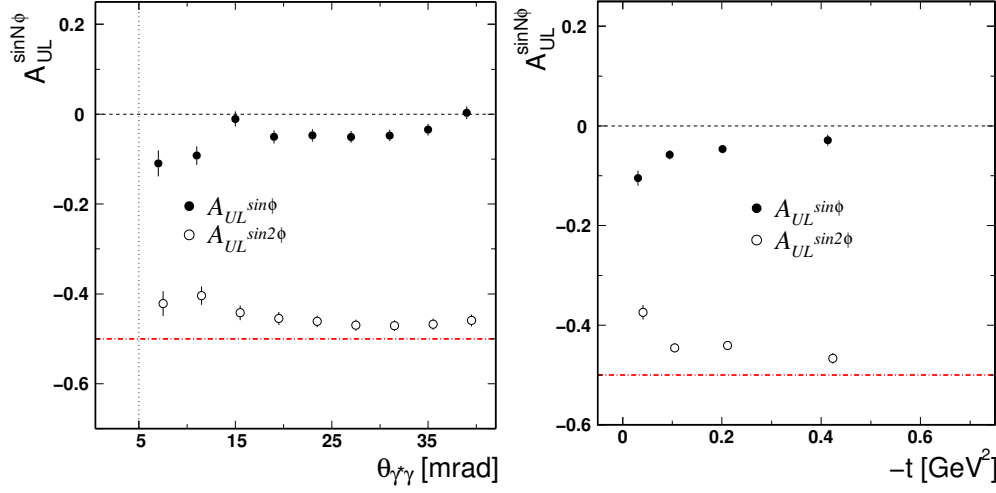


Figure 7.13: Dependence of the reconstructed LTSA amplitudes  $A_{UL}^{\sin\phi}$  and  $A_{UL}^{\sin 2\phi}$  on  $\theta_{\gamma^*\gamma}$  (left) and  $-t$  (right). The input asymmetry is a  $\sin 2\phi$  harmonic with the amplitude  $A = -0.5$  (indicated with dash-dotted lines).

an additional contribution due to cross talk. Although  $A_{UL}^{\sin\phi}$  is smeared only by about  $-2\%$  (diagonal element in table 7.6), the amplitude is affected by the large cross talk from the  $\sin 2\phi$  harmonic,  $17\%$  (non-diagonal element). The situation is opposite in the case of the amplitude  $A_{UL}^{\sin 2\phi}$  that is affected mostly from smearing.

The dependence of the reconstructed  $A_{UL}^{\sin 2\phi}$  and its cross talk contribution to  $A_{UL}^{\sin\phi}$ , on  $\theta_{\gamma^*\gamma}$  and  $-t$  is shown in figure 7.13. Large smearing and cross talk from  $A_{UL}^{\sin 2\phi}$  dominate in the region of small  $\theta_{\gamma^*\gamma}$  (figure 7.13, left) mainly due to the momentum resolution of the scattered positron, which results in an uncertainty in  $\theta_{\gamma^*\gamma}$  of 3 mrad (for details see section 6.4). Due to the discussed correlation between the variables  $\theta_{\gamma^*\gamma}$  and  $t$  (see figure 6.10), the region of small  $\theta_{\gamma^*\gamma}$  corresponds to the first  $t$ -bin, where largest smearing and cross talk are observed (figure 7.13, right).

Increasing the lower  $\theta_{\gamma^*\gamma}$  cut up to 0.015 would reduce the average smearing and cross talk by about a factor of 2. Since most of the accumulated data corresponds to the small  $\theta_{\gamma^*\gamma}$  and  $-t$ -region, increasing the cut would reduce the number of accepted events by a factor of 2, as well. Due to the limited statistics and due to the fact that the systematic error caused by smearing and cross talk is of about 3 times smaller than the statistical one, the cut is kept at the lower value.

A study of the smearing effect with an input amplitude  $A = -0.2$  (see

Eq. 7.18) reproduces the discussed results.

#### 7.4.9 Number of Bins in $\phi$

As it was discussed in section 7.2, the amplitudes of the asymmetry harmonics extracted with the *fit method* depend on the number of  $\phi$ -bins used for the calculation of the azimuthal dependence. In order to study such binning effect, MC data is used with an asymmetry generated as described in section 7.4.8. In order to exclude the influence of the smearing effect from the result, the non-smearing value of the azimuthal angle  $\phi$  is used for the extraction of the amplitude.

Since the amplitude  $A_{UL}^{\sin 2\phi}$  is more sensitive to the binning effect than  $A_{UL}^{\sin \phi}$ , results of the study of the binning effect are shown only for an asymmetry with a generated  $\sin 2\phi$  harmonic. The dependence of the relative difference between reconstructed and initial amplitudes on the number of  $\phi$ -bins is shown in table 7.7. Although a better reconstruction is clearly seen for 14  $\phi$ -bins and more, even for 10  $\phi$ -bins the systematic shift of the  $A_{UL}^{\sin 2\phi}$  reconstruction is still much smaller than the one from the smearing effect. The number of  $\phi$ -bins should be selected in such way that every bin contains at least 5 events to ensure a reliable calculation of the statistical error. This limitation is especially important for measurements of kinematic dependences of the asymmetry where statistics in the last  $Q^2$ - and  $x_B$ -bins are rather limited. Due to this reason the number of  $\phi$ -bins used in this analysis is set to be 10, as in earlier DVCS analyses [Ell04, Kra05].

	Number of $\phi$ -bins				
	10	12	13	14	16
$(A - A_{UL}^{\sin 2\phi}) / A$	6.4%	5.0%	4.0%	2.6%	2.0%

Table 7.7: Relative difference between the reconstructed amplitude  $A_{UL}^{\sin 2\phi}$  and the initial amplitude  $A = -0.5$ , depending on the number of  $\phi$ -bins. The smearing effect is excluded.

The stability of the measured asymmetry amplitudes extracted with the *fit method* for various numbers of  $\phi$ -bins is shown in figure 7.14. The extracted amplitudes are consistent for all numbers of  $\phi$ -bins.

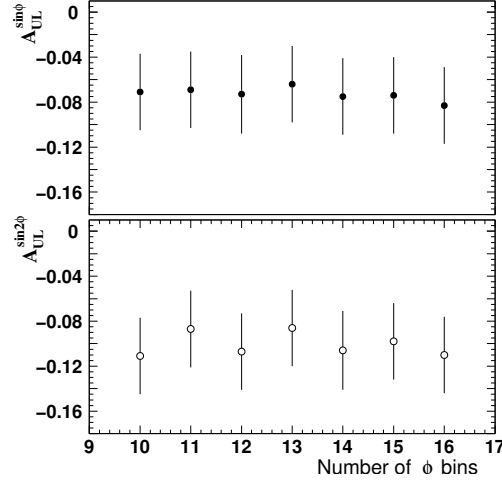


Figure 7.14: Dependence of the measured amplitudes  $A_{UL}^{\sin \phi}$  and  $A_{UL}^{\sin 2\phi}$  extracted with the *fit method*, on the number of  $\phi$ -bins.

## 7.5 Systematic Uncertainties

Based on the studies discussed above, the following systematic uncertainties were found to make a sizeable contribution to the overall systematic error:

**Target Polarization Measurement:** the uncertainty due to the measurement of the target polarization. The average target polarization for 1996 and 1997 data taking period used in this analyses is  $\langle |P_t| \rangle = 0.824 \pm 0.035$  (for detail see section 4.2.1) that results in a relative error of the measured asymmetry about 4.2%.

**Calorimeter Miscalibration:** the uncertainty due to the miscalibration of the calorimeter used for photon energy measurement, with respect to the tracking system used for measurement of the positron momentum (see section 7.4.6).

**Calorimeter Misalignment:** the uncertainty due to the misalignment of the calorimeter with respect to the tracking system used for photon and positron trajectory measurement, respectively (see section 7.4.6).

**Smearing and Binning Effects:** the uncertainty due to the finite detector resolution and due to limitations of the *fit method* used in the extraction of asymmetry amplitudes (see sections 7.4.8 and 7.4.9).

**Background Asymmetry:** the uncertainty due to the contamination of semi-inclusive and exclusive  $\pi^0$  background into the selected sample (see section 7.4.5).

The corresponding systematic uncertainties are calculated for every kinematic bin separately. Their contributions to the total systematic uncertainty are added quadratically. Numerical results are summarized in table 7.8. As can be seen, the main two contributions to the overall systematic uncertainty are from the smearing effects and from the background asymmetry.

Radiative effects are not taken into account in the systematic uncertainty. Although these effects can lead to a reduction of the cross section of the BH process up to 20% (see Ref. [V<sup>+</sup>00]), it was demonstrated in Ref. [AKM05] that one-loop QED corrections to the leptonic part of the interaction give a negligible contribution to the LTSA at HERMES energies. This kind of correction is the only model-independent correction to the BH/DVCS cross section that can generate a single spin asymmetry (other corrections require model assumption on the nucleon structure). Therefore no error is assigned to the uncertainty caused by the radiative effects. Note that external radiation is taken in account by the simulation of the particle tracking through the detector in MC studies. Therefore possible contribution of external radiation to the systematic uncertainty is taken into account by the smearing.

Another uncertainty not included into the overall systematic error is the so-called “bin-centering” effect of the *fit-method*, discussed in detail in Ref. [Kra05]. The asymmetry measured in this analysis depends on several kinematic variables but due to the limited statistics it can be binned only in one or two of them at the same time. In this case amplitudes of the asymmetry extracted with the *fit-method* are integrated over the not binned variables. As a result, the measured amplitudes at the average kinematics differ from the integrated ones due to the contribution of the acceptance function to the latter. As it was demonstrated by MC studies in Ref. [Kra05], in case of considering the  $t$ -dependence of the measured amplitudes the amplitude of the  $\sin \phi$  harmonic can be underestimated by this effect by up to 10% of its absolute value (the distortion for the  $\sin 2\phi$  case is smaller). For the case of the  $\cos \phi$  and  $\cos 2\phi$  harmonics this effect is much bigger due to their possible coupling to the acceptance function which itself has a  $\cos \phi$  dependence. It was demonstrated by MC studies in Ref. [Kra05], since their results have very strong model dependences, hence it is unclear how to apply this information to the measured results and no correction is applied to the measured LTSA.

kinematic bin		Systematic Error					
		total	1.	2.	3.	4.	5.
$A_{UL}^{sin(\phi)}$							
$-t$ , GeV <sup>2</sup>	0.00 - 0.06	<b>0.019</b>	0.000	0.001	0.002	0.014	0.013
	0.06 - 0.14	<b>0.043</b>	0.003	0.004	0.019	0.014	0.035
	0.14 - 0.30	<b>0.061</b>	0.006	0.008	0.021	0.017	0.054
	0.30 - 0.70	<b>0.079</b>	0.008	0.016	0.007	0.009	0.076
$Q^2$ , GeV <sup>2</sup>	1.0 - 1.5	<b>0.031</b>	0.003	0.003	0.000	0.008	0.029
	1.5 - 2.3	<b>0.042</b>	0.001	0.003	0.002	0.033	0.025
	2.3 - 3.5	<b>0.036</b>	0.003	0.005	0.003	0.009	0.035
	3.5 - 6.0	<b>0.044</b>	0.003	0.005	0.008	0.029	0.032
	6.0 - 10.	<b>0.172</b>	0.013	0.020	0.157	0.010	0.066
$x_B$	0.03 - 0.07	<b>0.015</b>	0.000	0.002	0.005	0.007	0.012
	0.07 - 0.10	<b>0.053</b>	0.006	0.004	0.012	0.040	0.031
	0.10 - 0.15	<b>0.037</b>	0.000	0.004	0.004	0.020	0.031
	0.15 - 0.20	<b>0.112</b>	0.010	0.012	0.005	0.014	0.110
	0.20 - 0.35	<b>0.172</b>	0.008	0.023	0.116	0.028	0.122
<b>all</b>		<b>0.035</b>	0.003	0.003	0.002	0.017	0.030
$A_{UL}^{sin(2\phi)}$							
$-t$ , GeV <sup>2</sup>	0.00 - 0.06	<b>0.019</b>	0.003	0.001	0.004	0.017	0.008
	0.06 - 0.14	<b>0.030</b>	0.005	0.004	0.013	0.013	0.022
	0.14 - 0.30	<b>0.047</b>	0.007	0.008	0.017	0.023	0.036
	0.30 - 0.70	<b>0.055</b>	0.004	0.016	0.038	0.009	0.035
$Q^2$ , GeV <sup>2</sup>	1.0 - 1.5	<b>0.034</b>	0.003	0.003	0.026	0.015	0.015
	1.5 - 2.3	<b>0.044</b>	0.007	0.005	0.021	0.030	0.022
	2.3 - 3.5	<b>0.021</b>	0.003	0.004	0.006	0.010	0.016
	3.5 - 6.0	<b>0.047</b>	0.007	0.006	0.019	0.034	0.025
	6.0 - 10.	<b>0.035</b>	0.000	0.019	0.024	0.011	0.013
$x_B$	0.03 - 0.07	<b>0.013</b>	0.002	0.002	0.003	0.009	0.007
	0.07 - 0.10	<b>0.053</b>	0.010	0.005	0.002	0.044	0.026
	0.10 - 0.15	<b>0.035</b>	0.004	0.005	0.018	0.018	0.023
	0.15 - 0.20	<b>0.045</b>	0.003	0.009	0.006	0.019	0.040
	0.20 - 0.35	<b>0.095</b>	0.005	0.023	0.064	0.028	0.060
<b>all</b>		<b>0.028</b>	0.005	0.003	0.001	0.020	0.019

Table 7.8: Contributions of various systematic uncertainties to the total systematic uncertainty for the  $\sin \phi$  and  $\sin 2\phi$  amplitudes of the LTSA measured on the proton from 1996-97 data. Here the sources of the uncertainties are: 1. - target polarization measurement, 2. - calorimeter miscalibration, 3. - calorimeter misalignment, 4. - smearing and binning effects, 5. - background asymmetry.



# Chapter 8

## Results and Discussion

The measurement of the longitudinal target spin asymmetry in exclusive real photon production is the main topic of this thesis. The data sample was accumulated at HERMES over the years 1996 and 1997 with a longitudinally polarized positron beam and a longitudinally polarized *proton* target. The asymmetry extraction is discussed in detail in chapter 7. The LTSA is measured at HERMES kinematics in the missing mass region  $-1.5 \text{ GeV} < M_x < 1.7 \text{ GeV}$ . The range of kinematic variables and their mean values for the exclusive sample are shown in table 8.1.

	$-t, \text{ GeV}^2$	$x_B$	$Q^2, \text{ GeV}^2$
range	0.00 - 0.70	0.03 - 0.35	1.0 - 10.0
mean	0.12	0.10	2.5

Table 8.1: The range of kinematic variables and their mean values for the exclusive sample.

The LTSA measured at average kinematics as a function of the azimuthal angle  $\phi$  is shown in figure 8.1. The amplitudes of the *sine* expansion of the LTSA are shown in table 8.2, as extracted with the *fit method*. Here and in the following the results of an analysis of the year 2000 deuteron data [Ye05] are included in the discussion, to allow for a more complete comparison with theoretical models. The dependence of the amplitudes  $A_{UL}^{\sin \phi}$  and  $A_{UL}^{\sin 2\phi}$  on the variables  $t$ ,  $Q^2$  and  $x_B$  is shown in figure 8.2. Bin ranges and their average kinematics together with the measured amplitudes are shown in tables 8.3 and 8.4. Additionally the kinematic dependence of the amplitude  $A_{UL}^{\sin 3\phi}$  is shown in table 8.5. The amplitude of the  $\sin 3\phi$  harmonic is extracted with a 4-parameter fit function defined in Eq. 7.10. Since this amplitude is expected to be kinematically suppressed with respect to the leading amplitude by a

	proton	deuteron
$A_{UL}^{\sin \phi}$	$-0.071 \pm 0.034(stat.) \pm 0.035(sys.)$	$-0.036 \pm 0.024(stat.) \pm 0.009(sys.)$
$A_{UL}^{\sin 2\phi}$	$-0.113 \pm 0.034(stat.) \pm 0.028(sys.)$	$-0.039 \pm 0.023(stat.) \pm 0.007(sys.)$

Table 8.2: The amplitudes  $A_{UL}^{\sin \phi}$  and  $A_{UL}^{\sin 2\phi}$  of the  $\sin \phi$  and  $\sin 2\phi$  harmonics of the longitudinal target-spin asymmetry on the proton and the deuteron [Ye05] for the average kinematics of the exclusive sample, as given in table 8.1.

factor of 0.03 and the measurement demonstrates its consistency with zero. The systematic uncertainty was not estimated for this amplitude.

The LTSA shown in figures 8.1, 8.2 is measured for the exclusive sample selected as discussed in section 5. In case of the proton the measured asymmetry receives contributions from exclusive production with either a proton or with a  $\Delta$ -resonance in the final state (about of 85% and 10% in the exclusive sample, respectively). The contribution of the exclusive and semi-inclusive  $\pi^0$  background is about of 5% in the exclusive sample. It is

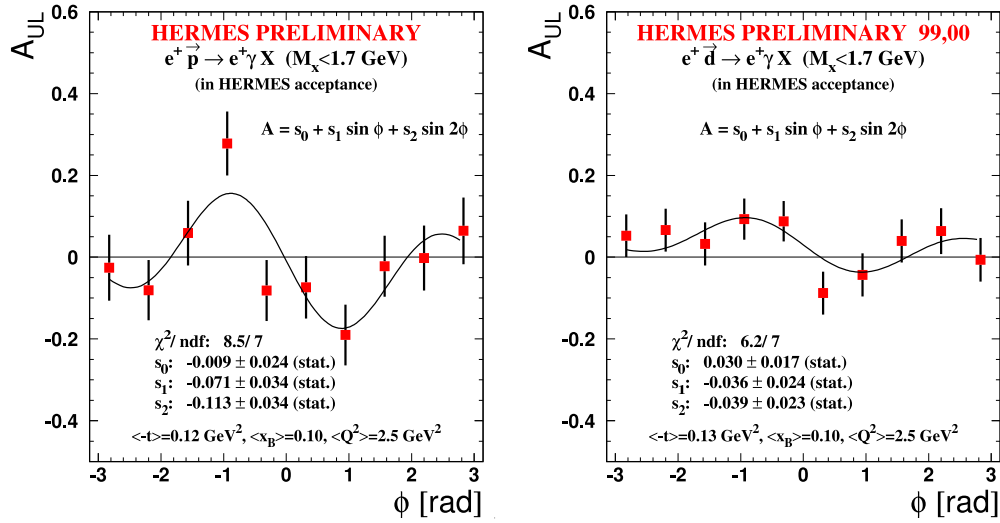


Figure 8.1: The longitudinal target spin asymmetry  $A_{UL}$  for hard electro-production of photons on proton (left) and deuteron (right), as a function of the azimuthal angle  $\phi$  for the exclusive sample. The solid curves represent the results of the indicated fits, numerical values are given in the figure as well. The shown central values and statistical errors are exactly the same as HERMES preliminary results released in May 2005 [KY<sup>+</sup>05, Kop05].

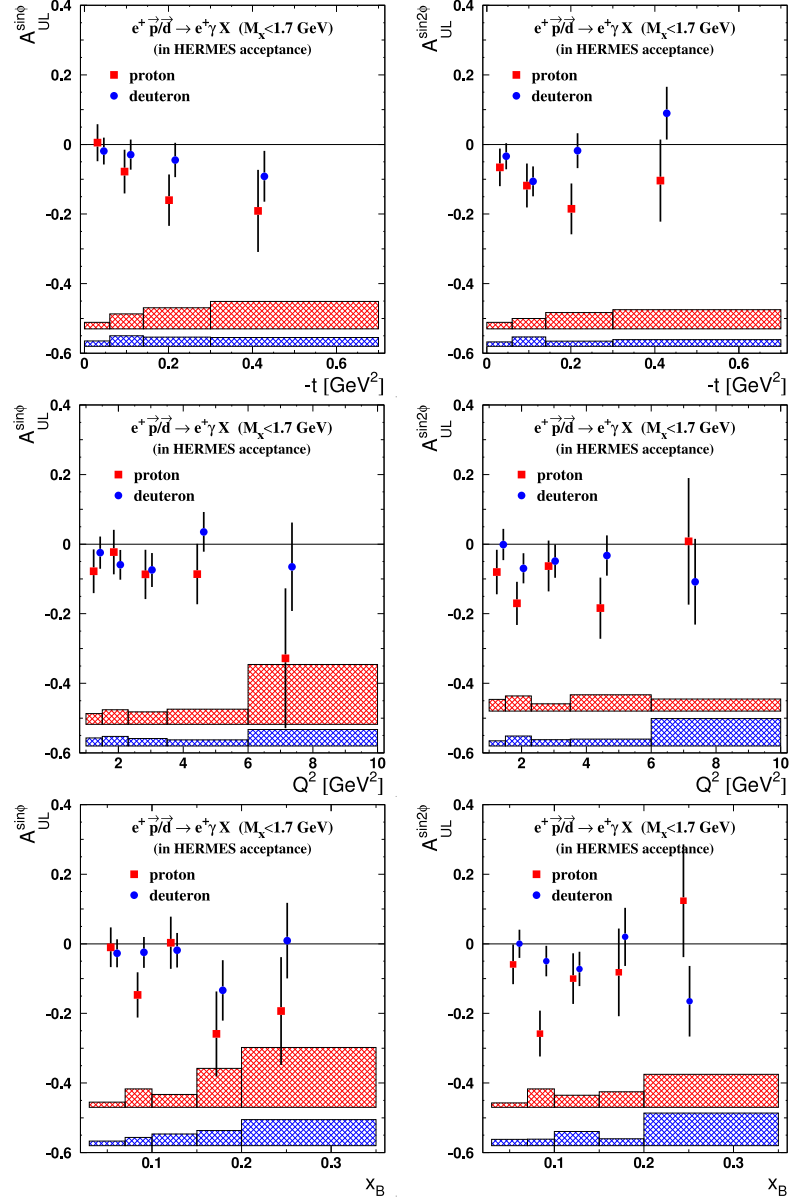


Figure 8.2: The longitudinal target spin asymmetry  $A_{UL}^{\sin \phi}$  (left) and  $A_{UL}^{\sin 2 \phi}$  (right) *vs*  $-t$ ,  $Q^2$  and  $x_B$  as measured on proton and on deuteron. The error bars (bands) represent the statistical (systematic) uncertainty. The shown central values and statistical errors are exactly the same as HERMES preliminary results released in May 2005 [KY<sup>+</sup>05, Kop05], while systematic errors are updated.

taken into account in the systematic uncertainty (see section 7.4.5).

For the case of the deuteron target, exclusive production can originate from either the coherent or the incoherent process. Coherent production is electroproduction from the deuteron as a whole with spin 1, where the deuteron stays intact in the final state. The parameterization of this process requires a set of 9 GPD functions  $H_1, H_2, H_3, H_4, H_5, \tilde{H}_1, \tilde{H}_2, \tilde{H}_3, \tilde{H}_4$  that are discussed in detail in Ref. [KM03]. In the case of incoherent production, within impulse approximation [Kra05] the virtual photon interacts with proton or neutron separately, as if they are in a free state (the binding energy of the deuteron is neglected). Within this approach, the LTSA on the deuteron can be written as:

$$A_{UL}^D \approx \frac{\sigma_p A_{UL}^p + \sigma_n A_{UL}^n}{\sigma_p + \sigma_n}, \quad (8.1)$$

where  $\sigma_p$  ( $\sigma_n$ ) and  $A_{UL}^p$  ( $A_{UL}^n$ ) are the cross section of the hard photoproduction off the proton (neutron) and the corresponding LTSA, respectively.

One reason to study the incoherent process is that the neutron contribution to the asymmetry makes it more sensitive to  $d$ -flavor GPDs. Another important reason is that the LTSA on the neutron is dominated by other GPDs: although the neutron asymmetry depends on the same GPDs as for the proton case, due to the fact that for the neutron the Dirac form factor  $F_1$  is suppressed with respect to the Pauli form factor  $F_2$ , as follows from Eq. 3.22, the contribution of the GPD  $\tilde{H}$  to the asymmetry is also suppressed. Hence the LTSA on the neutron becomes more sensitive to the GPD  $H$ , and also to  $\tilde{E}$  at higher  $t$ .

Since recoiling particles from the DVCS process were not detected at HERMES up to now, the only way to separate the coherent from the incoherent process is to use their different  $t$ -behavior, as it was shown in Ref. [Kra05]. From MC studies it was found that the contribution of the coherent process on the deuteron is sizable only in the first  $t$ -bin, being there about 40% of the total cross section. For higher  $t$ -values the contribution of the coherent process is strongly suppressed and can be essentially neglected.

The results show no difference between the measurement on proton and deuteron in the first  $t$ -bin (see figure 8.2), where an effect from coherent scattering on the deuteron can be expected. For higher  $t$ -bins, where the scattering is mostly incoherent, the asymmetry on proton and deuteron tends to be different. This can be due to different contributions of various GPDs to the LTSA for proton and neutron, as indicated above.

## 8.1 Comparison with Theoretical Calculations.

Results of the LTSA measurement on proton and deuteron are compared with calculations based on the phenomenological approach that was developed in Ref. [GPV01] and discussed in section 2.4. Calculations of GPDs can be done up to twist-3 accuracy within the Wandzura-Wilczek approximation, with either the Regge inspired or factorized ansatz of the  $t$ -dependence. For valence quarks the parameter of the profile function  $b_v$  (see Eq. 2.20) is set to 1 and for sea quarks  $b_s$  is set either to 1 or to infinity (the latter meaning no skewness of GPDs).

In figures 8.3, 8.4 and 8.5, respectively, are shown the amplitudes of the LTSA measured on proton and deuteron, together with corresponding results of model calculations [GPV01] carried out at the average kinematics of every  $t$ -,  $Q^2$ -,  $x_B$ -bin. The calculations were performed in the context of this thesis using the computer code [VGG01].

The amplitudes of the  $\sin\phi$  harmonics  $A_{UL}^{\sin\phi}$  are well described by the model both for proton and deuteron. The skewness of sea quark GPDs does not strongly influence the behavior of the LTSA and with the present statistical accuracy the data can not yet distinguish between different values of model parameters.

The deuteron is more sensitive to the ansatz of the  $t$ -dependence. This can be explained by the fact that  $A_{UL}^{\sin\phi}$  on the proton is dominated by the contribution of the GPD  $\widetilde{H}$  that in this model has only the factorized ansatz and hence the difference between both ansätze for the proton is ruled by the suppressed contributions of the GPDs  $H$  and  $E$  (see Eqs. 3.19, 3.22). In case of the deuteron, due to the neutron contribution the asymmetry gets a sizable contribution from the GPD  $H$  that is directly sensitive to the selected ansatz for the  $t$ -dependence.

The cross section  $\sigma_n$  is smaller than  $\sigma_p$  by a factor of 8 in the first  $t$ -bin, where the electric form factor dominates, and by a factor of 4 at higher  $t$ , where the magnetic form factor becomes sizable and hence leads to an increase of the neutron cross section. This fact, according to Eq. 8.1, reduces the influence of the neutron on to the deuteron asymmetry. Nevertheless the above mentioned reasons explain the difference of model calculations of the LTSA between deuteron and proton targets. The measured difference of the amplitudes  $A_{UL}^{\sin\phi}$  between the proton and the deuteron tends to agree with the difference predicted by the model.

The observed amplitude of the  $\sin 2\phi$  harmonic  $A_{UL}^{\sin 2\phi}$  tends to be of the same size or even bigger in magnitude than  $A_{UL}^{\sin\phi}$ , both for proton and deuteron. According to the GPD formalism  $A_{UL}^{\sin 2\phi}$  is expected to be kinematically suppressed with respect to  $A_{UL}^{\sin\phi}$  by the factor  $K_{sup.}$  (see Eq. 3.17)

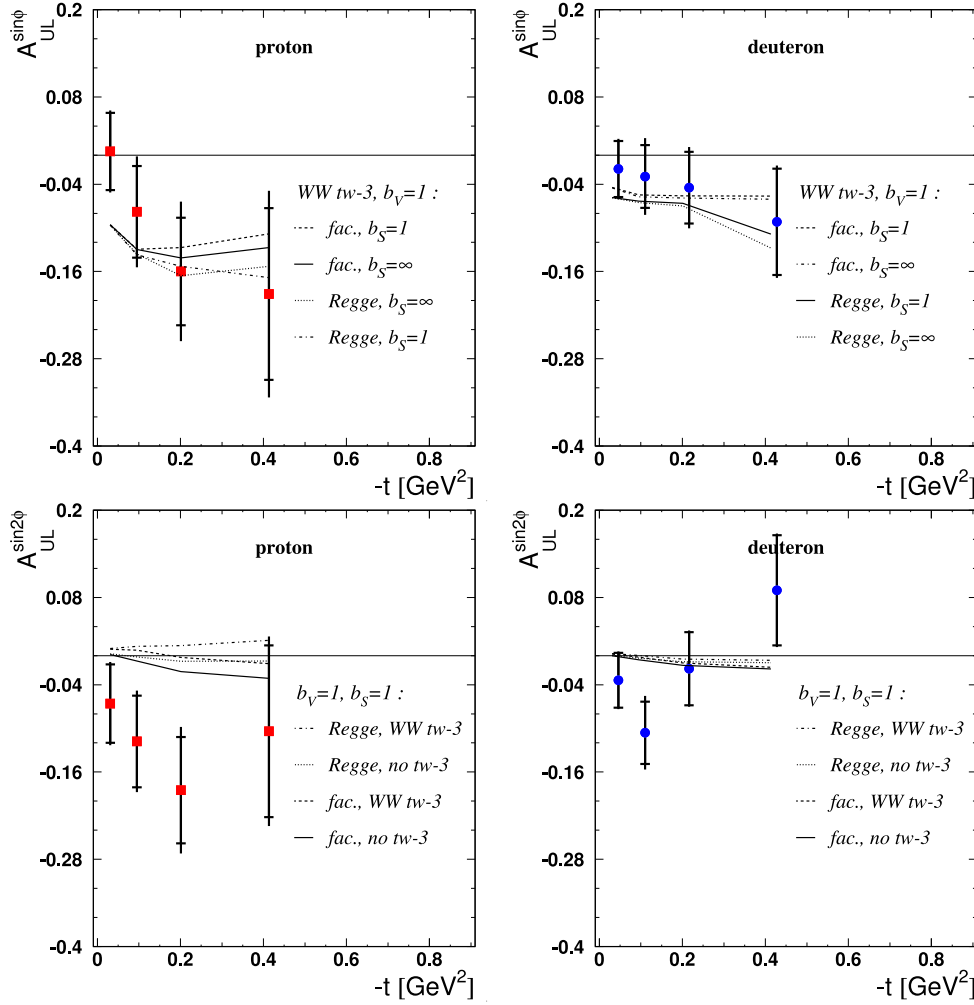


Figure 8.3: The  $\sin\phi$  (top) and  $\sin 2\phi$  (bottom) amplitudes of the longitudinal target-spin asymmetry on the proton (left) and the deuteron (right) as a function of  $-t$ . The inner error bars represent the statistical uncertainty and the full error bars the quadratic superposition of statistical and systematic uncertainties. The measurement is compared with theoretical calculations [GPV01]. For details on the model parameters see text.

that is of the order of 0.2 [Mül04] at the average HERMES kinematics. The value of  $K_{sup.}$  is big enough to make it possible to have sizable contributions from higher than twist-two effects to the LTSA. The similar magnitude of the leading amplitude compared to that of the kinematically suppressed one can be due to the possibly big contribution of sea quark GPDs to the CFF  $\tilde{\mathcal{H}}$  with

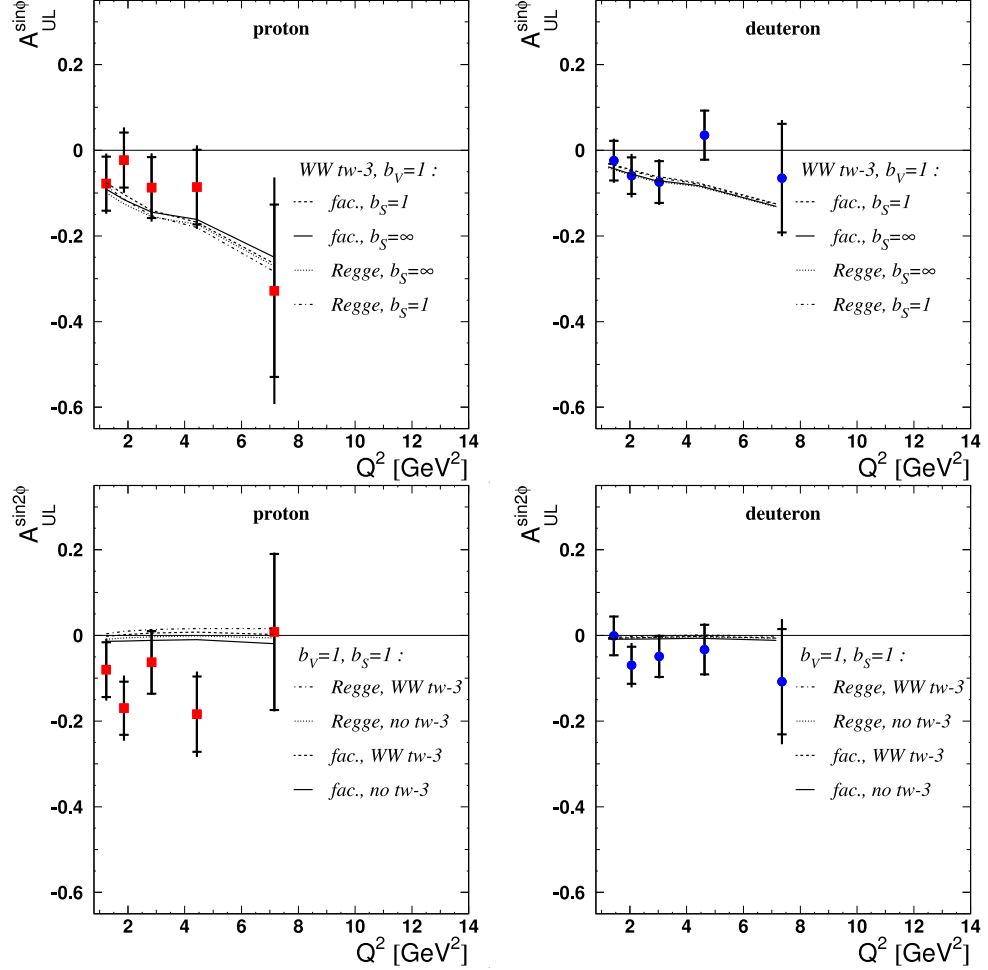


Figure 8.4: The  $\sin\phi$  (top) and  $\sin 2\phi$  (bottom) amplitudes of the longitudinal target-spin asymmetry on the proton (left) and the deuteron (right) as a function of  $Q^2$ . Notations are the same as in figure 8.3.

a sign opposite to that from GPDs of valence quarks, hence compensating each other in case of the  $\sin\phi$  amplitude [Mül04].

In order to demonstrate the influence of the  $WW$  twist-three term (see Eq. 2.9) on the amplitude  $A_{UL}^{\sin 2\phi}$ , all model calculations were performed in two different scenarios: a)  $WW$  twist-three and b) only twist-two accuracy. The parameters of the profile function (see Eq. 2.20)  $b_v$  and  $b_s$  were fixed to 1, as the influence of the skewness of sea quarks on the amplitude was found to be negligible. The measured amplitudes tend to disagree with the model; the influence of the  $WW$  term on the amplitude is not strong and

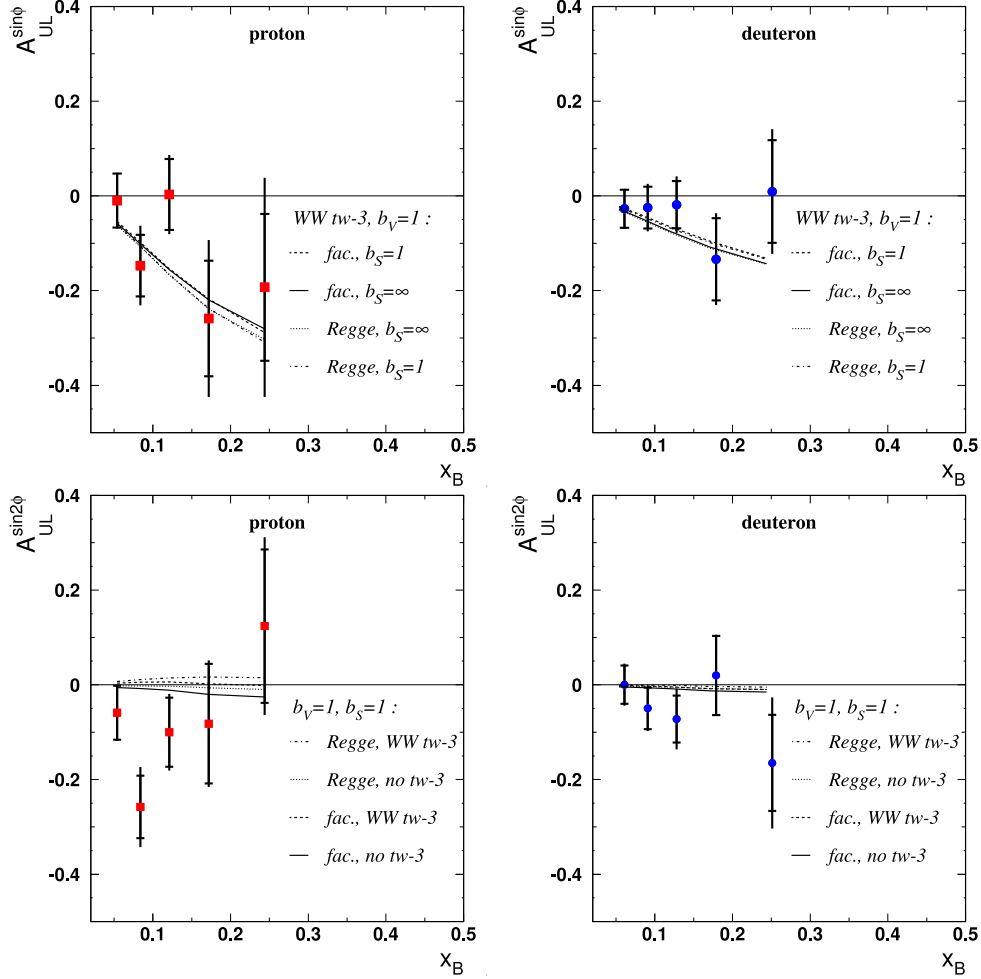


Figure 8.5: The  $\sin\phi$  (top) and  $\sin 2\phi$  (bottom) amplitudes of the longitudinal target-spin asymmetry on the proton (left) and the deuteron (right) as a function of  $x_B$ . Notations are the same as in figure 8.3.

the data tend to prefer the model without it. As discussed in section 2.2.2, the WW approximation describes twist-three effects only partially, taking into account only their twist-two part. The other part of twist-three GPDs related to quark-gluon correlations in the nucleon is poorly known from the theoretical point of view and can therefore not be reliably parameterized at the moment.

The proton measurement is also compared with the model prediction made by D. Müller [Mül04]. The model used for calculations is based on the phenomenological approach similar to the one discussed above in this work,



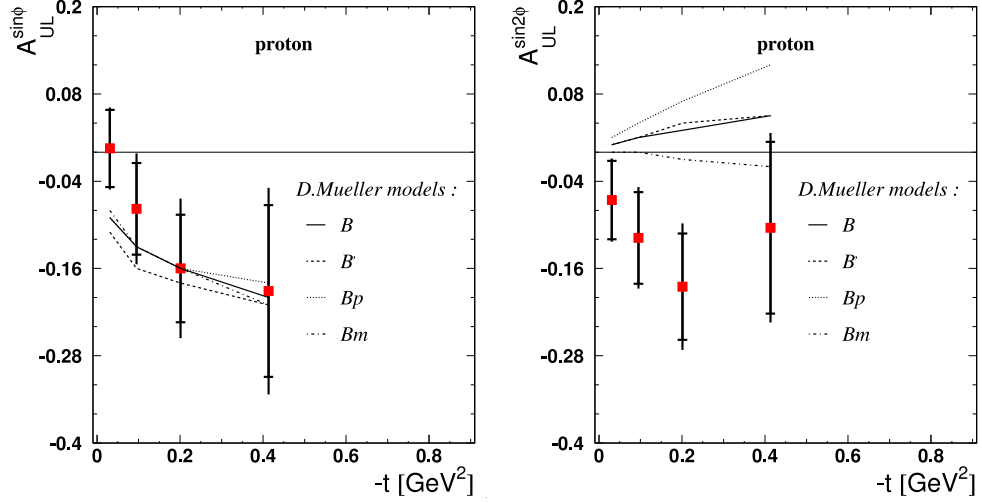


Figure 8.6: The  $\sin \phi$  (left) and  $\sin 2\phi$  (right) amplitudes of the longitudinal target-spin asymmetry on the proton as a function of  $-t$ . The inner error bars represent the statistical uncertainty and the full error bars the statistical and systematic uncertainties added in quadrature. The measurement is compared with theoretical calculations [BMK02, Mül04].

with some differences discussed in detail in Ref. [BMK02]. These calculations are very informative for the interpretation of the measured LTSA on the proton due to two reasons. First, the contributions of valence and sea quark GPDs to the asymmetry are separated so that one can demonstrate their influence on the  $\sin \phi$  amplitude. Second, an upper estimate of the *dynamical* twist-three contribution is included to the GPDs, which as such represents unique information available at the moment. This allows to demonstrate the sensitivity of the  $\sin 2\phi$  amplitude of the LTSA to full twist-three effects.

In this model, the unpolarized GPDs have no skewness neither for valence nor for sea quarks ( $b_v = b_s = \infty$ ). In case of the GPD  $\widetilde{H}$ , valence quarks have skewness ( $b_v = 1$ ) and sea quarks do not ( $b_s = \infty$ ). Such settings of the model parameters for the unpolarized GPDs and the GPD  $\widetilde{H}$  correspond to the models  $B$  and  $GS A$  in Refs. [BMK02, KM03], respectively. Note that  $GS$  stands for the type of the parameterization of polarized PDFs defined in Ref. [GS96].

The model of GPDs calculated up to the twist-three level within WW approximation with contribution both valence and sea quarks is denoted here as  $B$ . Without sea quark contribution the model is denoted as  $B'$ . An estimate of the influence of the *dynamical* twist-three term  $F_{\pm}^{qGq}$  (see Eq. 2.9)

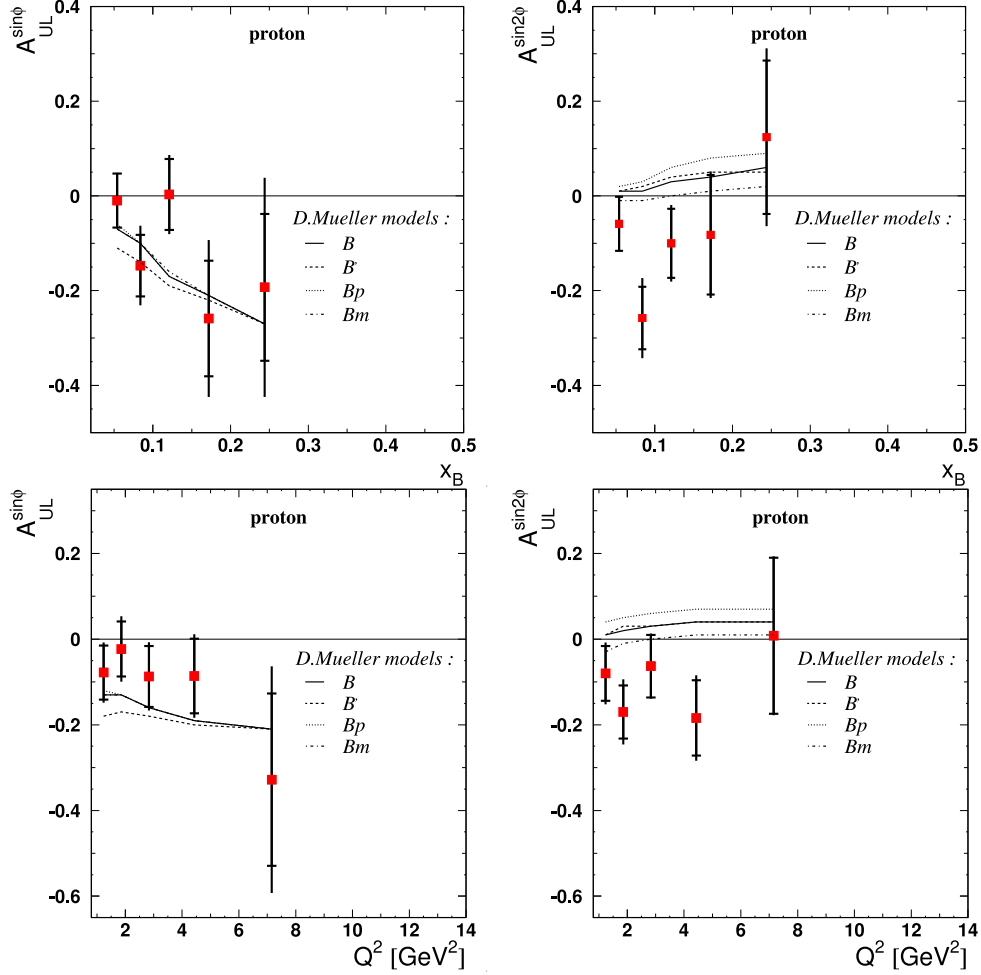


Figure 8.7: The  $\sin \phi$  (left) and  $\sin 2\phi$  (right) amplitudes of the longitudinal target-spin asymmetry on the proton as a function of  $x_B$  (top) and  $Q^2$  (bottom). Notations are the same as in figure 8.6.

on the asymmetry is included into the models  $Bp$  and  $Bm$  where  $F_{\pm}^{qGq}(\phi^{qGq} = -\pi/4$ , see Eq. 179 in Ref. [BMK02]) is added to and subtracted from GPDs calculated in model  $B$ , respectively.

The  $t$ -dependence of the measured LTSA together with the model calculations according to Ref. [Mül04] is shown in figure 8.6. The model  $B$  demonstrates good agreement with the measured amplitude  $A_{UL}^{\sin \phi}$ . A sizable contribution of sea quarks to the CFF  $\mathcal{H}$  can be seen in the case of the model  $B'$  that gives a somewhat large magnitude for the amplitude without sea quark GPDs. As it can be expected, the influence of the twist-three

GPDs on  $A_{UL}^{\sin\phi}$  is very small and the amplitudes predicted by models  $Bp$  and  $Bm$  are very close to the one of model  $B$ .

For the amplitude  $A_{UL}^{\sin 2\phi}$  the situation seems to be opposite. Sea quarks do not play an important role in this case. Although the model  $B$  predicts an amplitude with a sign opposite to that of the measured result, the contribution of the dynamical twist-three GPDs can have a sizable influence on the amplitude. Hence, despite the fact that twist-three effects are expected to be suppressed, this can give a sizable contribution to the  $\sin 2\phi$  amplitude. Still, the  $t$ -dependence of  $A_{UL}^{\sin 2\phi}$  shown by the data can not be reproduced by any version of this model, as it was the case for the model discussed before.

The  $x_B$ - and  $Q^2$ -dependences of the amplitudes  $A_{UL}^{\sin\phi}$  and  $A_{UL}^{\sin 2\phi}$  are compared with the model in figure 8.7. Similar to the case of the  $t$ -dependence, the amplitude  $A_{UL}^{\sin\phi}$  is in good agreement with the model predictions. The amplitude  $A_{UL}^{\sin 2\phi}$  in mostly tends to have opposite sign with respect to the model prediction.

## 8.2 Comparison with the CLAS Measurements

The latest results from the CLAS experiment (JLAB) [M<sup>+</sup>03] was reported recently (May 2006) on the single-spin asymmetry in DVCS with respect to the longitudinally polarized proton target [CABE06] (this asymmetry is also referred to as the LTSA). The azimuthal dependence of the LTSA was measured with an electron beam at 5.7 GeV beam energy. The average kinematics accessible by CLAS is  $\langle Q^2 \rangle = 1.82 \text{ GeV}^2$ ,  $\langle -t \rangle = 0.31 \text{ GeV}^2$  and  $\langle \xi \rangle = 0.16$  (for the  $\xi$ -definition see Eq. 2.7) which differs from that at HERMES  $\langle Q^2 \rangle = 2.5 \text{ GeV}^2$ ,  $\langle -t \rangle = 0.12 \text{ GeV}^2$  and  $\langle \xi \rangle = 0.05$ . In order to extract the amplitudes of the *sine* harmonics of the LTSA, its azimuthal dependence was fitted with a function  $\alpha \sin\phi + \beta \sin 2\phi$ , where the azimuthal angle  $\phi$  is defined as in this thesis in figure 3.3, but with an inverted sign. The extracted amplitudes  $\alpha = 0.252 \pm 0.042(\text{stat.}) \pm 0.020(\text{sys.})$  and  $\beta = -0.022 \pm 0.045(\text{stat.}) \pm 0.021(\text{sys.})$  correspond to the amplitudes reported in this thesis  $-A_{UL}^{\sin\phi} = 0.071 \pm 0.034(\text{stat.}) \pm 0.035(\text{sys.})$  and  $-A_{UL}^{\sin 2\phi} = 0.113 \pm 0.034(\text{stat.}) \pm 0.028(\text{sys.})$ , respectively. Note that the amplitudes measured by the two experiments are related to each other with inverted sign due to the difference in the definition of the angle  $\phi$ .

The amplitudes of the  $\sin\phi$  and  $\sin 2\phi$  harmonics of the LTSA measured at CLAS are different from those measured at HERMES. The magnitude of the amplitude  $\alpha$  tends to be bigger than that of  $A_{UL}^{\sin\phi}$ . The  $\sin 2\phi$  term  $\beta$  is consistent with zero, while the amplitude  $A_{UL}^{\sin 2\phi}$  measured at HERMES tends to be negative. The observed difference in the amplitudes can be

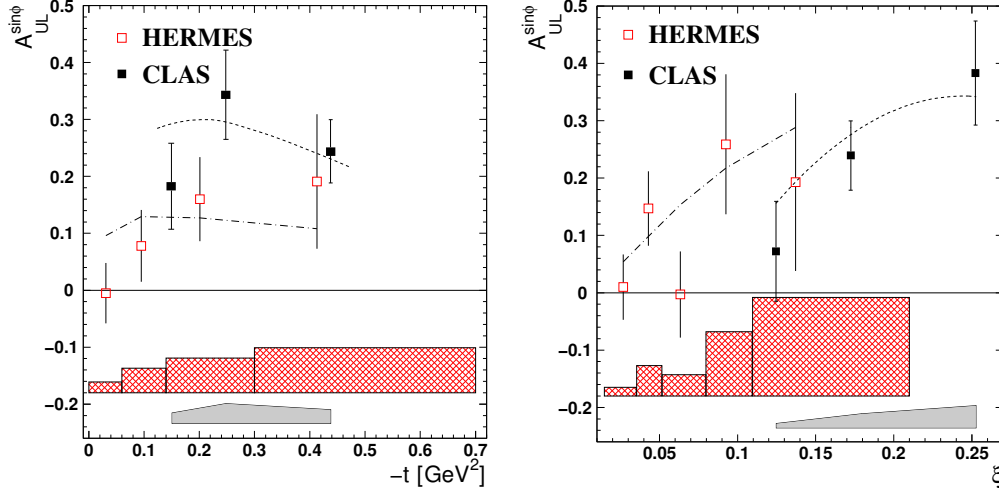


Figure 8.8: The  $\sin\phi$  amplitudes of the longitudinal target-spin asymmetry as functions of  $-t$  (left) and  $\xi$  measured at HERMES and CLAS. The measurements are compared with theoretical calculations [VGG01] using the  $\xi$ -dependent GPD parameterization ( $b_{val} = b_{sea} = 1$ ). The dash-dotted (dashed) lines correspond to the calculations at the HERMES (CLAS) kinematics. The CLAS measurements and the corresponding model calculations are reproduced from Ref. [CABE06].

presumably explained by the different kinematic domains accessible in the two experiments.

The  $t$ - and  $\xi$ -dependences of the  $\sin\phi$  amplitude measured by HERMES and CLAS are shown in figure 8.8. Also shown in figure 8.8 is the difference in the ranges in  $t$  and  $\xi$  accessible by the two experiments. The measurements are compared with calculations based on the phenomenological approach [GPV01] discussed in section 2.4 of this thesis. The code [VGG01] was used for calculations with similar settings of the main model parameters at the kinematics of both experiments. Note that the model calculations made using this code were already discussed in section 8.1 of this thesis. In case of the  $t$ -dependence the results of the measurements are consistent within statistical accuracy over the common  $t$ -region of both experiments. The model calculations, also shown in figure 8.8, demonstrate the difference in the magnitude of the  $\sin\phi$  amplitude at HERMES and CLAS kinematics due to the difference in corresponding  $\langle Q^2 \rangle$  and  $\langle \xi \rangle$  at these experiments. In case of the  $\xi$ -dependence the results of CLAS can be compared with those of HERMES only in the last  $\xi$ -bin of the  $\xi$ -region accessible by HERMES. In this  $\xi$ -bin the amplitudes measured by the two experiments are consistent.

Since no kinematic dependence is published by CLAS for the amplitude of the  $\sin 2\phi$  harmonic, only results at the average kinematics can be compared. As it can be seen in figure 8.8, the higher  $t$  values of the  $t$ -range accessible by HERMES correspond to the  $t$ -range of CLAS. In order to compare the  $\sin 2\phi$  amplitude at  $\langle -t \rangle$  similar for both experiments, the  $A_{UL}^{\sin 2\phi}$  amplitude was extracted for HERMES data in the  $t$ -range  $0.18 \text{ GeV}^2 < -t < 0.7 \text{ GeV}^2$  which corresponds to  $\langle -t \rangle = 0.30 \text{ GeV}^2$ . The corresponding average kinematics is  $\langle Q^2 \rangle = 3.2 \text{ GeV}^2$  and  $\langle \xi \rangle = 0.06$ . The  $\sin 2\phi$  amplitude measured at this kinematics is  $A_{UL}^{\sin 2\phi} = -0.149 \pm 0.074(\text{stat.})$ . The difference between this amplitude and that measured by CLAS is  $-0.171 \pm 0.076$  which is consistent with zero within 2.25 standard deviations.

The difference in the amplitudes of the *sine* harmonics at the average kinematics of the two experiments tends to be more sizable in case of the LTSA than in case of the BSA. The comparison of the BSA measurements made earlier by HERMES and CLAS shows better agreement between the corresponding amplitudes of the leading  $\sin \phi$  harmonics. The measured amplitudes  $\alpha = 0.202 \pm 0.021(\text{stat.}) \pm 0.013(\text{sys.})$  (CLAS) [S<sup>+</sup>01] and  $-A_{LU}^{\sin \phi} = 0.18 \pm 0.03(\text{stat.}) \pm 0.03(\text{syst.})$  (HERMES) [ESV03] agree within one standard deviation. Note that data used for the BSA measurements at CLAS were accumulated at the beam energy 4.5 GeV ( $\langle Q^2 \rangle = 1.25 \text{ GeV}^2$ ,  $\langle -t \rangle = 0.19 \text{ GeV}^2$  and  $\langle \xi \rangle = 0.1$ ) that differs from that for the LTSA measurements.

One of the possible reasons of the higher sensitivity of the LTSA to the kinematics of the two experiments than in case of the BSA can be the contributions of the kinematically suppressed GPDs to these asymmetries. The contribution of the GPD  $H$  ( $\widetilde{H}$ ) to the LTSA (BSA) is suppressed by a factor of  $\xi$  with respect to the GPD  $\widetilde{H}$  ( $H$ ) (see Eqs. 3.12 and 3.13). Since in case of the LTSA (BSA) measurements  $\langle \xi \rangle$  at CLAS is about 3 (2) times as big as that at HERMES, the contribution of the GPD  $H$  ( $\widetilde{H}$ ) to the LTSA (BSA) is less suppressed at CLAS than at HERMES. Due to the dominance of the unpolarized GPD  $H$  over the polarized GPD  $\widetilde{H}$ , the contribution of  $H$  to the LTSA is more sizable than that of  $\widetilde{H}$  to the BSA. Hence the LTSA is more sensitive to the kinematic difference between CLAS and HERMES.

$-t$ Bin (GeV <sup>2</sup> )	$\langle -t \rangle$ (GeV <sup>2</sup> )	$\langle x_B \rangle$	$\langle Q^2 \rangle$ (GeV <sup>2</sup> )	$A_{UL}^{\sin\phi} \pm \text{stat.} \pm \text{sys.}$
0.00 - 0.06	0.03	0.08	2.0	$0.005 \pm 0.053 \pm 0.019$
0.06 - 0.14	0.10	0.10	2.6	$-0.078 \pm 0.063 \pm 0.043$
0.14 - 0.30	0.20	0.11	2.9	$-0.160 \pm 0.074 \pm 0.061$
0.30 - 0.70	0.41	0.12	3.5	$-0.191 \pm 0.118 \pm 0.079$

$Q^2$ Bin (GeV <sup>2</sup> )	$\langle Q^2 \rangle$ (GeV <sup>2</sup> )	$\langle -t \rangle$ (GeV <sup>2</sup> )	$\langle x_B \rangle$	$A_{UL}^{\sin\phi} \pm \text{stat.} \pm \text{sys.}$
1.0 - 1.5	1.2	0.08	0.06	$-0.078 \pm 0.063 \pm 0.031$
1.5 - 2.3	1.9	0.10	0.08	$-0.023 \pm 0.064 \pm 0.042$
2.3 - 3.5	2.8	0.12	0.11	$-0.087 \pm 0.071 \pm 0.036$
3.5 - 6.0	4.4	0.17	0.15	$-0.086 \pm 0.087 \pm 0.044$
6.0 - 10.0	7.2	0.23	0.25	$-0.328 \pm 0.201 \pm 0.172$

$x_B$ Bin (GeV <sup>2</sup> )	$\langle x_B \rangle$	$\langle -t \rangle$ (GeV <sup>2</sup> )	$\langle Q^2 \rangle$ (GeV <sup>2</sup> )	$A_{UL}^{\sin\phi} \pm \text{stat.} \pm \text{sys.}$
0.03 - 0.07	0.05	0.10	1.4	$-0.010 \pm 0.057 \pm 0.015$
0.07 - 0.10	0.08	0.10	2.1	$-0.147 \pm 0.065 \pm 0.053$
0.10 - 0.15	0.12	0.12	3.1	$0.003 \pm 0.075 \pm 0.037$
0.15 - 0.20	0.17	0.17	4.3	$-0.259 \pm 0.122 \pm 0.112$
0.20 - 0.35	0.24	0.21	6.2	$-0.193 \pm 0.155 \pm 0.172$

Table 8.3: The amplitude  $A_{UL}^{\sin\phi}$  of the  $\sin\phi$  harmonic of the longitudinal target-spin asymmetry on the proton per kinematic bin in  $-t$ ,  $Q^2$  and  $x_B$  at the respective average kinematics.

$-t$ Bin (GeV <sup>2</sup> )	$\langle -t \rangle$ (GeV <sup>2</sup> )	$\langle x_B \rangle$	$\langle Q^2 \rangle$ (GeV <sup>2</sup> )	$A_{UL}^{\sin 2\phi} \pm \text{stat.} \pm \text{sys.}$
0.00 - 0.06	0.03	0.08	2.0	$-0.066 \pm 0.054 \pm 0.019$
0.06 - 0.14	0.10	0.10	2.6	$-0.118 \pm 0.063 \pm 0.030$
0.14 - 0.30	0.20	0.11	2.9	$-0.185 \pm 0.073 \pm 0.047$
0.30 - 0.70	0.41	0.12	3.5	$-0.104 \pm 0.118 \pm 0.055$

$Q^2$ Bin (GeV <sup>2</sup> )	$\langle Q^2 \rangle$ (GeV <sup>2</sup> )	$\langle -t \rangle$ (GeV <sup>2</sup> )	$\langle x_B \rangle$	$A_{UL}^{\sin 2\phi} \pm \text{stat.} \pm \text{sys.}$
1.0 - 1.5	1.2	0.08	0.06	$-0.080 \pm 0.064 \pm 0.034$
1.5 - 2.3	1.9	0.10	0.08	$-0.170 \pm 0.062 \pm 0.044$
2.3 - 3.5	2.8	0.12	0.11	$-0.063 \pm 0.073 \pm 0.021$
3.5 - 6.0	4.4	0.17	0.15	$-0.184 \pm 0.088 \pm 0.047$
6.0 - 10.0	7.2	0.23	0.25	$0.008 \pm 0.182 \pm 0.035$

$x_B$ Bin (GeV <sup>2</sup> )	$\langle x_B \rangle$	$\langle -t \rangle$ (GeV <sup>2</sup> )	$\langle Q^2 \rangle$ (GeV <sup>2</sup> )	$A_{UL}^{\sin 2\phi} \pm \text{stat.} \pm \text{sys.}$
0.03 - 0.07	0.05	0.10	1.4	$-0.059 \pm 0.057 \pm 0.013$
0.07 - 0.10	0.08	0.10	2.1	$-0.258 \pm 0.066 \pm 0.053$
0.10 - 0.15	0.12	0.12	3.1	$-0.100 \pm 0.073 \pm 0.035$
0.15 - 0.20	0.17	0.17	4.3	$-0.082 \pm 0.126 \pm 0.045$
0.20 - 0.35	0.24	0.21	6.2	$0.124 \pm 0.162 \pm 0.095$

Table 8.4: The amplitude  $A_{UL}^{\sin 2\phi}$  of the  $\sin 2\phi$  harmonic of the longitudinal target-spin asymmetry on the proton per kinematic bin in  $-t$ ,  $Q^2$  and  $x_B$  at the respective average kinematics.

$-t$ Bin (GeV <sup>2</sup> )	$\langle -t \rangle$ (GeV <sup>2</sup> )	$\langle x_B \rangle$	$\langle Q^2 \rangle$ (GeV <sup>2</sup> )	$A_{UL}^{\sin 3\phi} \pm \text{stat.}$
0.00 - 0.06	0.03	0.08	2.0	$0.038 \pm 0.053$
0.06 - 0.14	0.10	0.10	2.6	$0.006 \pm 0.063$
0.14 - 0.30	0.20	0.11	2.9	$-0.081 \pm 0.077$
0.30 - 0.70	0.41	0.12	3.5	$0.140 \pm 0.122$

$Q^2$ Bin (GeV <sup>2</sup> )	$\langle Q^2 \rangle$ (GeV <sup>2</sup> )	$\langle -t \rangle$ (GeV <sup>2</sup> )	$\langle x_B \rangle$	$A_{UL}^{\sin 3\phi} \pm \text{stat.}$
1.0 - 1.5	1.2	0.08	0.06	$0.059 \pm 0.063$
1.5 - 2.3	1.9	0.10	0.08	$-0.034 \pm 0.064$
2.3 - 3.5	2.8	0.12	0.11	$0.011 \pm 0.072$
3.5 - 6.0	4.4	0.17	0.15	$-0.040 \pm 0.089$
6.0 - 10.0	7.2	0.23	0.25	$0.274 \pm 0.204$

$x_B$ Bin (GeV <sup>2</sup> )	$\langle x_B \rangle$	$\langle -t \rangle$ (GeV <sup>2</sup> )	$\langle Q^2 \rangle$ (GeV <sup>2</sup> )	$A_{UL}^{\sin 3\phi} \pm \text{stat.}$
0.03 - 0.07	0.05	0.10	1.4	$0.076 \pm 0.057$
0.07 - 0.10	0.08	0.10	2.1	$-0.121 \pm 0.066$
0.10 - 0.15	0.12	0.12	3.1	$0.062 \pm 0.076$
0.15 - 0.20	0.17	0.17	4.3	$-0.040 \pm 0.122$
0.20 - 0.35	0.24	0.21	6.2	$0.080 \pm 0.170$

Table 8.5: The amplitude  $A_{UL}^{\sin 3\phi}$  of the  $\sin 3\phi$  harmonic of the longitudinal target-spin asymmetry on the proton per kinematic bin in  $-t$ ,  $Q^2$  and  $x_B$  at the respective average kinematics. The amplitude is extracted with the fit function defined in Eq. 7.10.



# Chapter 9

## Conclusions and Outlook

In this thesis the measurement of the single-spin asymmetry in the cross section of Deeply-Virtual Compton Scattering (DVCS) with respect to the polarization of a *longitudinally* polarized proton target is described for the first time. The asymmetry, also referred to as the Longitudinal Target Spin Asymmetry (LTSA), allows access to the Generalized Parton Distribution (GPD)  $\widetilde{H}$ . The amplitudes  $A_{UL}^{\sin\phi}$  and  $A_{UL}^{\sin 2\phi}$  of the corresponding harmonics of the azimuthal dependence of the asymmetry are sensitive to the twist-two and twist-three part of the GPD  $\widetilde{H}$ , respectively.

The LTSA is measured at average HERMES kinematics ( $\langle -t \rangle = 0.12$  GeV<sup>2</sup>,  $\langle x_B \rangle = 0.10$  and  $\langle Q^2 \rangle = 2.5$  GeV<sup>2</sup>) in the range  $-t < 0.7$  GeV<sup>2</sup>,  $0.03 < x_B < 0.35$  and  $1 \text{ GeV}^2 < Q^2 < 10 \text{ GeV}^2$ . The measured amplitudes  $A_{UL}^{\sin\phi}$  and  $A_{UL}^{\sin 2\phi}$  tend to be both negative. Although  $A_{UL}^{\sin 2\phi}$  is expected to be suppressed with respect to  $A_{UL}^{\sin\phi}$  by a factor of 0.2, the measured magnitude of  $A_{UL}^{\sin 2\phi}$  tends to be not smaller than that of  $A_{UL}^{\sin\phi}$ . This can be due to possible sea quark contributions to the latter, which are expected to reduce it.

The azimuthal dependence of the asymmetry on the variables  $-t$ ,  $x$ ,  $Q^2$  is measured as well. The results on the proton are compared with the results of the LTSA measurements on the deuteron from Ref. [KY<sup>+</sup>05]. In case of the  $t$ -dependence no difference is observed between proton and deuteron in the first  $t$ -bin, where a sizable contribution of coherent scattering on the deuteron is expected. For the other  $t$ -bins the azimuthal dependence of the LTSA tends to be different between proton and deuteron. This could be due to the contribution of the neutron to the incoherent scattering on the deuteron. The LTSA on the neutron is more sensitive to the GPD  $H$  than to  $\widetilde{H}$ , compared to the proton case.

The kinematic dependences of the LTSA on proton and deuteron are compared with theoretical calculations from Refs. [VGG01, Mül04]. The models

used in these calculations are based on the phenomenological approach developed in Refs. [GPV01, BMK02]. The calculations are done with and without skewness of the quarks, and with either the Regge-inspired or the factorized ansatz for the  $t$ -dependence. The amplitude  $A_{UL}^{\sin\phi}$  is found to be in good agreement with both model calculations. The skewness has a weak influence on the asymmetry. Due to limited statistics the data can not separate the ansatz of the  $t$ -dependence. The proton results of these calculations are less sensitive to the ansatz of the  $t$ -dependence because in the available models the GPD  $\widetilde{H}$  has only a factorized  $t$ -dependence.

The measured amplitude  $A_{UL}^{\sin 2\phi}$  tends to disagree with the model calculations that include only twist-two or Wandzura-Wilczek twist-three parts of GPDs. The difference could be due to that part of twist-three GPDs which is related to quark-gluon correlations in the nucleon and which is poorly known from the theoretical point of view, at the moment. The upper estimate for the full twist-three effects that contribute to the GPD  $\widetilde{H}$  is included in the model calculations in Ref. [Mül04]. Although in case of  $A_{UL}^{\sin 2\phi}$  also this model tends to disagree with the data, it demonstrates that the *dynamical* twist-three part of GPDs could be a possible explanation of the sizable amplitude  $A_{UL}^{\sin 2\phi}$  measured in this work. Hence more theoretical activity is needed in this direction.

The measured LTSA is compared with the measurement of the LTSA in DVCS on proton by the CLAS collaboration (JLAB) [CABE06]. The amplitudes of the  $\sin\phi$  and  $\sin 2\phi$  harmonics measured at average kinematics of CLAS tend to be different from those reported in this thesis. The possible difference can be due to the different kinematic regions accessible by the two experiments. The energy of the electron beam exploited by CLAS is much smaller than that used by HERMES. Due to this fact the mean  $\xi$  at CLAS is higher than that at HERMES, hence increasing the contributions of other GPDs to the LTSA, with respect to the case of HERMES kinematics. The  $-t$  and  $\xi$ -dependences of the  $\sin\phi$  amplitudes measured by both experiments, together with theoretical calculations based on the formalism from Ref. [GPV01], are compared. Although the calculations show differences in the amplitudes at the kinematics of HERMES and CLAS, in the kinematic regions of  $-t$  and  $\xi$  common for both experiments the measured amplitudes are consistent.

Since the recoiling proton was not detected in the data sample used for this analysis, the missing-mass technique is used for the selection of exclusive BH/DVCS events. Monte-Carlo studies are done in order to estimate the contribution of background processes to the measured asymmetry. Due to the finite spectrometer resolution, the contribution of associated production (excitation of nucleon resonances) to the selected sample is about 10%.

Semi-inclusive DIS and exclusive  $\pi^0$  production contribute at the level of 4% and 1%, respectively. Since presently nothing is known about the asymmetry of resonances produced in the DVCS process, their contribution to the measured asymmetry is included into the result. Exclusive and semi-inclusive  $\pi^0$  background is taken into account in the systematic uncertainty.

With a newly installed Recoil Detector (RD) [HER02] at HERMES most of the produced recoiling particles will be detected. This will strongly improve the event selection in BH/DVCS analyses. The contribution of associated production to the selected exclusive sample is expected to be reduced to 1% and that of semi-inclusive background to much less than 1% [Kra05]. Hence a clean event separation will allow to improve earlier HERMES measurements of beam-spin and beam-charge asymmetries [A<sup>+</sup>01a, Ell04]. The RD will be operated only with an unpolarized target. Since the RD is supposed to be used until the end of HERMES running, the LTSA measured in this analysis uses all the data with longitudinally polarized target ever accumulated at HERMES, and hence constitutes a final result.

The data with transverse target polarization taken in the period 2002-2005 allow to measure the transverse target-spin asymmetry at HERMES. It is expected to constrain the total angular momentum of  $u$  and  $d$ -quarks for the first time [ENVY05].



# Bibliography

- [A<sup>+</sup>88] Ashman, J.; et al. (EMC): A measurement of the spin asymmetry and determination of the structure function  $g_1$  in deep inelastic muon-proton scattering. In: *Phys. Lett.*, volume B206:p. 364, 1988.
- [A<sup>+</sup>98a] Ackerstaff, K.; et al. (HERMES): HERMES spectrometer. In: *Nucl. Instrum. Meth.*, volume A417:pp. 230–265, 1998. [hep-ex/9806008](#).
- [A<sup>+</sup>98b] Adeva, D.; et al. (SMC): Polarised quark distributions in the nucleon from semi-inclusive spin asymmetries. In: *Phys. Lett.*, volume B420:p. 180, 1998. [hep-ex/9711008](#).
- [A<sup>+</sup>98c] Avakian, H.; et al.: Performance of the electromagnetic calorimeter of the HERMES experiment. In: *Nucl. Instr. and Meth.*, volume A417:p. 69, 1998. [hep-ex/9810004](#).
- [A<sup>+</sup>99] Ackerstaff, K.; et al. (HERMES): Flavor decomposition of the polarized quark distributions in the nucleon from inclusive and semi-inclusive deep-inelastic scattering. In: *Phys. Lett.*, volume B464:p. 123, 1999. [hep-ex/9906035](#).
- [A<sup>+</sup>01a] Airapetian, A.; et al. (HERMES): Measurement of the beam-spin azimuthal asymmetry associated with deeply-virtual Compton scattering. In: *Phys. Rev. Lett.*, volume 87:p. 182001, 2001. [hep-ex/0106068](#).
- [A<sup>+</sup>01b] Andreev, A.; et al.: Multiwire proportional chambers in the HERMES experiment. In: *Nucl. Instrum. Meth.*, volume A465:pp. 482–497, 2001.
- [A<sup>+</sup>02] Akopov, N.; et al.: The HERMES dual-radiator ring imaging Cerenkov detector. In: *Nucl. Instrum. Meth.*, volume A479:pp. 511–530, 2002. [physics/0104033](#).

- [A<sup>+</sup>03] A.Airapetian; et al. (HERMES): Measurement of single-spin azimuthal asymmetries in semi-inclusive electroproduction of pions and kaons on a longitudinally polarized deuterium target. In: *Phys. Lett.*, volume B562:p. 182, 2003. [hep-ex/0212039](#).
- [A<sup>+</sup>05a] Airapetian, A.; et al. (HERMES): The HERMES polarized hydrogen and deuterium gas target in the HERA electron storage ring. In: *Nucl. Instrum. Meth.*, volume A540:pp. 68–101, 2005.
- [A<sup>+</sup>05b] Aktas, A.; et al. (H1): Measurement of deeply virtual Compton scattering at HERA. In: *Eur.Phys.J.*, volume C44:p. 1, 2005. [hep-ex/0505061](#).
- [ABR99] Akushevich, I.; Böttcher, H.; Ryckbosch, D.: RADGEN 1.0: Monte Carlo generator for radiative events in DIS on polarized and unpolarized targets. In: *Hamburg 1998/1999, Monte Carlo generators for HERA physics*. 1999. [hep-ph/9906408](#).
- [AEL95] Anselmino, M.; Efremov, A.; Leader, E.: The theory and phenomenology of polarized deep inelastic scattering. In: *Phys. Rept.*, volume 261:pp. 1–124, 1995. Erratum-ibid. **281**, 399 (1997), [hep-ph/9501369](#).
- [AGIS83] Anderson, B.; Gustafson, G.; Ingelman, G.; Sjöstrand, T.: Parton fragmentation and strings dynamics. In: *Phys. Rev.*, volume 97:p. 31, 1983.
- [AKM05] Afanasev, A.V.; Konchatnij, M.I.; Merenkov, N.P.: Single-spin asymmetries in the Bethe-Heitler process  $e^- + p \rightarrow e^- + \gamma + p$  from QED radiative corrections. 2005. [hep-ph/0507059](#).
- [B<sup>+</sup>78] Brasse, F. W.; et al.: Separation of sigma-L and sigma-T in eta - electroproduction at the resonance s11 (1535). In: *Nucl. Phys.*, volume B139:p. 37, 1978.
- [B<sup>+</sup>93] Barber, D. P.; et al.: The HERA polarimeter and the first observation of electron spin polarization at HERA. In: *Nucl. Instrum. Meth.*, volume A329:pp. 79–111, 1993.
- [B<sup>+</sup>94] Barber, D. P.; et al.: High spin polarization at the HERA electron storage ring. In: *Nucl. Instrum. Meth.*, volume A338:pp. 166–184, 1994.

- [B<sup>+</sup>98] Bernreuther, S.; et al.: The HERMES back drift chambers. In: *Nucl. Instrum. Meth.*, volume A416:pp. 45–58, 1998. [hep-ex/9803005](#).
- [B<sup>+</sup>01a] Benisch, T.; et al.: The luminosity monitor of the HERMES experiment at DESY. In: *Nucl. Instrum. Meth.*, volume A471:pp. 314–324, 2001.
- [B<sup>+</sup>01b] Brack, J. T.; et al.: The HERMES forward tracking chambers: Construction, operation, and aging effects. In: *Nucl. Instrum. Meth.*, volume A469:pp. 47–54, 2001.
- [B<sup>+</sup>02] Beckmann, M.; et al.: The longitudinal polarimeter at HERA. In: *Nucl. Instrum. Meth.*, volume A479:pp. 334–348, 2002. [physics/0009047](#).
- [Bec00] Beckmann, M.: *Extraction of polarised quark distributions of the nucleon from deep inelastic scattering at the HERMES experiment*. Ph.D. thesis, Albert-Ludwigs-Universität Freiburg, 2000. DESY-THESIS-2000-029.
- [Bec03] Beckmann, M.: Target polarisation values and their uncertainties used by the Deltaq analysis group for the 1996 to 2000 running periods. HERMES int. note 03-005, March 2003.
- [BM00] Belitsky, A.V.; Müller, D.: Twist-three effects in two-photon processes. In: *Nucl. Phys.*, volume B589:p. 611, 2000. [hep-ph/0007031](#).
- [BMK02] Belitsky, A.V.; Müller, D.; Kirchner, A.: Theory of deeply virtual compton scattering on the nucleon. In: *Nucl. Phys.*, volume B629:p. 323, 2002. [hep-ph/0112108](#).
- [BMT59] Bargmann, V.; Michel, L.; Telegdi, V. L.: Precession of the polarization of particles moving in a homogeneous electromagnetic field. In: *Phys. Rev. Lett.*, volume 2:p. 435, 1959.
- [BS86] Buon, J.; Steffen, K.: HERA variable energy 'mini' spin rotator and headon e p collision scheme with choice of electron helicity. In: *Nucl. Instr. Meth.*, volume A245:p. 248, 1986.
- [C<sup>+</sup>03] Chekanov, S.; et al. (ZEUS): Measurement of deeply virtual Compton scattering at HERA. In: *Phys. Lett.*, volume B573:p. 46, 2003. [hep-ex/0305028](#).

- [CABE06] Chen, S.; Avakian, H.; Burkert, V.; Eugenio, P. (the CLAS): Measurement of deeply virtual Compton scattering with a polarized proton target, May 2006. [hep-ex/0605012](#).
- [CER93] CERN-Computing and Networks Division: GEANT - detector description and simulation tool. In: *CERN Program Library Long Writeup*, volume W5013, 1993. URL <http://wwwasdoc.web.cern.ch/wwwasdoc/geant/geantall.html>.
- [CER94] CERN-Computing and Networks Division: MINUIT - users guide. In: *CERN Program Library Long Writeup*, volume D506, Jan 1994. URL <http://wwwasdoc.web.cern.ch/wwwasdoc/minuit/minmain.html>.
- [CF99] Collins, J.C.; Freund, A.: Proof of factorization for deeply virtual Compton scattering in QCD. In: *Phys. Rev.*, volume D59:p. 074009, 1999. [hep-ph/9801262](#).
- [Col77] Collins, P.D.B.: *An introduction to Regge theory and high-energy physics*. Cambridge University Press, 1977.
- [Dia98] Diakonov, D.: Chiral quark-soliton model. In: *Peniscola 1997, Advanced school on non-perturbative quantum field physics*. 1998. [hep-ph/9802298](#).
- [Die03] Diehl, M.: Generalized parton distributions. In: *Phys. Rep.*, volume 388:p. 41, 2003. Habilitation thesis: DESY-THESIS-2003-018, [hep-ph/0307382](#).
- [DS05] Diehl, M.; Sapeta, S.: On the analysis of lepton scattering on longitudinally or transversely polarized protons. In: *Eur.Phys.J.*, volume C41:p. 515, 2005. [hep-ph/0503023](#).
- [Dür95] Düren, M.: The HERMES experiment: From the design to the first results. In: *Hamburg DESY - Int.Rep.HERMES-95-02*, 1995. Habilitation thesis.
- [E<sup>+</sup>01] Ent, R.; et al.: Radiative corrections for  $(e, e'p)$  reactions at GeV energies. In: *Phys. Rev.*, volume C64:p. 054610, 2001.
- [Ell04] Ellinghaus, F.: *Beam-Charge and Beam-Spin Azimuthal Asymmetries in Deeply-Virtual Compton Scattering*. Ph.D. thesis, Humboldt-Universität zu Berlin, Feb 2004. DESY-THESIS-2004-005.



- [Ely02] Ely, J. H.: *Measurement of the single spin azimuthal asymmetry in the predominantly exclusive electroproduction of photons from the proton*. Ph.D. thesis, Colorado University, 2002. UMI-30-57756.
- [ENVY05] Ellinghaus, F.; Nowak, W. D.; Vinnikov, A. V.; Ye, Z.: Can the total angular momentum of u-quarks in the nucleon be accessed at HERMES? 2005. Acc. by EPJC, [hep-ph/0506264](#).
- [ESV03] Ellinghaus, F.; Shanidze, R.; Volmer, J. (HERMES): Deeply-virtual compton scattering on deuterium and neon at hermes. In: *AIP Conf. Proc.*, volume 675:pp. 303–307, 2003. [hep-ex/0212019](#).
- [FB<sup>+</sup>97] Fallot-Burghardt, W.; et al.: *HELIX128-x User Manual*. ASIC Labor Heidelberg, 1997. HD-ASIC-33-0697, URL <http://wwwasic.kip.uni-heidelberg.de/~trunk/projects/Helix/helix/helix.html>.
- [FMS03] Freund, A.; McDermott, M.F.; Strikmann, M.: Modelling generalized parton distributions to describe deeply virtual Compton scattering data. In: *Phys. Rev.*, volume D70:p. 036001, 2003. [hep-ph/0208160](#).
- [FPS98] Frankfurt, L.L.; Polyakov, M.V.; Strikman, M.:  $N$  to  $\Delta$ , exclusive DIS processes and skewed quark distributions at large  $N_c$  limit. 1998. [hep-ph/9808449](#).
- [GKW<sup>+</sup>02] Gregor, I.M.; Kopytin, M.; W.Lange; M.Reinecke; C.Shearer; J.Stewart; A.Vandenbroucke: Test-beam results of the first prototype for the HERMES silicon recoil detector. HERMES int. note 02-053, Dec 2002.
- [GMV03] Guichon, P.A.M.; Mosse, L.; Vanderhaegen, M.: Pion production in deeply virtual Compton scattering. In: *Phys. Rev.*, volume D68:p. 034018, 2003. [hep-ph/0305231](#).
- [GPV01] Goeke, K.; Polyakov, M.V.; Vanderhaegen, M.: Hard exclusive reactions and the structure of hadrons. In: *Prog. Part. Nucl. Phys.*, volume 47:p. 401, 2001. [hep-ph/0106012](#).
- [GS96] Gehrmann, T.; Stirling, W. James: Polarized parton distributions in the nucleon. In: *Phys. Rev.*, volume D53:pp. 6100–6109, 1996. [hep-ph/9512406](#).

- [Had04] Hadjidakis, C.: Sept 2004. Private Communication.
- [HER02] HERMES Collaboration: The HERMES recoil detector. In: *DESY-PRC 02-01*, 2002. HERMES int. note 02-003.
- [HMG<sup>+</sup>05] Hristova, I.; Murray, M.; Gregor, I.M.; Nowak, W.D.; Reinecke, M.; Stewart, J.; Vandenbroucke, A.: HERMES recoil silicon detector calibration to MIPs at T22 at DESY. HERMES int. note 05-014, April 2005.
- [IER97] Ingelman, G.; Edin, A.; Rathsman, J.: LEPTO 6.5 - a Monte Carlo generator for deep inelastic lepton-nucleon scattering. In: *Comput. Phys. Commun.*, volume 101:p. 108, 1997. [hep-ph/9605286](#).
- [Ji97a] Ji, X.: Deeply virtual compton scattering. In: *Phys. Rev.*, volume D55:p. 7114, 1997. [hep-ph/9609381](#).
- [Ji97b] Ji, X.: Gauge-invariant decomposition of nucleon spin and its spin-off. In: *Phys. Rev. Lett.*, volume 78:p. 610, 1997. [hep-ph/9603249](#).
- [Ji98] Ji, X.: Off-forward parton distributions. In: *J.Phys.*, volume G24:p. 1181, 1998. [hep-ph/9807358](#).
- [JM97] Ji, X.; Melnitchouk, W.: Spin-dependent twist-four matrix elements from  $g_1$  data in the resonance region. In: *Phys. Rev.*, volume D56:p. 1, 1997. [hep-ph/9703363](#).
- [Kai97] Kaiser, R.: Particle identification at HERMES. HERMES int. note 97-025, 1997.
- [KGL<sup>+</sup>05] Kopytin, M.; Gregor, I.; Lange, W.; Nowak, W.D.; Reinecke, M.; Stewart, J.; Vandenbroucke, A.: HELIX128-3.0 production tests. HERMES int. note 05-002, Jan 2005.
- [KLS<sup>+</sup>02] Kopytin, M.; Lange, W.; Shearer, C.; Stewart, J.; Vandenbroucke, A.: Decision on the readout chip for the new HERMES silicon recoil detector. HERMES int. note 02-020, June 2002.
- [KM03] Kirchner, A.; Müller, D.: deeply virtual Compton scattering off nuclei. In: *Eur. Phys. J.*, volume C32:p. 347, 2003. [hep-ph/0302007](#).

- [KN02] Korotkov, V.A.; Nowak, W.-D.: Future measurements of deeply virtual Compton scattering at HERMES. In: *Eur. Phys. J.*, volume C23:p. 455, 2002. [hep-ph/0108077](#).
- [Kop05] Kopytin, M. (HERMES): Measurement of deeply virtual Compton scattering at HERMES. In: *AIP Conf. Proc.*, volume 792:pp. 424–427, 2005. DEEP INELASTIC SCATTERING: 13th International Workshop on Deep Inelastic Scattering; DIS 2005.
- [Kor05] Korotkov, V.: March 2005. Private Communication.
- [Kra05] Krauss, B.: *Deeply-Virtual Compton Scattering and HERMES-Recoil-Detector*. Ph.D. thesis, Friedrich-Alexander-Universität Erlangen-Nürnberg, February 2005. DESY-THESIS-2005-008.
- [KY<sup>+</sup>05] Kopytin, M.; Ye, Z.; et al.: Longitudinal target-spin asymmetry from DVCS process on longitudinally polarized proton and deuterium targets. HERMES release report, April 2005.
- [LW ] LW group: *Lambda Wheels online manual*. NIKHEF, Netherlands. URL [http://www.nikhef.nl/pub/experiments/Hermes/Instrumentation/LambdaWheels/Descriptions\\_Manuals/begin.html](http://www.nikhef.nl/pub/experiments/Hermes/Instrumentation/LambdaWheels/Descriptions_Manuals/begin.html).
- [M<sup>+</sup>94] Mueller, D.; et al.: Wave functions, evolution equations and evolution kernels from light-ray operators of QCD. In: *Fortsch. Phys.*, volume 42:p. 101, 1994. [hep-ph/9812448](#).
- [M<sup>+</sup>03] Mecking, B. A.; et al. (CLAS): The CEBAF large acceptance spectrometer (CLAS). In: *Nucl. Instrum. Meth.*, volume A503:pp. 513–553, 2003.
- [MSV92] Mankiewicz, L.; Schafer, A.; Veltri, M.: PEPSI - a Monte Carlo generator for polarized leptonproduction. In: *Comput. Phys. Commun.*, volume 71:p. 305, 1992.
- [MT69] Mo, L.W.; Tsai, Y.-S.: Radiative corrections to elastic and inelastic  $ep$  and  $\mu p$  scattering. In: *Rev. Mod. Phys.*, volume 41:p. 205, 1969.
- [Mül04] Müller, D.: Nov. 2004. Private Communication.
- [Nar02] Nardo, L. De: *Measurement of the Structure Function  $g_1^d$  at HERMES and Extraction of Polarized Parton Distributions*. Ph.D. thesis, University of Alberta, 2002.

- [Now05] Nowak, W.-D.: Deeply virtual Compton scattering: results & future. In: *Hadron Physics 13 Topical Workshop, St. Andrews, Scotland, Sep 2004*. 2005. DESY-05-033, [hep-ex/0503010](#).
- [P<sup>+</sup>98] Petrov, V.; et al.: Off-forward quark distributions of the nucleon in the large  $N_c$  limit. In: *Phys. Rev.*, volume D57:p. 4325, 1998. [hep-ph/9710270](#).
- [Pic05] Pickert, N. (HERMES): The HERMES recoil detector: A combined silicon strip and scintillating fiber detector for tracking and particle identification. In: *HEP-EPS 2005*. Jul 2005. DESY-HERMES-05-41.
- [PPG00] Penttinen, M.; Polyakov, M.V.; Goeke, K.: Helicity skewed quark distributions of the nucleon and chiral symmetry. In: *Phys. Rev.*, volume D62:p. 014024, 2000. [hep-ph/9909489](#).
- [R<sup>+</sup>04] Reinecke, M.; et al.: A silicon strip recoil detector for momentum measurement and tracking at hermes. In: *IEEE Trans. Nucl. Sci.*, volume 51:pp. 1111–1116, 2004.
- [Rad96] Radyushkin, A.V.: Asymmetric gluon distributions and hard diffractive electroproduction. In: *Phys. Lett.*, volume B385:p. 333, 1996. [hep-ph/9605431](#).
- [Rad01] Radyushkin, A.V.: Generalized parton distributions, 2001. [hep-ph/0101225](#).
- [S<sup>+</sup>75] Stein, S.; et al.: Electron scattering at 4-degrees with energies of 4.5-gev - 20-gev. In: *Phys. Rev.*, volume D12:p. 1884, 1975.
- [S<sup>+</sup>01] Stepanyan, S.; et al. (CLAS): First observation of exclusive deeply virtual Compton scattering in polarized electron beam asymmetry measurements. In: *Phys. Rev. Lett.*, volume 87:p. 182002, 2001. [hep-ex/0107043](#).
- [Sch02] Schill, C.: *Azimutale Asymmetrien von Pionen und Kaonen bei der tiefinelastischen Elektron-Deuteron Streuung*. Ph.D. thesis, Albert-Ludwigs-Universität Freiburg, 2002.
- [Sjö94] Sjöstrand, T.: High-energy physics event generation with PHYTHIA 5.7 and JETSET 7.4. In: *Comput. Phys. Commun.*, volume 82:p. 74, 1994.

- [ST64] Sokolov, A.A.; Ternov, I.M.: On polarization and spin effects in the theory of synchrotron radiation. In: *Sov. Phys. Doklady*, volume 8:p. 1203, 1964.
- [V<sup>+</sup>00] Vanderhaeghen, M.; et al.: QED radiative corrections to virtual Compton scattering. In: *Phys. Rev.*, volume C62:p. 025501, 2000. [hep-ph/0001100](#).
- [Vel03] Velthuis, J.J.: *Radiation hardness of the ZEUS MVD frontend chip and strangeness production in ep scattering at HERA*. Ph.D. thesis, Universiteit van Amsterdam, March 2003.
- [VGG01] Vanderhaeghen, M.; Guichon, P.A.M.; Guidal, M.: Computer code for the calculation of DVCS and BH processes in the reaction  $ep \rightarrow ep\gamma$ , 2001. Private Communication.
- [Wan97] Wander, W.: *Reconstruction of High Energy Scattering Events in the HERMES Experiment*. Ph.D. thesis, Friedrich-Alexander-Universität Erlangen-Nürnberg, June 1997.
- [Wen03] Wendland, J.: *Polarized parton distributions measured at the HERMES experiment*. Ph.D. thesis, Simon Fraser University, 2003. DESY-THESIS-2003-032.
- [Y<sup>+</sup>05] Ye, Z.; et al.: Target spin asymmetry from DVCS process on transversely polarised proton target. HERMES release report, June 2005.
- [Ye05] Ye, Z.: May 2005. Private Communication.



## Appendix A

# HELIX128 3.0 Production Tests

A silicon recoil detector (see figure A.1) is presently being commissioned at the HERMES experiment [HER02]. The main goal of the detector is to detect and to measure the energy deposited by recoiling protons that originate from exclusive processes like Deeply Virtual Compton Scattering or meson production (see details in section 4.6). The detector contains 8 detector modules positioned around the target cell inside of the HERA beam vacuum. Every silicon detector module contains two silicon sensors of the

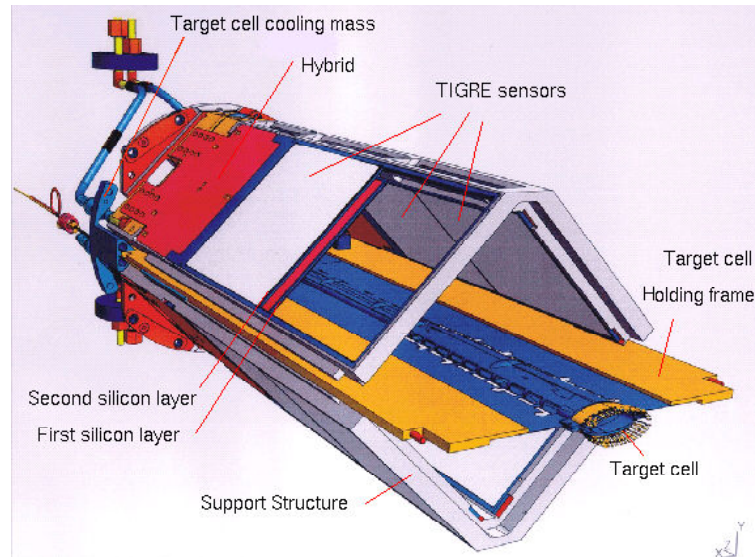


Figure A.1: HERMES Silicon Recoil Detector

TIGRE design produced by MICRON Semiconductors Ltd. The sensors are 300  $\mu\text{m}$  thick,  $99 \times 99 \text{ mm}^2$  double-sided silicon strip detectors with a readout pitch of 758  $\mu\text{m}$  and 128 readout channels per side. The silicon detector is designed to detect protons within the momentum range from 0.1 GeV/c to 1.5 GeV/c that corresponds to the dynamic range of the energy deposited in the silicon of 1 - 70 Minimum Ionizing Particles (MIPs).

The HELIX128 3.0 chip was chosen as frontend electronics for the silicon sensor readout [KLS<sup>+</sup>02]. The dynamic range of the HELIX chip is not sufficient for proton detection within the desired momentum range. A charge division method was proposed to be used in order to fit the dynamic range requirement [HER02]. The charge from the silicon sensor is shared between a high and a low gain chip. The high gain chip gets most of the charge and is needed to measure particles whose deposited energy in the sensor is up to 20 times the amount deposited by a MIP. For lower energy particles this chip is saturated and the low gain chip that gets a smaller fraction of the deposited charge is used. This method was proven to be functional for the first HERMES silicon recoil detector prototype [GKW<sup>+</sup>02], and it was implemented to the final detector as well [HMG<sup>+</sup>05].

Because of the charge division lay-out the number of readout channels is doubled. It results in 512 readout channels (4 HELIX chips) per module side and 8192 channels (64 HELIX chips) for the whole silicon detector. On each side of the silicon module the chips are daisy chained (4 chips) in order to reduce the number of readout lines (1 readout line instead of 4). The total number of required chips for the HERMES silicon recoil project is 104. It includes 64 chips for the final detector readout plus 40 spare. These chips were selected out of 6 wafers. Each wafer contains approximately 62 chips to be tested.

Because of various possible production defects the chips can not be used for the final detector without a full check of their functionality. This appendix describes the procedure of chip selection, according to certain test and quality criteria. The HELIX chip has been used by other experiments before. But the unique design of the HERMES silicon recoil detector brings additional requirements to the chip selection: The large sensor pitch requires that all chip channels are fully functioning and the energy measurement requires a uniform response to the injected charge over the channels.

The structure of this appendix is as follows. A short overview of the silicon detector module is given in section A.1. The HELIX chip is described in section A.2. The requirements to the chip are described in two sections, the first one is about the test method (section A.3) and the other one about the analysis of the chip's response (section A.5). The test procedure and the production test stand are described in section A.4. Chip sorting is discussed



in section A.6.

## A.1 Layout of the Silicon Module Control

Every silicon detector module is connected through the Analog Clock Control (ACC) module with the HeLix Control Unit (HLCU) and the Helix ADC (HADC) (see figure A.2).

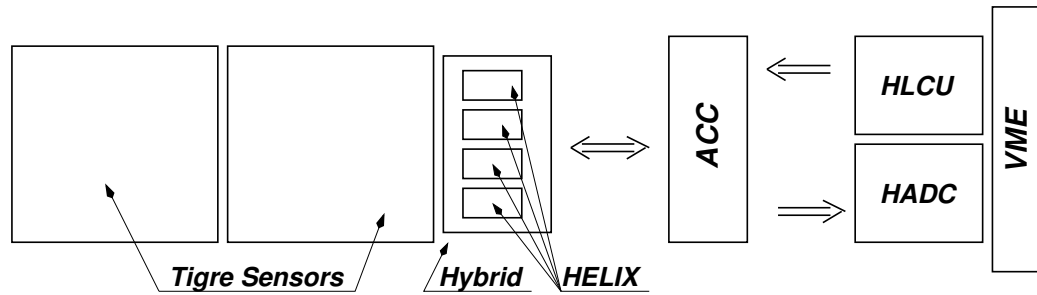


Figure A.2: Schematic diagram of the silicon module control sequence. The module contains 8 chips for readout, 4 chips per side.

The two silicon sensors of the module have 512 channels to be read out. Because of the charge division layout the number of the readout channels doubles, resulting in 1024 channels for one module.

The frontend readout chip HELIX128 3.0 has 128 input channels. For reading out one module 8 chips are needed. The readout of the sensor's p-side and n-side is done via 4 daisy chained chips on every side. Every daisy chain of chips is mounted on a separate circuit carrier, the so-called hybrid. The hybrid is needed to distribute power, control and token signals among the chained chips. It contains line drivers, pitch adaptor and charge division capacitors. The hybrid is vacuum compatible and it was designed at DESY especially for this project [R<sup>+</sup>04].

HLCU and HADC are VME modules. They were designed at NIKHEF for the control and readout of the HELIX chips [LW]. The HLCU supplies the module with all the necessary clock and control signals. One HLCU channel is needed for the module control. Every of eight chips of the module has a unique address that allows the HLCU to access every chip separately. The HADC digitizes the HELIX output. Additionally it can perform online zero suppression and signal correction (see details in section A.5.1).

The ACC module is a repeater. It provides an interface for long signal cables which will be used in the final setup.

## A.2 HELIX128 3.0

The HELIX128 3.0 [FB<sup>+</sup>97] was designed by the ASIC laboratory of Heidelberg University and manufactured in the 0.8  $\mu\text{m}$  CMOS process by Austria Mikrosysteme International GmbH. The chip contains 128 channels, each of them (see figure A.3) has a charge sensitive preamplifier, followed by a shaper whose output is sampled with the sampling clock  $Rclk$  into an analog memory with 136 cells. The memory stores the charge until the *trigger* signal arrives. Once the *trigger* arrives, the slice of the memory, which is defined by

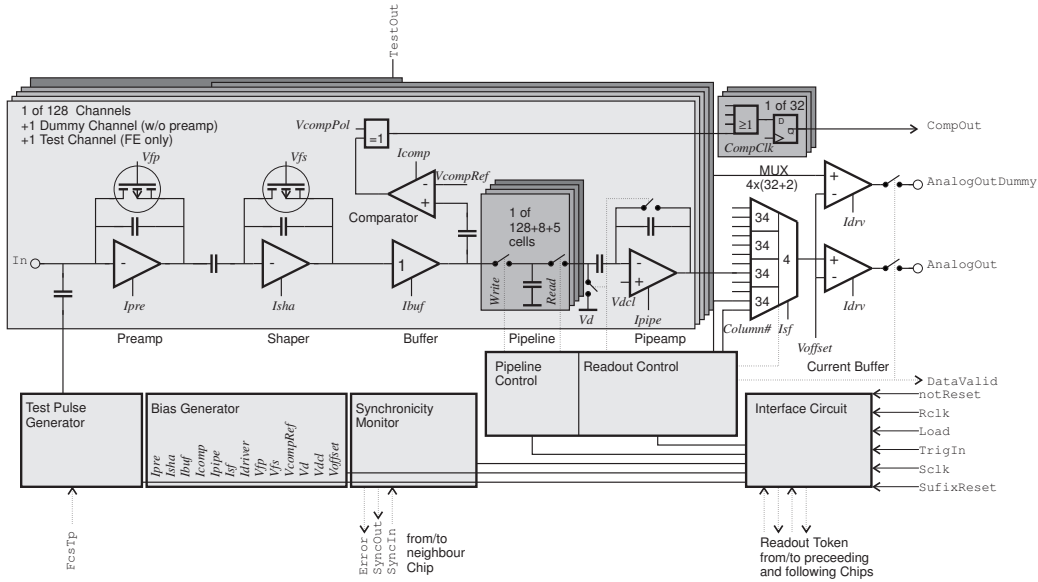


Figure A.3: Schematic diagram of the HELIX128 chip

a programmable chip parameter *latency*, is read out. The parameter *latency* defines the number of  $Rclk$  clocks between the moment the event happened and the moment when the *trigger* signal was received by the chip.

For all 128 channels of the chip the analog data from the selected memory slice are transferred via a multiplexer to a serial readout line. The output signal is synchronized with a readout clock  $Rclk$  (figure A.4). After the chain of 128 analog output values a sequence of 8 digital ones follows, referred to as *trailer*. This is digital information that contains the binary address of the triggered memory slice. Altogether the chip's output is a sequence of 136

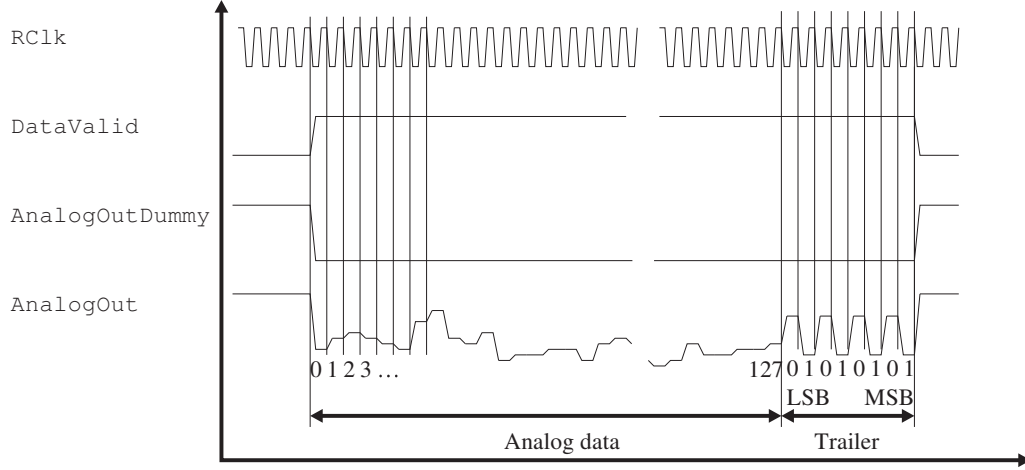


Figure A.4: Schematics of the HELIX serial readout.

values (128 analog + 8 digital values, not to be mixed up with the number of memory slices) and it is referred to as *AnalogOut*.

In order to reduce the sensitivity of the output signal to the chip's internal fluctuations there exists an additional channel which has no input. This extra channel has a complete electronic chain apart from the preamplifier. The signal from this channel, referred to as *AnalogDummyOut*, is read out in parallel to the other channels. It can be subtracted from the *AnalogOut* signal in order to cancel the signal's fluctuations generated by the chip.

Over the chip's output the logic signal *DataValid* is generated. Since the multiplexer gives an uncertainty in the readout moment of up to 4 clock cycles, the chip's output is not synchronized with the event trigger. Hence the signal *DataValid* can be used as a trigger for the readout system.

Several HELIX128 chips can be daisy-chained in order to use one serial line for their output readout. The output synchronization is done via a set of readout tokens sent between chips in the daisy chain (see figure A.5). The right side tokens (*HTI*, *RTO*,  $\overline{RTO}$ ) stand for communication with the previous chip in the daisy chain and the left side tokens (*HTO*, *RTI*,  $\overline{RTI}$ ) stand for communication with the next chip. For the last chip in the chain *HTO*, *RTI* must be either short cut or for the chip versions 3.0 or higher the chip must be programmed as the last one in order to get the daisy chain running.

A special feature of the HELIX128-3.0 version is a failsafe mechanism that allows to exclude broken chips from the readout chain (e.g. the central chip on figure A.5). This is implemented via introduction of a second set of

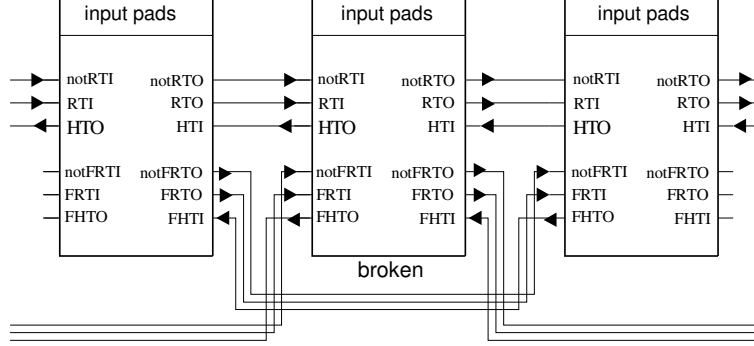


Figure A.5: Schematics of the HELIX daisy chain tokens and fail safe tokens. For the broken chip, fail safe tokens of the next and the previous chips are used. In this case the broken chip is excluded from the readout in order to keep the chain running.

synchronization tokens ( $FHTO$ ,  $FRTI$ ,  $\overline{FRTI}$  and  $FHTI$ ,  $FHTO$ ,  $\overline{FHTO}$ ) that can be switched on separately for the left or the right side, in order to leave out the next or the previous (faulty) chip.

A set of programmable DAC registers allows to adjust the analog characteristics of the chip. This makes it possible to select the most appropriate operating point for the chip and reduce the negative effects of radiation damage. Additionally, a set of programmable registers is available for the chip's timing adjustment (e.g. *latency* sets the number of clock cycles between the moment the event was acquired and the moment of the system trigger decision). In order to program the chip's parameters, the chip must be switched to a programmable mode by a *serial load* ( $Sload$ ) signal. The chip's address, the register's code and the register's setting are sent in series as a sequence of digital signals through the line of the *trigger* signal. Six address pads can be used to set the individual addresses for up to 64 chips.

For testing of the chip's amplification stages, the HELIX can work in the Test Pulse (TP) mode. With the rising edge of an externally supplied signal (called TP signal) the charge equivalent to

- +2 MIP is injected into channels 1, 5, 9 ...
- +1 MIP is injected into channels 2, 6, 10 ...
- -1 MIP is injected into channels 3, 7, 11 ...
- -2 MIP is injected into channels 4, 8, 12 ...

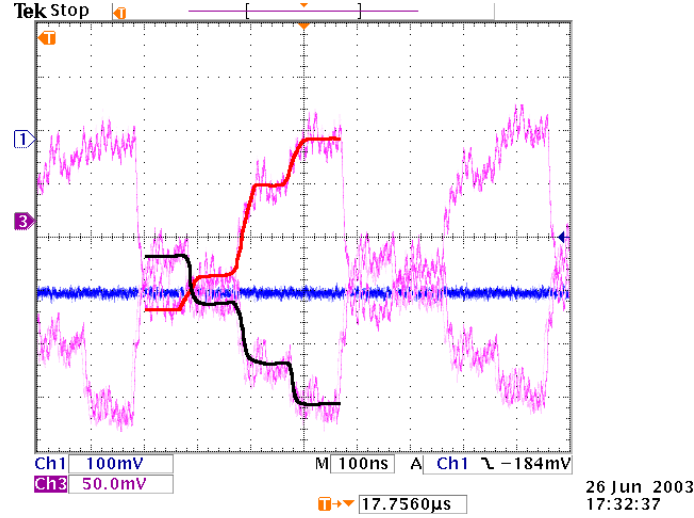


Figure A.6: Oscilloscope picture of the chip’s test pulse output for two TP signal cycles. The output signal has a stair case shape that correspond to the shape of the injected charge. For every next TP cycle the chip’s response swaps the charge.

with 1 MIP being the charge equivalent to that produced by a Minimum Ionizing Particle (MIP) traversing a silicon layer of  $300\text{ }\mu\text{m}$  thickness (the most probable amount of deposited charge is  $24.000\text{ }e^-$ ). With every next incoming TP signal the polarity of the injected charge is swapped. In the TP mode the chip’s output looks like a stair case that goes up or down with every new externally supplied TP signal (see figure A.6).

The comparator circuit implemented in the chip for the fast trigger option is beyond the scope of this work because this feature is be used in the HERMES recoil silicon detector.

## A.3 Test Method

Being an advanced electronic device the HELIX chip has a big variety of parameters that must be checked before the chip can be used. The production test procedure and chip selection criteria were developed based on test results of the first 30 chips. The test procedure was done in two steps. First, the online chip tests were performed and data were taken to test the chip’s analog signal properties offline. This section describes the test method for those chip parameters that can be checked online. Then an offline analysis of the taken data was performed, which will be discussed in section A.5.

### A.3.1 Programming of the Chip's Registers

In total 17 DAC registers allow to control the chip's performance. They can be divided into two groups. The first and the largest group is a set of DACs that controls the chip's behavior through all the amplification stages. The second group controls the chip's communication within the daisy chain. The test methods for these two groups are different.

#### DAC Registers

Out of 17 chip registers 12 ones control the analog signal characteristics, namely *Ipre*, *Isha*, *Ibuf*, *Icomp*, *Ipipe*, *Isf*, *Idriver*, *Vfp*, *Vfs*, *Vd*, *Vdcl* and *Voffset*. There are several methods to check the proper register programming and DAC settings. Their advantages and disadvantages are discussed below:

- i) Measurements of output voltage levels of the DACs (the corresponding pads are available on the chip).
  - + the most direct and simple method to check the DAC settings.
  - long cables and a voltmeter are needed, bringing additional noise and instability to the system.
  - most of the pads are located in the central part of the chip. That makes the probability for an accidental chip scratch too high.
- ii) Signal offline analysis for the default register settings.
  - + No additional hardware is needed.
  - Since data for at least two settings of every register must be taken, the test time of every chip increases drastically. The amount of stored information and the complexity of the offline analysis increases as well.
- iii) Power consumption measurements.
  - + Almost no additional influence on the system.
  - Not all the DAC registers can be checked via this method.

Method i) was rejected because of the technical problems mentioned above. A combination of methods ii) and iii) was used for checking DAC settings. The signal analysis is a general method of the overall control of the chip functionality and it is described later in section A.5. It was used as a cross check to the power consumption method.

Register	Register setting		Default
	Min. Current	Max. Current	
<i>Ipre</i>	not reliable		80
<i>Isha</i>	20	220	40
<i>Ibuf</i>	10	220	40
<i>Icomp</i>	10	210	40
<i>Ipipe</i>	10	220	32
<i>Isf</i>	10	220	40
<i>Idriver</i>	10	220	36
<i>Vfp</i>	not sensitive		142
<i>Vfs</i>	not sensitive		208
<i>VcompRef</i>	not needed		—
<i>Vref</i>	220	10	142
<i>Vd</i>	not sensitive		80
<i>Vdcl</i>	10	220	186
<i>Voff</i>	not sensitive		186

Table A.1: Register settings for the maximum and minimum chip's power consumption for the power line +2 V. The last column shows the default settings of the chip registers.

The settings of the chip's registers influence the chip's behavior and its power consumption. With a DC meter connected to the power line +2 V the difference between the maximum and minimum power consumption of the chip was measured for every register (while the other registers were programmed to their default values) in order to make a decision on the proper functionality of the register's DAC. Settings of the chip's registers for the maximum and minimum power consumption were determined from the measurements of the first 30 tested chips, where every register was scanned over its DAC setting range (from 0 to 220) with a step of 10 (see figure A.7). The results of the measurements together with chip's default settings are given in table A.1.

As it follows from the power scan results, the method can not be used for the registers *Ipre*, *Vfp*, *Vfs*, *Vd* and *Voff*. Those need a special treatment:

***Ipre*** The chip was switched into TP mode and *Ipre* was set to 1 (minimal register value). In this case the chip's preamplifiers do not work and only pedestal levels are at the chip's output. The absence of the TP at the chip's output was used as a criterion for the proper register programming.

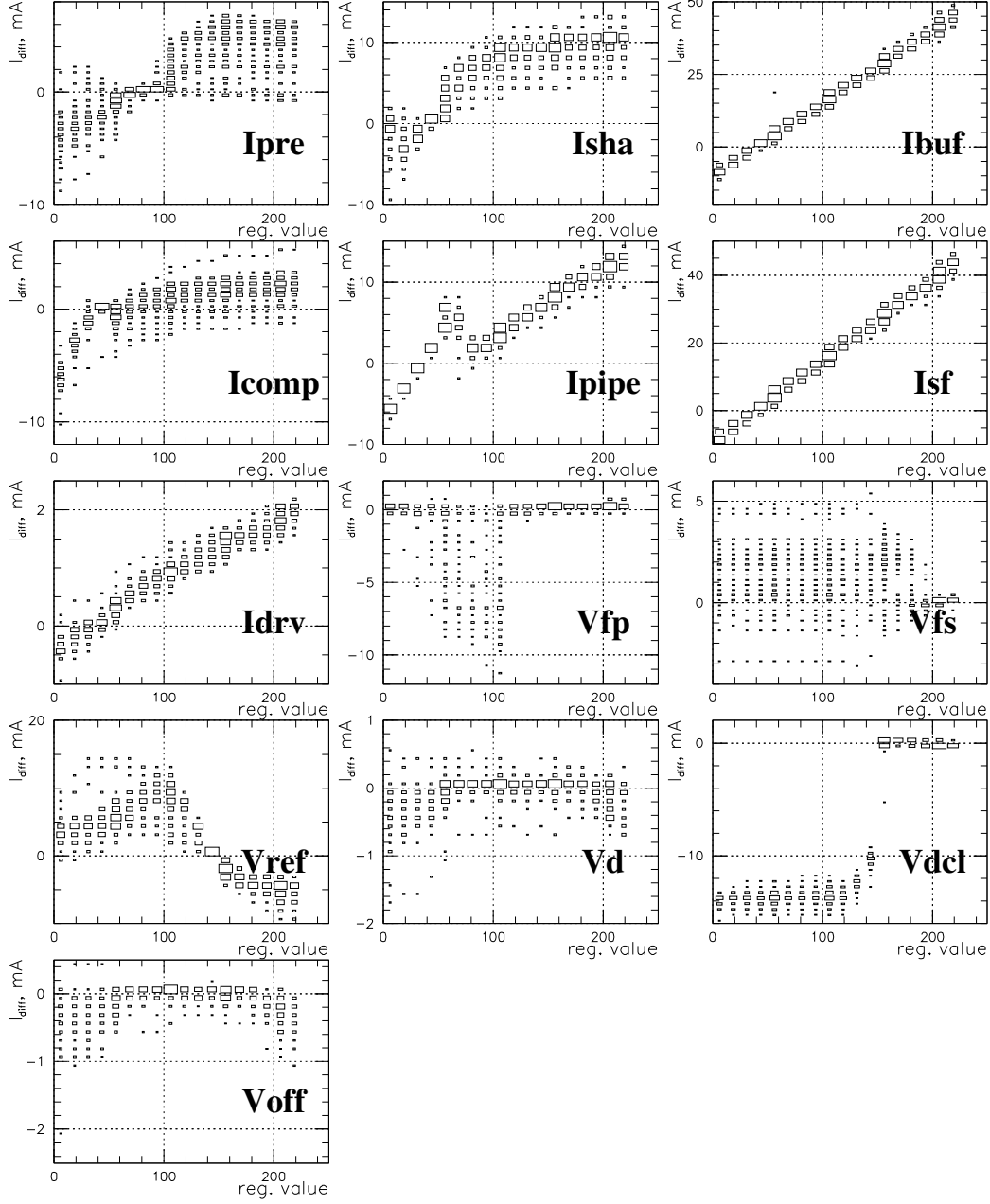


Figure A.7: Dependence of the chip's current consumption vs. the register setting. The other registers are set to their default values. The current consumption for the default register settings  $309 \pm 56$  mA is subtracted. The measurements are done for the power line +2 V.



***Vfs, Vd, Voff*** For these registers there are ranges in their settings within which the chip is not functional. In order to check the proper programming of these registers they were programmed to be in such a mode, namely *Vfs* was set to 80, *Vd* to 20, *Voff* to 220. The absence of any output from the chip was the required criterion.

***Vfp*** This register doesn't affect the chip's behavior until the chip is irradiated [Vel03]. Hence for a non irradiated chip the only way to check the proper *Vfp* DAC setting is to probe the pad # 271 [FB<sup>+</sup>97] that is located in the middle of the chip. This method was not used because of the danger to scratch the chip during probing and this register was left unchecked.

### Communication Registers

There are several other registers used for timing adjustment, control of the functionality of the chip's logics and the communication of the daisy chain:

***latency*** The timing of the system must be carefully adjusted in order to readout the chip's response to the injected charge correctly. The chip was switched to TP mode (for detail see section A.4.2) and the proper TP running mode was a criterion of the correct register programming,

***clkdiv*** switches the chip between normal daisy chain running mode and fail safe mode. Its proper programming was checked together with the chip's tokens (see section A.3.2),

***SyncReg*** defines the generated *Error* signal (for detail see section A.3.4). This feature is not used in the project, therefore it was not checked,

***TokenDelay*** defines the number of *Rclk* cycles until the chip starts its analog output. For the production test stand this means the delay in output between the driver chip and the chip under test in the daisy chain (for detail see section A.3.2). The proper chip's trailer digitalization assured the proper register programming.

### A.3.2 Running Modes and Control Tokens

In the final silicon detector 4 chips are daisy chained. This brings the requirement of a full check of the synchronization token set (*HTO*, *RTI*, *HTI*, *RTO*) as well as the fail safe token set (*FHTO*, *FRTI*, *FHTI*, *FRTO*) (see figure A.5). For every chip its ability to run as the first and as the last in the daisy chain was checked as well.

Driver Chip			ChUT				Failure Case	
1st	Last	FS <sub>L</sub>	1st	Last	FS <sub>R</sub>	FS <sub>L</sub>	Jumper	runs   Comment
1	0	0	0	0	0	0	Closed	N   <i>HTO</i> or <i>RTI</i> is bad
1	0	0	0	1	0	0	Opened	N   Can not be the last one
			1	0	0	0	Closed	N   Can not be the 1st one
			1	1	0	0	Opened	N   Can not be the 1st and the last one together
1	0	0	0	0	0	0	Opened	Y   Always is the last one
			1	0	0	0	Opened	Y   Being the 1st, runs always as the last one
1	0	1	0	0	1	0	Closed	N   FS <sub>R</sub> fails
1	0	0	0	0	1	0	Closed	Y   FS <sub>R</sub> is not ON
1	0	1	0	1	1	0	Opened	N   FS <sub>R</sub> is not ON when ChUT is the last one
1	0	0	0	0	0	1	Closed	N   FS <sub>L</sub> fails
1	0	0	0	0	0	1	Opened	N   FS <sub>L</sub> is not ON
			1	0	0	1	Opened	N   FS <sub>L</sub> is not ON when ChUT is the first one
1	0	1	0	0	1	1	Opened	N   FS <sub>R</sub> and FS <sub>L</sub> do not work together

Table A.2: The settings of the *driver chip* and the *chip under test* (ChUT). The ChUT was programmed as the first (1st) or/and last (last) one in the daisy chain; into fail safe modes for the left and right sides fail safe tokens (FS<sub>L</sub> and FS<sub>R</sub>, respectively). Values 1 (0) denote that the corresponding mode of the chip is activated (not activated). The position of the *jumper* (Jumper) between *HTO* and *RTI* tokens of the ChUT is shown (opened or closed). Running condition of the daisy chain of the two chips (either running (Y) or not (N)) is a criterion of the failure of the tokens. Short explanation is given in a Comment column.

In order to check these two sets of synchronization tokens a daisy chain of two chips was made allowing to run in both regular and fail safe mode. The first chip in the daisy chain is referred to as the **driver chip**. It was used as the reference chip with proved functionality of the daisy chain tokens and Fail Safe Mechanism (FSM). The second chip was the **Chip Under Test** (ChUT). In this case the proper functionality of the right side tokens (*HTI*, *RTO*, *FHTI*, *FRTO*) was checked automatically, for the left side tokens (*HTO*, *RTI*, *FHTO*, *FRTI*) a *jumper* between *HTO* and *RTI* was implemented (see figure A.9). Programming of the two chips in various running modes together with the opened or closed *jumper* allowed to check the functionality of the tokens of the ChUT. The settings of the chips and the *jumper* position used for the token tests are shown in table A.2. The chip's running modes were varied by setting the register *clkdiv*, therefore proper programming of this register was checked automatically. As result the ChUT was checked for the following possible problems:

- *RTO* or *HTI* token is out of order,
- can not run as the last chip,
- always runs as the last chip,
- does not switch into right side FSM,
- does not switch into right side FSM when the chip is the last one,
- does not switch into left side FSM,
- left side FSM doesn't work when the chip is the first one,
- *HTO* or *RTI* token is out of order,
- does not run as the first chip,
- can not run being programmed as the first and the last chip in the chain,
- always runs as the last chip being programmed as the first one,
- left side FSM works only when the chip is the last one,
- can switch into right FSM but does not work in this mode,
- can not run as the first chip,
- can not run being completely switched into fail safe mode (both sides).

Two interesting features of the FSM were found from the chip token test:

- Being programmed as the last chip it does not work in right side FSM (communication with the previous chip in the daisy chain). As a workaround of this problem **the pads of *RTI* and *HTO* tokens must be bonded together for the last chip in the daisy chain.** This allows the chip to run not being programmed as the last chip in the daisy chain.
- The chip stops running when both its left and right sides are programmed to work in FSM. No workaround of this feature was found but for the silicon recoil detector, where the daisy chain is made out of 4 chips, this mode is never needed.

### A.3.3 Reset

The memory slice counter is reset once the chip receives the *reset* (low level of  $\overline{reset}$ ) signal. In order to test it the timing of the  $\overline{reset}$  signal and the *latency* were adjusted in such a way that in the case of the proper chip reset the second memory slice of the chip's memory was read out (for detail see section A.4.2). Hence the corresponding trailer information was a proof of the chip's proper reset.

### A.3.4 Synchronicity Monitor

The synchronicity monitor circuit checks the signals of the neighboring chips in the daisy chain to assure synchronous operation. Depending on the setting of the register *SyncReg* and the input signals *SyncIn*<*i*> from the next chip in the daisy chain the chip generates the set of output synchronization signals *SyncOut*<*i*> (*i* = 1...5). An *error* signal is generated in the case of some system deviations, allowing to trace problems. In the case of the HERMES silicon recoil detector this monitoring feature is used only partially. The *error* signal is not read out and only the *SyncOut*<5>, *SyncIn*<5> and *SyncOut*<4>, *SyncIn*<4> signals are used in order to make the system's **Data Valid** signal, needed for ADC triggering (see section A.4.2 for details).

The output synchronization signals *SyncOut*<5> and *SyncOut*<4> were probed by an oscilloscope in order to check their levels and widths.

### A.3.5 Addressing

Every chip can be set into the most appropriate running conditions by varying the programmable registers. A unique address can be assigned to the chip

by applying high (+2 V, logical 1) or low (−2 V, logical 0) levels to its 6 address pads ( $Id<0>$  ...  $Id<5>$ ). These pads were checked by setting all possible address combinations for the chip under test. For each combination the chip was programmed and its response was detected.

## A.4 Production Test Stand

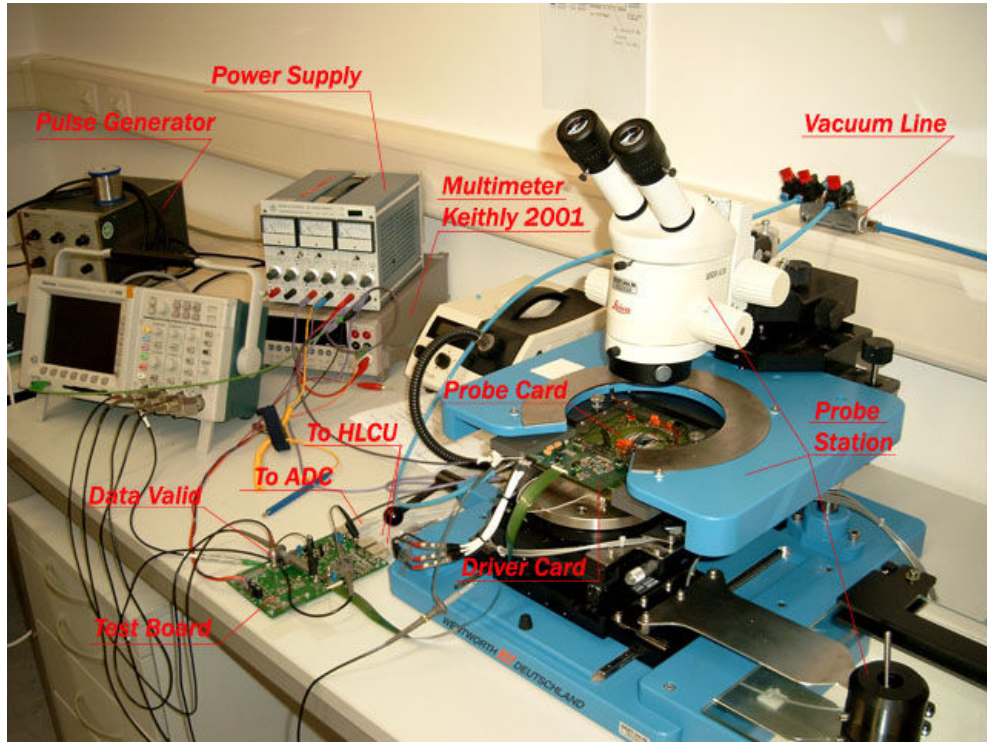


Figure A.8: Production test stand

For the HELIX production tests a test stand was designed and assembled at DESY Zeuthen (see figure A.8). The test stand included a pulse generator that simulated the HERA clock (10.4 MHz) needed for running the chip. A power supply module with floating ground provided the power levels +2 V and −2 V. A multimeter Keithly 2001 was used for measurements of the chip's power consumption. The main components of the stand were the HELIX *probe card* and the HELIX *driver card* mounted on the *probe station*, connected through the *test board* to the HLCU and ADC.

The HELIX *probe card* gave access to all the necessary pads of the ChUT (see figure A.10), the *driver card* supplied all the control signals and voltage

levels to the reference HELIX chip (*driver chip*) mounted on the card and to the *probe card* (see figure A.9). The *driver chip* and the ChUT run in daisy chain mode. This allowed to make tests of the daisy chain tokens and fail safe tokens of the ChUT without direct measurements of the token signals (see section A.3.2). The *driver chip* was also used for monitoring the system stability.

In order to test the parameters of the final ACC module (see figure A.2), the *test board* was used for the signal transfer and power supply interface. Since the output of the HELIX chip has an uncertainty of up to four clock cycles with respect to the event trigger, an additional signal is needed to trigger the ADC. Important feature of the *test board* was the generation of the signal correlated with the output of the daisy chain; this is referred to as *Data Valid* (not to be mixed up with the *data valid* signal generated by the HELIX chip).

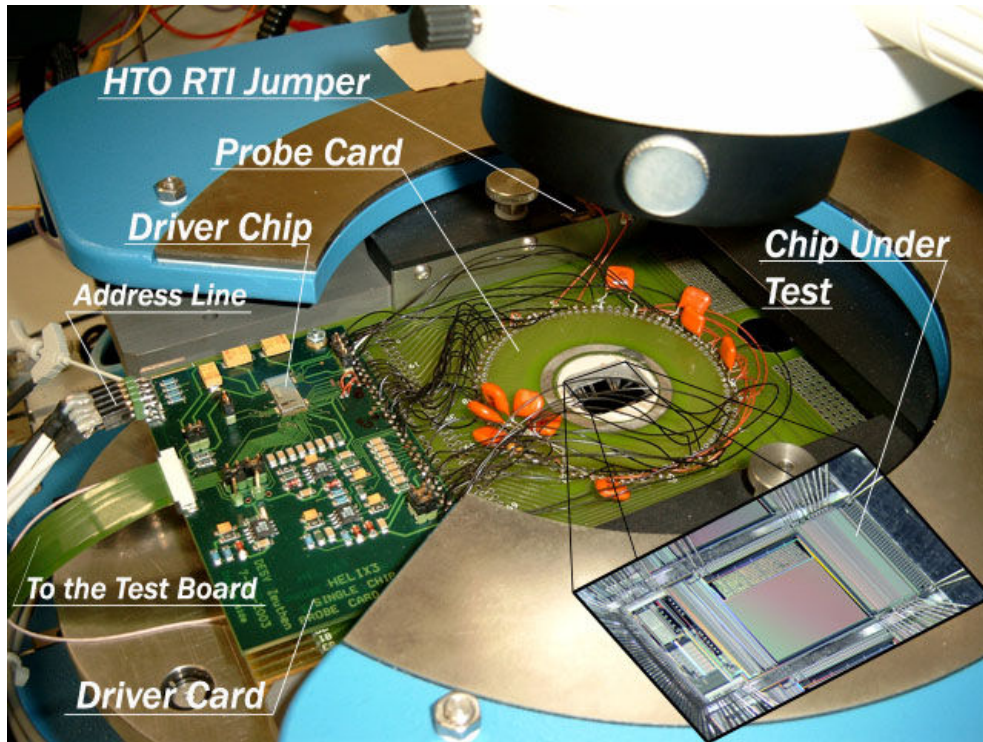


Figure A.9: *Driver card* with the *driver chip* mounted on top of it and the *probe card*. The insert shows a magnification of the chip under test.

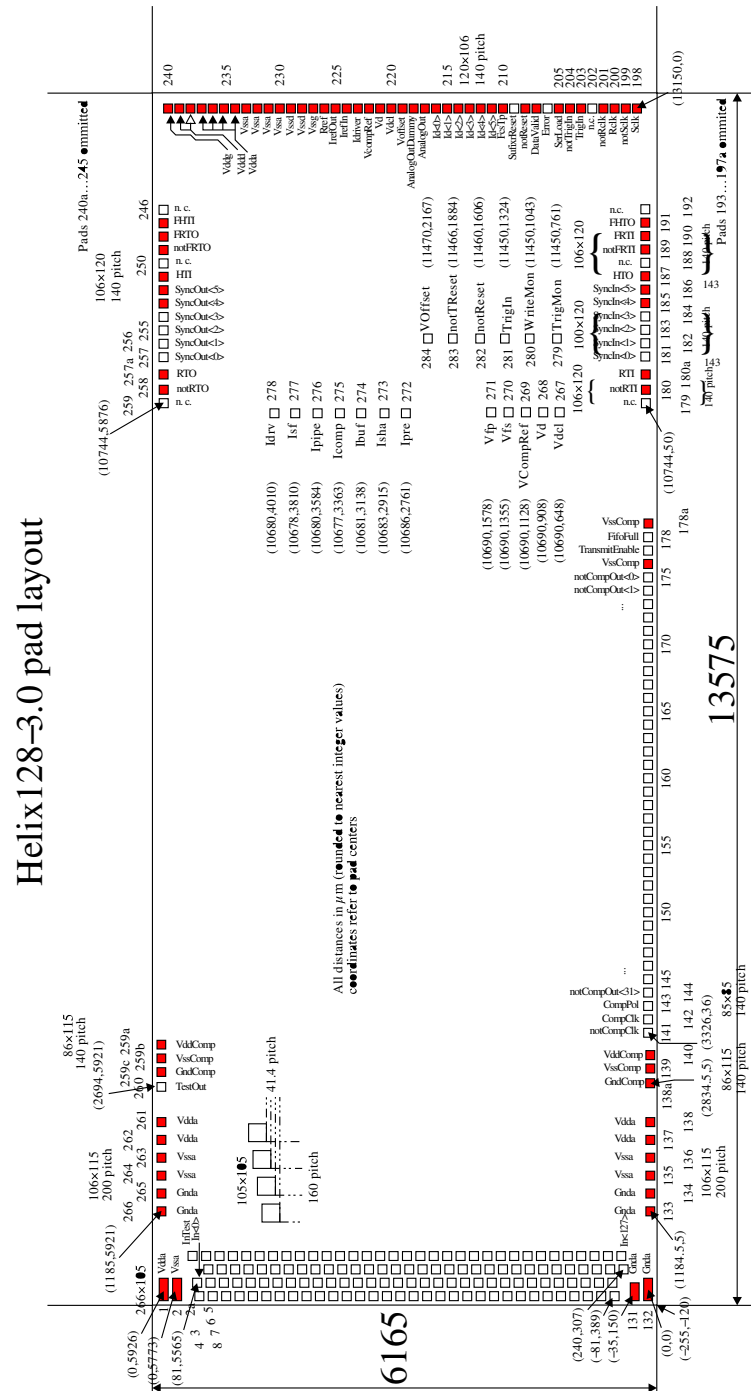


Figure A.10: Probe Card Map. The dark pads are probed by the card.

### A.4.1 Hardware Components

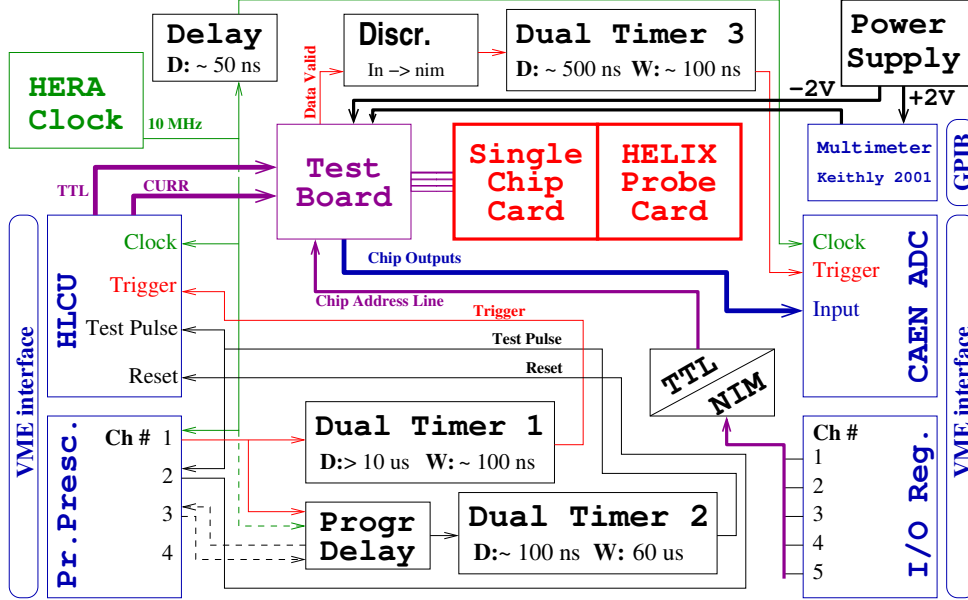


Figure A.11: Schematics of the production test stand.

The electronics scheme of the test stand is shown in figure A.11. The HERA clock frequency was imitated with a pulse generator. The trigger signal for the chip was produced from the prescaled clock signal via a programmable prescaler SIS3802. The test pulse and the HELIX reset signals were delivered from the delayed trigger signal. A programmable delay (figure A.12) was set up for the automatization of the production tests. Using this delay the data taking process for the chip latencies 10 and 100 did not need manual timing adjustments.

Control signals were supplied to the chain of two chips (through the *test board*) by the HLCU module. This module with a VME interface was designed by NIKHEF [LW] and produced by Glasgow University. The chip's address levels were set remotely by the I/O register SIS 3610. The output signal of the two daisy chained chips was digitized by a CAEN V729A ADC (originally the readout of the test stand was supposed to be done via HADC, but because of its production delay another ADC was finally used in the test stand). Additionally, various NIM electronics have been used, namely 4 dual timer modules from CAEN for fine time tuning.



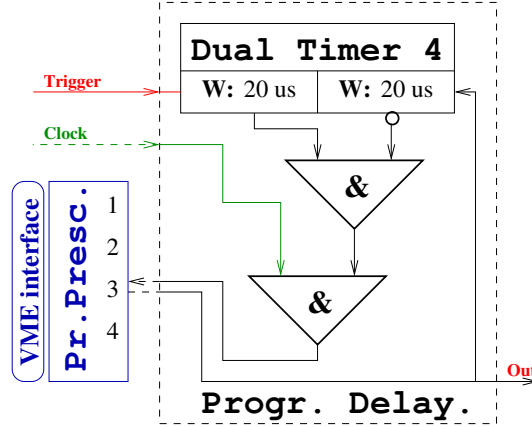


Figure A.12: Schematics of the programmable delay. The delay is based on the programmable prescaler, therefore the step of the delay is defined by the clock frequency (for 10.4 MHz the delay step is 96 ns). Delay limitations: The maximum delay length is defined by the width of the signal after the *dual timer* module. The trigger period should be at least twice as shorter as the signal width after the *dual timer* module.

### A.4.2 Test Stand Timing

The HELIX chip requires several control signals, namely the sampling clock (*Sclk*), readout clock (*Rclk*), trigger, test pulse (TP), serial load (Sload), reset signals (reset) (for detail see section A.2). Synchronization of these signals is essential for proper chip functionality.

The input signal after amplification and shaping must be sampled possibly at its maximum as shown in figure A.13. The sampling moment is defined by the delay *Sclk Delay* of the falling edge of the *Sclk* clock with respect to the event moment. For the production tests the test pulse of the chip was used

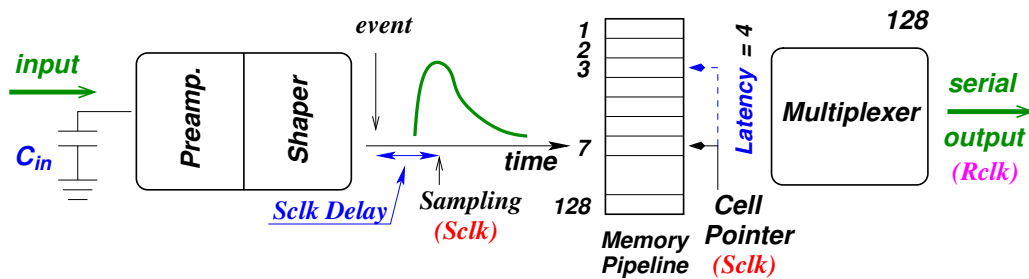


Figure A.13: HELIX timing

for the simulation of the charge produced due to a physics event at the chip's input. Hence the delay *Sclk Delay* between the rising edge of the test pulse (event moment) and the falling edge of the sampling clock must be adjusted in such a way that the chip's output signal gets its maximum. Note that since *Sclk* and *Rclk* are the same signals for the silicon recoil detector, the readout moment of the chip also depends on the delay *Sclk Delay*.

Another important issue is the parameter *latency* programmed into the chip for proper event readout. In general, this value can be evaluated as:

$$latency = trigger\ decision\ time \cdot sampling\ clock\ frequency,$$

where the *trigger decision time* is the time needed by the system for the trigger decision after the moment when the event happened. Since for the test stand the event was simulated by the test pulse, the *latency* parameter can be calculated as:

$$latency = (trigger\ moment - test\ pulse\ moment) \cdot clock\ frequency.$$

The chips were tested with the *latency* 10 and 100, meaning 10 and 100 *Sclk* cycles between the event moment and the moment the chip receives *trigger*.

The timing of the control signals, chip tokens and chip's output signal for two daisy chained chips are shown in figures A.14 and A.15. The time related requirements to the HELIX control signals at the production test stand are as following (see figure A.11):

**Sclk** is the same as the HERA clock but delayed by HLCU. Since *Sclk* also defines readout clock *Rclk*, in order to simplify timing adjustment of the test stand, *Sclk* was used as a reference for adjustment of other signals.

**Test pulse** is a prescaled clock signal. It passes through the HLCU without modification. TP was additionally delayed within one clock cycle with respect to the *Sclk*, in order to set the proper sampling moment of the of the injected charge. Note that the TP signal must be longer than the chip's output in order to avoid its influence on the chip's output.

**Trigger** is a prescaled clock signal as the TP. It must be additionally delayed with respect to the TP signal in order to comply with the latency value 100 ( $100 \cdot 96\text{ ns} = 9.6\text{ }\mu\text{s}$ ). Since the trigger is synchronized by the HLCU with *Sclk* [LW], in order to avoid ambiguity in synchronization the trigger signal must contain exactly one full clock cycle of the HERA clock.

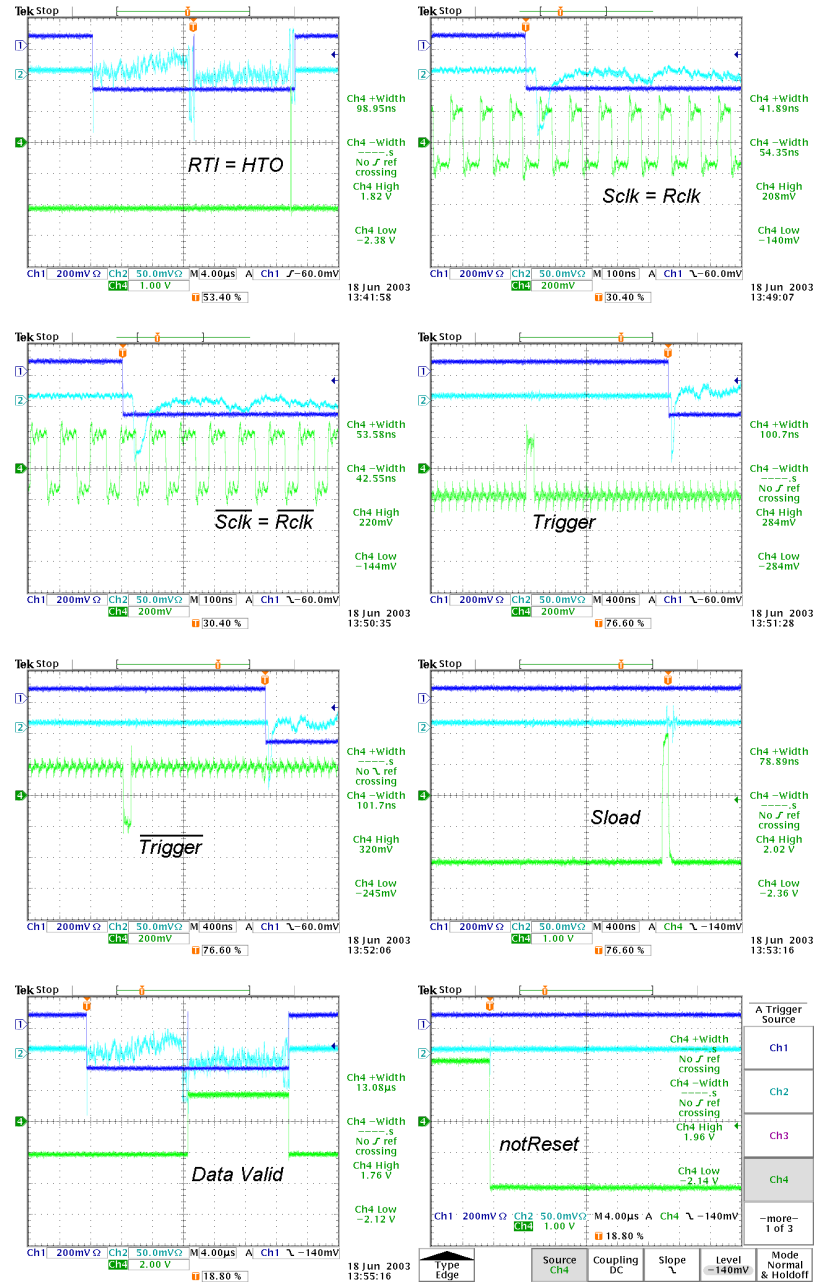


Figure A.14: Oscilloscope plots for the control signals of the chip under test. The uppest curve stands for the *Data Valid* signal, generated by the *test board*. The middle curve for the output signals of the *driver chip* and CHuT. The lowest curve for the measured signal.

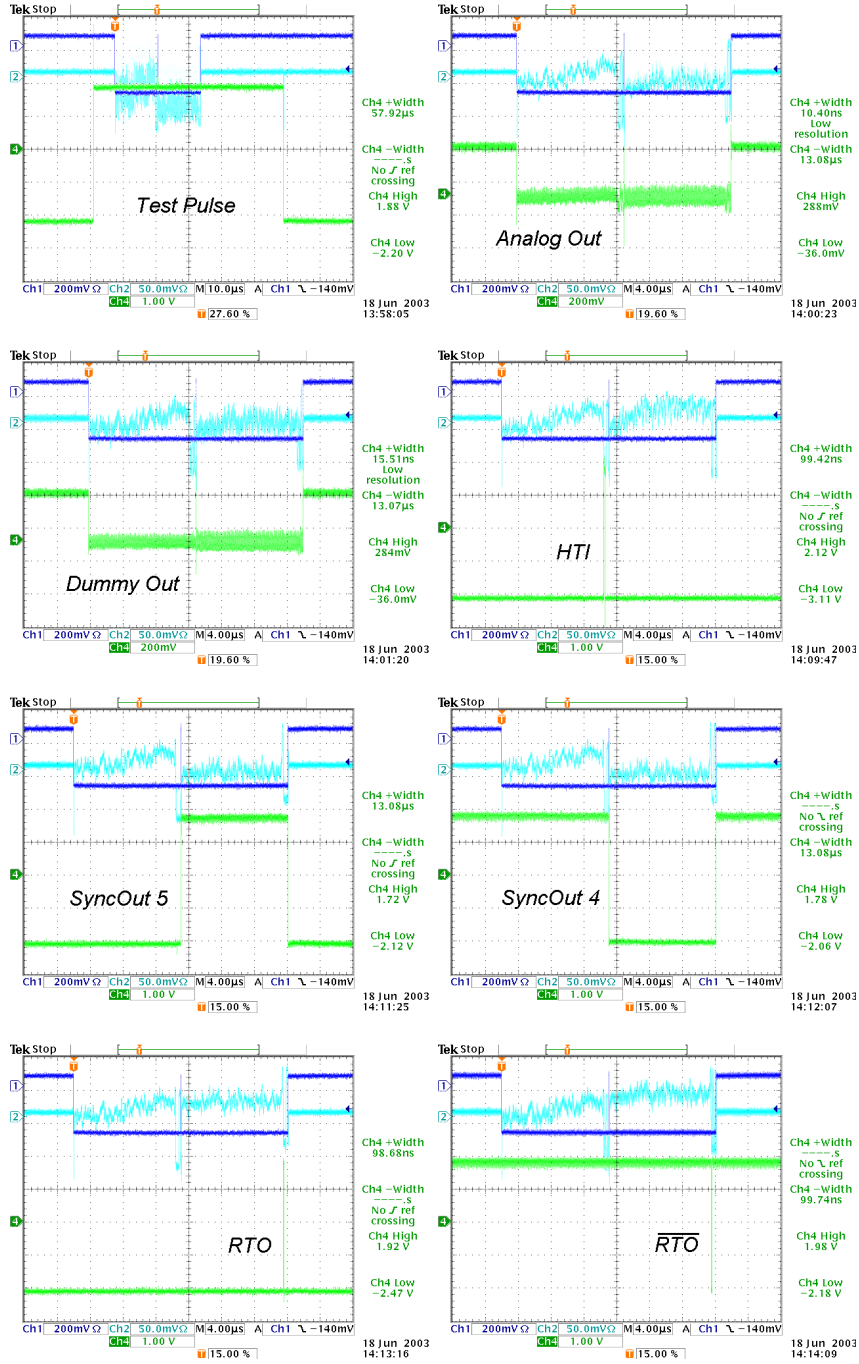


Figure A.15: Oscilloscope plots for the control signals of the chip under test. Notations are the same as in figure A.14

**Serial load** is generated by the HLCU and is synchronized with *Sclk*. Normally no adjustment is needed.

**Reset** is supplied externally and is synchronized with *Sclk* by the HLCU. At the test stand this signal was derived from the TP signal.

Note that the HLCU synchronizes almost all the HELIX control signals. Hence the signals must be measured after the HLCU module. The module allows also additional fine timing adjustments via its programmable delays.

As it was mentioned before the chip's output signal is not synchronized with the event trigger signal because of the up to 4 *Rclk* cycles ambiguity in the multiplexer output. There are several ways of getting the HELIX readout trigger synchronized with the chip's output, namely:

1. Using the chip's internal *data valid* signal.
2. Making it out of *SyncOut*<4> or *SyncOut*<5>. These two signals are the logical multiplication of the *data valid* signals of all the chips in the daisy chain (*SyncOut*<4> is the logically inverted *SyncOut*<5>). This method is more suitable for daisy chained chips.
3. Producing the trigger out of the chip's output signal.

Since in the silicon recoil detector daisy chains are implemented, the second method is used there. For the production test stand the third method was used because of its simplicity.

Finally one should take care about the proper signal sampling at the ADC input.

### A.4.3 Labeling of Chips

The chips supplied for tests were originally produced on wafers. Then the wafers were cut and the chips were glued onto a special "blue tape". Only after that the chips were labeled and tested. Being on the "blue tape" the chips kept the position they had on the wafer. The schematics of the wafer and the labeling method is shown in figure A.16. For every column a letter from "A" to "G" and for every row a number from 1 to 14 was assigned and therefore every chip on the wafer got a unique label, for instance "D8" meant the chip from the column D and the row 8.

To every wafer a number from 1 to 6 was assigned:

- Wafer # 904 6DA00 015 → # 1
- Wafer # 904 6DA00 002 → # 2

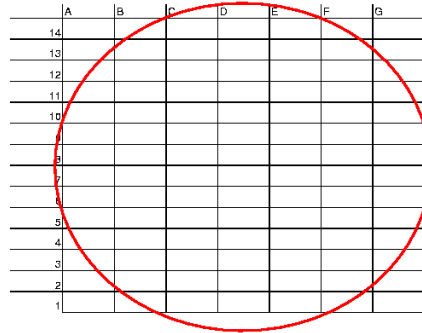


Figure A.16: Schematics of the chip's labeling. The wafer's labels are located on its bottom side.

- Wafer # 904 6DA00 021 → # **3**
- Wafer # 920 3EA00 034 → # **4**
- Wafer # 920 3EA00 032 → # **5**
- Wafer # 920 3EA00 033 → # **6**

The final chip's label contained both the wafer number and the chip's location on the wafer, for instance W2B8, where W2 stands for the wafer and B8 stands for the location on the wafer.

#### A.4.4 Test Sequence

During the production test most of the chip parameters were checked fully automatically. The whole test procedure was done by one program that navigated the test stand operator through the procedure, asking to perform various actions needed for the test. The test procedure was set up in the following way:

1. The operator puts a new untested chip under the probe card and gets the system of two daisy chained chips running. Note that the first chip in the daisy chain is the chip on the driver card (*driver chip*), it remains the same for testing all other chips. The last chip in the chain is a Chip Under Test (ChUT).
2. The program requires to enter the unique chip label. All information related to the test is stored in the directory named as the ChUT.

3. Both chips are initially programmed to the default values by the program. The *latency* is set to 10, the ChUT is NOT programmed as the last chip in the daisy chain.
4. Check of the control tokens of the ChUT (see section A.3.2).
5. The operator is asked to check the *SyncOut*<4> and *SyncOut*<5> signals with the oscilloscope's probe. The signals must have the levels  $\pm 2$  V and their width must be the same as that of the *AnalogOut* signal.
6. At this point the probe station must be covered by a light tight cover in order to avoid light influence on the system up to the end of the test.
7. The chip address is varied via the I/O register. The chip's address pads 1 ... 5 are checked.
8. Registers *Vfs*, *Vd* and *Voff* of the ChUT are programmed one after another to values 80, 20 and 200, respectively. Each register is accepted as functional if the ChUT stops running for this register being programmed to the corresponding value (see section A.3.1).
9. The ChUT is switched to test pulse mode. The operator is asked to confirm it. This point is important in the test sequence, since the proper functionality of the test pulse means not only that the chip's memory cell parameters can be tested but also that the *latency* register is programmed properly.
10. The register *Ipre* of the ChUT is set to 1. In this case the preamplifiers of the chip are turned off and amplification of the input charge becomes impossible. Hence no test pulse at the chip's output can be observed. Absence of the TP for the ChUT is a criterion of register functionality.
11. HELIX *reset* signal is switched on. Once the signal comes to the chip the memory cell counter is reset. The timing of the system was adjusted in such a way that after the reset the memory slice number 2 was read out every time when the chip was triggered. If the trailer of the ChUT shows the readout slice number to be 2, the *reset* of the chip is accepted to be good.
12. The system is switched into so-called "resonance" mode. In this mode the *trigger* is prescaled in such a way that the same memory slice is accessed with every readout. This effect was observed for the first time during the setup mounting and was used for accessing all the slices of the chip memory. The operator is asked to confirm the chip being in

such a mode (the trailer of the ChUT must show the same read out memory slice). If it is not the case the operator is asked to run a special program that looks for the “resonance” prescaler factor of the *trigger*. Once this factor is found it is increased by 1, increasing the *trigger* delay by 1 HERA clock cycle. That allows access to the next memory slice with every new *trigger*.

13. The registers that affect the chip’s power consumption are tested (see section A.3.1). The difference between maximum and minimum power consumption for every register was measured by the multimeter Keithly 2001 controlled by the labview program via the GPIB interface.
14. *latency* 10 measurements. For the pedestal measurements 10000 events are taken. For the test pulse mode 20000 events. The factor two in the number of events comes from the fact that two different charges are injected into every HELIX channel in case of the TP.
15. *latency* 100 measurements. The same amount of data is taken as for the *latency* 10 measurements.
16. The test results are written into an automatically generated log file. The test is over. The operator disconnects the probe card and moves to the next untested chip.

## A.5 Analysis of the Memory Cell Properties

The offline analysis of the data accumulated for every chip in the pedestal and test pulse measurements was done in two steps. First, individual properties of the memory cells were studied, namely pedestal levels, noise and influence on the amplification of the injected charge. Then the chips were selected according to the requirements of the silicon recoil detector project.

For the noise measurements (see detail in section A.5.1) pedestal runs each of 10000 events were taken. The chip’s internal test pulse was the only option to test the amplification properties without probing the chip’s input channels (this would have increased the price of the probe card and would have made its operation more difficult). For the test pulse 20000 events were taken per chip. Every memory cell of every chip was probed (128 channels · 136 slices results in 17408 cells per chip). The average number of events accumulated per memory cell is 70 (minimal 50), hence the average statistical error of the measured parameter is about 12%.



In total 372 chips were tested (6 wafers) from which 150 passed all the requirements. Only 104 chips are needed for the recoil project. A procedure developed to select the best chips for the project is described in section A.6.

The expected value of the *latency* for the final detector is about 10, therefore the data taken for this *latency* is in the scope of interest. The data for *latency* 100, meaning long storage time of the charge by the memory cells, is used to reject the chips with charge leakage in the memory cells.

### A.5.1 Representation of the Chip's Output Signal

The chip's output signal  $PH_i^{k,m}$  can be described as a sum of the following components:

$$PH_i^{k,m} = S_i^{k,m} + P^{k,m} + N_i^{k,m} + C_i, \quad (\text{A.1})$$

where  $i$  and  $k$  denote the event and the channel number respectively,  $m$  is the memory slice number and:

$S_i^{k,m}$  is the response of the chip to the injected charge;

$P^{k,m}$  is the DC-offset of the memory cell (pedestal level);

$N_i^{k,m}$  is the individual random noise contribution of the memory cell (Gaussian distributed);

$C_i$  is a random voltage offset, common for all channels of the chip, with mean value zero, usually called Common Mode Noise (CMN).

After the pedestal measurements (with no charge injected to the chip's input:  $S_i^{k,m} = 0$ ) the pedestal level of every memory cell can be calculated as:

$$P^{k,m} = \frac{1}{N_{events}^m} \sum_{i=1}^{N_{events}^m} PH_i^{k,m}, \quad (\text{A.2})$$

where  $N_{events}^m$  is the number of events taken for the memory slice  $m$ . The CMN can be calculated for each event individually by evaluating the following formula:

$$C_i = \frac{1}{N_{channels}^*} \sum_{k=1}^{N_{channels}^*} (PH_i^{k,m} - P^{k,m}), \quad (\text{A.3})$$

where  $P^{k,m}$  is taken from the pedestal measurements (Eq. A.2) and averaging is done over the channels without hits ( $N_{channels}^*$  is the number of such channels. Note that  $N_{channels}^* = N_{channels}$  in the case  $S_i^k = 0$ , where  $N_{channels}$  is

the total number of channels used for CMN calculation). Hence the response of the chip to the injected charge, corrected for the CMN, can be extracted:

$$S_i^{k,m} + N_i^{k,m} = PH_i^{k,m} - P^{k,m} - C_i. \quad (\text{A.4})$$

For the case of pedestal measurements ( $S_i^k = 0$ ) the RMS of  $N_i^{k,m}$  distribution for each memory cell can be extracted, yielding the memory cell's noise levels.

In this formalism the properties of the single memory cell can be studied, namely its influence on the injected charge amplification and its noise.

### HADC Signal Correction

The signal representation shown in Eq. A.1 differs from the one that was used in earlier analyses [KLS<sup>+</sup>02] and implemented in the online signal correction of the HADC module. The pedestal subtraction and CMN compensation of the HADC is based on a representation where the parameters are averaged over all memory cells in the channel. The signal representation in this case is

$$PH_i^{k,m} = \tilde{S}_i^{k,m} + \tilde{P}^k + N_i^{k,m} + \tilde{C}_i, \quad (\text{A.5})$$

where the indices are the same as in Eq. A.1 and

$$\tilde{P}^k = \frac{1}{N_{events}} \sum_{i=1}^{N_{events}} PH_i^{k,m}, \quad (\text{A.6})$$

where the sum runs over all the events with  $\tilde{S}_i^{k,m} = 0$  for all the memory cells. Hence  $\tilde{P}^k$  represents the pedestal level of the channel  $k$  (averaged over  $m$ ). The common mode noise correction in this case is

$$\tilde{C}_i = \frac{1}{N_{channels}^*} \sum_{k=1}^{N_{channels}^*} (PH_i^{k,m} - \tilde{P}^k), \quad (\text{A.7})$$

where  $N_{channels}^*$  is the same as in Eq. A.3. The relation between two CMN definitions (Eq. A.3 and Eq. A.7) can be derived as:

$$\tilde{C}_i = C_i + \frac{1}{N_{channels}^*} \sum_{k=1}^{N_{channels}^*} (P^{k,m} - \tilde{P}^k), \quad (\text{A.8})$$

where the difference comes from the offset between the memory cell pedestal  $P^{k,m}$  and the channel pedestal  $\tilde{P}^k$ , which is averaged over the memory cells. The difference in the signal representation for these two methods can be derived:

$$\tilde{S}_i^{k,m} - S_i^{k,m} = (P^{k,m} - \tilde{P}^k) - \frac{1}{N_{channels}^*} \sum_{k=1}^{N_{channels}^*} (P^{k,m} - \tilde{P}^k). \quad (\text{A.9})$$

Eqs. A.6 and A.8 show that the chip's signal  $S_i^{k,m}$  contains more information than  $\tilde{S}_i^{k,m}$  because the latter does not include individual memory cell properties that are averaged in  $\tilde{P}^k$  and  $\tilde{C}_i$ , giving additional smearing to the signal. The difference in the signal representations shown in Eq. A.9 is required to be small with respect to the noise of the system  $N_i^{k,m}$ . If not it must be calibrated out.

### A.5.2 Chip Selection

The primary goal of the production test was to select good chips out of the tested ones. This means that the chip must be fully operational (as discussed in section A.3) and must have no faulty channels or memory cells. For this task the signal representation was used as it is defined in Eq. A.1. This method is better with respect to the HADC method (see Eq. A.5), where individual memory cell parameters are integrated over, making it possible to hide single cell failures. For instance, a broken memory cell (see figure A.17), being the most common failure of the HELIX chip, can only be detected by analyzing the individual memory cell properties.

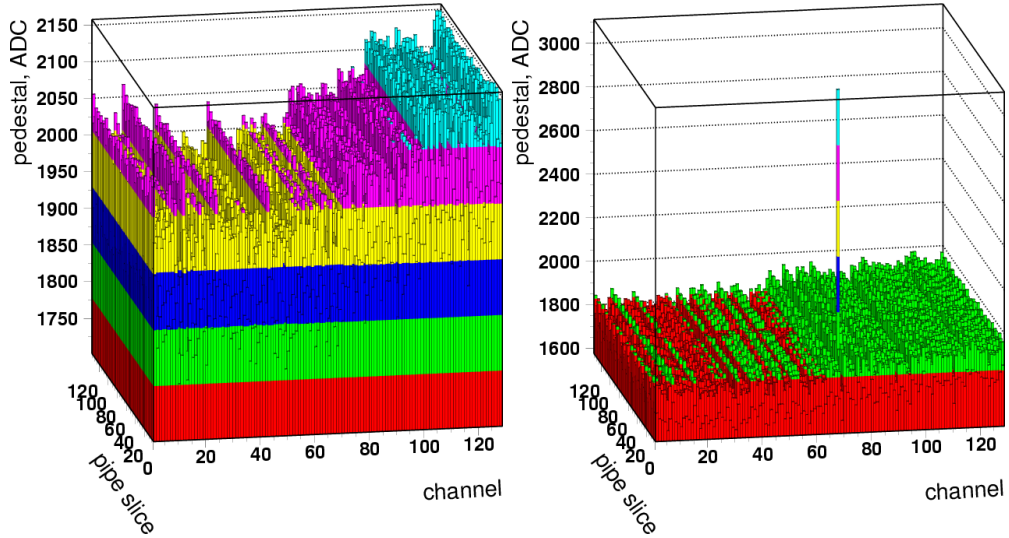


Figure A.17: The pedestal levels of the HELIX memory cells. The left side plot is for a good chip. The right one shows the case of a single broken memory cell. Its pedestal level is far above the level of the other cells.

### Parameters to be Checked

The chip selection was done in two steps. First, the distributions of the test parameters were obtained which allowed to define the accepted ranges of the parameters. Afterwards the chips with outlying parameters were rejected. The chip properties monitored during the chip selection procedure are listed below:

1. Pedestal levels of the chip (figure A.18.a): Chips with one or more broken channels were rejected,
2. Memory cell noise (RMS of pedestal distribution of the memory cells) (figure A.18.b): Chips with unstable (noisy) memory cells were rejected,
3. Difference of the pedestal levels between individual memory cells and averaged over the cells of the channel (figure A.18.c): Chips with broken memory cells were rejected,
4. Response of the channel to the test pulse (both stair cases): Reject the channels with faulty amplifiers,
5. Difference in the response to the test pulse between individual memory cells and averaged over the cells of the channel (figure A.19): Rejects broken memory cells,
6. Level of the high bit and low bit trailers,
7. Trailer level spread: Rejects instable trailers.

As a result 153 chips were found to have no defects. The next task was to select the best 104 chips for the silicon recoil detector.

### Parameters of the Selected Chips

In order to understand the measured chip properties the setup must be calibrated. This was done by using the response difference of every channel to the positive and negative injected test pulses, scaled down by the documented charge difference in equivalent MIP units (for the channels that get charge equivalent to  $\pm 2$  MIPs, the scale factor is 4, for  $\pm 1$  MIP it is 2). After averaging over all the channels and chips, **the signal equivalent to the one produced by a MIP was set to be equivalent to 150 ADC channels for the test stand measurements.**

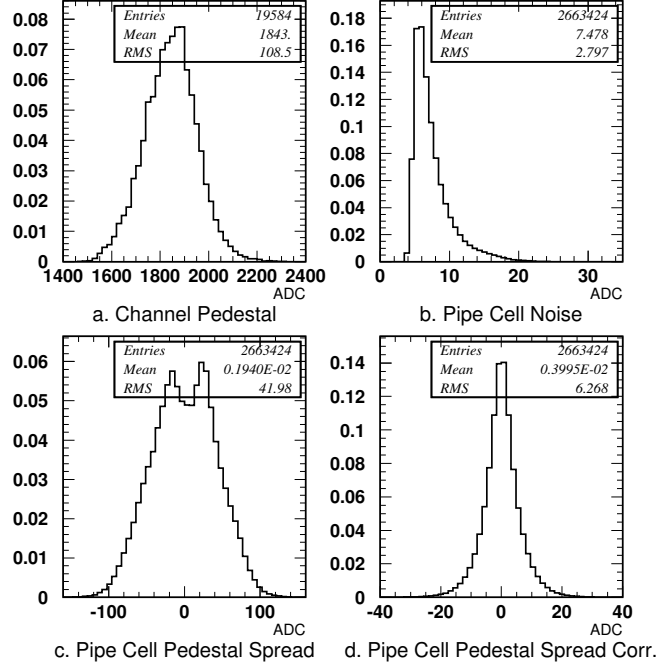


Figure A.18: Normalized distributions of the pedestal related parameters for all chips that passed the selection. Panel a: pedestal levels of the channels of all such chips. Panel b: noise of all the memory cells. Panel c: spread of the pedestal levels of the memory cells within one channel. Panel d: the same as panel c, but the spread is measured after the CMN correction, as defined in Eq. A.5 (HADC method).

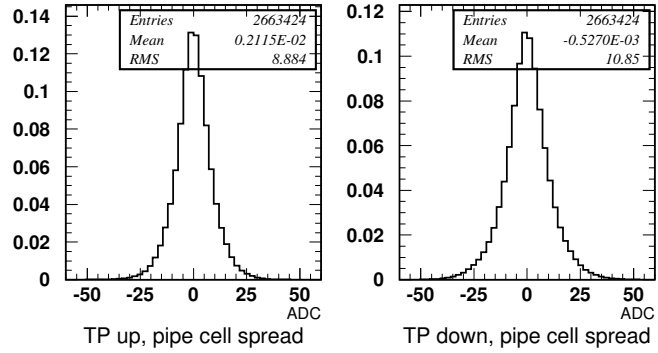


Figure A.19: Normalized distributions of the memory cell spread in test pulse amplification within one channel for all channels of all chips that passed the selection.

According to the recoil detector requirements the most important parameters are those that stand for the efficiency of 1 MIP detection, namely the noise of the system and the memory cell uniformity within a channel for both pedestal levels and signal amplification. For the production test stand **the noise was about 7.4 ADC channels, corresponding to 0.05 MIP** (see figure A.18.b). The non-uniformity of the injected charge amplification within a channel (dependence of the amplification on the memory cell number) can be calibrated out, but a method is needed that can give reliable calibration results for every memory cell within reasonable time. At the moment no such method is available. In this work the measured memory cell spread was found to be about 10 ADC channels or 0.066 MIP (see figure A.19), no dependence on the amount of charge or its sign was found.

The memory cell spread of the pedestal levels within a channel was measured to be 42 ADC channels or 0.28 MIP (figure A.18.c). It contributes the highest uncertainty to the measured signal and makes the efficiency of a MIP registration too low. The uncertainty in memory cell pedestal levels can be easily calibrated out by regular pedestal measurements in order to compensate the known fluctuations of the chip's pedestal levels. The restriction is that the memory cell pedestal measurements need reliable statistics for every cell; this requires too long time of data taking in the present HERMES DAQ configuration.

### Spread of the Pedestal Levels of the Memory Cells

The measured memory cell spread (see figure A.18.c) would make the registration of MIPs extremely inefficient. However the situation improves when the HADC compensation of the CMN (see Eq. A.5) is applied to the chip's output signal. In figure A.18.d the memory cell spread corrected according to the HADC method is shown. In this case the spread is 6.2 ADC channels or 0.04 MIP giving a factor seven of improvement with respect to the correction of the CMN for every memory cell.

In order to find the reason of such an improvement the difference between the two CMN definitions should be investigated. The spread of the pedestal levels of the memory cells within a channel is given by  $P^{k,m} - \tilde{P}^k$ , where  $P^{k,m}$  and  $\tilde{P}^k$  are defined in the Eqs. A.2 and A.6, respectively. The spread corrected by HADC is given by  $\tilde{P}^{k,m} - \tilde{P}^k$ , where  $\tilde{P}^{k,m}$  is the pedestal level of the memory cell  $m$  of the channel  $k$  calculated as in Eq. A.2, but with contribution of the CMN  $\tilde{C}_i$  (see Eq. A.7):

$$\tilde{P}^{k,m} = \frac{1}{N_{events}^m} \sum_{i=1}^{N_{events}^m} (PH_i^{k,m} - \tilde{C}_i), \quad (A.10)$$

with notations as in Eq. A.2. Since the sum in Eq. A.10 does not run over all memory cells of the channel as in Eq. A.7, the mean value of  $\tilde{C}_i$  is not zero and therefore the pedestal level of a memory cell  $\tilde{P}^{k,m}$  is biased. Using Eq. A.8 the biased pedestal level of the memory cell can be written as:

$$\tilde{P}^{k,m} = P^{k,m} - \frac{1}{N_{channels}^*} \sum_{k=1}^{N_{channels}^*} (P^{k,m} - \tilde{P}^k). \quad (\text{A.11})$$

Hence the corrected by HADC memory cell pedestal spread is defined as:

$$\tilde{P}^{k,m} - \tilde{P}^k = (P^{k,m} - \tilde{P}^k) - \frac{1}{N_{channels}^*} \sum_{k=1}^{N_{channels}^*} (P^{k,m} - \tilde{P}^k), \quad (\text{A.12})$$

meaning that the improvement in the corrected memory cell spread comes from the fact that the sum  $\frac{1}{N_{channels}^*} \sum_{k=1}^{N_{channels}^*} (P^{k,m} - \tilde{P}^k)$  is close to the value of the “real” spread  $(P^{k,m} - \tilde{P}^k)$ . This can be explained by the existence of a structure for every memory slice along the chip channels that shows up in a similar offset of the memory cells pedestal levels from their channel’s pedestal levels within the given cell slice. The visual explanation of this effect can be

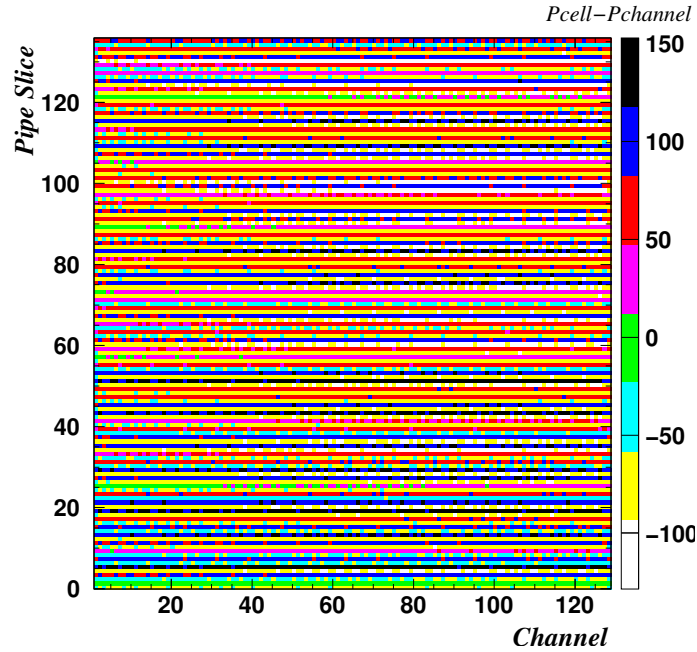


Figure A.20: Difference between the pedestal levels of the memory cells and the corresponding pedestal levels of the channels.

seen in figure A.20, where the difference between the memory cell pedestals and the channel pedestal is shown for one chip. **The difference is similar over all the channels within the same memory slice.** Hence according to Eq. A.12 the CMN calculated with the HADC method (see Eq. A.7) corrects the measured signal for the spread of the memory cell pedestals within a channel.

Since the HADC is used in the silicon recoil detector, this undocumented HELIX feature implies that the uncertainty for the memory cell pedestal spread is about 0.04 MIP (see figure A.18.d). Hence this uncertainty contributes to the measured signal similar to the noise and the amplification memory cell spread (see figure A.19). Note that the zero suppression implemented in the HADC modules does not affect the signal, because it is done after the CMN correction.

## A.6 Chip Sorting

As the result of the chip selection procedure 153 chips passed all requirements. These chips had no defects and could be used in the project. For the readout of the silicon recoil detector only 104 chips are needed - 16 hybrids will be mounted for the silicon sensor readout and the others will be used as spares ones (one hybrid contains 4 daisy chained chips). In order to select the best chips out of 153 for the project, a chip sorting procedure was performed as described below in this section.

The selected chips were divided into two groups. The group with the best chip's performance is used for high gain readout in order to get higher efficiency of MIPs detection. The other group are used for the low gain channel readout. Within these two groups the best chips will be used for the sensor's n-side because of its higher capacitance that causes higher losses of the deposited charge [GKW<sup>+</sup>02].

### A.6.1 Sorting Procedure

As it was already discussed in section A.5.2 three chip parameters stand for the efficiency of the MIP detection and the resolution of the deposited energy. The parameters are the chip noise, spread of the memory cells in pedestal levels and in amplification. The other chip parameters were not included in the sorting procedure. A method based on assigning scores to the relevant parameters was developed. These parameters are:

**Average Chip Noise (ACN):** mean value of the noise distribution of all



the memory cells of a single chip. Note that the RMS of the distribution was not included in the sorting procedure, as it was found to be small.

**Pedestal Memory Cell Spread (PMCS):** RMS of the distribution of the pedestal spread of the memory cells within the channels for a single chip.

**Amplification Memory Cell Spread (AMCS):** the RMS of the distribution of the amplification spread of the memory cells within the channels for a single chip.

The distributions of these three parameters were made for all 153 selected chips (see figure A.21, left panels). The obtained ranges of the parameters were divided into 5 equal subranges. Each subrange was assigned the score 20, 10, 5, 1 or 0.5, where the subrange with the best value of the parameter got the highest score.

In addition, the contribution of every parameter was weighted. The highest weight factor 3 was assigned to the parameter **AMCS** because it is very difficult to calibrate this uncertainty out. The **ACN** parameter got the smaller weight factor 2 because, on the one hand, the least noisy chips are required, but on the other hand, the noise conditions in the production test area can be completely different for the final setup. The **PMCS** parameter got the lowest weight factor 1 because of the possibility to calibrate this uncertainty out. After being weighted the scores for the parameters were summed up and the total score for every chip was evaluated. The chips that got the highest scores were the best according to the project's requirements.

Next, the chips were divided into 3 groups. First, for the chips that are used in the project (first two groups) the upper cuts were set to the parameters, namely for **AMCS** it was set to 14, for **PMCS** and **ACN** to 10. Then the score range was divided into 3 subranges so that the groups 1 and 2 contained the necessary number of chips (52 each). The dependence of the parameters **AMCS**, **PMCS** and **ACN** on the chip's score with the cuts applied for every chip group is shown in figure A.21.

### A.6.2 Results

As the result of the online chip tests, offline chip selection and sorting procedure, two chip groups (52 chips each) were selected for the silicon detector. The distributions of the parameters **AMCS**, **PMCS** and **ACN** for each group are shown in figure A.22 and, as it was expected, the chips from the *group 1* (high gain chips) have better performance than the chips from the *group 2* (low gain chips).

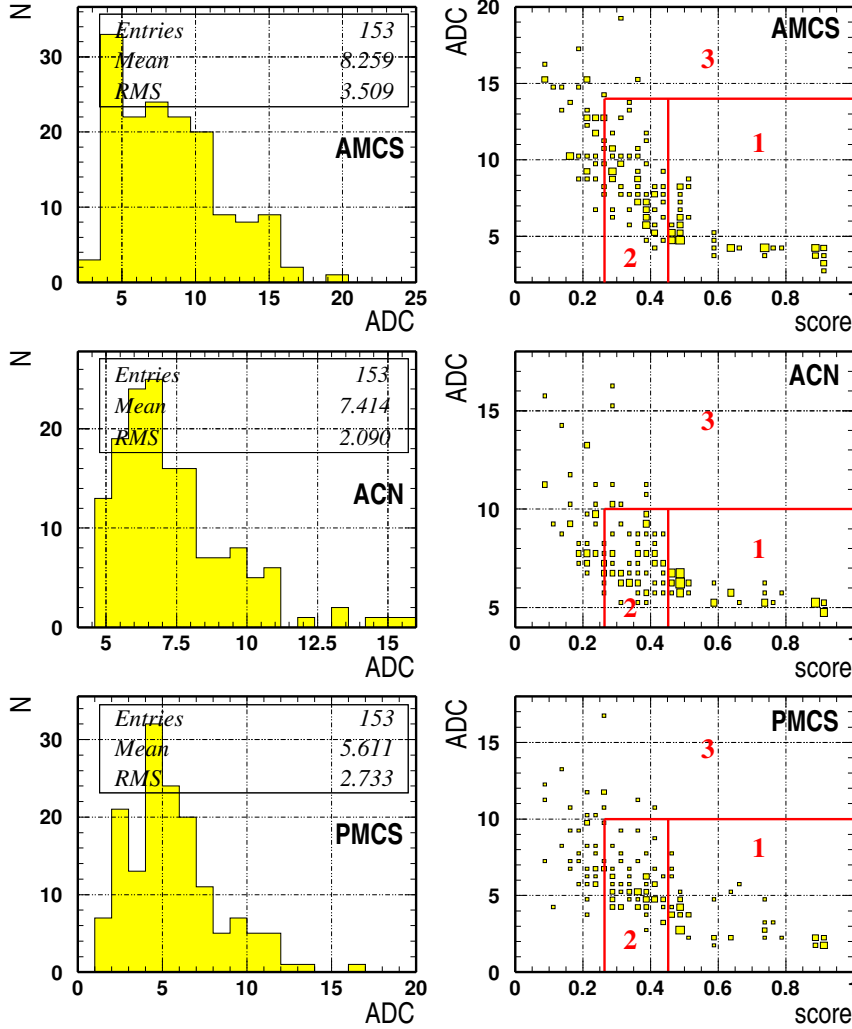


Figure A.21: Left: distribution of the chip's parameters used for the sorting procedure. Right: dependence of the chip parameter on the chip's score. The numbers correspond to the groups (explained in the text).

Note that although the influence of these parameters on the final detector performance is very important, under the running conditions of the production test stand the chip behavior can be different from that in the real detector due to the facts that:

- the chip under test was connected to the supply signals and voltage via the probe card needles that work as input capacitance to all the chip's pads and also as antenna,

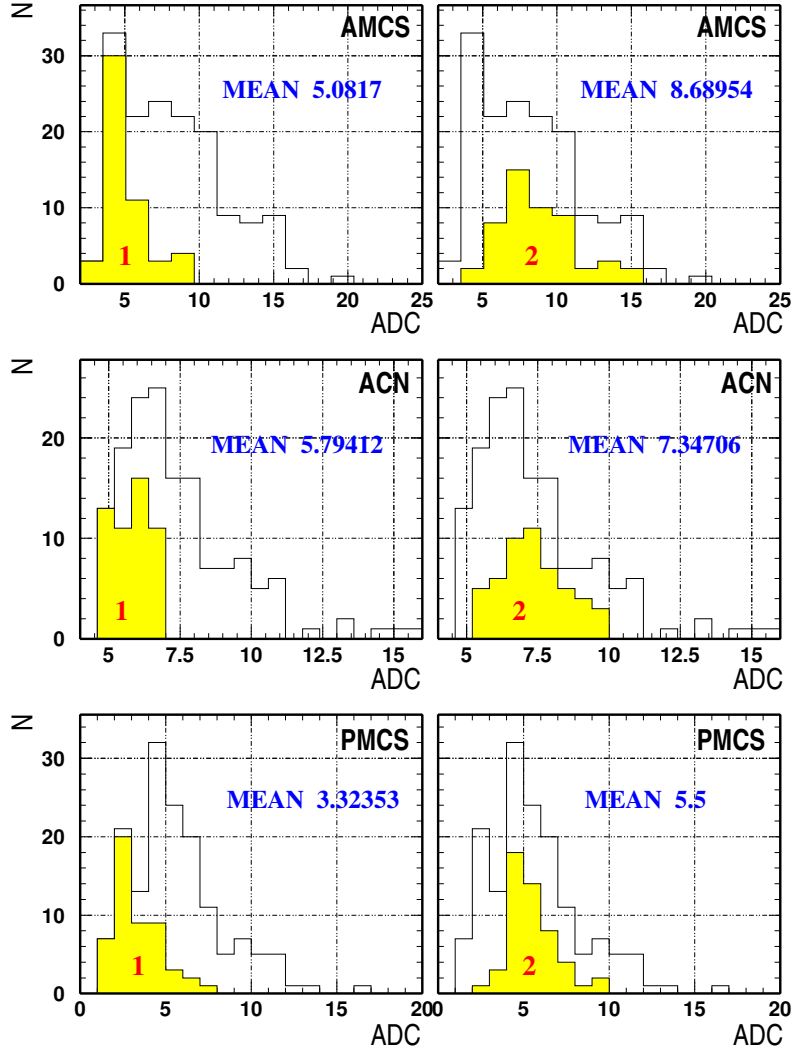


Figure A.22: Distributions of the chip's parameters for the chips selected for the silicon detector project. Left panels are for the chips of the *group 1* (high gain chips). Right panels are for the chips of the *group 2* (low gain chips). The open histogram shows the distributions for all the chips that passed the production test.

- the *driver card* and the *probe card* were connected together via long cables.
- the connection contacts of the probe card to the chip under test were not perfect.

These points give additional uncertainties to the behavior of the chip under test. Hence the described production tests and the chip's sorting procedure should be considered as the way to study the relative chip's properties without absolute calibration of the measured parameters of the chips.

## A.7 Conclusion

For the HERMES silicon recoil detector the production test of the frontend readout chip HELIX128 3.0 is done. The production test stand was designed and built at DESY Zeuthen. It included unique components, specially designed for this production test, such as the chip's *probe card* and the chip's *driver card*. The daisy chain of the *driver chip* and the chip under test was used in order to test the daisy chain and the fail safe tokens. The power consumption test method was developed and used for checking proper register programming. Every memory cell of the chip's analog memory was probed and checked for the possible defects.

Based on the analysis of the test results, 153 chips out of about 350 tested (6 wafers) were selected as those without faults.

A three-parameter chip sorting was performed in order to select the best chips for the silicon detector. As result 104 chips were selected for the project. The best 52 chips will be used for high gain channel readout and the other 52 for the low gain channels. Within these two groups the better chips were selected to read out the n-side of the silicon sensor.

# Acknowledgments

First of all, I would like to thank my advisor Dr. Wolf-Dieter Nowak. His guidance over the whole time of my working on this thesis was always very wise and friendly. Especially I would like to thank him for his support over the last year, for his advises that very often turned complications into elegant solutions. And of course for his time and patience spent for proofreading of this thesis.

I would like to thank Prof. Dr. Hermann Kolanoski, my official adviser from the Humboldt-Universität zu Berlin. Especially for the opportunity he offered to me to work with HU students. That was really exciting experience for me as a person who had been a student not so long ago. Also I would like to thank him for his efforts in bringing this unique spirit of universities to DESY students.

I am very appreciated to the DVCS group of HERMES. Especially to Frank Ellinghaus, Bernhard Krauss and Zhenyu Ye. Frank helped me to start my analysis and I benefitted a lot from his advises. Bernhard was always opened for questions. Especially I would like to thank him for our evening discussions at DESY Bistro in Hamburg. Thanks to Zhenyu for his very useful comments and for his work on the systematic uncertainty of the LTSA on deuteron.

I would like to thank Dr. Andrey Vinnikov for the discussions that were always very fruitful, no matter if it is on physics or non-physics subjects. Very valuable were his advises on the theoretical issues I wrote in this thesis.

And I would like to thank Ivana Hristova, my office-mate. Her company over the lunch time and tea-drinking breaks was always very supportive. Her wish to help and friendliness make me especially thankful. Our discussions on physics, silicon detector, paw and also on general things were so interesting.

I started working at DESY Zeuthen in the project of the silicon recoil detector. At the beginning we were a small group of enthusiasts that later evolved into the team that brought the detector to the commissioning. Here I would like to thank Dr. James Stewart, first of all, for the opportunity to work in this project. And of course for his support and the proper words

for us, who were in the lab trying to get the things running. Here “us” is related to me and Arne Vandenbroucke. We have worked together on many steps of the project. I would like to thank Dr. Wolfgang Lange for his huge help whenever I needed it. Also I would like to thank Mathias Reinecke for his contribution to the recoil detector project and for his help.

I would like to thank Dr. Elke-Caroline Aschenauer for her help at very important for me moment when I decided to join the DESY Zeuthen group. Also I would like to thank her for permanent efforts in keeping the HERMES experiment running and improving.

Finally I would like to thank my family for their support that was essentially important for me during these several years of being abroad. And special thanks to my brother. Our long evening phone calls really gave me so the necessary connection with home.

# Lebenslauf

Name:	Mikhail Kopytin
Geburtsdatum	21.09.1977
Geburtsort	St. Petersburg, Russland
Staatsangehörigkeit	russisch
Jan. 2002–Jul. 2005	Wissenschaftliche Hilfskraft am Forschungsinstitut DESY in Zeuthen.
Jul. 2000–Dec. 2001	Wissenschaftliche Hilfskraft am Forschungsinstitut St. Petersburg Nuclear Physics Institute (PNPI), Russland.
Sep. 1994–Jun. 2000	Studium an der Saint-Petersburg State Technical University, St. Petersburg, Russland; Fach: Technische Physik.
Sep. 1985–Jun. 1994	physikalisch-mathematische Schule #470, St. Petersburg, Russland.
Sep. 1984–Jun. 1985	Schule #111, St. Petersburg, Russland.





# Selbständigkeitserklärung

Hiermit erkläre ich, die Dissertation selbständig und nur unter Verwendung der angegebenen Hilfen und Hilfsmittel angefertigt zu haben.

Ich habe mich anderwärts nicht um einen Doktorgrad beworben und besitze einen entsprechenden Doktorgrad nicht.

Ich erkläre die Kenntnisnahme der dem Verfahren zugrunde liegenden Promotionsordnung der Mathematisch-Naturwissenschaftlichen Fakultät I der Humboldt-Universität zu Berlin.

Berlin, 16.05.2006

Mikhail Kopytin.